RMIT University

School of Aerospace, Mechanical and Manufacturing Engineering

Numerical Modelling of Fluid-Structure Interactions for Fluid-Induced Instability in the Upper Airway

Mohammad Rasidi Rasini

Submitted in total fulfilment of the requirements of the degree of Doctor of Philosophy

March 2012

Abstract

This study is concerned with fluid-structure interactions (FSI) involved in the human upper airway, in particular, those associated with snoring and obstructive sleep apnoea/hypopnoea syndrome (OSAHS). Further examining this area of interest, the goal of the current research is to contribute further understanding and enhance development of computational modelling, for retroglossal obstruction and palatal snoring. To that end, the investigation was divided into three major parts. Firstly, extending previous laminar, 2-D reduced Navier-Stokes model, an idealised 3-D computational model was constructed for studying retroglossal obstruction. A full Navier-Stokes solver in an Arbitrary Lagrangian-Eulerian (ALE) framework was coupled to a linear thin shell, where both laminar and turbulent flow was investigated. Numerical results showed increase flow-induced tongue replica deflection under turbulent conditions and demonstrated cross-flow pressures that may encourage side wall collapse. In the second part of the thesis, palatal snoring was further examined and its potential to detect retroglossal obstruction was proposed. In order to investigate this, flow-induced instability of a cantilever plate in an obstructed channel was modeled and a relationship between critical velocity and obstruction depth was established. Correlating the critical velocity with typical breathing flow curve, a time difference between palatal snoring episodes or onset of palatal snoring, may represent a key variable for non-invasive measurement of retroglossal obstruction severity. Further enhancement of the 2-D computational model by including contact was proposed using an immersed boundary method (IBM). This may represent a more complete model of palatal snoring by modelling pre- and post-contact response of unstable cantilever plate, which showed potential to capture

more complicated palatal snoring signals. Finally, the third part of this thesis examined flow-induced instability of a soft palate in a 3-D realistic upper airway. To model this, a full 3-D Navier-Stokes solver under an ALE framework was coupled to a non-linear soft palate model. Appropriate soft palate properties were applied giving palatal snoring frequency within range of clinically measured values. Palatal flutter was observed at high flow rates, demonstrating irreversible transfer of flow energy to soft palate. This computational model may perhaps be exploited for future investigation of more accurate palatal snoring, necessary for developing non-invasive snoring signals for measurement or diagnosis of retroglossal obstruction.

Declarations

This is to certify that:

1. *except where due acknowledgement has been made, the work is that of the author alone;*
2. *the work has not been submitted previously, in whole or in part, to qualify for any other academic award;*
3. *the content of the thesis is the result of work which has been carried out since the official commencement date of the approved research program;*
4. *any editorial work, paid or unpaid, carried out by a third party is acknowledged; and*
5. *ethics procedures and guidelines have been followed*

MOHAMMAD RASIDI RASANI

Acknowledgements

I would like to express my gratitude to both my supervisors, Professor Jiyuan Tu and Dr. Kiao Inthavong for their advice and guidance during my PhD experience. I would like to thank the Ministry of Higher Education, Malaysia and Universiti Kebangsaan Malaysia for funding my studies and travels.

I would like to thank my fellow research colleagues, in particular, Qinjiang Ge and Pongpat Thavornpattanapong for their assistance and time during this project. I would also like to thank the High Performance Computing (HPC) facility group in RMIT University and LEAP Australia for all their technical support. In addition, I would like to thank Professor Charles S. Peskin, Professor Anthony D. Lucey and Dr. Franz Chouly for sharing their expertise in our many fruitful communications. I would also like to acknowledge Mrs. Jenny Smith in University of Melbourne for her proof-reading feedbacks.

Finally, special thanks to my family, relatives and friends for all their support and patience.

Contents

List of Figures

List of Tables

Nomenclature

Abbreviations

1-D	One–Dimensional
2-D	Two–Dimensional
3-D	Three–Dimensional
AHI	Apnoea-Hypopnoea Index
ALE	Arbitrary Lagrangian-Eulerian
BC	Boundary Condition
BMI	Body-Mass Index
CFD	Computational Fluid Dynamics
CPAP	Continuous Positive Airway Pressure
CT	Computed Tomogram
DNS	Direct Numerical Simulation
EDS	Excessive Daytime Sleepiness
EMG	Electromyogram
EVP	Eigenvalue Problem
FEM	Finite Element Method
FSI	Fluid-Structure Interaction
FVM	Finite Volume Method
IBM	Immersed Boundary Method
LES	Large Eddy Simulation
LHS	Left Hand Side
LNSE	Linearised Navier-Stokes Equations
MRI	Magnetic Resonance Imaging
NSE	Navier-Stokes Equations
PDE	Partial Differential Equation
PSG	Polysomnography
ODE	Ordinary Differential Equation
OSAHS	Obstructive Sleep Apnoea / Hypopnoea Syndrome
RANS	Reynolds-Averaged Navier-Stokes
RDI	Respiratory Disturbance Index
RHS	Right Hand Side
rms	Root Mean Square
RNSP	Reduced Navier-Stokes Prandtl
ROM	Reduced Order Model
SDB	Sleep-Disordered Breathing
SST	Shear Stress Transport
UARS	Upper Airway Respiratory Syndrome

Chapter 1

Introduction and Motivation

The behaviours of many dynamic systems are influenced by interaction between the fluid and structural components that are involved in the system. Typical examples include the flapping of insect wings, the flutter of flags under windy conditions, the hydrodynamic propulsion of swimming eels, the vibration of bridges during gusts, the oscillations of marine risers with sea currents and the aeroelasticity of aircraft wings. In recent years, with increasing interest in the multidisciplinary field of biomedical engineering, a lot of fluid-structure interactions (FSI) research has been applied to investigate and understand physiological systems in the human body. The opening and closing of real and artificial heart valves, the flow of blood in arteries, the opening and reopening of lung airways and the vibration of the vocal cords are some of the FSI system which have attracted much interest. Not least, research on dynamics of the upper airway is also involved with FSI. The interaction between the inhaled and exhaled air with the soft tissues of the upper airway, may lead to flow-induced instability and dynamics of surrounding tissues.

Obstructive sleep apnoea / hypopnoea (OSAH) and snoring are closely related conditions in the upper airway that are associated with FSI. A common condition during sleep, snoring may be either benign or perhaps an indication of a more serious disorder - obstructive sleep apnoea / hypopnoea syndrome, which has been linked to hypertension and cardiac failures. Coupled with experimental investigation and clinical studies, computational modelling and simulations have enriched our understanding of

the physiology and pathology involved with these conditions. The current research is primarily concerned with applying fluid-structure interaction modelling to further study these dynamics in the upper airway.

This introduction is organised into three parts. In the following section 1.1, the upper airway is presented to describe the relevant physiology and facilitate introduction for the rationale of the current project. Section 1.2 presents the motivation and objectives of the research, in view of current literature. Finally, the proceeding section 1.3 outlines the approach applied to answer the objectives of the project, together with the layout and overview of the thesis.

1.1 Flow-Induced Dynamics of Upper airway

1.1.1 Anatomy

The human airway, the primary organ involved in the respiratory system, can be broadly classified into the upper and lower airways. Apart from the important function of transferring oxygen into the blood and relieving the blood of carbon dioxide, the organs in the airway are also involved with speech production and transfer of solids or fluids into the digestive system. While the lower airway extends from the larynx and trachea to the bronchial tree and lungs, the upper airway, which is the primary focus of this thesis, extends from both the nasal and oral inlets to the larynx.

Air flows into the upper airway either through the nostrils or mouth (or both) and into the respective space inside the nose or mouth i.e. the nasal or oral cavity. The nasal cavity is divided by the nasal septum into two halves (left and right) that joins the nasopharynx via the posterior nares (left and right internal openings connecting the nasal cavity and the pharynx). The nasal and oral cavity are separated by the roof of the mouth, or palate. The hard and bony portion of the palate, located towards the front of the mouth, is the hard palate. Further behind, is a soft and fleshy portion of the palate called the soft palate that tapers down to a hanging, flapping piece of tissue called the uvula or velum.

Both nasal and oral cavities lead towards the pharynx, the tissue in the upper airway most vulnerable to collapse due to its lack of bony support. Its compliant walls are surrounded by dilator and constrictor muscles, which influence the patency of the pharynx, in competition with the aerodynamic forces generated from inspiratory and expiratory flow inside the pharynx. The pharynx is further divided into four sections, named according to the adjoining tissue where the pharyngeal section is located i.e. nasopharynx, velopharynx, oropharynx and hypopharynx. This is better illustrated in figure 1.1.

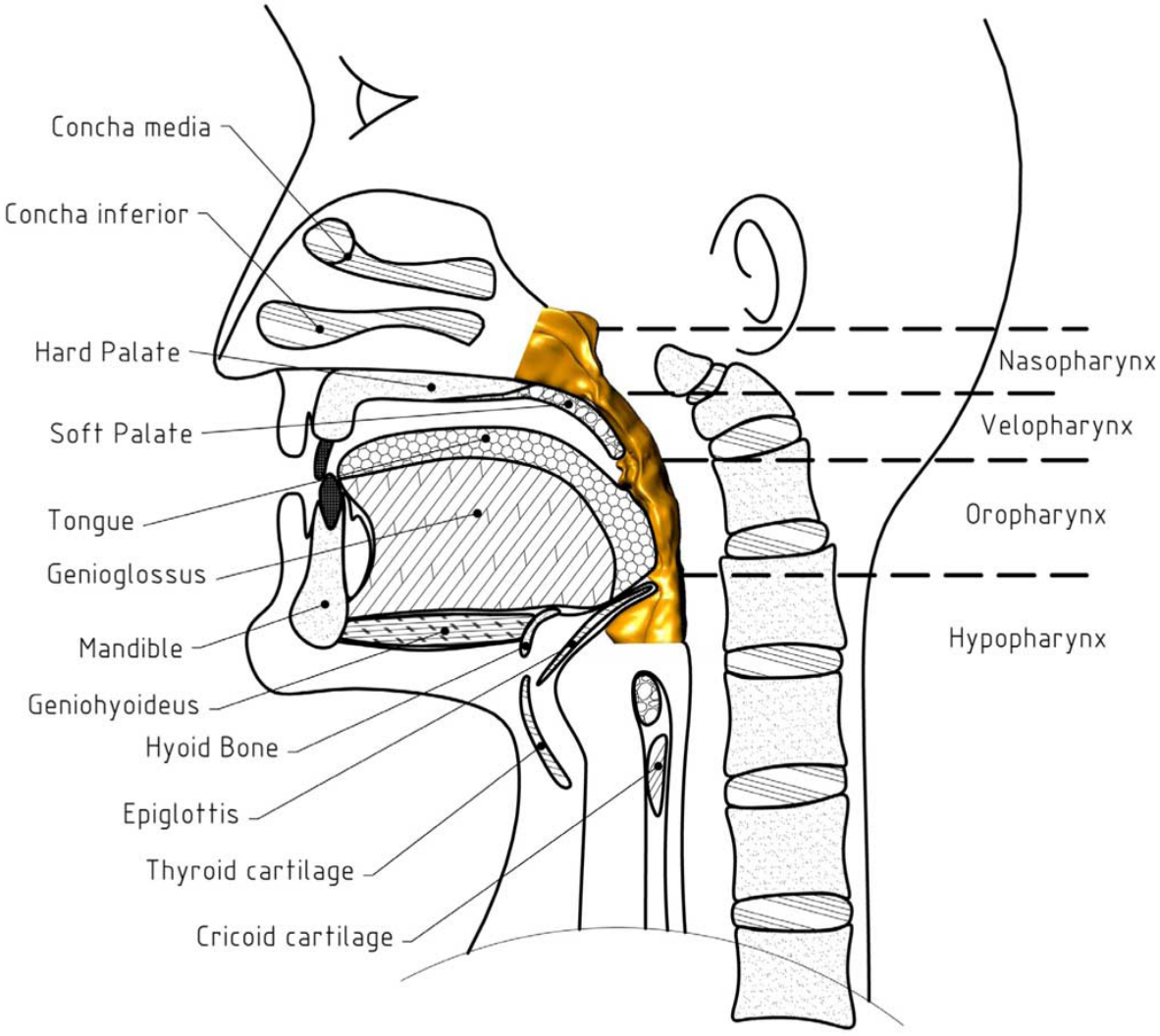

Figure 1.1: Mid-sagittal cross-section of the upper airway highlighting relevant anatomical structures and the pharynx (coloured), courtesy of Lucey *et al.* (2010).

In summary:

1. The *nasopharynx* extends from the end of the nasal septum (i.e. from the two posterior nares openings) to the upper surface of the soft palate or velum.

2. Further downstream, the *velopharynx*, is the portion of the pharynx adjacent to the soft palate (or velum).

3. From the free end of the velum to the hyoid bone or epiglottis, is the section of the pharynx behind the tongue or mouth, called the *oropharynx*.

4. The final inferior section of the pharynx, the *hypopharynx* or *laryngopharynx*, lies below the epiglottis adjoining the larynx.

1.1.2 Obstructive Sleep Apnoea / Hypopnoea Syndrome (OSAHS)

Disorders of the upper airway are fundamentally associated with respiratory issues or syndromes. Among these, sleep disordered breathing has attracted increasing attention in the medical field due to the increased awareness among the general public and the serious illnesses linked to some of these conditions. Obstructive sleep apnoea / hypopnoea syndrome (OSAHS), a primary type of sleep disordered breathing, affects an estimated 2-4% of the adult working population (Young *et al.*, 1993). In Australia, the prevalence of this syndrome is highlighted in a localised volunteer study by Bearpark *et al.* (1995), indicating 10-26% of middle-aged men in the sample having sleep apnoea of varying severity.

These OSAHS episodes are characterised by brief and repeated difficulty of breathing during sleep, associated with the collapse of the soft tissues within the upper airway. These disruptions could either be complete cessation of breathing during sleep, associated with the full collapse of the upper airway tissues, called apnoea, or significantly reduced breathing, associated with a partial collapse of the soft tissues in the upper airway during sleep, called hypopnoea (Malhotra & White, 2002; Ayappa & Rapoport,

2003; Eckert & Malhotra, 2008). Not surprisingly, this deprives the body and brain of essential oxygen, accompanied perhaps by recurring sleep arousals, which affects the quality of sleep. As a result, apnoeic individuals often exhibit excessive daytime sleepiness (EDS) or hyper-somnolence, fatigue and lack of concentration, which invariably, increases risk of accidents.

More seriously, apart from those obvious hazards just mentioned, the lack of oxygen saturation during sleep in apnoeic conditions has been linked to hypertension and heart failures (Bertram, 2008). Clinical evidence has implicated the elevated levels of hypoxemia (deficient oxygenation in the blood) and hypercapnia (increased carbon dioxide in the blood) associated with OSAHS, to the risk of developing hypertension (Peppard *et al.*, 2000; Malhotra & White, 2002). This is further supported by clinical trials showing marked reduction in blood pressure in individuals treated for OSAHS using Continuous Positive Airway Pressure (CPAP) therapy (Robinson *et al.*, 2004).

Although snoring does not necessarily mean an individual has sleep apnoea, an individual with OSAHS typically snores (Carroll *et al.*, 1995; Eckert & Malhotra, 2008). Huang *et al.* (1995) estimates that 10% of snorers are at risk of OSAHS. Based on the work by Bearpark *et al.* (1995), snoring among middle-aged Australian men is quite common (81% snore for 10% of the night) but, as mentioned earlier, a much lower proportion of the sample exhibit signs of sleep apnoea. However, it was noted that among the 22% who snore for 50% of the night, only 48% had no evidence of sleep apnoea, suggesting perhaps, a greater risk of OSAHS among habitual snorers. In fact, the study by Young *et al.* (1993) indicated that habitual snorers (either men or women) in their sample, showed a much severe degree of apnoeic episodes.

Consequently, diagnosing OSAHS from benign snoring (albeit, habitual snoring), requires identification of typical symptoms and further confirmation using polysomnography. From typical polysomnographic data, both flow rate and saturation levels of oxygen in the blood can be measured. Due to the subjective assessment of the accompanying symptoms, a typical apnoea episode is defined as when complete cessation of

breathing for at least 10s occurs, while, a typical hypopnoea episode is defined when oxygen desaturation exceeds 3-4%. The preceding criteria have been used in previous studies (for example, (Young *et al.*, 1993; Bearpark *et al.*, 1995)) and have been widely accepted (Chicago criteria) to interpret apnoea-hypopnoea episodes (Malhotra & White, 2002).

The average frequencies of apnoea or hypopnoea episodes per hour gives the apnoea-hypopnoea Index (AHI) or Respiratory Disturbance Index (RDI) scores, which reflects the severity of OSAHS in individuals. Young *et al.* (1993) categorise individuals with $5 \leqslant \text{RDI} \leqslant 15$ and accompanying symptoms of hyper-somnolence as having mild OSAHS. In some severe cases, RDI of more than 100 have also been reported (Eckert & Malhotra, 2008) and due to its relation to cardiovascular risks, individuals with high RDI are still classified as having the disorder, although no hyper-somnolence is exhibited (Malhotra & White, 2002).

1.1.3 Snoring

Snoring is sounds generated from the vibration of either individual or combination of multiple soft tissues in the upper airway. Apart from the unwanted noise to sleeping partners, snoring could either be tolerated or perhaps a symptom of much serious sleep disorder in the individual. Similar to OSAHS, several sites or types of snoring, which are associated with the vibrating soft tissue, have been identified. Palatal snoring is characteristically loud with low frequencies compared to snoring generated from vibration of the tongue or pharyngeal walls (Osborne *et al.*, 1999; Quinn *et al.*, 1996; Agrawal *et al.*, 2002). The loud but low snoring frequency of the flappy soft palate is perhaps not surprising, considering its relatively lower stiffness and size. This translates to lower fundamental frequencies and tendency for much larger oscillations (which may also impact the pharyngeal walls) generating louder noise compared to vibrations of other soft tissues.

The biomechanics of snoring is very similar to OSAHS and fundamentally involves

flow-induced instability of soft tissues in the upper airway (Huang *et al.*, 1995; Huang, 1995; Balint & Lucey, 2005). Thus, the stiffness and neuro-muscular tone of soft tissues, which influence the patency and collapsibility of the airway in OSAHS, also affects the propensity of snoring. Hence, not surprisingly, snoring signals may carry relevant information on the behaviour of airway tissues and have been a subject of much interest for OSAHS diagnosis (see for example, Mesquita *et al.* (2010); Fiz *et al.* (1996); Sol-Soler *et al.* (2007, 2002); Cavusoglu *et al.* (2008); Abeyratne *et al.* (2005); Lee *et al.* (2001); Dalmasso & Prota (1996). In addition, many of the treatments for OSAHS are equally effective in treating snoring, such as oral appliances (Stouder *et al.*, 2007) or surgical interventions (Jones *et al.*, 2005).

1.2 Motivation and Objectives

The current study is motivated by an intention to further understand the biomechanics involved in the dynamics of the pharyngeal airway, with a view to further explore computational methods as a tool in enhancing diagnosis and/or treatment for Obstructive Sleep Apnoea (OSA). Obstructive sleep apnoea and snoring has attracted much research, be it clinical, experimental or computational. The past two decades have seen much interest in modelling and understanding such episodes (see for example, (Lucey *et al.*, 2010; Xu *et al.*, 2009; Jeong *et al.*, 2007; Xu *et al.*, 2006; Balint & Lucey, 2005; Huang *et al.*, 1995)). From a fundamental perspective of investigating the biomechanics of both OSAHS and snoring, the pharyngeal airway has been likened to a collapsible tube or a starling resistor.

Collapse of the human pharyngeal airway during sleep affects 2-4% of adults (Chouly *et al.*, 2008) with an estimated 10% of snorers being at risk of obstructive sleep apnoea (Bertram, 2008). These episodes of partial or full cessation of breathing seem to occur either by the base of the tongue butting against the soft palate and posterior velo/oropharyngeal wall, or by the collapse of the side oropharyngeal walls, slightly further downstream. Extensive experiments on flow in Starling resistors and numerical

modelling of flow in compliant tubes, have revealed a rich variety of dynamics and instability modes involved in such systems (see for example, (Bertram, 2008; Luo & Pedley, 1995, 1996; Hazel & Heil, 2003; Heil & Waters, 2008)). In particular, highlighting the physics involved with collapse and self-excited oscillations of tubes under both external pressures (with/without wall tension) and internal flows. These perhaps resemble more a case of pharyngeal side wall collapse, where the walls are continuous and of somewhat homogeneous properties.

For investigating a case of a tongue butting against the velo/oropharynx, Chouly *et al.* (2008, 2009) and Van Hirtum *et al.* (2005) idealised the tissues of the tongue and pharyngeal wall as respectively, a hydrostatically pressurised latex tube and a rigid cylindrical wall. The collapse of the tongue replica onto the pharyngeal wall was simulated via in-vitro experiments to validate their model assumptions and numerical results. In the interest of obtaining reliable, real-time simulation, they had developed a two-dimensional asymptotic Navier-Stokes equation coupled to linear elastic shell elements to model flow-induced deformation of a simplified tongue subjected to expiratory flow. In general, narrowing of the airway promotes increased transmural pressure via a venturi effect, resulting in partial collapse of the airway and a non-linear flow rate retardation as the intraluminal pressure difference is increased - a typical observation in collapsed channel called flow rate limitation.

However, a three-dimensional full Navier-Stokes analysis had not been performed for this tongue occlusion replica. Furthermore, the development of a two-dimensional reduced Navier-Stokes model using asymptotic Prandtl's approximation by Chouly *et al.* (2008), represents a novel step towards efficient and real-time diagnostic models, which perhaps requires, for the next step, further assessment in contrast to full three-dimensional Navier-Stokes models (Van Hirtum *et al.*, 2007).

In addition, further investigation of the FSI effects of a turbulent flow instead of a laminar flow regime within the idealised airway is yet to be performed. Although, the Reynolds number of typical breathing flow is expected to be within a laminar or

transitional regime, the complex geometry of an actual pharyngeal airway may trigger earlier onset of transition or turbulence (Shome *et al.*, 1998) and is not unexpected, as indicated by recent CFD investigations (see for example, Mihaescu *et al.* (2008); Jeong *et al.* (2007); Mylavarapu *et al.* (2009); Xu *et al.* (2006)) that have adopted LES and RANS based turbulence models in their airway simulations.

The current accepted method of diagnosing OSAHS involves a full night's (8-10 hours') sleep polysomnography (PSG) that requires patients to be wired to a multitude of recorders and instruments, which is time-consuming, expensive and inconvenient (Lee *et al.*, 2001; Sol-Soler *et al.*, 2007). More importantly, this severely limits the capacity for mass screening of OSAHS in the general population which predominantly remains undiagnosed (Young *et al.*, 1997), especially with recent statistical data showing high prevalence of snoring and the high risk of OSAHS associated with habitual snorers (see for example, (Sol-Soler *et al.*, 2007; Abeyratne *et al.*, 2005)). Thus, the development of low-cost, simple and non-invasive techniques for screening OSAHS suitable for home testing and mass-screening has received much attention, not least via analysis of snoring signals.

Palatal snoring has been modelled using 2-D channel flow surrounding flexible cantilever plates by Huang (1995) and Balint & Lucey (2005), while, the biomechanics of pharyngeal-based snoring have been idealised as flow-induced oscillations of collapsible tubes or starling resistors (Huang *et al.*, 1995). Flutter and divergence mechanisms have been shown to generate instability in the soft palate and a critical Reynolds number or velocity for onset of this growth in palatal oscillation was demonstrated in a uniform channel cross-section (Balint & Lucey, 2005; Tetlow & Lucey, 2009). Further investigation of a non-uniform channel cross-section, representing some localised obstruction, may perhaps be useful for the analysis of snoring signals in occluded airways. In addition, further quantification of critical velocity for palatal flutter under localised occlusion may be of interest in developing non-invasive techniques for diagnosis of OSAHS in the mass population.

The unstable growth of palatal oscillation may eventually impact the pharyngeal walls, as demonstrated by idealised experiments in Huang *et al.* (1995). In their second experiment, collision between pharyngeal walls was characterised by a localised jump in oscillation frequency (Huang *et al.*, 1995), while Van Hirtum *et al.* (2007) alluded to influence of collision on onset of instabilities in their experiments on vocal cords. In addition, brief complete closure representative of airway walls colliding have been associated with snores of complex waveforms, while, vibrations without complete closure generates snores of simpler waveforms (Beck *et al.*, 1995). In summary, review of previous literature suggests the potential influence of soft tissue collision on snoring signals. However, thus far, 2-D channel models for palatal flutter have not included impact modelling and have not analyzed the influence of impact on the palatal oscillations or instability. Thus, further extending the current 2-D channel models to include collision modelling may assist in analyzing palatal snoring signals and may add further understanding of palatal flutter.

Development of computational models for diagnosis and treatment of OSAHS or snoring, with current computational resources, may favour simplified and efficient models for real-time clinical analysis. However, idealised models need to be verified with realistic models or clinical experiments, in order to appropriately assess its accuracy and assumptions. To the author's knowledge thus far, a realistic flow-induced instability investigation of the soft palate is yet to be undertaken, although many recent investigations on the upper airway have employed realistic geometries (see for example, Lucey *et al.* (2010); Mihaescu *et al.* (2008)). Hence, realistic 3-D upper airway computational models of flow and soft palate oscillation may improve understanding and enhance analysis of palatal snoring.

In summary, the specific research questions in the present work are:

- In comparison to development of 2-D tongue replica occlusion model, how does a full 3-D model and different flow regime affect the fluid-structure interaction?

- What is the relationship between severity of localised obstruction and onset of palatal snoring, and could it be employed to detect palatal-tongue occlusion?
- How does palatal collision with surrounding pharyngeal walls influence soft palate oscillation and hence, palatal snoring signals?
- How does a realistic 3-D model compare with simplified 2-D channel model of the upper airway for predicting palatal snoring?

1.3 Approach of the Present Study and Overview of Thesis

The current study is concerned with further understanding of upper airway dynamics in relation to soft tissue collapse and snoring in the vicinity of the palatal-tongue site. A computational approach is employed to develop models for analysis and contribute to further knowledge that may assist in diagnosis and treatment of OSAHS or snoring, although this thesis is not intended for clinical treatment or clinical studies of these conditions.

Although there are multiple sites for airway occlusion and snoring, this thesis is focused on the palatal-tongue region. It is proposed that the OSAHS mode of tongue-palatal collapse idealised in the earlier work of Chouly *et al.* (2008) be extended to a full 3-D model considering both laminar and low-Re turbulent flow conditions. Following this, computational modelling of palatal snoring is undertaken with a view to investigate potential non-invasive technique via snoring signals that may perhaps be employed for measurement and detection of tongue-palatal type OSAHS. Further computational analysis of palatal collision is performed in order to perhaps, enhance understanding of variation in palatal snoring signals. Finally, a realistic 3-D upper airway computational model is developed and analyzed to further validate and enhance analysis of palatal snoring.

The approach taken to answer the research questions are documented over the

following seven chapters. An overview of these chapters is presented below.

In chapter 1, the upper airway is introduced and the subject of OSAHS and snoring is presented. In view of current literatures and computational developments, the motivation and objectives of the present work is outlined and research questions formulated. Chapter 2 reviews literature relevant to this present work in more detail, summarizing current developments, approaches adopted in previous research and documenting current findings.

In order to answer the above research questions, the required techniques are first presented in chapter 3 under theory and computational methods. The mathematical formulations and discretization strategy for each fluid and structural domain is outlined, followed by formulation of the fluid-structure coupling. The numerical algorithm for implementing this fluid-structure interaction is described, in conjunction with stability issues and the means of mitigating them.

To meet the objective outlined in the first research question, chapter 4 presents the development of a simplified 3-D replica of the pharyngeal airway and tongue system. An ALE framework is employed to couple the quasi-steady 3-D flow to a quasi-static pressurised elastic shell representing the tongue replica. Prior to performing the required analysis, the model is first verified for grid-independence and sensitivity to outlet lengths, followed by comparisons to available fluid and structural results in the literature. Next, both laminar and low-Re turbulent conditions are simulated for quasi-steady breathing from $0 - 200$ Pa inlet pressures, for several variations of the parameters of interest, the details of which are provided in chapter 4.

Next, chapter 5 focuses on palatal snoring and introduces the current approach of modelling this using 2-D channel flow around flexible cantilever plates or beams. In order to answer the second research question, transient plate dynamics were coupled to unsteady 2-D channel laminar flow at several cases of localised obstruction depths and critical inlet velocities for onset of plate flutter is estimated for each obstruction case. A system perturbation of introducing initial second mode shape deflection in

the cantilever plate is used to assess stability in the fluid-structure system, similar to that employed by Balint & Lucey (2005); Tetlow & Lucey (2009). Correlating the results with breathing flow curves or snoring recordings, a method for exploiting palatal snoring signals for non-invasive detection of localised palatal-tongue occlusion is proposed. Following this, the third research question is also addressed in chapter 5 employing an immersed boundary method to model the elastic beam coupling with unsteady 2-D channel flow. The unsteady FSI simulation is extended several time steps to allow the unstable immersed beam oscillation to grow and impact the channel walls. Post collision beam profile is then further analyzed.

In chapter 6, the development of a realistic upper airway model coupled to a soft palate is presented. In order to meet the final objective, an unsteady 3-D flow of the airway, in an ALE framework, is coupled to transient dynamics of the 3-D soft palate. Similar to the 2-D case, an initial soft palate deflection is employed for system perturbation and the stability of the soft palate is analyzed by examining its deflection amplitude or system energy with time. Cases of oronasal inhalation, nasal inhalation and oral inhalation were experimented numerically and their respective stability analyzed in contrast to corresponding two-dimensional models.

Finally in chapter 7 responses and findings in relation to the proposed research questions are summarised, along with recommendations for future work.

Chapter 2

Literature Review

This chapter will briefly review literatures pertinent to investigations of the upper airway that involve fluid-structure interaction - in particular, those relevant to upper airway obstruction and snoring. A summary of this review chapter is presented in the final section, highlighting the research direction of the current thesis.

2.1 Computational Investigations

Detailed experimental or clinical studies to investigate flows in biomechanics may often be expensive or impractical due to the intrusive techniques or instrumentation involved. Alternatively, researchers have resorted to non-invasive approaches, such as computational fluid dynamics (CFD), to investigate flow physics and biomechanics in medical fields.

2.1.1 Realistic Upper Airway Modelling for OSAHS

Recent years have seen increasing computational modelling employing realistic models of the upper airway. Mihaescu *et al.* (2008) modelled a portion of the pharynx covering the nasopharynx, retropalatal and retroglossal sections, reconstructed from the magnetic-resonance images (MRI) of a patient with obstructive sleep apnoea. Both Reynolds-Averaged Navier-Stokes (RANS) and Large-Eddy Simulation (LES) were applied to model the transitional/turbulent flow in the pharynx. However, since the objective was to evaluate turbulence models under the complex flow curvatures of the

pharyngeal airway, interaction of the flow with the pharyngeal walls was not necessary to be considered and a pure CFD approach was employed. LES simulations under inspiratory flow proved more accurate than a RANS $k-\epsilon$ and RANS $k-\omega$ model in capturing flows with high curvatures and separation that are involved in the pharynx. In addition, computations of near wall pressure distribution suggest that between the RANS models, the largest deviation is exhibited between the LES and RANS $k-\epsilon$ results.

On the other hand, comparisons between more extensive turbulence models with experiments using an anatomically accurate physical model of the upper airway was performed by Mylavarapu *et al.* (2009). Axial MRI scans from the nasal to the trachea were obtained from a patient in supine position, allowing the airway boundaries to be identified at several elevations and the full 3-D surface (excluding oral cavity) to be reconstructed via surface triangularization, from which a 2:1 scale 3-D volume model was generated for CFD and experimental fabrication. SLA resin materials were used to fabricate the experimental model via a stereo lithography technique and multiple pressure ports were appropriately mounted along the 2:1 scaled model. Comparisons between a RANS $k-\omega$, RANS $k-\epsilon$, a SST variant of the RANS $k-\omega$ model, a one-equation Spallart-Allmaras model and LES turbulence models with experimental measurements were conducted under 200L/min expiratory conditions. Near wall static pressures results show RANS $k-\omega$ computations to be closest to the experimental measurements (to within 20%) compared to other turbulence models. Reasonable agreement with experiments suggest the validity of CFD as a non-invasive tool for capturing flows in the upper airway, and although pressure measurements are essential for predicting collapse in OSAHS, further velocity measurements may perhaps be necessary to complement and further assess the most appropriate CFD model. Although the realistic model is more extensive than those presented by Mihaescu *et al.* (2008), the oral cavity is not included and the airway walls are assumed to be rigid.

Xu *et al.* (2006) presented OSAHS investigation on children by reconstructing

patient-specific upper airway models from the MRI scans of 3 OSAHS patients and 3 non-OSAHS control subjects. A similar rapid prototyping technique of stereo lithography using a transparent polymer material, was employed to fabricate the airway specimen with several pressure taps fitted for measurements, which were used to validate the CFD simulations. A RANS $k-\omega$ turbulence model was used in the CFD model where atmospheric pressure was prescribed at the nostrils and appropriate sinusoidal velocity corresponding to inspiration and expiration flow rates was prescribed at the trachea. Although the scales differed between the in-vitro experiment and CFD models, dynamic similarity was maintained for both unsteady flow simulations and measurements at all pressure taps showed good agreement with CFD computations. Both nasal and pharyngeal resistance were measured as ratios, respectively of pressure at the choanae to the volumetric flow rate and of pressure difference between choanae and narrowest overlap region (velopharynx), to volumetric flow rate. Their results indicate that, in contrast to control subjects where a significant pressure drop occurred in the nasal section, for OSAHS subjects the pressure drop is largest in the pharyngeal section, corresponding to increased pharyngeal resistance associated with airway narrowing. In addition, both in-vitro experiments and CFD simulations suggest the likelihood of progressive narrowing during expiration, due to insufficient positive pressure developing in the narrowed pharynx as atmospheric pressure is recovered in the wider nasal passages. As in the previous investigation, the oral cavity was not included and a non-deforming pharynx wall was assumed, although a lumped-parameter model was proposed to qualitatively explore the effects of airway narrowing.

An anatomically-correct upper airway model reconstructed from computed tomogram (CT) scans was used by Jeong *et al.* (2007) in their CFD simulations of an OSAHS patient during steady quiet breathing. The airway cavity was identified via a threshold and segmentation function, from which further boundary smoothing algorithm was applied to generate a final 3-D model. In order to capture the transition from laminar to turbulent, a low-Re RANS $k-\epsilon$ model was employed, which was first validated

by comparison with LES, RANS $k-\epsilon$ model and experimental measurements for a stenotic circular tube setup as described in Luo *et al.* (2004) and Ahmed & Giddens (1983). Detailed computational results for a rigid upper airway suggest that minimum intraluminal pressures occur at the narrow velopharynx region, where high aerodynamic forces are generated as a result of turbulent jet forming through the constricted velopharynx cross-section.

In a much earlier work, Shome *et al.* (1998) constructed a 3-D anatomically-accurate model of the pharynx from digitised MRI scans of an OSAHS patient and various pharynx morphology representing three types of treatment - CPAP, mandibular repositioning device and surgical treatment. A pure CFD model with a rigid pharynx under steady flow conditions was assumed. Both RANS $k-\omega$ and RANS $k-\epsilon$ turbulence models were compared with a laminar model for a low inhalation flow rate corresponding to a laminar flow of $Re = 600$. Although it is accepted that a $k-\epsilon$ turbulent model is not necessarily accurate for highly curved flows, the $k-\epsilon$ pressure distribution closely matches the laminar pressure profile under these conditions, and is thus used for the remaining flow investigations. Computations at typical average and peak inspiratory flow rate show that flow Re in the pharynx lies within the laminar to turbulence flow regime, and that the pressure drop in the pharynx may vary from 200-500 Pa, with a 40% increase in pressure drop predicted if flow is turbulent in comparison to if flow is laminar. Their simulations also showed reductions in pressure drop corresponding to surgical alteration in the pharynx, application of CPAP or application of mandibular repositioning devices, hence, suggesting the effectiveness of these treatments in reducing the risk of pharynx collapse during sleep. In addition, despite relatively marginal improvements in cross-sectional area, a significant reduction in pressure drop was predicted for both CPAP and mandibular repositioning treatments, highlighting the influence of transitional to turbulent flow in the pharynx.

A numerical comparison of soft palate movement and flow characteristics between an OSAHS patient and a healthy subject during a relaxed breathing cycle (inhalation

/ exhalation) was undertaken by Sun *et al.* (2007). Although an idealised oral passage was used, a patient-specific upper airway model was reconstructed from CT scans of the nasal to the oropharynx. A RANS $k - \epsilon$ turbulence model was employed for the unsteady flow simulation, where atmospheric pressure condition was defined at the nasal inlets, while a sinusoidal velocity at the outlet was prescribed, corresponding to regular inspiratory and expiratory flow rates. For the soft palate, water-like properties were assumed and Young's modulus of $E = 1$ MPa, corresponding to simulated values for snoring from Auregan & Depollier (1995), was employed, in conjunction with linear strain-displacement theory. Fluid-structure interaction simulations showed higher displacements of the soft palate corresponding to development of a higher pressure and velocity gradient in the airway of the OSAHS subjects than in the healthy subject, which may be explained by the elongated soft palate of the OSAHS patient restricting the airway passage.

Classification of OSAHS severity is ascertained by the Apnoea-Hypopnoea Index (AHI) through overnight polysomnography, which is time-consuming and may not directly identify the source of occlusion in the airway. Vos *et al.* (2007) attempted to correlate image-based dimensions and resistance from CFD simulations to apnoea-hypopnoea indices, in order to predict the severity of OSAHS and help to assess the outcome of recommended OSAHS treatments. To meet their objective, 20 OSAHS patients underwent digitised CT scans, which enabled the airway cavity to be rapidly identified via some segmentation threshold and further smoothed to generate a 3D CAD model of the pharynx region in each patient. A steady, laminar flow simulation was undertaken with boundary conditions corresponding to polysomnography data, using a CFD solver, allowing the upper airway resistance to be estimated. Their results suggest the close correlation of minimum cross-sectional area and resistance, in combination with Body-Mass Index (BMI), to AHI results and thus represent potential markers for predicting degrees of OSAHS.

More recently, unlike previous MRI and CT scans, Lucey *et al.* (2010) inserted an

endoscopic optical probe through a fixed transparent catheter into a subject and captured multiple cross-sectional images using anatomical optical coherence tomography (aOCT) technique . This enabled 3-D reconstruction of various pharynx morphology over time, corresponding to the complete quasi-steady inhalation cycle. Steady flow simulation was undertaken using a RANS $k - \omega$ shear stress transport (SST) turbulence model with various time-dependent pharynx geometry, assuming quasi-static conditions. Flow computations suggest presence of strong cross-flow pressure gradient with suction side wall pressures, that are further aggravated by soft palate displacement and side wall deformation. In addition, an index-law correlation between pressure and cross-sectional area, which closely trends 1-D Bernoulli theory, was demonstrated and proposed, suggesting the possibility of pressure prediction in patients.

In a closely related set of articles, mid-sagittal and para-sagittal slices from MRI scans of normal and OSAHS subjects were used to reconstruct anatomically-accurate, but 2-D model (Huang *et al.*, 2005*a*,*b*) and a partially 3-D model (Huang *et al.*, 2007*b*) of the pharyngeal airway, including the soft palate and tongue. A finite element method (FEM) was employed to solve both structural (soft palate and tongue) deformation and flow dynamics in the pharynx, which was assumed laminar with prescribed inlet and outlet pressures. Their fluid-structure interaction simulation was used to predict the collapse pressure when the tongue and/or soft palate occluded the airway, for various surgical treatments (anatomical excisions and stiffening) and simulated mandibular advancement. Furthermore, a novel genioglossal muscle contraction model, based on correlation with in-vivo electromyogram (EMG) reading, was presented in Huang *et al.* (2005*a*) to simulate the effect of tongue response to both negative airway pressure and sleep/awake states, hence considering another factor in maintaining airway patency - muscle activity.

2.1.2 Idealised Models for OSAHS

The recurring partial or full collapse of the pharyngeal airway during OSAHS is very closely related to flow in compliant tubes or channels that experience a Venturi effect. Extensive experiments on flow in Starling resistors (an elastic fluid-filled collapsible-tube mounted inside a chamber filled with air) have revealed a rich variety of dynamics involved in such compressed collapsible tube systems (Bertram *et al.*, 1990, 1991). Not surprisingly, many numerical models have been developed to simulate the system and theorise the mechanisms involved during the collapse and self-excited oscillations seen in the experiments. Earlier models include lumped parameter models (Katz *et al.*, 1969) which integrated the flow variables along the whole vessel and various one-dimensional models (eg. Luo & Pedley (1995); Pedley (1992); Shapiro (1977)), taking into account variation of flow variables in the longitudinal direction along the vessel but assuming those variables do not vary within each cross section.

More complicated two-dimensional models have been developed capturing the compliant wall oscillations and more realistic flow separations. Starting out with successive iterations for coupling two-dimensional steady flow with a thin membrane, Luo & Pedley (1995) demonstrated numerical breakdown of steady solutions at conditions close to self-excited oscillations observed in experiments. Following that work, Luo and Pedley solved a two-dimensional flow interaction with a thin membrane, revealing the conditions (a function of Reynolds number and membrane tension) in which steady solutions become unstable as the upper membrane tension falls below a certain critical value under the influence of self-excited oscillation and vorticity waves in the flow. This critical value decreases as the Reynolds number increases (Luo & Pedley, 1996). The influence of wall inertia on the two-dimensional collapsible channel flow was also investigated, showing higher frequency flutter-like mode dominating the self-excited oscillations (Luo & Pedley, 1998).

More recently, three-dimensional models of the collapsible tube have also been developed. Hazel & Heil (2003) applied a fully coupled approach to the steady three-

dimensional Navier-Stokes equation for a geometrically non-linear shell, to capture both strong buckling of the tube and the developments of flow field downstream of the tube collapse. A further study aimed at developing time-dependant three-dimensional flow interaction with shell tubes, revealed a mechanism for flow-wall energy extraction and possible critical Reynolds number for onset of self-excited oscillations (Heil & Waters, 2008). In general, non-linear membrane and shell theories have been applied to both the two- and three-dimensional collapsible tube models to account for large wall deformations, allowing complex structural responses to be simulated.

The current challenge, following Bertram (2008), is to apply or adopt these developments of flow in collapsible tubes to actual physiological phenomena. Chouly *et al.* (2008, 2009) and Van Hirtum *et al.* (2005) developed an asymptotic Navier-Stokes equation coupled to linear elastic shell elements to model flow-induced deformation of a simplified tongue subjected to expiratory flow. The collapse of the tongue onto the pharyngeal wall was also simulated via in-vitro experiments using a hydrostatically pressurised latex tongue replica interacting with air flow through a circular duct, in order to validate their model assumptions and numerical results. In general, narrowing of the airway promotes increased transmural pressure through a Venturi effect. This results in partial collapse of the airway and a non-linear flow rate retardation as the intraluminal pressure difference is increased - a typical observation in collapsed channel called flow rate limitation. Indeed, based on the Reynolds number, the flow is expected to be within the laminar ($Re < 2000$) or transitional ($2000 < Re < 10000$) regime. However, the complex morphology of the pharyngeal airway could give rise to three-dimensional flow features which triggers transition and turbulence at lower Reynolds number (Shome *et al.*, 1998). In fact, observation by Hahn (1992) suggests turbulence kinetic energy at approximately 5% of the inlet velocity is not unexpected in the nasal cavity.

2.1.3 Flow-induced Instabilities

Boundary layer transition from laminar to turbulent over a rigid structure is caused by growth of instability modes in the form of Tollmien-Schlichting waves and is hence classified as purely flow-based instability. However, for a compliant or flexible structure in flows, apart from this flow-based instability, structural-based instability induced by the flow may also be present (Balint, 2001). This flow-induced instability of the structure may be classified as either quasi-static divergence type instability or travelling wave flutter type instability. Unlike Tollmien-Schlichting waves, which are stabilised by irreversible energy transfer from the flow to the compliant structure, travelling wave flutter is destabilised by this flow to structure energy exchange.

Instability of cantilever plates or beams interacting with air flow have been studied extensively to model physical phenomenon such as flag flutter and palatal snoring. Earlier investigation on these aeroelastic instabilities had assumed 2-D flows that are inviscid, which lends to development of analytical models using potential flow and Bernoulli principles. Auregan & Depollier (1995) investigated a cantilever beam immersed in channel flow, both analytically and experimentally, intended to understand snoring. Using linear small deflection beam theory, the dynamic equilibrium between internal bending forces and inertia of the beam is balanced by the applied pressure difference on the beam surfaces. This fourth-order partial differential equation for beam bending was solved by employing a Galerkin method and expressing the beam deflection as linear combination of its fundamental modes. Neglecting frictional losses and assuming quasi-parallel flow, the pressure difference applied on the beam was estimated from mass conservation and Bernoulli equation. In addition, an in-vitro experiment on a flexible elastomer beam inserted with piezo-electric film to record its motion inside a channel of flowing air, was also performed. Close agreement between theoretical and experimental results confirmed the flutter type instability exhibited by the soft palate.

Unlike Auregan & Depollier (1995), Huang (1995) modelled a flexible cantilever plate immersed in axial flow not bounded by channel walls. A similar fourth-order

partial differential governing equation for linear beam bending under pressure differential was solved using finite expansion of the orthogonal in-vacuo fundamental mode series of the beam. For the flow, although viscous effect of circulation is indirectly imposed by the Kutta-Zhukovskii condition at the trailing edge of the plate, viscosity is neglected and potential flow theory was used, with pressure loads estimated from Theodorsen's classical solution for wing aerodynamics. This enabled Huang to show that the circulatory component of the fluid loading resulting from reaction to the trailing wake vortices are responsible for the irreversible, flow to plate energy transfer that destabilises the system. Further wind tunnel experiments were also undertaken to verify the linear theoretical results, showing short cantilever plates, relevant to palatal snoring, undergoing gradual flutter.

Guo & Paidoussis (2000) analytically investigated linear stability of rectangular plates with different leading and trailing edge support conditions, assuming inviscid 2-D channel flow. Similarly, a Galerkin method is applied to solve the 1-D linear plate motion equation where plate deflections were recast as expansion series of beam eigenmodes, while a Fourier technique was applied to solve the perturbation pressure estimated from potential flow theory. Their numerical results suggest that plates supported (either clamped or pinned) at both leading and trailing edges, first lose their stability through divergence before other types of instability modes, due to large, destabilising fluid pressures. While, single-mode and coupled-mode flutter dominate for plates with a free trailing edge and free-free edges, respectively.

More recent computational investigations of axial flow surrounding cantilever plates were developed by Tang & Paidoussis (2007, 2008) but considering non-linear large plate deflection using an inextensibility condition. Although a separate viscous drag was coupled into the plate motion equation, the flow was assumed inviscid and the imposed pressure difference on the plate was estimated using an unsteady lumped vortex model. Thus, the effects of drag on the plate tension and the coupling of large bending with in-plane forces in the plate were taken into account. Analytical results

shows increase in critical flutter velocity and frequency with increase in drag coefficients (Tang & Paidoussis, 2007). In addition, experimental observations have reported sudden flutter vibration at critical velocities, but if instead flow velocity is reduced from an initial plate flutter, the onset of stability is lowered - demonstrating hysteresis behavior with subcritical bifurcation. Tang & Paidoussis (2007) demonstrated the possibility of this hysteresis phenomenon by introducing a steady von-Karman vortex street in their simulation. Further theoretical investigation on the effect of trailing edge wakes on plate instability, shows plates of increasing lengths exhibiting higher critical frequencies, suggesting the diminishing influence of the wake with increasing plate length Tang & Paidoussis (2008).

The investigations described above have assumed inviscid flows to develop analytical models for flow-induced instability, which demonstrate two types of flutter (Balint & Lucey, 2005). For external flows without bounding walls, the finite length of the cantilever plate promotes wake-induced aerodynamic loads that are out-of-phase with the plate motion, as investigated in Huang (1995); Tang & Paidoussis (2007, 2008). While in bounded flows, the out-of-phase pressure loads with the cantilever plate motion, as the plate alternately restrict the top and bottom channel cross-section, may also lead to flutter as demonstrated in Auregan & Depollier (1995); Guo & Paidoussis (2000); Balint & Lucey (2005).

Balint & Lucey (2005) and Tetlow & Lucey (2009) instead considered viscous effects in their instability analysis by solving the Navier-Stokes equation in a 2-D channel flow surrounding a cantilever plate. In Balint & Lucey (2005), a linear plate bending theory under differential pressure was used and solved using finite difference method, while in Tetlow & Lucey (2009), an in-plane shear force was added to the linear plate equation of motion. In both investigations, the finite element method was employed to solve the unsteady, laminar Navier-Stokes equation and estimate fluid loads interfacing with the plate, which was explicitly coupled to the structural finite difference solver. Numerical results demonstrate that when both upper and lower inlets are open, a flutter-type

instability is initiated at a critical Reynolds number, due to viscous effects rather than time-dependent flow separation off the plate trailing edge. Instead, if one of the inlets is closed, a divergence-type instability occurs at a critical velocity. Despite predicting lower flow to plate energy exchange, Tetlow & Lucey (2009) showed that similar flutter phenomenology is demonstrated if the 2-D channel is driven by pressure difference instead of velocity-driven flow as applied in Balint & Lucey (2005).

2.2 Clinical Studies

2.2.1 Obstructive Sleep Apnoea

Obstructive sleep apnoea / hypopnoea syndrome (OSAHS) is characterised by recurring episodes of partial or full collapse of the human pharyngeal airway during sleep. It has been reported that OSAHS affects 2-4% of adults (Young *et al.*, 1993) with an estimated 10% of snorers being at risk to obstructive sleep apnoea (Bertram, 2008). These episodes of partial or full cessation of breathing influence the quality of sleep, reduce brain oxygen saturation and have been linked to hypertension and heart failures (Bertram, 2008). Both neurological and physiological factors have been implicated with apnoeic syndrome. Previous studies, including Rodenstein *et al.* (1990), Maltais *et al.* (1991) and Yucel *et al.* (2005), have shown that apnoeic patients have, in general, a narrower opening in the oropharynx region (perhaps due to obesity or tissue build-up). Furthermore, snorers with and without sleep apnoea have smaller pharyngeal cross-sectional areas than non-snorers and snorers with sleep apnoea have a further decrease with a reduction in lung volume (Bradley *et al.*, 1986). Pharyngeal compliance among apnoeic and non-apnoeic subjects have also been shown to vary significantly, especially during expiratory flow (Brown *et al.*, 1985).

Rodenstein *et al.* (1990) studied 17 male subjects, with complaints of snoring, under full night polysomnography to classify subjects with OSAHS or simple-snorers. Further MRI scans of the pharynx of each subject, in addition to 8 healthy subjects, were captured, in order to assess potential markers in terms of shape and dimensions that

(a)

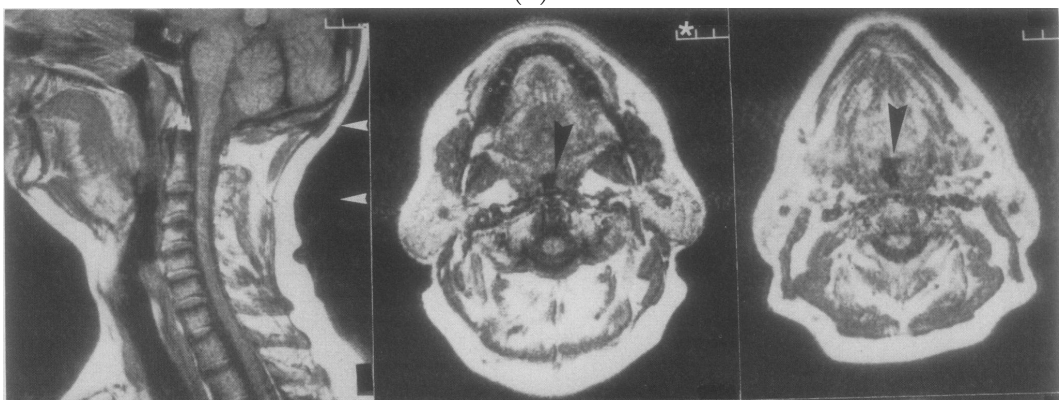

(b)

Figure 2.1: MRI scans, courtesy of Rodenstein *et al.* (1990), showing the sagittal slice on the left image and two transverse slices taken at the heights indicated by the white arrows (middle image at top arrow and right image at bottom arrow) corresponding to (a) A normal subject and (b) An OSAHS patient

may distinguish between each group. Their study shows that apart from the obvious reduction in pharyngeal diameter in groups with OSAHS, a change in cross-sectional shape of the pharynx may indicate a risk of developing sleep apnoea. It was reported that in normal subjects the pharynx is elliptical in shape with the major axis aligned in the left-right direction, while in snorers or OSAHS subjects the pharyngeal cross-section may be circular or elliptical but with the major axis aligned in the anterior-posterior direction, which is illustrated in Figure 2.1 (reproduced from Figures 3 and 5 in Rodenstein *et al.* (1990)).

Factors

Previous clinical studies have suggested certain factors as having higher propensity of OSAHS. The major risk factors include obesity, sex (males have higher have a higher

risk of OSAHS), ageing, alcohol consumption and to a lesser extent, menopause for women and smoking (Strobel & Rosen, 1996; Malhotra & White, 2002; Owens *et al.*, 2008). In their study, Bearpark *et al.* (1995) showed significant correlation between high body-mass index subjects with sleep apnoea and according to Malhotra & White (2002), obesity accounts for an estimated 70% of OSAHS patients. In regards to prevalence of OSAHS with gender, Young *et al.* (1993) showed in their middle-aged adult sample that 24% of men compared to 9% of women exhibit RDI $\geqslant 5$.

Although the narrowest segment of the velopharynx is a likely site for airway obstruction, some OSAHS patients could perhaps have multiple sites of airway collapse. These include tongue contact with the soft palate that butts against the posterior upper airway walls and the collapse of the side pharynx walls in the velopharynx-oropharynx region (Lucey *et al.*, 2010). Both anatomical and neurological factors have been implicated in the pathogenesis of this tissue collapse in OSAHS, which could explain the risk factors mentioned previously. The collapsibility and patency of the upper airway is influenced by both the passive mechanical properties of its soft tissues and the activation of dilator muscles supporting it, in competition with luminal pressures developed during breathing (Malhotra & White, 2002; Ayappa & Rapoport, 2003). Reflexes of various upper airway muscles, often stimulated by negative breathing pressures, are somewhat reduced during sleep, rendering their increased compliance (Huang & Williams, 1999; Huang *et al.*, 2005*a*).

In order to assess anatomical factors and isolate neuromuscular factors, complete muscular paralysis (via general anaesthesia) was applied in various investigations by Isono *et al.* (1997*a*,*b*, 1998) showing a tendency of OSAHS patients to have significantly smaller cross-sectional areas in critical segments of the airway than normal individuals, which interacts with breathing efforts, influencing flow impedance and increasing critical pressures at which these segments collapse. Reduction in airway opening is often due to hypertrophy of tissues and increased fat deposits on tissues around the upper airway, explaining the propensity of OSAHS with obesity (Davies *et al.*, 1992; Malhotra

& White, 2002). Other anatomical factors, such as upper airway length and soft palate size have also been argued to increase compliance of the upper airway, suggesting the male predisposition to OSAHS compared to females (Malhotra *et al.*, 2002). Indeed, although not entirely conclusive, ageing is also expected to increase the compliance of tissues in the upper airway and thus, increased prevalence of OSAHS, as shown by the reduction in elasticity of the genioglossal muscle (Veldi *et al.*, 2004) and development of potential anatomical markers for OSAHS with age (Maltais *et al.*, 1991; Johnston & Richardson, 1999).

Treatment

Treatments of OSAHS have been focused mainly on addressing the physiological factors involved with the disorder. Among these, the nasal Continuous Positive Airway Pressure (CPAP) has proven to be most common and effective (Engleman *et al.*, 1994*b*; Robinson *et al.*, 2004). This therapy involves doses of positive air pressure supplied to OSAHS patients in order to maintain patency of the upper airway during sleep. Additional air pressure is supplied via a mask and tube connected to a motorised pump and normally, a system is in place to detect pressure or flow resistance during breathing, in order to control the doses of air titration required. Major drawbacks detracting patients from using CPAP (some 5-50% reject its usage within the first week, according to Engleman & Wild (2003)) are mainly related to comfort of use to the somewhat obtrusive device and tolerance to pressures supplied (Engleman *et al.*, 1994*a*). Some examples include reports of nasal congestion, sinus infections, dizziness, irritations and a much serious, fungi infection. Significantly, however, cognitive behavioural interventions have been shown to improve patients' receptivity to CPAP (Engleman & Wild, 2003; Richards *et al.*, 2007).

Another possible treatment of OSAHS involves using oral appliances to adjust the mandible and tongue postures to improve airway patency, such as custom made Mandibular Advancement Splints (MAS) mouthguards (Gotsopoulos *et al.*, 2002; Zhao *et al.*, 2010). Although its efficacy is lesser than CPAP, studies have indicated improve-

ments in Apnoea-Hypopnoea Indices (AHI) and more importantly, it is tolerated and preferred by more OSAHS patients (Schmidt-Nowara *et al.*, 1995; Ferguson *et al.*, 2006).

Normally a final option, surgery could also be recommended to remove or manipulate relevant soft tissues in the upper airway, which could alleviate snoring, reduce collapse of the soft tissues or improve upper airway patency. These include uvulopalatopharyngoplasty (excision of portions of the uvula/soft palate), inferior sagittal mandibular osteotomy and genioglossal advancement, maxillomandibular osteotomy and advancement (Sher *et al.*, 1996; Huang *et al.*, 2005*b*; Huynh *et al.*, 2009) or stiffening the soft palate via implants (Walker *et al.*, 2004) or radiofrequency scarring (Troell *et al.*, 2000). The main problem with this treatment is the fact that it is often irreversible and reported efficacy is not necessarily as good as either CPAP therapy or using oral appliances, which could perhaps be explained by patients having multiple obstruction sites and thus requiring multiple surgeries rather than single operation (Sher *et al.*, 1996; Owens *et al.*, 2008). Hence, pre and post-operative strategies to identify critical sites and predicting success of surgical options are essential in these situations.

The degree of interaction between anatomical (for example, airway cross-sectional size, soft palate volume etc.) and neurological factors (such as sensitivity to respiratory resistance, onset of arousal etc.) to the pathology of OSAHS may likely vary between patients (Eckert & Malhotra, 2008). Hence, the importance of identifying and assessing the extent of each pathophysiological causes to OSAHS for each patient and recommending the appropriate treatment strategy.

2.2.2 Snoring

Snoring may be classified by different sites of snoring that produce distinct noises at different frequencies. Palatal snoring is characterised by relatively loud peaks at low frequencies Osborne *et al.* (1999); Quinn *et al.* (1996). Quinn *et al.* (1996) recorded snoring signals from 10 subjects that showed distinct difference in waveforms between

palatal and tongue-based snoring. Palatal snoring demonstrate low frequency sounds within a narrow spectral band, while tongue-based snoring exhibits higher frequencies with much broader spectral range. Osborne *et al.* (1999) deduced palatal rattling frequency occurring at approximately 20 Hz from digital recordings of subjects under sleep endoscopy, which is within the 20-320 Hz frequency reported for palatal snoring by Brietzke & Mair (2006) in their clinical findings. In another clinical study, Agrawal *et al.* (2002) reported palatal-based snoring occurring at low frequencies with peaks at 137 Hz, while tongue-based snoring had much higher frequency peaks of 1243 Hz and medium-range frequencies (with peaks of 490Hz) were associated with epiglottic snores.

Snoring and OSAHS share similar biomechanics, and several studies have suggested that OSAHS is more likely in snorers than non-snorers (Huang *et al.*, 1995; Sol-Soler *et al.*, 2007). Not surprisingly, this close relationship between snoring and OSAHS has prompted many clinical studies to detect OSAHS via snoring signals, which may facilitate mass-screening of OSAHS in the general population. Perez-Padilla *et al.* (1993) analyzed snoring signals from 10 non-apnoeic snorers and 9 OSAHS patients. Post-apnoeic snores demonstrate a distinctively broad spectrum with many high frequencies, which may allow the ratio of power above and below 800 Hz to be exploited for differentiating simple snorers from OSAHS patients.

In several articles, a research group in Spain has undertaken active clinical studies exploiting snoring signals for diagnosis of OSAHS. In their clinical investigation, Jan *et al.* (2003) and Sol-Soler *et al.* (2005) showed snore signal variability to be higher in OSAHS patients, which may increase with severity of OSAHS, and thus may represent a potential marker to detect OSAHS. In an earlier study, Sol-Soler *et al.* (2002) investigated the correlation between both mean and standard deviation of the pitch in snoring signals with AHI as a means to estimate the severity of OSAHS. It was also found that the standard deviation of formant frequencies in OSAHS snoring spectrum are significantly higher than those in simple snorers (Sol-Soler *et al.*, 2003). While, in a

clinical study by Fiz *et al.* (1996), snoring power spectrum are clustered in a narrower band with lower peak frequency in OSAHS patients than in simple snorers.

In a clinical study by Lee *et al.* (2001), analysis of formant frequencies in conjunction with bispectrum plots of acoustics from snoring subjects show distinct differences between apnoeic and benign snores, suggesting another means of distinguishing OSAHS from simple snorers. Cavusoglu *et al.* (2008) analyzed the mean, standard deviation and coefficient of variation (CoV) in duration of snoring episodes, separation between snoring episodes and average power of snoring episodes from snoring sound records of 30 subjects. Their clinical findings showed that OSAHS patients tended to have higher variations of these parameters than simple snorers and further proposed a combined mean, standard deviation and CoV spider chart to strongly discriminate between simple snorers and OSAHS patients.

2.3 Experimental Studies

Huang *et al.* (1995) performed in-vitro experiments idealizing palatal and pharyngeal snoring. A piece of soft leather attached to a plate of wood is mounted inside a perspex tube with air flow generated by a suction pump, to simulate palatal snoring in the airway. Their experiments showed presence of a critical velocity, above which, the hanging soft leather starts to oscillate at small amplitudes, which grows over several cycles before flapping violently and hitting the tube wall, consistent with the phenomenon of flutter. Idealizing the pharynx by a thin, compliant rubber tube attached to a suction pump in one end and exposed to the atmospheric pressure at the other end, pharyngeal snoring was simulated. Although, flutter was not evident in their experiments, static divergence was demonstrated prior to impact or collapse of the tube walls, which then reopens rapidly much like a 'water-hammer' condition.

The latter experiment performed in Huang *et al.* (1995) resembles that of a Starling resistor (an elastic fluid-filled collapsible-tube mounted inside a chamber filled with air). The Starling resistor analogy has been used to describe the dynamics of OSAHS or

snoring. Extensive experiments of flow in Starling resistors have revealed a rich variety of dynamics involved in such compressed collapsible tube systems (Bertram *et al.*, 1990, 1991). In-vitro experiments by Bertram & Tscherry (2006) carefully predicted the critical Reynolds number for the onset of self-excited oscillations and showed the influence of viscosity on the stability of the collapsible tube system. Although this may not entirely reflect airway conditions, where the wall density is greater than the fluid density, this may provide some insight into phenomenon of flow-rate limitation and flow-induced instability of the pharynx.

2.4 Summary of Literature Review

Although many aspects of OSAHS and snoring have been investigated and reported in the literature, further configuration proposed in this thesis may yet be explored. To reiterate, the specific research questions in the present work are:

- In comparison to development of a 2-D tongue replica occlusion model, how does a full 3-D model and different flow regime affect the fluid-structure interaction?
- What is the relationship between the severity of localised obstruction and onset of palatal snoring, and could it be employed to detect palatal-tongue occlusion?
- How does palatal collision with surrounding pharyngeal walls influence soft palate oscillation and hence palatal snoring signals?
- How does a realistic 3-D model compare with a simplified 2-D channel model of the upper airway in regards to predicting palatal snoring?

Chapter 3

Theory and Computational Methods

This chapter describes the theoretical background involved in computational modelling of fluid-structure interactions, which fundamentally requires simultaneous solution of both fluid and structural fields such that at their common interface, the kinematic and dynamic boundary conditions are satisfied. In general, this coupling could be solved numerically, either through a monolithic approach or by a partitioned approach. In a monolithic approach, the governing equations for both the fluid and structural fields (including the intra-field influence at the common interface) are augmented and solved together. Although such scheme is devoid of 'added-mass' instabilities in the fluid-structure coupling, it obviously lack the ability to use available highly-developed solvers in each field and typically suffers from oversized, ill-conditioned matrices. Although much improvement has been made, for example, with the application of preconditioners and efficient GMRES schemes to improve robustness of the approach (see for example (Heil, 2004)), a segregated or partitioned approach is still considered attractive.

In this thesis, a partitioned approach is undertaken using the commercial software ANSYS, either version 12.0 or 13.0. The theory for the partitioned fluid-structure coupling begins with the formulation for the fluid solver in section 3.1, followed by the formulation for the structural solver in section 3.2. In section 3.3, the fluid-structure interface conditions are presented, highlighting the coupling scheme and numerical

issues involved with this partitioned approach. Finally, section 3.4 presents the theory for the immersed boundary method and describes its implementation inside ANSYS using user-defined routines.

3.1 Mathematical Formulation for Fluid

3.1.1 Laminar Flow

It is assumed that compressibility and influence of temperature are negligible in the flow during breathing. Furthermore, the fluids involved are assumed Newtonian, implying a linear relationship between shear stresses and rate of shear (velocity gradient) in the fluid, by a constant kinematic viscosity. Thus, the well-known incompressible form of the Navier-Stokes equation and the continuity equation should be sufficient to describe the physics in this study. In a fixed Eulerian frame of reference in space (non-deforming grid) of the fluid domain, for a laminar flow, these are given by

$$\frac{\partial u_i}{\partial t} + u_j \frac{\partial u_i}{\partial x_j} = -\frac{1}{\rho}\frac{\partial p}{\partial x_i} + \frac{\partial}{\partial x_j}\left\{\nu(\frac{\partial u_i}{\partial x_j} + \frac{\partial u_j}{\partial x_i})\right\} \tag{3.1}$$

$$\frac{\partial u_i}{\partial x_i} = 0 \tag{3.2}$$

where u_i and p are respectively the fluid velocities and pressure ($i = 1, 2, 3$ for three-dimensional analysis), ρ is the constant fluid density and ν represents the fluid kinematic viscosity. Equation (3.1) represents the conservation of momentum, balancing the fluid acceleration (terms on the LHS) with the applied fluid stresses (terms on the RHS). The first term on the LHS represents the localised acceleration (or unsteady) term, followed by the non-linear convective terms ($\mathbf{u}\cdot\nabla\mathbf{u}$). While, the first term on the RHS represents the pressure gradient (a source term that encourages flow depending on the sign of the gradient) and the second term on the RHS represents the diffusion terms (relating to frictional viscous losses that inhibit flow). Equation (3.2) describes the conservation of mass in the fluid domain. Equations (3.1) and (3.2) represent the fluid governing equations which are solved by the fluid solver.

3.1.2 Turbulent Flow

Turbulent flow involves highly fluctuating flow variables with varying eddy scales, which may be modeled more accurately using Direct Numerical Simulation (DNS) or Large Eddy Simulation (LES). However, such methods are computationally intensive and more practical Reynolds-Averaged Navier Stokes (RANS) models are typically preferred. In the current work, unsteady, incompressible, turbulent flow is described using the Reynolds-Averaged Navier Stokes (RANS) equations coupled to a Shear Stress Transport (SST) k-ω turbulent model, which is essentially similar in form to the laminar transport equations above, except for instead employing time-averaged flow variables and the addition of a turbulent stress tensor (ANSYS Inc., 2010):

$$\frac{\partial \overline{u}_i}{\partial t} + \overline{u}_j \frac{\partial \overline{u}_i}{\partial x_j} = -\frac{1}{\rho}\frac{\partial \overline{p}}{\partial x_i} + \frac{\partial}{\partial x_j}\left\{\nu(\frac{\partial \overline{u}_i}{\partial x_j} + \frac{\partial \overline{u}_j}{\partial x_i})\right\} + \frac{\partial \tau_{ij}^R}{\partial x_j} \tag{3.3}$$

$$\frac{\partial \overline{u}_i}{\partial x_i} = 0 \tag{3.4}$$

where in this case, $\overline{u}_i$ and $\overline{p}$ are the mean or time-averaged velocities and pressure ($i = 1, 2, 3$ for three-dimensional analysis), ρ is the fluid density and τ_{ij}^R represent the turbulent Reynolds stress tensor,

$$\tau_{ij}^R = -\overline{u_i' u_j'} \tag{3.5}$$

where u_i' represents the turbulent fluctuating velocity. Using Boussinesq's assumption, this Reynolds stress tensor is related to the mean velocities by the turbulent eddy viscosity:

$$\tau_{ij}^R = \nu^T \left(\frac{\partial \overline{u}_i}{\partial x_j} + \frac{\partial \overline{u}_j}{\partial x_i} - \frac{2}{3}\frac{\partial \overline{u}_k}{\partial x_k}\delta_{ij}\right) \tag{3.6}$$

where $\nu^T = k/\omega$ is the turbulent eddy viscosity.

Therefore, in order to close the RANS equations (3.3) and (3.4) above, only the turbulent viscosity is required, which is determined by using two unknowns i.e. turbulent kinetic energy k and turbulent rate of dissipation ω. The principle behind the SST k-ω model is to blend the original well known k-ϵ and k-ω models together such that near the wall, the accuracy and robustness of the k-ω model is captured, while away from

the wall (i.e. in free stream or free shear regions), the accuracy of the k-ϵ is captured (see for example (Tu *et al.*, 2007), for further details on these original models). Thus, the additional two equations required to solve for scalar variables k and ω are (ANSYS Inc., 2010):

$$\frac{\partial(\overline{u}_j k)}{\partial x_j} = \frac{\partial}{\partial x_j}\left\{\left(\nu + \frac{\nu^T}{\sigma_k}\right)\frac{\partial k}{\partial x_j}\right\} + P_k - 0.09k\omega \tag{3.7}$$

$$\frac{\partial(\overline{u}_j \omega)}{\partial x_j} = \frac{\partial}{\partial x_j}\left\{\left(\nu + \frac{\nu^T}{\sigma_\omega}\right)\frac{\partial \omega}{\partial x_j}\right\} + 2(1-F_1)\frac{1}{\sigma_{\omega 2}\omega}\frac{\partial k}{\partial x_i}\frac{\partial \omega}{\partial x_i} + \alpha\frac{\omega}{k}P_k - \beta\omega^2 \tag{3.8}$$

where σ_k, σ_ω, $\sigma_{\omega 2}$, α and β are model constants (blended from the original k-ϵ and k-ω model constants), F_1 represents the blending function which is dependant on the wall distance, P_k is the production of turbulence due to viscous forces (function of the mean velocities) and thus, the last two terms in both equations effectively represent the production and destruction of each k and ω. The turbulent production rate term P_k is determined by (ANSYS Inc., 2010; Denissen *et al.*, 2008)

$$P_k = \nu^T\left(\frac{\partial \overline{u}_i}{\partial x_j} + \frac{\partial \overline{u}_j}{\partial x_i}\right)\frac{\partial \overline{u}_i}{\partial x_j} - \frac{2}{3}\frac{\partial \overline{u}_m}{\partial x_m}\left(3\nu^T\frac{\partial \overline{u}_n}{\partial x_n} + k\right) \tag{3.9}$$

while the blending function F_1 is determined from (ANSYS Inc., 2010; Denissen *et al.*, 2008)

$$F_1 = \tanh(arg_1^4) \tag{3.10}$$

where

$$arg_1 = \min\left\{\max\left(\frac{\sqrt{k}}{\beta^*\omega y}, \frac{500\nu}{y^2\omega}\right), \frac{4\rho k}{CD_{k\omega}\sigma_{\omega 2}y^2}\right\} \tag{3.11}$$

with y being the nearest wall distance and $CD_{k\omega}$ defined as

$$CD_{k\omega} = \max\left(2\rho\frac{1}{\sigma_{\omega 2}\omega}\frac{\partial k}{\partial x_j}\frac{\partial \omega}{\partial x_j}, 1.0\times 10^{-10}\right) \tag{3.12}$$

In addition, the SST model is further refined by employing a blending of the turbulent eddy viscosity formulation, allowing more accurate prediction of the eddy viscosity both near to and away from the walls:

$$\nu^T = \frac{a_1 k}{max(a_1\omega, SF_2)} \tag{3.13}$$

where a_1 is a model constant, S represents an invariant measure of the strain rate and F_2 is another blending function (similarly depending on the wall distance) given by (ANSYS Inc., 2010; Denissen *et al.*, 2008)

$$F_2 = \tanh(arg_2^2) \tag{3.14}$$

where

$$arg_2 = \max\left(\frac{2\sqrt{k}}{\beta^*\omega y}, \frac{500\nu}{y^2\omega}\right) \tag{3.15}$$

3.1.3 Dynamic Grids

In order to account for a deforming or dynamic fluid domain (and thus for moving fluid grids), an Arbitrary Lagrangian Eulerian (ALE) description is appropriately employed (Donea *et al.*, 2004; Xia & Lin, 2008) in the fluid equations above. Considering the velocity of the fluid grids ($\widetilde{u_j}$) and applying the Reynolds transport theorem for time derivative over moving volumes, equations (3.1) and (3.2) are recast (Donea *et al.*, 2004) into

$$\frac{\partial u_i}{\partial t} + (u_j - \widetilde{u_j})\frac{\partial u_i}{\partial x_j} = -\frac{1}{\rho}\frac{\partial p}{\partial x_i} + \frac{\partial}{\partial x_j}\left\{\nu(\frac{\partial u_i}{\partial x_j} + \frac{\partial u_j}{\partial x_i})\right\} \tag{3.16}$$

$$\frac{\partial(u_i - \widetilde{u_i})}{\partial x_i} = 0 \tag{3.17}$$

where effectively, in an ALE framework, the mesh velocity $\widetilde{u_j}$ is subtracted from the material velocity u_j inside the differential operator on the left hand side of both equations (3.1) and (3.2), implying that a relative convective velocity is considered in these conservations of momentum and mass. As a result, apart from solving the usual fluid variables of velocities u_i and pressure p, an additional nodal unknown (i.e. mesh velocity $\widetilde{u_j}$) needs to be computed.

This mesh update (or dynamic meshing) is either implemented by completely remeshing the fluid domain or via a mesh regularization technique. Although complete remeshing is desirable in terms of controlling mesh quality, the computational

burden is somewhat of a drawback. Instead, although limited to mildly substantial boundary deformations, in a mesh regularization, existing computational grids are used but are deformed such that grids are as regular as possible, avoiding excessive squeezing or distortion (Donea *et al.*, 2004). Typically, in a mesh regularization, one of the boundary motions is known *a priori* (implying a Lagrangian description for the mesh along this surface i.e. $\widetilde{u_j}$ = surface velocity), while the remaining boundaries are fixed (i.e. $\widetilde{u_j} = 0$). As a result, the mesh displacement or velocity ($\widetilde{u_j}$) in between these boundaries are interpolated and distributed, so as to appropriately satisfy the prescribed motion at the boundaries. This strategy includes treating the mesh motion as a pseudo-structural problem with pseudo-elastic stiffness, much like a network of spring analogy (see for example (Farhat & Lesoinne, 2000; Slone *et al.*, 2002)), interpolating the mesh movement via an exponential damping function combined with localised averaging to smooth the grid positioning as in Xia & Lin (2008) or applying some smoothing algorithm via a Laplacian (or Poisson) model (Donea *et al.*, 2004). The latter technique is employed by ANSYS via a diffusion model, which allows sufficient dexterity by smoothing the nodal displacement in the fluid domain according to a Laplace differential equation (ANSYS Inc., 2010):

$$\nabla \cdot (\Gamma_{disp} \nabla \delta) = 0 \tag{3.18}$$

where δ is the nodal displacement relative to previous mesh positions and Γ_{disp} is a mesh stiffening parameter, allowing equation (3.18) to be solved subject to specified nodal movement at the boundaries. The grid velocity ($\widetilde{u_j}$) is then estimated from the difference in nodal displacements over the timestep size.

Solving flow problems in a moving mesh described in an ALE framework requires any mesh update scheme, and the numerical scheme involved in the solver, to obey a Geometric Conservation Law (GCL) for mathematical consistency (Thomas & Lombard, 1979; Lesoinne & Farhat, 1996; Farhat & Lesoinne, 2000). Upon discretisation, this GCL is given by (Donea *et al.*, 2004)

$$\left|\Omega_e^{n+1}\right| - \left|\Omega_e^n\right| = \int_{t^n}^{t^{n+1}} \left(\int_{S_t} \widetilde{u_j} \cdot \mathbf{n} dS \right) dt \tag{3.19}$$

effectively, implying that changes in volume of each element e from time t^n to t^{n+1} must equal the volume swept by its boundaries S in the timestep $\Delta t = t^{n+1} - t^n$. Clearly, given a mesh update scheme, the terms on the LHS could be computed exactly and it is therefore necessary to choose a consistent, appropriate numerical scheme in the solver to compute the flux and grid velocities on the RHS that matches this volumetric change. In particular, for a fluid-structure interaction problem where different temporal schemes are used in the structural and/or mesh update solvers, the computed grid velocities (and thus, velocity continuity) at the fluid-structure interface does not necessarily satisfy GCL, resulting in erroneous perturbation of kinetic energy transfers between the two fields (Lesoinne & Farhat, 1996; Farhat & Lesoinne, 2000).

In ANSYS, a finite volume scheme is employed to solve the integral forms of equations (3.16) and (3.17), together with either a first-order or second-order scheme for time integration. A consistent scheme is applied for both volumetric integration of transient terms and surface integration involved in estimating the volume swept by the moving boundary inside the convective terms, therefore satisfying GCL (ANSYS Inc., 2010).

3.2 Mathematical Formulation for Structure

The governing equation for dynamics of a structure in motion is similarly, a conservation of momentum equation given by Cauchy's equation, typically described in a Lagrangian frame of reference to allow tracking of material deformation. Effectively, the inertia (or acceleration) of the structural mass is balanced by the external forces and resisting internal forces. Including damping, this dynamic equilibrium (see for example, (Xia & Lin, 2008)) is given by

$$\rho_s \ddot{\mathbf{d}} = \mathbf{f} - c\dot{\mathbf{d}} + \nabla \cdot \sigma_{ij} \tag{3.20}$$

where ρ_s is the structural density, $\mathbf{d}$ represents the structural displacements, c is the damping coefficient, $\mathbf{f}$ is the external forcing term and σ_{ij} is the stress tensor ($i = 1, 2, 3$ for three-dimensional structures), whose divergence represents the internal elastic forces. In particular, for fluid-structure interaction problems, the external force would include fluid pressure and shear applied by the surrounding or interfacing fluid.

The relationship between the stress tensor and strain, represents the constitutive behaviour of the structural material which, depending on the material, may be linear or non-linear. In general, this constitutive relationship is of the form $\sigma = D\varepsilon$ where ε is the strain vector and D is the constitutive elastic stiffness matrix (which is typically a function of the Young's modulus E and Poisson ratio ν of the structural material). For moderately large nonlinear displacements, further strain-displacement relationships could be described using a Green-Lagrange tensor (Xia & Lin, 2008)

$$\varepsilon_{ij} = \frac{1}{2}\left\{\frac{\partial d_i}{\partial x_j} + \frac{\partial d_j}{\partial x_i} + \frac{\partial d_k}{\partial x_i}\frac{\partial d_k}{\partial x_j}\right\} \tag{3.21}$$

where d_i represents the displacement tensor ($i = 1, 2, 3$ for three-dimensional structures). Thus, the last term in equation (3.20) could also be described as a function of displacements $\mathbf{d}$. For the special case of a thin plate undergoing large deformation (as prescribed in ANSYS for most of the structural simulations in this thesis), the in-plane and lateral displacements are coupled and the Green-Lagrange strain tensor reduces to (Zienkiewicz & Taylor, 2000),

$$\left\{\begin{array}{c}\varepsilon_x\\ \varepsilon_y\\ \varepsilon_{xy}\end{array}\right\} = \left\{\begin{array}{c}\frac{\partial u}{\partial x} + \frac{1}{2}\left(\frac{\partial w}{\partial x}\right)^2\\ \frac{\partial v}{\partial y} + \frac{1}{2}\left(\frac{\partial w}{\partial y}\right)^2\\ \frac{\partial u}{\partial y} + \frac{\partial v}{\partial x} + \frac{1}{2}\frac{\partial w}{\partial x}\frac{\partial w}{\partial y}\end{array}\right\} - Z\left\{\begin{array}{c}\frac{\partial^2 w}{\partial x^2}\\ \frac{\partial^2 w}{\partial y^2}\\ \frac{\partial^2 w}{\partial x \partial y} + \frac{\partial^2 w}{\partial y \partial x}\end{array}\right\} \tag{3.22}$$

where displacements d_i in the x, y and z directions are denoted as u, v and w respectively (not to be confused with the velocity variables in fluid dynamics) and Z represents the position through the thickness of the plate. Thus, the first term in the RHS represents the in-plane strains and the second represents the bending strains.

In a finite element formulation, a weighted residual integral form of (3.20) and its boundary conditions, are typically employed. In addition, the continuum displacement,

$\mathbf{d}$, are approximated to the discretised element nodal displacements, $\mathbf{d_j}$, using some interpolation basis function, $\mathbf{N_j}$, typically of the form $\mathbf{d} = \mathbf{N_j d_j}$, reducing equation (3.20) into a well known discretised finite element form for structural dynamics (Onate *et al.*, 1994; Zienkiewicz & Taylor, 2000)

$$\mathbf{M\ddot{d}} + \mathbf{C\dot{d}} + \mathbf{Kd} = \mathbf{f} \tag{3.23}$$

where $\mathbf{M}$, $\mathbf{C}$, $\mathbf{K}$ and $\mathbf{f}$ represent respectively the mass matrix, damping matrix, stiffness matrix and external nodal force vectors. The inertial term $\mathbf{M\ddot{d}}$ corresponds to the LHS of equation (3.20) and the term $\mathbf{Kd}$ represents the internal force, corresponding to the last term of equation (3.20).

Solutions for transient problems using the finite element method often involve solving recurrence relations obtained by approximating unknown current $\mathbf{d^{n+1}}$ and $\mathbf{\dot{d}^{n+1}}$ as functions of both previously known quantities and current unknown acceleration ($\mathbf{d}$, $\mathbf{\dot{d}}$, $\mathbf{\ddot{d}}$, $\mathbf{\ddot{d}^{n+1}}$) via a truncated collocated Taylor series (Zienkiewicz & Taylor, 2000). Two of the algorithms that fall into this category, Newmark and HHT methods, are employed in ANSYS for solving implicit transient dynamics in the finite element solver (see for example, Zienkiewicz & Taylor (2000), for further details on these time integration methods).

3.3 Fluid-Structure Coupling

The interaction between the fluid and structural fields is achieved by enforcing kinematic and dynamic continuity conditions at the common interface between these domains. The kinematic continuity condition follows from the requirement that no mass flow across the interface. As a result, for an inviscid fluid that is free to slip tangentially along the interface, the normal displacement and velocities are matched (Donea *et al.*, 2004):

$$\mathbf{d^f} \cdot \mathbf{n} = \mathbf{d^s} \cdot \mathbf{n} \tag{3.24a}$$

$$\mathbf{u} \cdot \mathbf{n} = \mathbf{\dot{d}^s} \cdot \mathbf{n} \tag{3.24b}$$

where $\mathbf{d^f}$ and $\mathbf{d^s}$ represent the fluid and structural displacement vectors at the interface, $\mathbf{u}$ and $\dot{\mathbf{d}}^{\mathbf{s}}$ are the fluid and structural velocity vectors, and $\mathbf{n}$ represents the common outward unit normal vector of the interface.

For a more general viscous fluid, a no-slip boundary condition for both normal and tangential components of displacements and velocities are imposed at the interface (Donea *et al.*, 2004; Gerstenberger & Wall, 2008):

$$\mathbf{d^f} = \mathbf{d^s} \tag{3.25a}$$

$$\mathbf{u} = \dot{\mathbf{d}}^{\mathbf{s}} \tag{3.25b}$$

In addition, the dynamic continuity condition is based on force equilibrium across the interface according to principle of action and reaction. Since the interface area is equal, this reduces to equality of traction between both fluid and structural fields, which reads (Donea *et al.*, 2004; Gerstenberger & Wall, 2008):

$$\sigma^{\mathbf{f}} \cdot \mathbf{n} = \sigma \cdot \mathbf{n} \tag{3.26}$$

where σ represents the Cauchy stress tensor for structural field and $\sigma^{\mathbf{f}}$ is the Cauchy stress tensor for the fluid field, which for a Newtonian fluid is given by $\sigma^{\mathbf{f}} = -p\mathbf{I} + \nu\left(\nabla\mathbf{u} + (\nabla\mathbf{u})^T\right)$, corresponding to pressure and shear stress terms. Consequently, for a special case of an inviscid fluid that does not exert any shear, the dynamic condition simplifies to $p\mathbf{n} = \sigma \cdot \mathbf{n}$.

In order to match these kinematic and dynamic conditions simultaneously in both fluid and solid solvers, a successive iteration is applied in an ANSYS Workbench platform. In this partitioned approach, segregated solvers for each fluid and structural field are employed and the interacting quantities at the interface from each field are exchanged sequentially. In order to match the relevant quantities of the fluid and structural solvers at the interface, for each timestep, a typical procedure would read:

1. The fluid variables are solved based on the initial or current geometrical configuration, i.e. based on the current displacement at the interface, $\mathbf{d}^n_{k-1}$, at time t^n

and coupling iteration $k-1$. These fluid pressure and shear forces at the interface are resolved to forces in all three x, y and z components, $\widetilde{\mathbf{f}}_k^n$. Using a coupling under-relaxation factor ω, the actual interface forces interpolated to the nodes on the structure are

$$\mathbf{f}_k^n = \omega\widetilde{\mathbf{f}}_k^n + (1-\omega)\mathbf{f}_{k-1}^n \tag{3.27}$$

2. Applying these fluid forces and boundary constraints pertinent to the structure, the structural solver solves for the deformation of the structure and current interface displacements, $\widetilde{\mathbf{d}}_k^n$.

3. These nodal deflections of the structure are then interpolated back to nodes on the interface boundary of the fluid, which is used to effect the mesh deformation on the fluid domain. Similarly, applying an under-relaxation factor ω, the actual displacements in all three x, y and z components interpolated to the interface nodes on the fluid domain are

$$\mathbf{d}_k^n = \omega\widetilde{\mathbf{d}}_k^n + (1-\omega)\mathbf{d}_{k-1}^n \tag{3.28}$$

4. The fluid solver then solves the unknown fluid variables using the current geometrical configuration, $\mathbf{d}_k^n$.

5. The process is repeated until the difference in nodal deflection and forces exchanged in steps 3 and 1, from current and previous coupling iterations, are within a specified tolerance - suggesting that at this timestep, the kinematic and dynamic continuity, equations (3.25) and (3.26), are satisfied at the interface (to within an acceptable numerical error) i.e.

   If ϕ represent the quantities transferred at the interfaces (forces and displacements in all three x, y and z directions), the L2 error norm employed in ANSYS for each quantity is given by (ANSYS Inc., 2010)

$$\|\phi\| = \frac{\sqrt{\sum(\phi_k - \phi_{k-1})^2}}{\sqrt{\sum {\phi_k}^2}} \tag{3.29}$$

Hence,

IF $\|\phi\| < \phi_{min}$, THEN solved for current time step

ELSE k = k + 1 and repeat step 1

(where ϕ_{min} represent the convergence target or error tolerance)

The overall process can be summarised as shown in Figure 3.1.

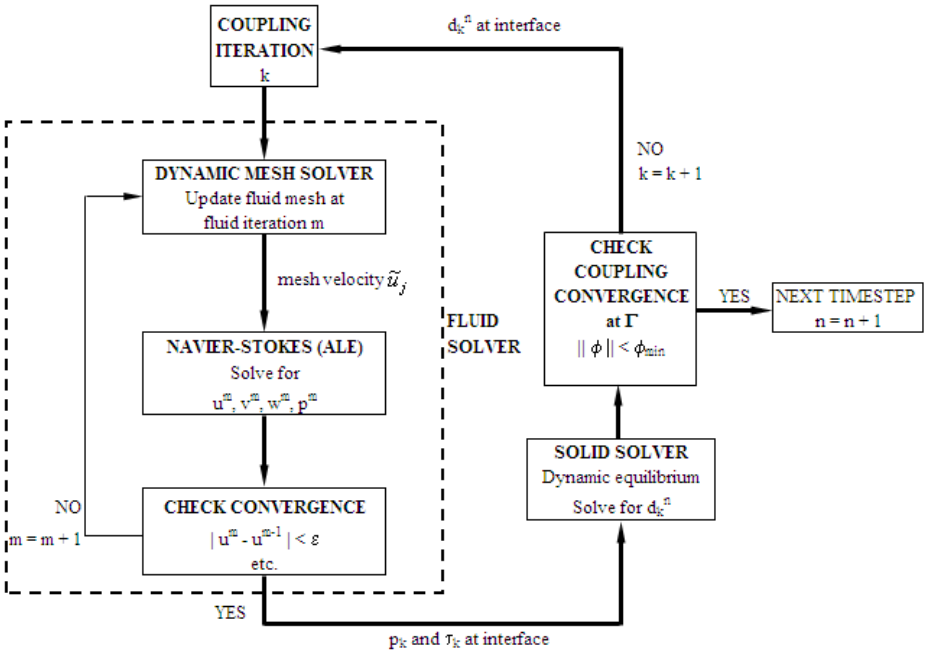

Figure 3.1: Fluid-structure coupling flowchart (m denotes inner fluid iteration and k denotes fluid-structure coupling iteration at current time step n)

3.3.1 Numerical Instability

Although each fluid and structural solvers could be solved implicitly, the staggered or sequential coupling between both solvers introduces inherent explicit influence into the computations. While this partitioned approach is attractive for efficiency, the numerical phase lag between fluid forces and structural motion introduces inherent instability, evident in cases involving incompressible flows (Causin *et al.*, 2005; Balint & Lucey, 2005; Wall *et al.*, 2006; Forster *et al.*, 2007). This error generates artificial energy transfer, acting as extra fluid mass on the fluid-structure interface and is dependant on the structural to fluid mass density ratios, thus leading to the term '*artificial added-*

mass effect' (Causin *et al.*, 2005; Wall *et al.*, 2006). Unstable added-mass conditions occur if (Causin *et al.*, 2005; Wall *et al.*, 2006)

$$\frac{m_f \mu_i}{m_s} > C \tag{3.30}$$

where m_f is related to the fluid density, m_s is the characteristic structural mass related to the structural density and μ_i is the largest eigenvalue of the added-mass operator, corresponding to the amplification factor in the explicit temporal iterations. Depending on the temporal discretisation recipe, limit C decreases with increasing accuracy or accumulated simulation time (Wall *et al.*, 2006). Thus, FSI problems with slender or low-density structures and/or fluids with comparable densities to the structure, are particularly exposed to unstable computations.

Numerical investigation shows that this added-mass instability increases with decreasing time steps Wall *et al.* (2006); Forster *et al.* (2007). This instability is caused by a large eigenvalue in the added-mass or amplification operator, corresponding to increased number of unstable Fourier modes with decreasing time steps especially when the structural inertia is negligible (Causin *et al.*, 2005; Degroote *et al.*, 2010). Clearly, a method to reduce the 'explicitness' or improve the 'implicitness' in the partitioned coupling is desirable to mitigate this computational instability.

Several schemes have been proposed to this effect. Employing an implicit time-marching scheme for the structure, Causin *et al.* (2005) showed that the coupling requires strictly low under-relaxation factors (depending on the ratio in (3.30)) for convergence, as time steps are reduced. This expensive coupling iterations for cases with small time steps or cases with unfavourable mass ratios, could be further improved by using an adaptive Aitken's under-relaxation factor (see for example Degroote *et al.* (2008)). In another approach, Degroote *et al.* (2009*b*) introduced a source term in the continuity equation of fluids near the interface to generate artificial compressibility, which diminishes as the iterations converge. This has the effect of including the expected variation in structural displacement with variation in fluid pressure in the flow

solver, resulting in a coupling algorithm that closely approximates an implicit scheme. More recently, Burman & Fernndez (2009) used Nitsche's method with consistent time penalty to stabilise the added-mass effect at the fluid-structure interface.

Newton or Quasi-Newton methods have also been attractive in implementing implicit partitioned coupling of fluid and structural solvers. The coupling at the interface could be formulated in terms of the algebraic equations arising from discretising each structural and fluid sub-problems above. Let $\mathbf{u}_f$ denote the variables in the algebraic fluid sub-problem (i.e. representing velocities u_i and pressure p) and let $\mathbf{u}_s$ denote the variables in the algebraic structural sub-problem (i.e. representing displacements $\mathbf{d}$). Hence, the fluid forces in the interface τ^{n+1} at current time step $n+1$, is determined in the fluid solver dependant on current interface position $\mathbf{X}^{n+1}$, which is in turn determined by the structural solver as a function of current fluid force near the interface τ^{n+1}. This could be formulated concisely as (Gerbeau & Vidrascu, 2003; Vierendeels *et al.*, 2007)

$$\tau^{n+1} = F^{n+1}(\mathbf{X}^{n+1}) \tag{3.31}$$

$$\mathbf{X}^{n+1} = S^{n+1}(\tau^{n+1}) \tag{3.32}$$

where F^{n+1} represent the algebraic fluid solver operator (using the current state of fluid variables $\mathbf{u}_f^{n+1}$) and S^{n+1} denotes the algebraic structural solver operator (using the current structural variables $\mathbf{u}_s^{n+1}$).

Therefore, the FSI problem could be reduced to (Gerbeau & Vidrascu, 2003; Fernandez & Moubachir, 2005),

$$\mathbf{X}^{n+1} = S^{n+1} \circ F^{n+1}(\mathbf{X}^{n+1}) \tag{3.33}$$

or in residual form

$$R = \mathbf{X}^{n+1} - S^{n+1} \circ F^{n+1}(\mathbf{X}^{n+1}) = 0 \tag{3.34}$$

which is suitable for Newton algorithms - typically requiring evaluation of derivatives of the fluid solver operator with respect to variation in interface position and derivatives

of the structural solver operator with respect to fluid force variations. These cross-derivatives or Jacobians were approximated using finite differences in a block-Newton method proposed by Matthies & Steindorf (2003), while in another work by Fernandez & Moubachir (2005), exact cross-Jacobians were estimated using shape derivative calculus. Vierendeels *et al.* (2008) and Degroote *et al.* (2009*a*) approximated the variation in fluid loads with respect to displacement at the interface by a reduced order model using least square methods, allowing either relatively simpler computation of the Jacobian matrix or indirect estimation of the Jacobian-vector product in the Newton iteration. Numerical comparisons have shown promising convergence rate of Newton or Quasi-Newton methods compared to monolithic or fixed-point iteration schemes (Gerbeau & Vidrascu, 2003; Fernandez & Moubachir, 2005; Degroote *et al.*, 2009*a*).

The fluid-structure system involved with the work in this thesis is related to air interacting with flexible, soft tissues in the upper airway, which perhaps would not violate the added-mass condition in equation (3.30), considering the low density of air in comparison with the soft tissue density. Nevertheless, an under-relaxation factor of 0.5 is used in the FSI simulations to slightly improve the 'implicitness' of the partitioned fluid-structure coupling.

3.3.2 Summary

In summary, the partitioned fluid-structure coupling is often considered a three-field problem, involving segregated solution and exchange of information between flow computations, structural dynamics (or statics) and dynamic mesh (Slone *et al.*, 2002; Farhat & Lesoinne, 2000). The increased modularity with this partitioned approach enables sophisticated, well-established solvers for each fluid and structural sub-problem to be efficiently employed. However, the sequential exchange of variables between fields render the coupling explicit, and in combination with the incompressible behaviour of the fluid, lends to numerical instability, which may be solved by improving the 'implicitness' of the partitioned coupling. In regards to the current investigation, this

'added-mass' instability may not be present considering the low density of the fluid involved and is further verified by the coupling convergence in the ANSYS Workbench framework.

3.4 Immersed Boundary Method

Apart from a moving mesh scheme using ALE methods, there is no less interest in developing fixed grid approaches to model fluid-structure interaction problems (see for example, Baaijens (2001); Wall *et al.* (2006); Gerstenberger & Wall (2008)). Such methods offer the significant benefit of doing away with the computational burden of solving mesh motion, but typically suffer from inaccurate flow field resolution near the structural boundaries. One of these fixed grid approaches, the immersed boundary method (IBM), has had much interest in the field of biomedical engineering (see for example, (Kim *et al.*, 2009; Griffith *et al.*, 2009; Le *et al.*, 2009)). A few variants of IBM exist but all are based on the same underlying principle of interpolating local fluid velocities and/or imposing appropriate source terms to replicate the presence of immersed boundaries or structures.

The interest in applying an immersed boundary method in this thesis stems from the intention of studying the influence of contact or impact between structures immersed in fluids. An ALE approach with mesh regularization on the fluid domain, would clearly lead to grid or mesh collapse as the fluid boundaries come into contact, while a full remeshing approach would be too computationally expensive.

3.4.1 Mathematical Formulation

In an immersed boundary method, a fixed Eulerian frame of reference is employed to describe and discretise the fluid governing equations, while a moving Lagrangian frame of reference is employed to model the immersed boundary or structure. In the formulation of IBM, the influence of the immersed elastic structure on the fluid is

represented as a body force in the standard Navier-Stokes equation:

$$\rho\left(\frac{\partial \mathbf{u}}{\partial t} + \mathbf{u}\cdot\nabla\mathbf{u}\right) = \nabla p + \mu\Delta\mathbf{u} + \mathbf{f} \tag{3.35}$$

$$\nabla\cdot\mathbf{u} = 0 \tag{3.36}$$

where an additional Eulerian body force density (or source) term $\mathbf{f}$ has been added to equation (3.1). These body forces are derived from the principle of virtual work, arising from the elastic traction on the immersed structure as a result of the immersed structure moving with local fluid velocities, following a no-slip condition (Peskin, 2002; Zhu & Peskin, 2002). In this thesis, the original method proposed by Peskin (Peskin, 2002; Zhu & Peskin, 2002) for an elastic immersed boundary (IB), is adopted. Although the body force formulation shown here is for a 1-D immersed elastic structure, similar principles of applying the Fréchet derivative on the elastic energy of the immersed structure, could be extended to more general 3-D cases.

Interaction Forces

For the purpose of this thesis, a 1-D flexible structure or IB fixed at one end is considered, under both stretching or compression and bending. The elastic energy of these two components (axial strain and bending) are respectively

$$E_s = T\tau \tag{3.37}$$

$$E_b = \frac{1}{2}K_b\int\left|\frac{\partial^2\mathbf{X}}{\partial s^2}\right|^2 ds \tag{3.38}$$

where $\mathbf{X}$ is the Lagrangian position of the IB as a function of its curvilinear coordinate s and time t, K_b is the flexural rigidity of the IB, and T and τ represent the axial tension force and unit tangent vector, given respectively by Hook's Law, equation (3.39), and equation (3.40) below.

$$T = K_s\left(\left|\frac{\partial\mathbf{X}}{\partial s}\right| - 1\right) \tag{3.39}$$

$$\tau = \frac{\frac{\partial\mathbf{X}}{\partial s}}{\left|\frac{\partial\mathbf{X}}{\partial s}\right|} \tag{3.40}$$

where K_s represent the axial stiffness of the IB.

The Lagrangian force density F (note that for a 1-D case, force density gives force per unit length), applied by the immersed structure on the fluid, is the sum of the strain and bending force densities, derived by taking the Fréchet derivative of the above energy functional.

$$\mathbf{F} = \mathbf{F_s} + \mathbf{F_b} = \frac{\partial}{\partial s}(T\tau) + \frac{\partial E_b}{\partial \mathbf{X}} \tag{3.41}$$

The key idea in IBM involves the transformation of variables in the Lagrangian description into Eulerian description (and vice versa) using a Dirac-delta function. In regards to this force interaction, the Eulerian force density in equation (3.35) is obtained from the IB Lagrangian force density via

$$\mathbf{f} = \int \mathbf{F}\delta(\mathbf{x} - \mathbf{X})\, ds \tag{3.42}$$

where $\mathbf{x}$ signifies the fixed Eulerian grid coordinates, $\mathbf{X}$ the Lagrangian grid coordinates of the IB, and $\mathbf{f}$ and $\mathbf{F}$ respectively, the Eulerian and Lagrangian force density as described above.

As a remark, integrating both sides of (3.42) over an arbitrary volume Ω, in the Eulerian grid $\mathbf{x}$, gives (Peskin, 2002)

$$\int_\Omega \mathbf{f} d\mathbf{x} = \int_{\mathbf{X}\in\Omega} \mathbf{F} ds$$

since $\int_\Omega \delta(\mathbf{x} - \mathbf{X})\, d\mathbf{x} = 1$ if the IB position $\mathbf{X}$ is within Ω and 0 otherwise. Thus, showing that $\mathbf{f}$ is indeed the Eulerian force density (note that for a 3-D Eulerian domain, $\mathbf{f}$ is in units of force per unit volume).

In a more recent variant of the IBM, the body force applied to impose a no-slip condition on the immersed boundary is derived from a control theory feedback scheme, allowing the body force to be iteratively adjusted to bring the local fluid velocity to the desired value, according to surrounding fluid velocities (Goldstein *et al.*, 1993; Huang *et al.*, 2007*a*):

$$\mathbf{F} = \alpha \int_0^t (\mathbf{U}_{ib} - \mathbf{U})\, dt' + \beta(\mathbf{U}_{ib} - \mathbf{U}) \tag{3.43}$$

where α and β are large negative constants, $\mathbf{U}_{ib}$ represents the fluid velocity at the immersed boundary (IB) based on interpolation of local fluid velocities in the vicinity of the IB, and $\mathbf{U}$ is the velocity of the immersed boundary itself. Intuitively, the first and second terms on the RHS represent respectively a stiff spring and damping system, which links the IB with neighbouring fluid velocity. As a result, this approach conveniently allows the immersed boundary or structural displacements to be solved separately using the standard equation of motion or dynamic equilibrium for structures (Huang *et al.*, 2007*a*; Huang & Sung, 2010).

Kinematic Interaction

Following kinematic continuity at the fluid-IB interface, a no-slip condition implies that the velocity of the IB matches the local velocity of the fluid at similar position. Similarly, a Dirac delta function is employed to relate the Lagrangian velocity of the IB to the co-located Eulerian velocity of the fluid

$$\mathbf{U} = \int \mathbf{u}\delta\left(\mathbf{x} - \mathbf{X}\right) d\mathbf{x} \tag{3.44}$$

where $\mathbf{U}$ is the Lagrangian IB velocity, $\mathbf{u}$ represents the Eulerian fluid velocity and as previously, $\mathbf{x}$ and $\mathbf{X}$ signify the fixed Eulerian fluid grid coordinates and moving Lagrangian IB grid coordinates respectively.

The displacement of the IB is then related to its velocity by

$$\frac{\partial \mathbf{X}}{\partial t} = \mathbf{U} \tag{3.45}$$

allowing the displacement of the IB to be estimated, which would then influence the magnitude of the Lagrangian force density reacted by the immersed boundary or structure.

Mass Interaction

The Eulerian density term, ρ in equation (3.35) is in fact non-uniform, involving both fluid and IB densities. Similar to force density, a Dirac delta kernel is employed to convert the Lagrangian mass density to an Eulerian mass density. Letting ρ_0 be the

constant fluid density and M the uniform mass per unit length (for a 1-D case) of the immersed boundary, this Eulerian-Lagrangian density relationship is given by (Peskin, 2002)

$$\rho = \rho_0 + \int M\delta\left(\mathbf{x} - \mathbf{X}\right) ds \tag{3.46}$$

which, if integrated by $\int_\Omega d\mathbf{x}$ on both sides, could also be shown to correspond to the correct Eulerian mass of the whole fluid and IB system.

In summary, IBM involves simultaneous solution of:

1. The purely Eulerian fluid governing equations (3.35) and (3.36)
2. Interaction equations (3.42), (3.44) and (3.46), which enforce the interaction between the Lagrangian to Eulerian variables and vice-versa.
3. The purely Lagrangian structural governing equation (3.41).

3.4.2 Numerical Implementation

The numerical solution of a viscous, incompressible fluid in Eulerian form, equations (3.35) and (3.36), are readily implemented by an integral finite volume solver in CFX, the fluid solver in ANSYS. The remaining input required are only the Eulerian body force and mass densities.

For this purpose, the strain and bending components of the Lagrangian force density on the immersed structure are estimated using a finite difference approach, following the works in Zhu & Peskin (2002) and Huang *et al.* (2007*a*). Consider a 1-D immersed structure, with Lagrangian curvilinear coordinate s, discretised into N number of elements with a set of nodes at $s = m\Delta s$, where integer m starts from 0 at the fixed end to $m = N$ at the free end, as shown in Figure 3.2.

The first and second order derivative of a variable, $\phi(s)$, is formally approximated

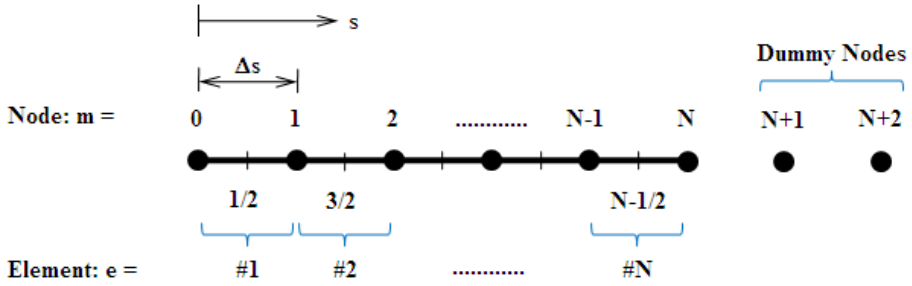

Figure 3.2: Schematic of 1-D flexible structure showing discretisation scheme and Lagrangian coordinates

using a central difference scheme,

$$\frac{\partial \phi}{\partial s} \approx D_s \phi = \frac{\phi(s + \frac{\Delta s}{2}) - \phi(s - \frac{\Delta s}{2})}{\Delta s} \tag{3.47}$$

$$\frac{\partial^2 \phi}{\partial s^2} \approx D_s(D_s \phi) = D_{ss}\phi = \frac{\phi(s + \Delta s) - 2\phi(s) + \phi(s - \Delta s)}{\Delta s^2} \tag{3.48}$$

Therefore, the axial tension and unit tangent vector in equations (3.39) and (3.40) respectively, could be defined for the 1-D IB at each element center $s = (m + 1/2)\Delta s$, for each time step n, by

$$T^n = K_s(|D_s \mathbf{X}^n| - 1) \tag{3.49}$$

$$\tau^n = \frac{D_s \mathbf{X}^n}{|D_s \mathbf{X}^n|} \tag{3.50}$$

and finally, the strain or tension force density in equation (3.41), defined at each node position $s = m\Delta s$ for each time step index n, is given by

$$(\mathbf{F}_s^n)_m = D_s(T^n \tau^n) = \frac{(T^n)_{m+1/2}(\tau^n)_{m+1/2} - (T^n)_{m-1/2}(\tau^n)_{m-1/2}}{\Delta s}, \qquad m = 1, 2, \ldots, N \tag{3.51}$$

Similarly, the bending energy in equation (3.38) could be expressed in terms of finite differences of the nodal values and numerically summed,

$$E_b = \frac{1}{2} K_b \sum_m |D_{ss}\mathbf{X}|^2 \Delta s = \frac{1}{2} K_b \sum_m \left[\frac{|\mathbf{X}_{m+1} - 2\mathbf{X}_m + \mathbf{X}_{m-1}|^2}{\Delta s^4} \right] \Delta s \tag{3.52}$$

which, upon taking the Fréchet derivative (3.41), yields the bending force density at each node position $s = m\Delta s$ and time step index n (Huang *et al.*, 2007*a*),

$$(\mathbf{F}_b^n)_m = K_b \frac{(D_{ss}\mathbf{X})_{m+1} - 2(D_{ss}\mathbf{X})_m + (D_{ss}\mathbf{X})_{m-1}}{\Delta s^2}, \qquad m = 1, 2, \ldots, N \tag{3.53}$$

noting that to evaluate $(\mathbf{F}_b)_m$ for $m = N-1$ and N at the free end, additional nodal positions are required. These 'dummy nodes' positions are evaluated from free end conditions of zero moment and zero shear, i.e. $\partial^2\mathbf{X}/\partial s^2 = 0$ and $\partial^3\mathbf{X}/\partial s^3 = 0$ respectively. Taking the second and third order finite differences, these 'dummy nodes' displacements could be estimated from known nodal displacements at N and $N-1$ within the IB, which gives (Balint, 2001),

$$\mathbf{X}_{N+1} = 2\mathbf{X}_N - \mathbf{X}_{N-1} \tag{3.54}$$

$$\mathbf{X}_{N+2} = 3\mathbf{X}_N - 2\mathbf{X}_{N-1} \tag{3.55}$$

Finally, the Eulerian body force density could then be estimated from the interaction equation (3.42) in discretised form (Zhu & Peskin, 2002),

$$\mathbf{f}^n = \sum_s \mathbf{F}^n \delta\left(\mathbf{x} - \mathbf{X}^n\right) \Delta s \tag{3.56}$$

Similarly, the Eulerian-Lagrangian mass density interaction, equation (3.46), is also discretised by

$$\rho^n = \rho_0 + \sum_s M\delta\left(\mathbf{x} - \mathbf{X}^n\right) \Delta s \tag{3.57}$$

In addition, the Lagrangian strain and bending force density above are functions of the IB displacements, which are in turn influenced by the no-slip interaction with the surrounding fluids, equation (3.44). This Eulerian to Lagrangian kinematic interaction is also discretised appropriately by (Peskin, 2002; Zhu & Peskin, 2002; Huang *et al.*, 2007*a*)

$$\frac{\mathbf{X}^{n+1} - \mathbf{X}^n}{\Delta t} = \mathbf{U}^{n+1} = \sum_{x \in g_h} \mathbf{u}^{n+1} \delta\left(\mathbf{x} - \mathbf{X}^n\right) h^2 \tag{3.58}$$

where n represents the time step and considering a fixed Cartesian square grid of uniform size h, $\Delta\mathbf{x}$ is discretised as h^2 for a 2-D fluid domain. g_h represent the region of influence of the Dirac-delta function, which shall be discussed next.

As shown earlier, all interaction equations, (3.56), (3.57) and (3.58), employ a Dirac-Delta function to transfer variables between Eulerian and Lagrangian descriptions. For discretisation purposes, this singular, sharp Dirac-delta function is replaced by a

smoothed, non-singular distribution function, δ_h, which approaches $\delta(\mathbf{x})$ as h reduces to zero and maintains $\sum \delta_h(\mathbf{x}-\mathbf{X})h^2 = 1$ for regions within the influence of the smoothed delta distribution (and would sum to zero elsewhere). The effect of Lagrangian force spreading to nearby discrete mesh of the fluid domain based on some δ_h function is shown in Figure 3.3. Further details on appropriate properties and construction of a smoothed δ_h could be referred in Peskin (2002).

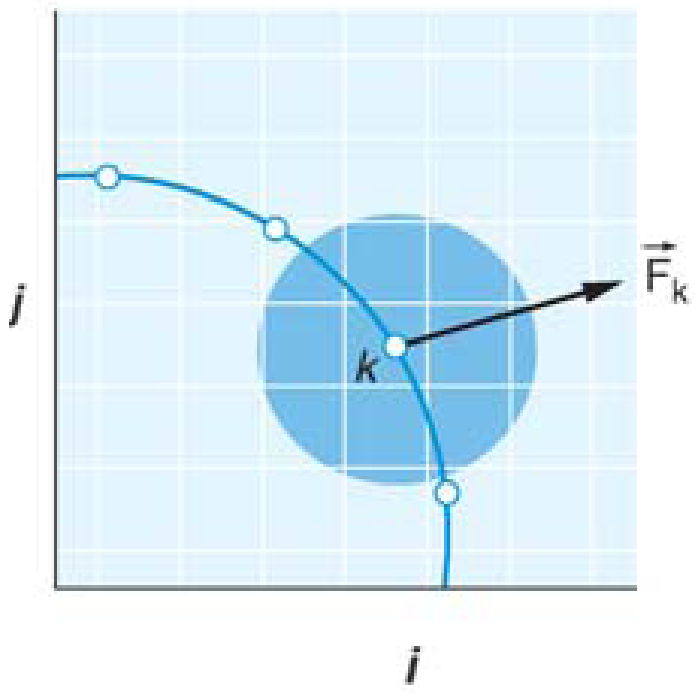

Figure 3.3: Spreading of Lagrangian force density $\mathbf{F}_k$ at IB node $\mathbf{X}_k$ to surrounding Eulerian fluid nodes. The shaded circle of influence represents the extent of force distribution as a result of smoothed delta function δ_h. Courtesy of Mittal & Iaccarino (2005)

In this thesis, a smoothed delta approximation introduced by Peskin (2002) is used

$$\delta_h = \frac{1}{h^2}\phi(\frac{x}{h})\phi(\frac{y}{h}) \tag{3.59}$$

where

$$\phi(r) = \begin{cases} \frac{1}{4}(1 + cos(\frac{\pi r}{2})) & \text{if } |r| \leqslant 2 \\ 0 & \text{otherwise} \end{cases}$$

giving a square region of influence, g_h, with a width of $2h$ on either side of each IB node, instead of a circle with radius $2h$.

Extending the application to three-dimensional problems follows similar lines as above, albeit increased complexity and computations. The three-dimensional local fluid velocity components that drives the motion of the immersed structure are determined from the more general, three-dimensional Navier-Stokes and continuity equations. Accordingly, the Lagrangian force density of the immersed structure that resist the fluid motion may then be estimated from its corresponding three-dimensional displacements using appropriate elasticity equations. Similarly, a smoothed dirac-delta function is required to map variables between the Lagrangian and Eulerian descriptions, but in terms of three-dimensional components, which results in a volumetric region of influence.

3.4.3 Summary

Numerical solution using IBM involves solving the discretised form of equations (3.35) and (3.36), which include a variable density term from (3.57) and captures the presence of IB by including a momentum forcing term from (3.56) that resists the deformation induced by fluid motions (3.58). The key idea of the approach is the conversion of variables between the Eulerian-Lagrangian frames of reference, that are involved in the interaction equations, discretised using a smoothed Dirac-Delta distribution.

At each time step, FORTRAN user-defined routines are programmed to input the Eulerian momentum forcing (in force per unit volume) and variable Eulerian density (in mass per unit volume) into the fluid Navier-Stokes solver. Within these user-defined routines, local Eulerian fluid velocities in the vicinity of the IB are read and the Lagrangian position of the IB nodes are tracked, at each time step in the computations.

As oppose to a partitioned approach in an ALE framework, IBM requires smaller time steps to avoid numerical instability. Stiffer IB or structures, generates larger Lagrangian force density F to resist the local fluid velocities, which may lead to unstable computations. This could be stabilised by using much smaller time steps (Peskin, 2011; Kim, 2003). Hence, IBM could perhaps offer an attractive approach to capture higher

order frequencies or dynamics in FSI problems.

Chapter 4

Oropharyngeal Tongue Collapse

This chapter presents the development and analysis of an idealised 3-D tongue collapse in the oropharynx - one of the common sites for occlusive sleep apnoea. A brief overview of related previous studies is presented in section 4.1. The computational formulation and model particular to the current investigation is described in section 4.2. A validation of the model by numerical sensitivity tests is presented in section 4.2.3 and comparison with existing experiments are presented in section 4.3. Finally, the results and analysis are discussed in sections 4.4, followed by a concluding remark at the end of the chapter.

The model development and investigation were published in Rasani *et al.* (2011*b*,*c*)

4.1 Introduction

Collapse of the human pharyngeal airways during sleep has serious health complications, with an estimated 10% of snorers being at risk of obstructive sleep apnoea (Bertram, 2008; Chouly *et al.*, 2008). These episodes of partial or full cessation of breathing seem to occur either by the base of the tongue butting against the soft palate and posterior velo/oropharyngeal wall or, slightly further downstream, by the collapse of the side oropharyngeal walls. Extensive experiments on flow in Starling resistors and numerical modelling of flow in compliant tubes, have revealed rich variety of dynamics and instability modes involved in such systems (see for example Bertram

(2008); Luo & Pedley (1995, 1996); Hazel & Heil (2003); Heil & Waters (2008)) and in particular, have highlighted the physics involved in collapse and self-excited oscillations of tubes under both external pressures (with and without wall tension) and internal flows. These perhaps resemble more a case of pharyngeal side wall collapse, where the walls are continuous and have somewhat homogeneous properties.

For investigating the case of a tongue butting against the velo/oropharynx, Chouly *et al.* (2008, 2009) and Van Hirtum *et al.* (2005) idealised the tissues of the tongue and pharyngeal wall as respectively a hydrostatically pressurised latex tube and a rigid cylindrical wall. The collapse of the tongue replica onto the pharyngeal wall was simulated via in-vitro experiments to validate their model assumptions and numerical results. They had developed an asymptotic Navier-Stokes equation coupled to linear elastic shell elements to model flow-induced deformation of a simplified tongue subjected to expiratory flow. In general, narrowing of the airway promotes increased transmural pressure via a Venturi effect, resulting in partial collapse of the airway and a non-linear flow rate retardation as the intraluminal pressure difference is increased - a typical observation in collapsed channel flow called flow rate limitation.

The coupling of a two-dimensional, quasi-steady, laminar, incompressible fluid flow with a shell model, developed by Chouly *et al.* (2008) and Van Hirtum *et al.* (2005) was successful in obtaining efficient real-time results and was validated in their experiments using pressurised latex material. Indeed, based on the Reynolds number, the flow is expected to be within the laminar ($Re < 2000$) or transitional ($2000 < Re < 10000$) regime. However, the complex morphology of the pharyngeal airway, could give rise to three-dimensional flow features which trigger transition and turbulence at lower Reynolds number (Shome *et al.*, 1998). In fact, observation by Hahn (1992) suggests turbulence kinetic energy at approximately 5% of the inlet velocity is not unexpected in the nasal cavity.

Both neurological and physiological factors have been implicated with apnoeic syndrome. Previous studies (for example, Brown *et al.* (1985)) have shown that apnoeic

patients have in general a narrower opening in the oropharynx region (often due to obesity or tissue build-up). Furthermore, snorers with and without sleep apnoea have smaller pharyngeal cross-sectional areas than non-snorers, and snorers with sleep apnoea have a further narrowing with a reduced lung volume (Bradley *et al.*, 1986). Pharyngeal compliance among apnoeic and non-apnoeic subjects have also been shown to vary significantly, especially during expiratory flow (Brown *et al.*, 1985).

Hence, the present study intends to instead consider a three-dimensional model of the expiratory fluid flow, coupled to a similar replication of the tongue, under different breathing regimes - using a laminar and a low-Re turbulent model. The effect of initial airway opening (i.e. pharyngeal cross-section) and tongue stiffness on the collapsibility and flow rate inside the pharyngeal airway is investigated parametrically. The fluid-structure-interaction (FSI) results may contribute to the understanding of the effects of airway geometry. Furthermore, they may be used as a tool for pre-surgical planning, and consequential predictions of surgical procedures such as uvulopalatopharyngoplasty that may be applied to open up the pharyngeal airways; since this procedure is, at best, effective in treating less than 50% of patients with obstructive sleep apnoea (OSA) syndrome (Sher *et al.*, 1996; Huang *et al.*, 2007*b*). In addition, some three-dimensional flow features and turbulence influence are also presented which could be useful in understanding delivery of drug-related treatments.

4.2 Development of Model

4.2.1 Geometrical Model

Following the experiments of Chouly *et al.* (2008) and Van Hirtum *et al.* (2005), a simplified three-dimensional flow model representing the pharyngeal airway is illustrated in Figure 4.1. The converging flow through the narrowest opening in the oropharynx (at the base of the tongue) is expected to produce a jet stream and flow separation downstream of the constriction, which is characterised by shear instability-induced turbulence (Chouly *et al.*, 2006). Shome *et al.* (1998) found that typical airflows in

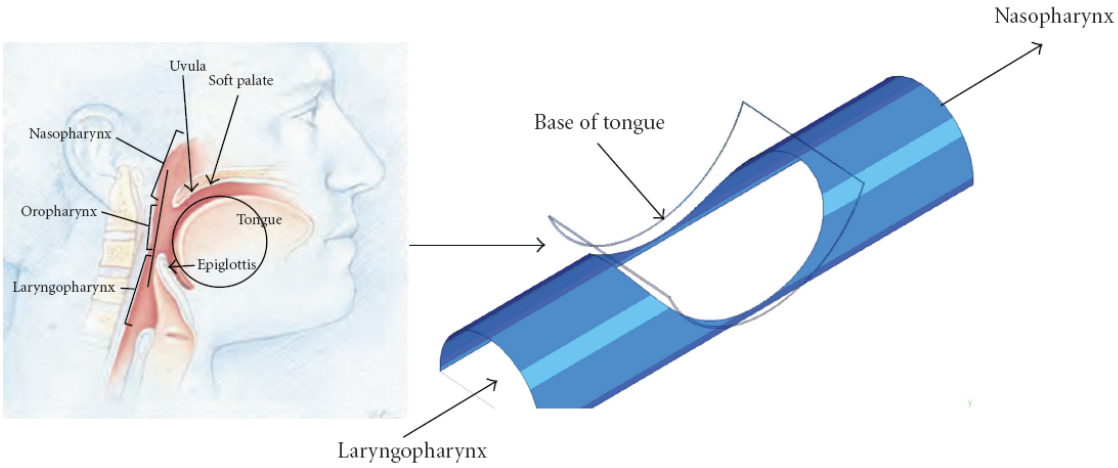

Figure 4.1: Pharyngeal airway model

the pharynx lie in the range of 200-500 Pa. Furthermore the onset of turbulence was found to increase the pressure drop by 40 % (Shome *et al.*, 1998). The two-dimensional asymptotic model by Chouly *et al.* (2008) however, used a laminar flow regime as a first approximation, neglecting the turbulence effects given that the flow may be laminar upstream of the tongue, with transition to turbulence after the tongue where the jet forms.

Accordingly, for the three-dimensional model in this study, a laminar flow condition is assumed as a first approximation. In addition, with Strouhal numbers in the order of 10^{-3} (Van Hirtum *et al.*, 2005; Chouly *et al.*, 2006), the flow is considered quasi-steady and could be characterised by the steady Navier Stokes equations. Neglecting the unsteady term in (3.16), in an ALE description, this is given by

$$(u_j - \widetilde{u_j})\frac{\partial u_i}{\partial x_j} = -\frac{1}{\rho}\frac{\partial p}{\partial x_i} + \frac{\partial}{\partial x_j}\left\{\nu(\frac{\partial u_i}{\partial x_j} + \frac{\partial u_j}{\partial x_i})\right\} \tag{4.1}$$

$$\frac{\partial(u_i - \widetilde{u_i})}{\partial x_i} = 0 \tag{4.2}$$

where u_i and p are the fluid velocities and pressure ($i = 1, 2, 3$ for three-dimensional analysis) and ρ is the fluid density. $\widetilde{u_j}$ represent the grid velocities, which as described in the previous chapter, are solved by a diffusion model (3.18) and are evaluated within the above equations such that GCL is satisfied. Equations (4.1), (4.2) and (3.18) represent the fluid governing equations which are solved by the fluid solver for a laminar

condition.

Following the laminar model, a comparative simulation is performed, making use of the newly developed transitional turbulence model developed by Langtry & Menter (2005) to allow for a transitional and turbulence flow regime. Avoiding the intensive computational efforts involved with a three-dimensional Large Eddy Simulation (LES) and Direct Numerical Simulation (DNS), a more practical approach is employed. Steady, incompressible, turbulent flow in the three-dimensional tube is described using the Reynolds-Averaged Navier Stokes (RANS) equations coupled to a Shear Stress Transport (SST) k-ω turbulent model. Similarly, neglecting the unsteady term in (3.3) and using an ALE framework, this reads

$$(\overline{u}_j - \widetilde{u_j})\frac{\partial \overline{u}_i}{\partial x_j} = -\frac{1}{\rho}\frac{\partial \overline{p}}{\partial x_i} + \frac{\partial}{\partial x_j}\left\{\nu(\frac{\partial \overline{u}_i}{\partial x_j} + \frac{\partial \overline{u}_j}{\partial x_i})\right\} + \frac{\partial \tau_{ij}^R}{\partial x_j} \tag{4.3}$$

$$\frac{\partial(\overline{u}_i - \widetilde{u_i})}{\partial x_i} = 0 \tag{4.4}$$

where in this case, $\overline{u}_i$ and $\overline{p}$ are the mean or time-averaged velocities and pressure ($i = 1, 2, 3$ for three dimensional analysis), ρ is the fluid density and τ_{ij}^R represents the turbulent Reynolds stress tensor, which is further determined or closed by considering two additional RANS equations, as outlined in chapter 3.

Equations (4.3), (4.4) and diffusion model (3.18) for solving grid velocities $\widetilde{u_j}$, represent the complete fluid model which is solved by the fluid solver for the k-ω SST model. A low-Re simulation with appropriate near wall behaviour are readily captured in the SST k-ω model employed in ANSYS.

Assuming the flow is symmetrical about its mid-vertical plane, a half-model of the problem is constructed, as depicted in Figure 4.2. The pharyngeal airway tube diameter d is set to 25 mm, giving a typical cross-sectional area of an adult pharynx anatomy. The conditions imposed at each boundary are summarised as follows:

At the inlet, a uniform upstream pressure p_{in} is imposed, which implies a parabolic velocity profile definition at the inlet. At the outlet, downstream pressure p_{out} is fixed to zero (i.e. atmospheric pressure), implying a typical stress-free condition, with

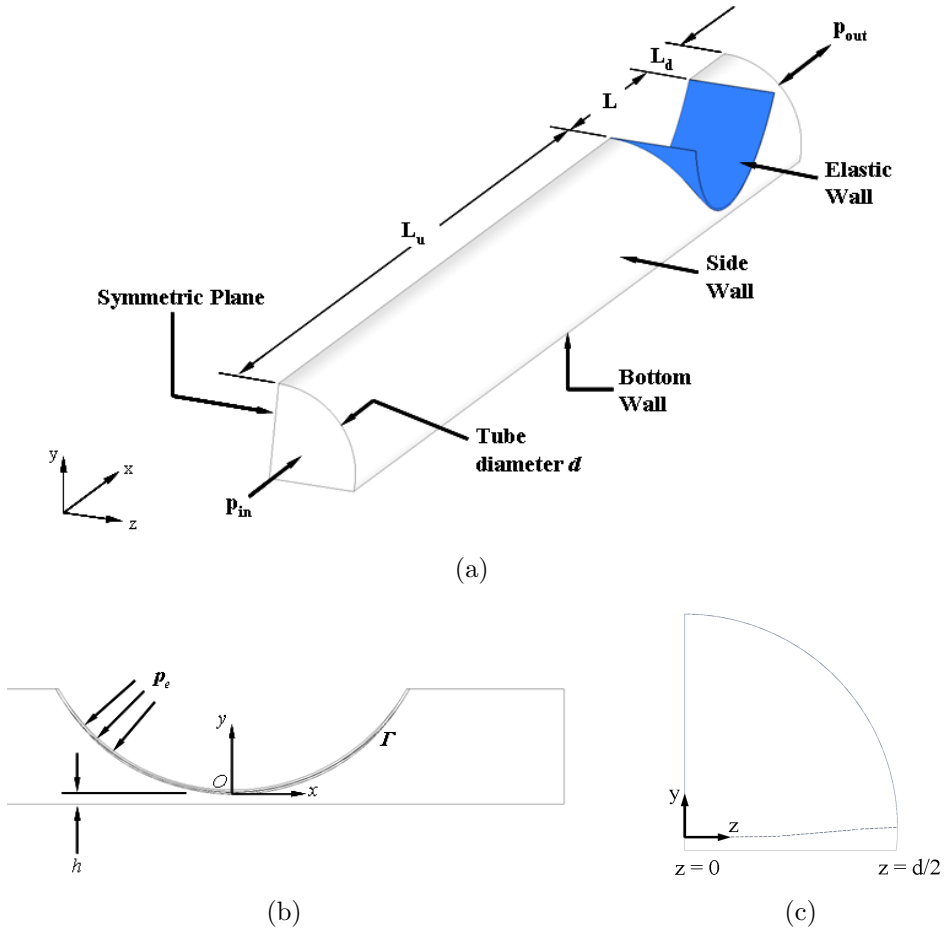

Figure 4.2: Model definition: (a) Isometric view; (b) Side view looking at symmetrical plane; (c) Frontal view looking from the inlet.

allowance for flow entrainment but in the normal direction to the boundary. No-slip boundary conditions at the walls implies that flow velocities u_i are zero at the rigid walls and at the elastic segment, u_i must match the elastic wall velocities U_i.

For a continuum undergoing *steady* deformation, Cauchy's equation (3.20) is effectively a static equilibrium equation. Neglecting the unsteady term, this is given by

$$\nabla \cdot \sigma_{ij} + \mathbf{f} = 0 \tag{4.5}$$

where σ_{ij} is the stress tensor and $\mathbf{f}$ is the external forcing term ($i = 1, 2, 3$ for three-dimensional structures) which in this case, includes external pressure p_e plus the fluid pressure and fluid shear at the interface Γ. The mechanical properties of the tongue are inhomogeneous and anisotropic, more so with varying degrees of muscle activation.

Inlet:	$p = p_{in}$	$x = -(L_u + L/2)$
Outlet:	$p = p_{out}$	$x = (L/2 + L_d)$
Rigid Side Walls:	$u_i = 0$	$y^2 + z^2 = \mathrm{d}$
Rigid Bottom Wall:	$u_i = 0$	$y = -h$
Elastic Wall:	$u_i = U_i$	on Γ
Symmetrical Wall:	$u_3 = 0$	$z = 0$

Table 4.1: Boundary conditions for 3-D tongue-oropharynx model

However for simplicity, the tongue is considered as a homogeneous, elastic, isotropic material - hence, with a constant Young's modulus, E and Poisson ratio, ν.

The tongue anatomy mainly consists of water (with reported density of 1040 kg/m^3 (Duck, 1990)) and is therefore generally accepted as incompressible (Payan *et al.*, 1998). Accounting for that incompressibility, a Poisson ratio ν of 0.499 was used by Chouly *et al.* (2008); Payan *et al.* (1998) and is also adopted here. Tissues along pharyngeal airway have been reported with a range of moduli: 10-30 kPa for the vocal folds (Min *et al.*, 1994), 12-25 kPa for the soft palate (Huang *et al.*, 2005*b*) and 6 kPa (Huang *et al.*, 2005*a*) to 15 kPa (Payan *et al.*, 1998) have been estimated for the tongue. In order to replicate the response of a real tongue, a hydrostatically pressurised latex shell tube was utilised by Chouly *et al.* (2008, 2009). Similarly, a simulated shell modulus E in combination with an external pressure p_e that mimics this response is followed in this study.

For linear small deformations, as found in this study, second order terms in the Green-Lagrange strain equation (3.21) can be neglected. Thus, the strain-displacement relationship can be described as

$$\varepsilon_{ij} = \frac{1}{2}\left\{\frac{\partial d_i}{\partial x_j} + \frac{\partial d_j}{\partial x_i}\right\} \tag{4.6}$$

where d_i is the displacement tensor. Equations (4.5) and (4.6) represent the quasi-steady structural model, capturing the static elastic wall deformation under external loads.

The elastic wall is assumed fixed everywhere except at the common face interfacing with the elastic segment of the fluid domain where an external pressure p_e is imposed

simultaneously with the pressure p applied from the fluid domain.

4.2.2 Computational Model

A commercial finite volume flow solver (CFX), in ANSYS, is used to solve the laminar and RANS equations (4.1), (4.2), (4.3) and (4.4) above, in an ALE framework. As specified in the previous chapter, the grid velocities are solved and smoothed using a diffusion model, subjected to nodal movements at the boundaries. The fluid domain is subdivided into 8-noded three-dimensional hexahedral elements leading to an assembly of discretised algebraic equations in terms of the nodal unknowns u_i and p. In general, finer meshes are located closer to the walls (elastic, rigid side and bottom) where higher velocity gradients are expected and flow separation or reattachment normally occur. In addition, denser meshes are also located in the vicinity of the constriction where sharp changes in pressure are expected.

The commercial finite element solver (ANSYS) is used to solve the partial differential equations (4.5) and (4.6). Similarly, the structural domain is discretised into 8-noded SOLID185 elements and equation 4.6 is approximated using interpolation functions in terms of the unknown nodal deformations. Minimization of the variational total potential energy or weighted galerkin residuals lead to an assembly of algebraic equation which could be solved as a function of imposed boundary conditions.

Coupling

As described in the previous chapter, the fluid-structure interaction is achieved by imposing kinematic and dynamic continuity at the common interface between the fluid and solid domains. For a quasi-steady case in this study, a continuity of displacement coupled with the usual force equilibrium is adequate.

In order to match these conditions simultaneously in both fluid and solid solvers, a successive iteration is employed in an ANSYS Workbench platform. The fluid variables are solved based on the initial geometrical configuration. The fluid pressure and shear forces at the elastic segment are interpolated to the nodes on the elastic wall. Applying

them together with the external pressure and imposed boundary conditions, the solid solver solves for the deformation of the elastic wall. These nodal deflections are then interpolated back to nodes on the elastic boundary of the fluid, which is used to effect the mesh deformation on the fluid domain. The fluid solver then solves the unknown fluid variables using the current geometrical configuration and the process is repeated until the difference in nodal deflection and forces (equation (3.26)) from current and previous coupling iterations are within a specified tolerance. The overall process can be summarised as shown in Figure 4.3 below.

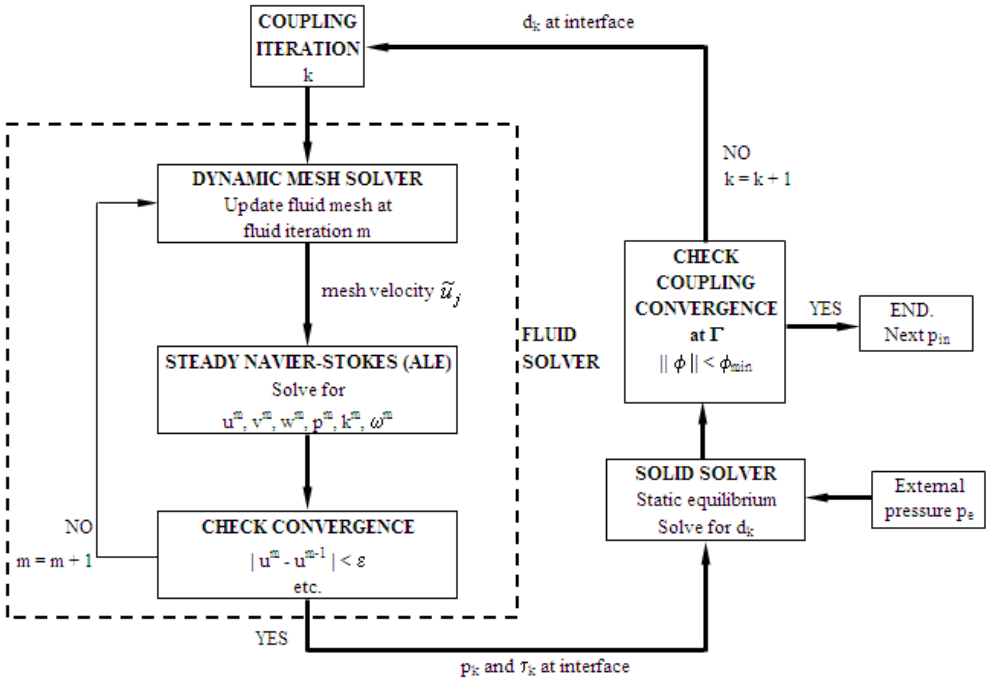

Figure 4.3: Fluid-structure coupling flowchart (where m denotes iteration of steady-state Navier-Stokes solver at current fluid-structure coupling iteration k)

Note that for steady conditions (where inertial effects are neglected and structural deformation reaches static equilibrium), elastic wall velocities U_i approach zero and equilibrium static structural displacement is reached.

4.2.3 Numerical Verification

Luo & Pedley (1995) reported that wall vorticity represents a sensitive measure of computational accuracy in such channel flow systems with sharp changes in wall profile.

Similarly, wall vorticity is used here as an indicator for numerical accuracy, albeit indirectly, by monitoring shear stresses near the walls of the 3-D channel. For numerical verification of this 3-D model, a case with constriction height $h = 0.8$ mm and $h = 1.2$ mm are used. These are the two narrowest openings underneath the tongue replica among all the cases that are simulated in this study, and should therefore represent the sharpest change in flow variables within the vicinity of the elastic tongue wall.

Monitoring the wall shear stress, several runs with different downstream length L_d suggest that numerical results are not sensitive to the outlet proximity, as shown in Figure 4.4. Therefore, in keeping with this and considering that wider constrictions may allow increased flow rates, an outlet length of 750 mm has been maintained in all the 3-D channel geometry.

The 3-D channel geometry was meshed using mapped grids, allowing consistent divisions across three types of mesh refinements i.e. coarse, medium and fine mesh densities corresponding to mesh sizes of 2.0, 1.0 and 0.5 mm respectively. These yielded numerical models with approximately 45000, 360000 and 2880000 elements respectively, which are used to assess and select an appropriate mesh density for this investigation. A typical mesh for the pharyngeal airway-tongue replica system is illustrated in Figure 4.5 for the case of medium mesh density, which also represents the current mesh size employed in all the simulation. Similarly, monitoring wall shear stresses for a case with obstruction height $h = 0.8$ mm, there are significant deviations in the coarse mesh simulation in comparison to the medium and finer mesh densities, as shown in Figure 4.6. While, finer mesh discretization shows negligible difference in overall wall shear distribution with the current mesh employed. In particular, similar separation location off the elastic wall (tongue replica) is predicted, suggesting that the mesh density used in this study is adequately grid-independent.

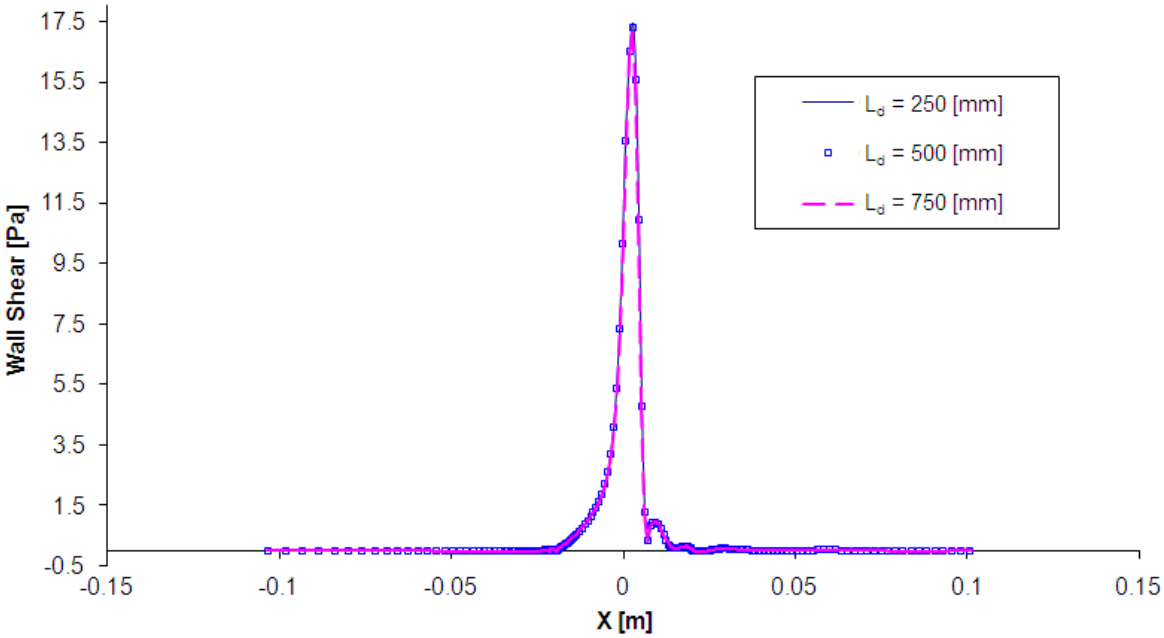

(a)

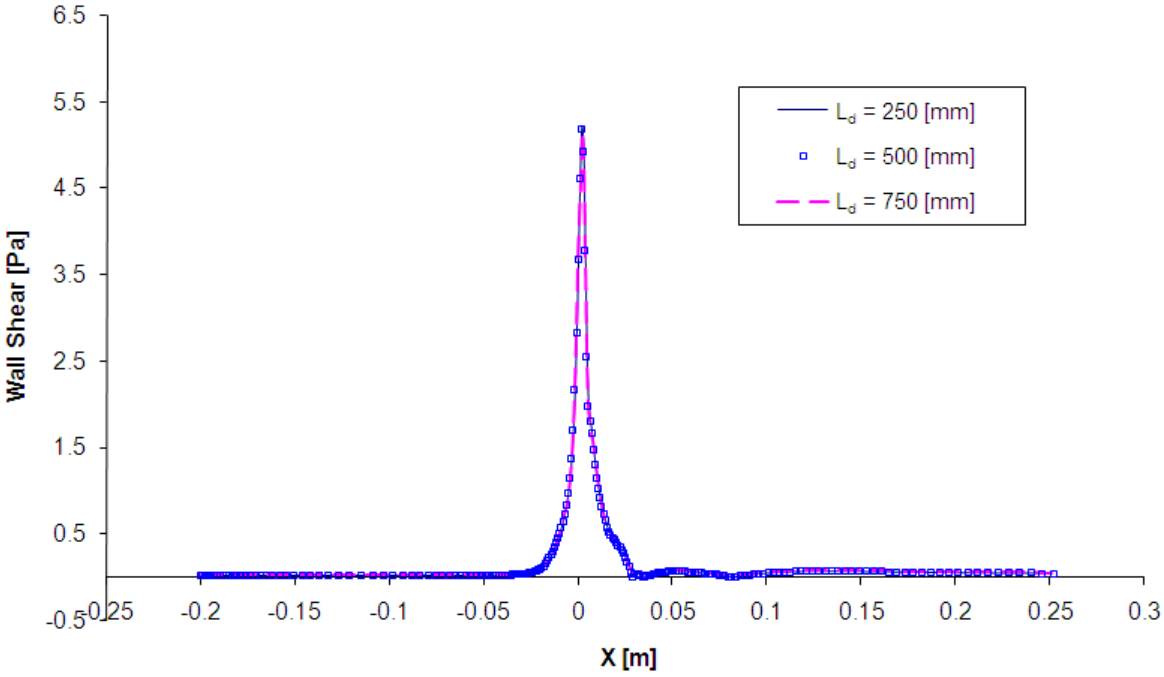

(b)

Figure 4.4: Wall shear distribution on symmetric plane of 3-D channel along (a) Top wall and (b) Bottom wall for a case of $h = 0.8$ mm with model outlet lengths $L_d = 250$, 500 and 750 mm (note that elastic wall is located within -0.02136 m $< x < 0.02136$ m)

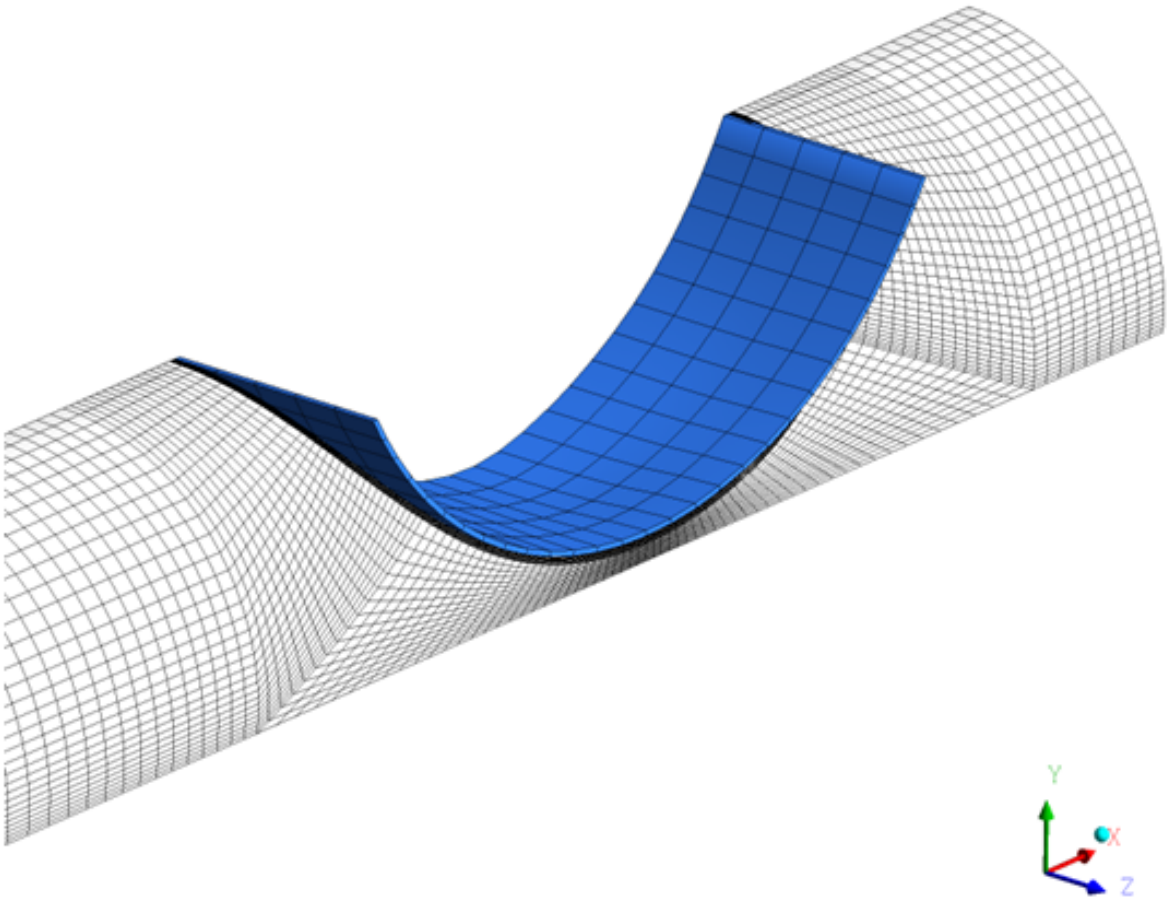

Figure 4.5: Finite volume mesh for the pharyngeal airway domain with 8-node hexahedral elements and finite element mesh for the tongue replica (in blue)

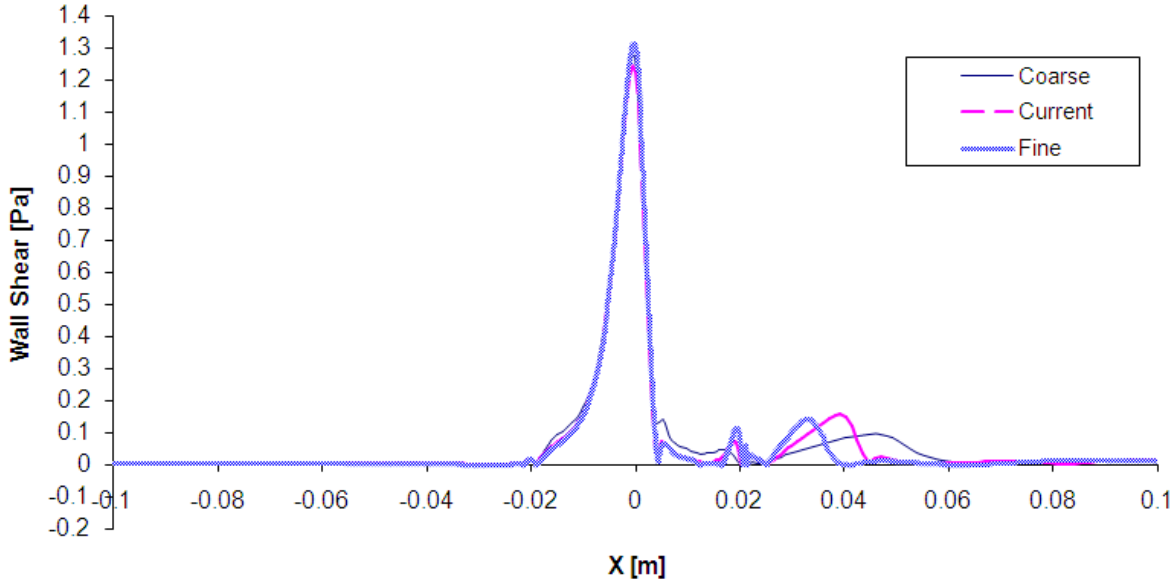

(a)

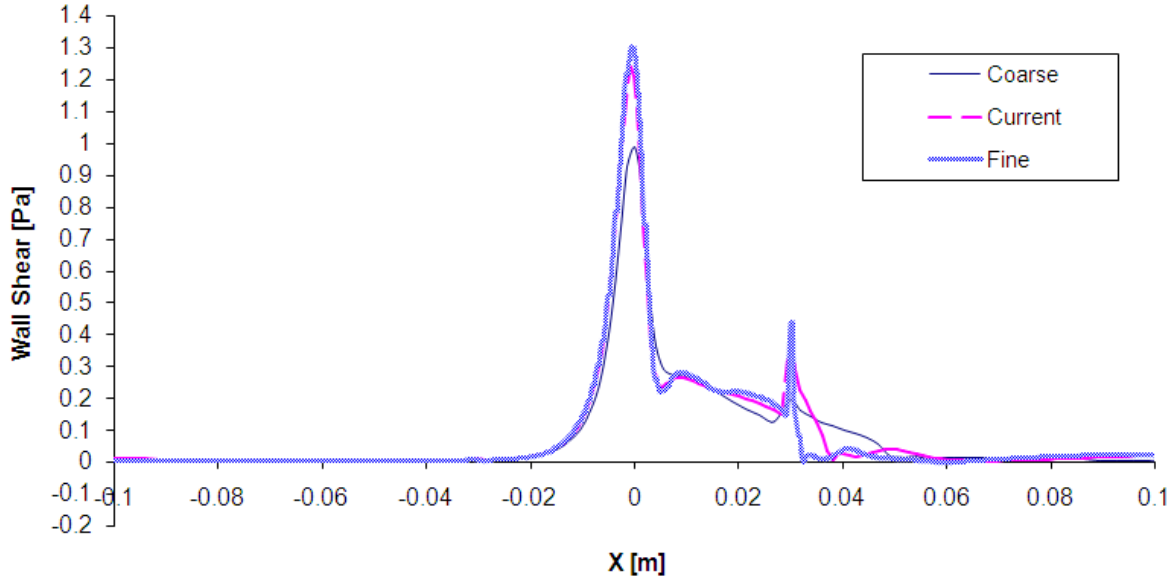

(b)

Figure 4.6: Wall shear distribution along symmetric plane of 3-D channel along (a) Top wall and (b) Bottom wall at different mesh refinements for a case of $h = 0.8$ mm(note that elastic wall is located within -0.02136 m $< x < 0.02136$ m)

4.3 Model Comparisons

In order to validate the current model, a laminar case with initial constriction height $h_o = 1.2$mm and applied external pressure p_e of 200 Pa was run. Both structural and fluid-structure interaction results were compared to the experiments and two-dimensional asymptotic model developed by Chouly *et al.* (2008, 2009) and Van Hirtum *et al.* (2005). A similar Poisson ratio of 0.499 and a Young's modulus $E = 1.75$ MPa for the isotropic elastic wall was used, with the current structural model giving a load-deflection response of the tongue replica similar to Chouly *et al.* (2008), as depicted in Figure 4.7. In general, good agreement is shown, despite the current linear structural model overpredicting the elastic wall collapse for applied pressures between $0.5 < P/P_o < 1.5$ but underpredicting the collapse for pressures $P/P_o < 0.5$.

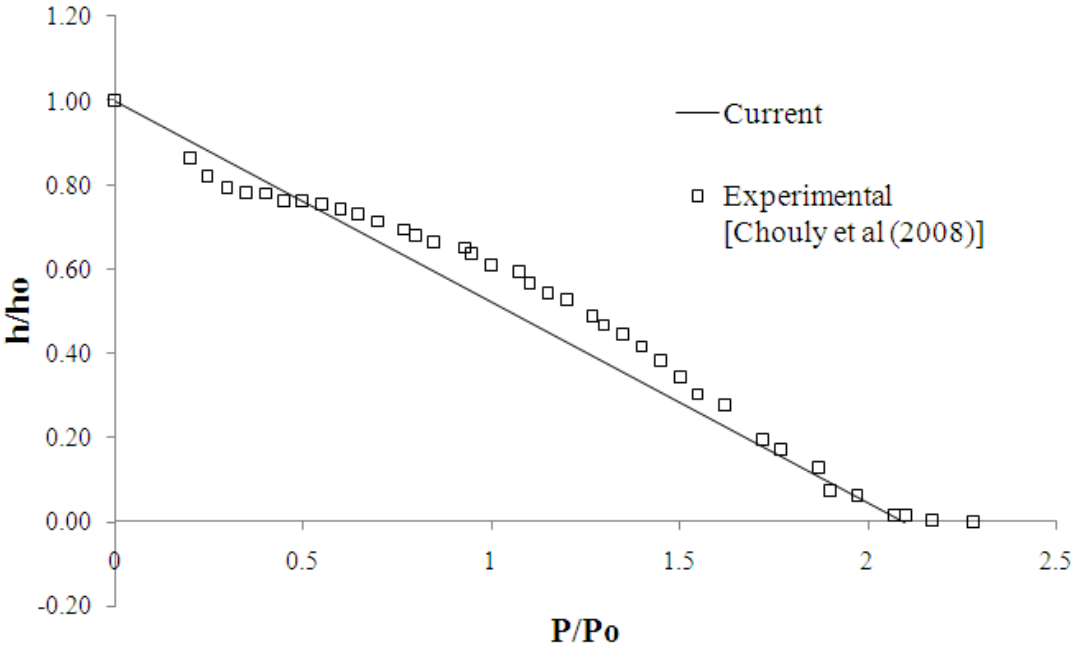

Figure 4.7: Pressure vs. deflection curve for elastic wall (deflection is measured as lowest point on the symmetric plane, $P_o = 1000$ Pa and $h_o = 1.6$ mm)

The variation in flow rate and constriction height as a function of the intraluminal pressure difference $\Delta p = p_{in} - p_{out}$ are plotted in Figure 4.8. The comparisons show reasonable agreement in terms of flow rate variation vs. intraluminal pressure difference

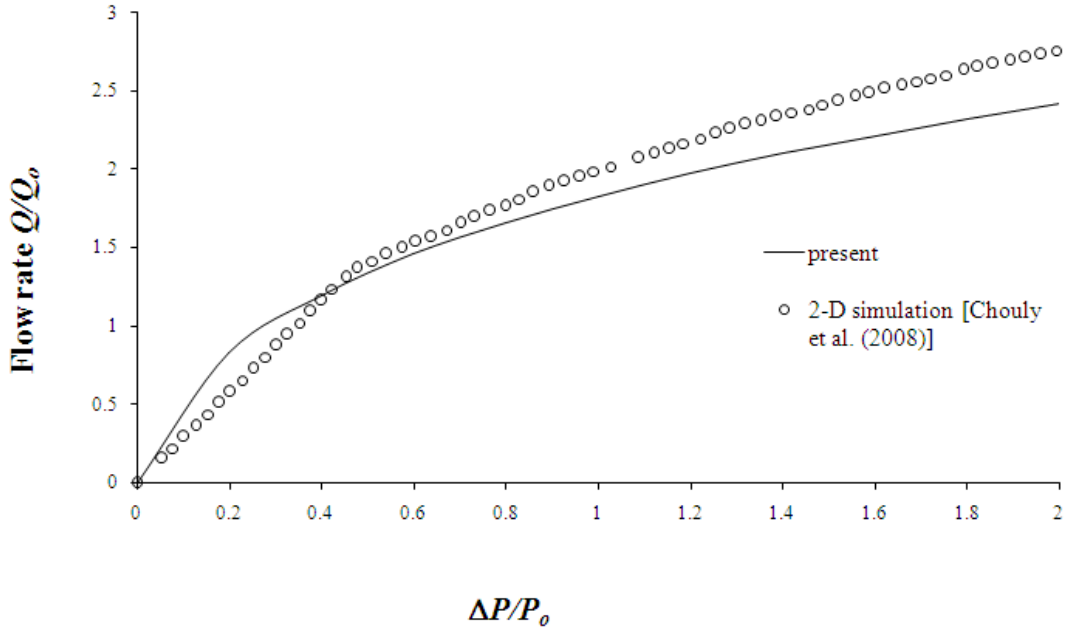

(a)

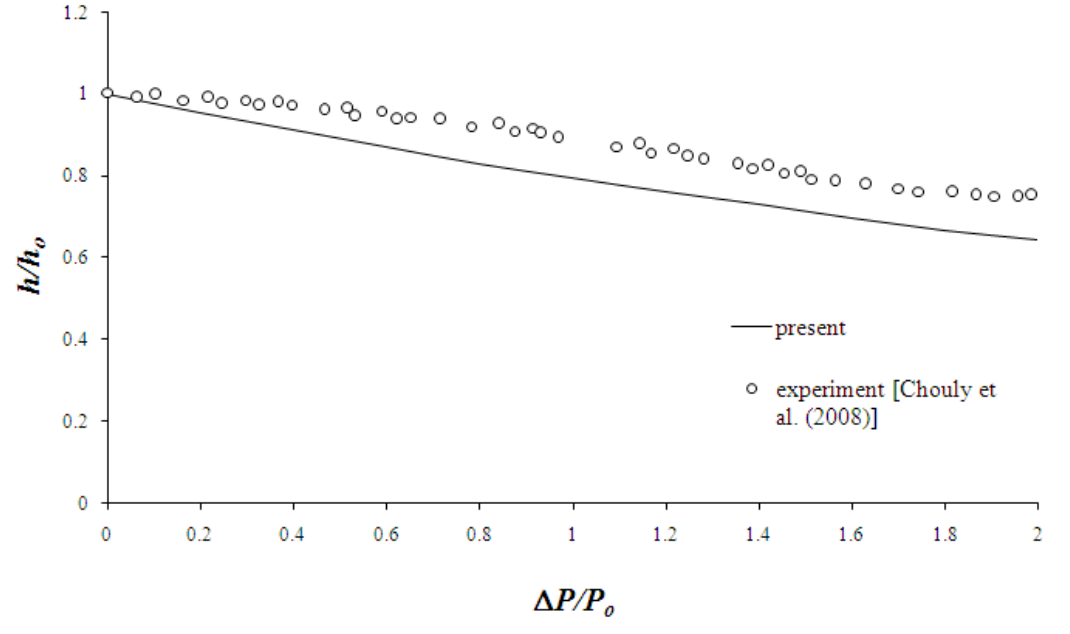

(b)

Figure 4.8: Model comparison: (a) Flow rate variation with pressure difference Δp; (b) Constriction height variation with pressure difference Δp (Q_o = 10 L/min, P_o = 100 Pa and h_o = initial constriction height = 1.2 mm)

Δp, with a maximum 12.5% difference from those reported in Chouly *et al.* (2008) at $\Delta P/P_o = 2$. More importantly, the current simulation also illustrates a similar trend of flow rate limitation (i.e. the exhalation flow rate does not increase linearly proportional with increasing breathing effort). Figure 4.8(b) compares the elastic wall collapse of the current laminar model with previous simulation and experimental data. In general, Figure 4.8(b) shows the current model predicts reasonably similar degree of elastic wall collapsibility with increasing breathing effort, but does exhibit increasing difference with Δp. The average difference is approximately 6% with a maximum difference, occurring at $\Delta P/P_o = 2$, of 15%. In both figures, the greatest difference occurs at maximum Δp. This is perhaps due to flow structures at maximum Δp, which corresponds to the unstable transition towards turbulence.

4.4 Results and Discussion

4.4.1 Parametric Investigation

For the purpose of studying the influence of the following physiological variations on the collapsibility and flow pattern in the pharyngeal airway, the following range of parameters were simulated under laminar conditions:

(i)	Initial constriction height (h_o)	0.8-11.0 mm
(ii)	Elastic wall modulus E	1.25-2.25 MPa

The initial constriction height is varied to simulate the effect of different degrees of opening behind the tongue within the oropharynx in apnoeic or non-apnoeic subjects. The opening gap behind the tongue is typically 11mm (Sforza *et al.*, 2000) but is perhaps lower when subjects are in sleeping position. A preliminary study by Chouly *et al.* (2006) reported an opening of between 1 to 2 mm during sleep supine position. Furthermore, this height is reflective of variations in patient conditions influenced by perhaps, obesity and hypertrophy of tissues surrounding the pharyngeal airway. Thus, with pre-planned scans to measure this initial height, the potential risk of collapse or snoring in relation to this height could be identified, assessed and managed accordingly.

In line with this, variations between 0.8 to 11.0 mm have been investigated in the current investigation.

The influence of the modulus of the tongue is also of interest. Variation of mechanical properties of the tongue in the human population is not unexpected. This could be influenced by variation in tongue composition, size and perhaps, ethnicity. The degree of variation in pharyngeal compliance measured by Brown *et al.* (1985) among apnoeic patients could offer some insight into the variation of stiffness in the retroglossal region. Variation in the tongue stiffness is also indicative of the degree of muscle activation (Duck, 1990) and has been used to capture the directional activation of muscle tissues. In this thesis, considering the replication of the tongue by an elastic shell, a ± 0.5 MPa variation is examined.

In order to investigate the first parameter, the elastic modulus E and external pressure p_e were fixed to 1.75 MPa and 200 Pa respectively, while the initial constriction height h_o was varied. The non-linear variation of the flow rate with intraluminal pressure difference $\Delta p = p_{in} - p_{out}$ is shown in Figure 4.9(a) for various h_o, revealing typical flow rate limitation phenomena with increased expiratory efforts. In particular, the increased flow rate and reduced degree of flow plateauing for higher h_o, suggest that there is less flow obstruction with increasing h_o. This is indeed the case, as shown by the h/h_o ratios in Figure 4.9(a), where the degree of elastic wall collapse is less severe with increasing initial opening. The approximately linear trend of collapse with increasing Δp is consistent with the Venturi effect, where the reduction in flow area underneath the elastic wall increases the flow velocity, thus generating low mean pressure (suction) that deflects the elastic wall downwards. With increasing Δp, the accompanying increase in flow rate imposes higher velocities underneath the constriction that generates much lower pressure, which instigates further collapse.

For the lowest case of $h_o = 0.8$ mm, the elastic wall collapses to a maximum of 42% of its initial opening, at maximum $\Delta p = 200Pa$. This compares to the case with widest opening, $h_o = 11$ mm, where the maximum collapse is approximately 5% of its

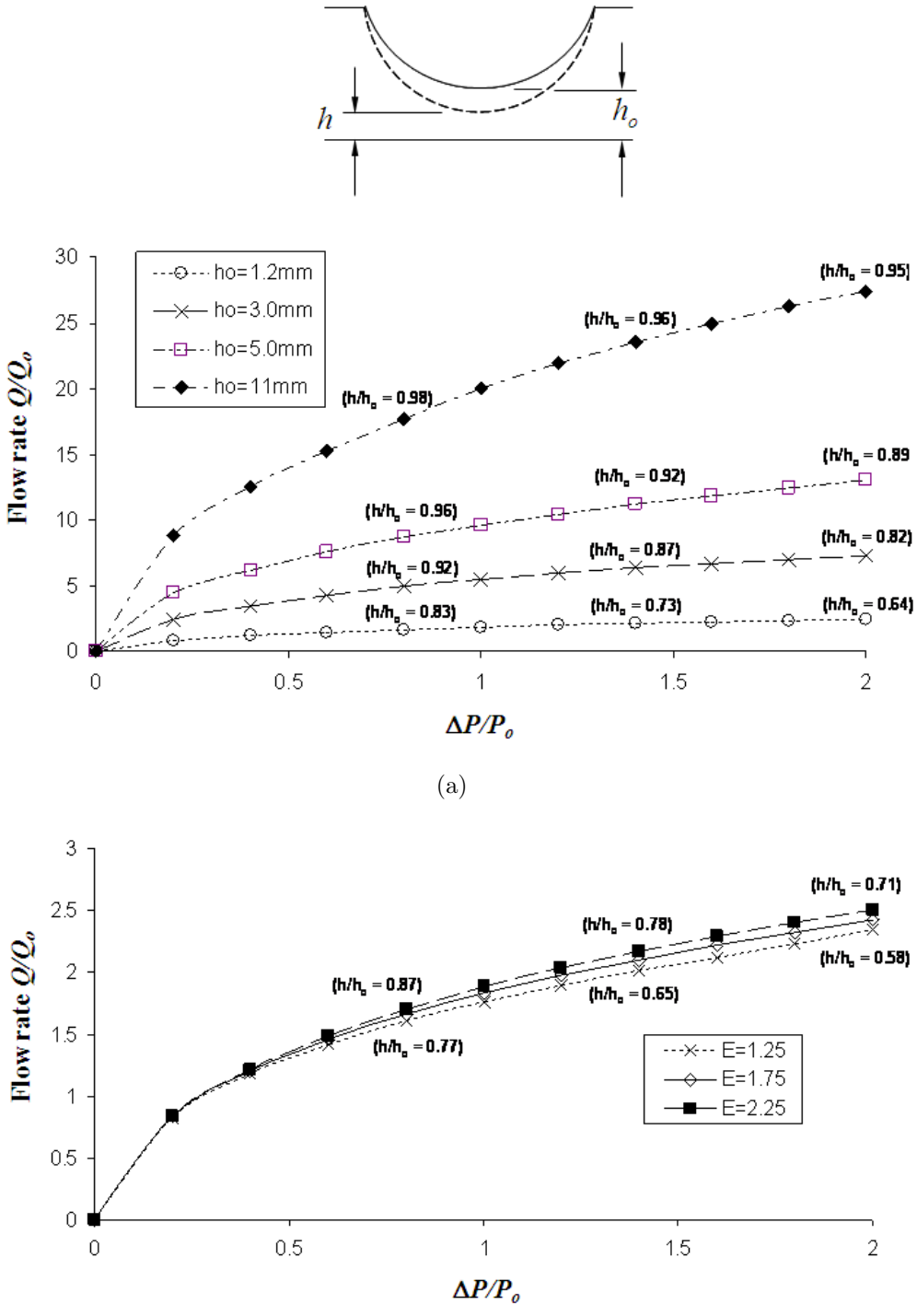

(a)

(b)

Figure 4.9: Parametric investigation under laminar flow conditions: (a) Effect of initial airway opening h_o on flow rate Q and constriction height h for a fixed tongue replica modulus $E = 1.75$ MPa and (b) Effect of tongue modulus E on flow rate Q and constriction height h for a fixed initial opening $h_o = 1.2$ mm (Note: $Q_o = 10$ L/min, $P_o = 100$ Pa and h_o = initial constriction height)

initial opening. This low degree of collapse suggests a near-rigid flow rate is achieved and demonstrates the relatively low obstruction in non-apnoeic patients. Thus, smaller cross-sectionals that are commonly found in already obstructed airways (for example, in obese patients), are more susceptible to pharyngeal collapse due to this Venturi effect. In addition, non-apnoeic patients with normal openings have better opportunity for unobstructed flow.

The second parameter investigated is the effect of tongue modulus on the expiratory flow interaction with the tongue. In order to investigate this parameter, a configuration with initial constriction height of 1.2 mm and $p_e = 200$ Pa was used. This effect of softening and stiffening of the tongue modulus ($1.25 < E < 2.25$ MPa) is summarised in Figure 4.9(b). Reduction in modulus translates to increased compliance of the airway cross-section to the applied pressures, as suggested by reduced constriction height h in Figure 4.9(b). This is shown by the greater collapse of the softer tongue with increasing intraluminal pressure difference Δp (for example, at maximum $\Delta p = 200$ Pa, $E = 1.25$ MPa gives $h/h_o = 0.58$ compared to $E = 2.25$ MPa which gives $h/h_o = 0.71$). Furthermore, this increased obstruction corresponds to decreased flow rates at lower modulus values, as depicted in Figure 4.9(b).

Thus, increased compliance of airway tissues (which is reflected here by softening of the tongue) exacerbates airway susceptibility to collapse and increases resistance to flow rate. Similarly, the approximately linear trend of collapse with increasing Δp is consistent with the Venturi effect, where the reduction in flow area underneath the elastic wall increases the flow velocity, thus generating much lower mean pressure (suction) that further collapses the wall.

Comparing the relative influence of both parameters, h_o and E, to the wall collapse and flow rate, suggests that both parameters are important. For instance, a 40% stiffening of the tongue replica modulus ($E = 1.25$ to 1.75 MPa) leads to approximately 11% reduction in wall collapse, while, for a 50% increase in initial airway opening ($h_o = 0.8$ to 1.2 mm), a 10% reduction in collapse is exhibited.

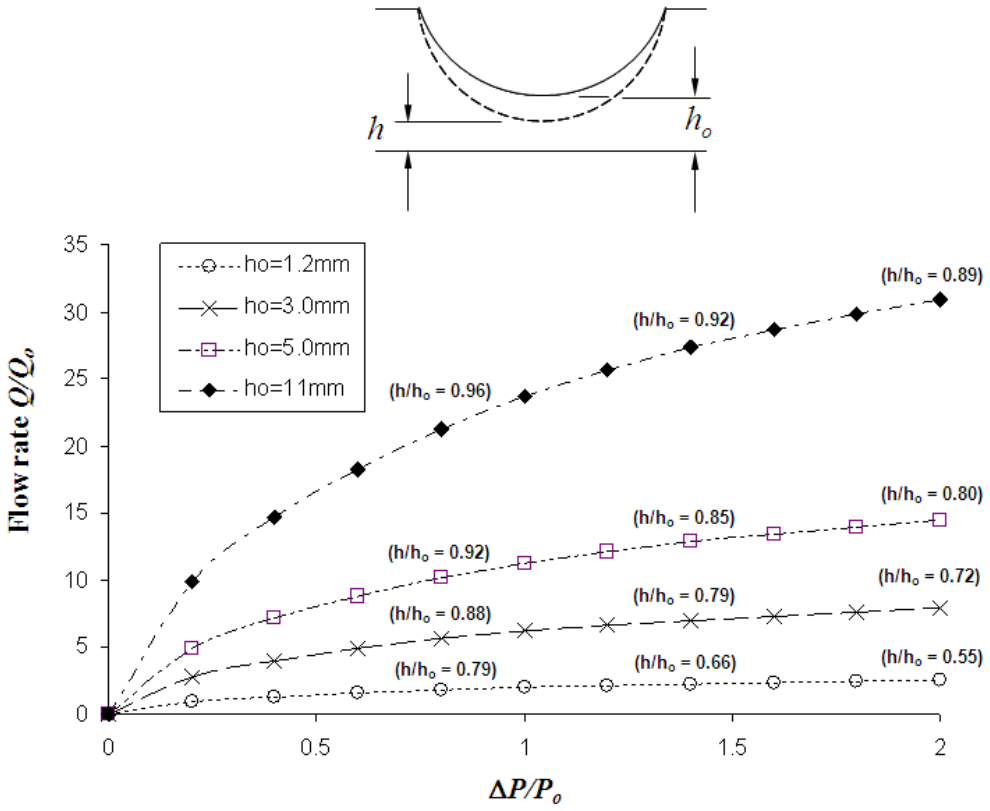

(a)

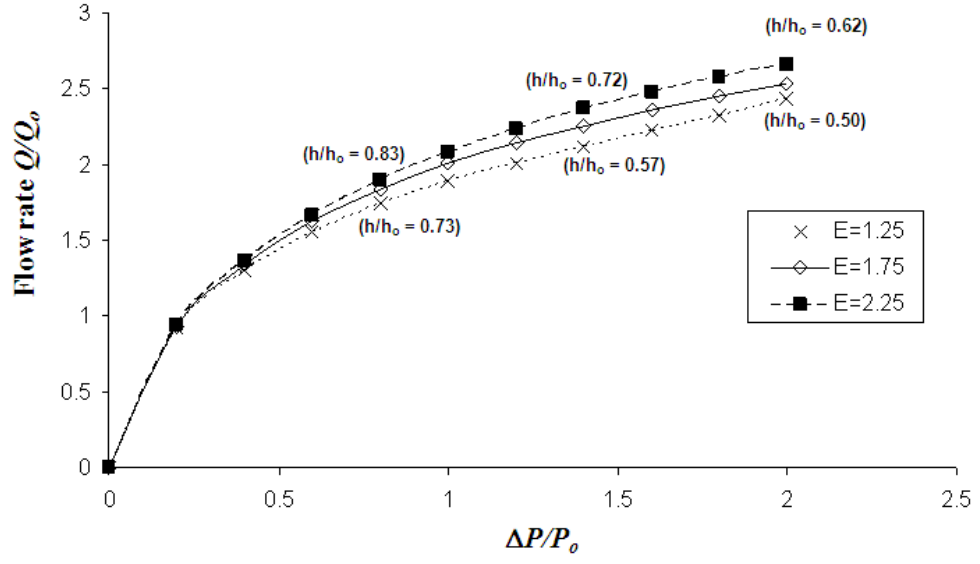

(b)

Figure 4.10: Parametric investigation using k-ω SST turbulence model: (a) Effect of initial airway opening h_o on flow rate Q and constriction height h for a fixed tongue replica modulus $E = 1.75$ MPa and (b) Effect of tongue modulus E on flow rate Q and constriction height h for a fixed initial opening $h_o = 1.2$ mm (Note: $Q_o = 10$ L/min, $P_o = 100$ Pa and h_o = initial constriction height)

A similar parametric investigation was also undertaken using a RANS k-ω SST turbulence model, examining both initial constriction height and modulus of tongue replica. Variation in both parameters exhibit similar trend of non-linear flow rate retardation with increasing expiratory efforts as a laminar case, as plotted in 4.10. However, the degree of tongue replica collapse is more significant than in a laminar case, as shown for example, for a case of $h_0 = 1.2$ mm, the final constriction ratio h/h_o is 0.64 under laminar conditions, compared to 0.55 in the case with k-ω SST turbulence model. Furthermore, closer comparison shows that a 40% stiffening of tongue replica modulus ($E = 1.25$ to 1.75 MPa) yields an 11% reduction in wall collapse, while, a 50% increase in initial airway opening ($h_o = 0.8$ to 1.2 mm), leads to a 9% reduction in collapse.

4.4.2 Elastic Wall Deflection

The deflection of the tongue replica along the symmetric plane (for a $h_o = 1.2$ mm case) is shown in Figure 4.11 for several intraluminal pressure differences ΔP. It is evident that the difference in intraluminal pressure 'pushes' the elastic tongue replica downstream in the x-direction. Concurrently, the contracting flow underneath the tongue replica leads to an increase in flow velocity, which is accompanied by a corresponding drop in pressure - a Venturi effect. This suction pressure effectively 'pulls' the tongue replica downwards in the y-direction, thus implying an increasingly upward and posterior collapse of the tongue with increasing expiratory effort. This may lead to increased airway obstruction and perhaps, expiratory snoring.

In addition, the cross-sectional deflection of the tongue replica at the narrowest opening (for a $h_o = 1.2$ mm case) is shown in Figure 4.12. As expected, in addition to increased deflection as ΔP is increased, the profile also reveals a larger opening area close to the side walls where the tongue replica is supported and tends to narrow non-linearly towards the symmetric plane $z = 0$. This profile perhaps influences the flow patterns, which is discussed in the next section. The difference in y-position at the side

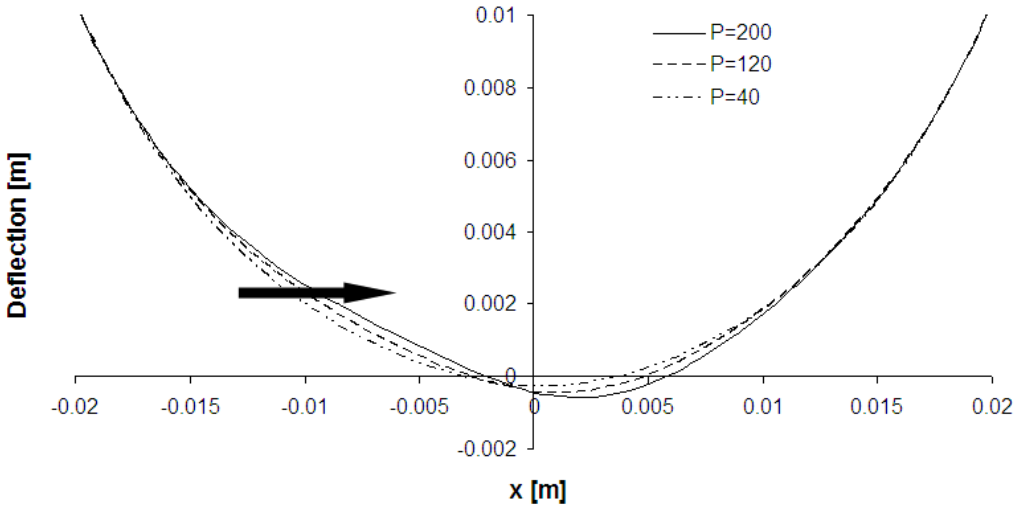

Figure 4.11: Elastic wall deflection measured on the symmetric plane $z = 0$ at intraluminal pressure difference $\Delta p = 40$, 120 and 200 Pa. Arrow shows direction of increasing intraluminal pressure difference.

wall ($z = 0.0125$) is due to the different downstream location of the narrowest opening. This is associated with the downstream deflection of the elastic wall as pressure is applied in the axial direction to the upstream portion of the wall, as described earlier.

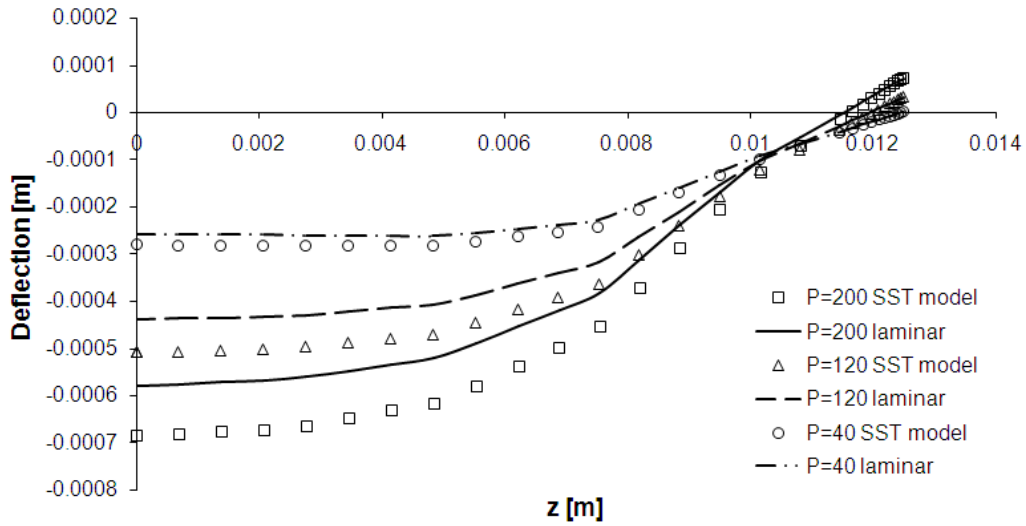

Figure 4.12: Deflection profile of tongue replica in the lateral direction across its narrowest opening (refer Figure 4.2(c)) at intraluminal pressure difference $\Delta p = 40$, 120 and 200 Pa

The diverging flow downstream of the narrowing oropharynx is likely to contribute to flow instabilities that lead to flow transitioning to turbulence. These flow structures include vortices and additional diffusion that affect the fluid-structure interaction. The

comparison between a laminar case and a case with k-ω SST turbulence model in Figure 4.12, shows the latter exhibiting much severe elastic wall collapse, particularly at higher Δp. Figure 4.13 summarises the minimum opening height underneath the elastic wall between the current laminar results and the k-ω SST model results. This shows minimal difference in elastic wall deflection between both flow regimes at $\Delta p/P_o < 0.5$, but increased deflection in the case with k-ω SST turbulence model as Δp is further increased.

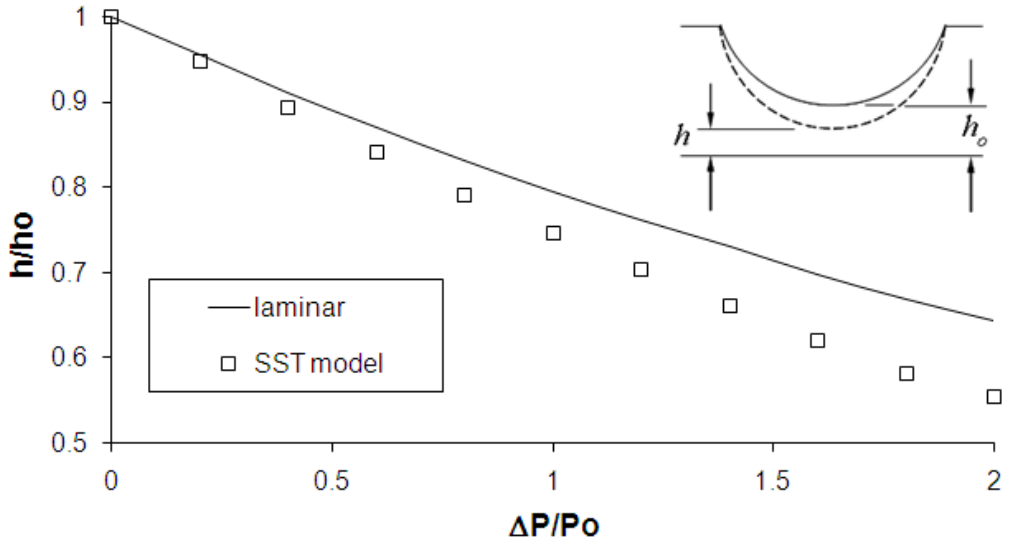

Figure 4.13: Elastic wall deflection with increasing ΔP for a $h_o = 1.2$ mm case (Normalization constants: $P_o = 100$ Pa and h_o = initial constriction height)

The increased deflection observed above would suggest a more severe pressure drop is experienced by the elastic wall in transitional or turbulent flow than in laminar flow. Indeed, examining the pressure distribution along the elastic wall on the symmetrical plane in Figure 4.14, at location $x = 0.0024$ m, a minimum suction pressure of -80.3 Pa at the constriction is predicted in the case with k-ω SST model compared to approximately -42 Pa for the laminar flow. This is consistent with numerical findings on a rigid pharynx modelled by Shome *et al.* (1998), where at similar flow rates, a 40% increase in pressure drop is predicted in turbulent flow compared to a laminar flow. This is expected to be more severe where the flow boundaries (i.e. tongue in this case) is considered elastic and collapsing, as indicated here by an increase of 100%. Thus,

the flow regime in the pharyngeal airway has significant effects on the degree of apnoeic obstruction and is important to be considered in pre-operative treatments.

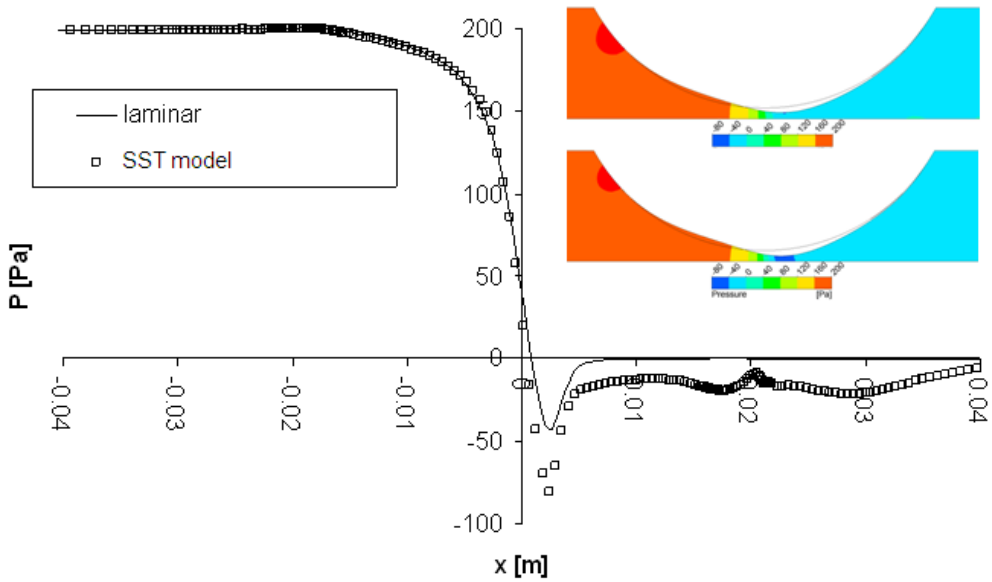

Figure 4.14: Pressure distribution along elastic wall on the symmetric plane of the idealised pharyngeal airway at $\Delta P = 200$ Pa for a $h_o = 1.2$ mm case (note that elastic wall is within -0.02136 m $< x < 0.02136$ m). Inset (top): Pressure contour on symmetric plane in laminar flow. Inset (bottom): Pressure contour on symmetric plane in flow with k-ω SST model.

4.4.3 Three-Dimensional Analysis

Typical flow patterns in the idealised airway are shown in Figure 4.15 for a case where laminar flow is assumed. In general, the flow is contracted towards the base of the elastic wall (constriction area) and separates from the elastic wall, forming a jet streaming towards the outlet. Three-dimensional recirculation is observed immediately downstream of the elastic wall, above the jet streams for all ΔP.

Streamlines released from upper and bottom half of the inlet reveals the tendency for the streamlines to migrate towards the side walls where the cross-sectional area is more open (recall Figure 4.12). This side stream (also visibly shown by the velocity contours peaking towards the side) is more pronounced at higher ΔP where the elastic wall deflection is further skewed downstream. Not surprisingly, swirling flow about the x-axis is also formed as the skewed stream underneath the constriction separates off the

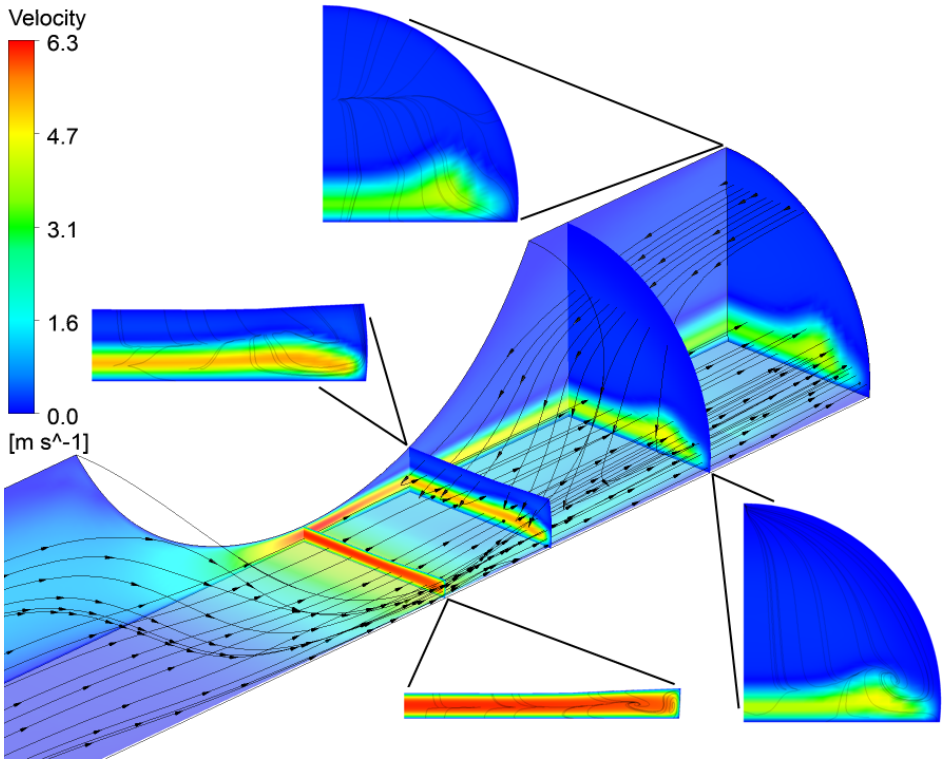

(a)

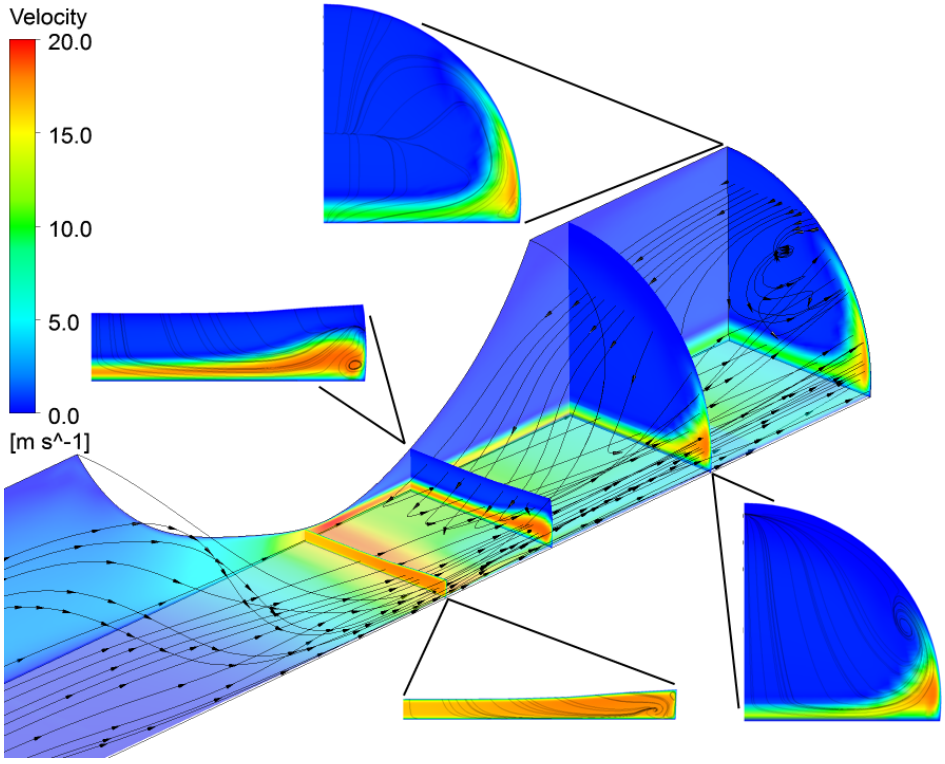

(b)

Figure 4.15: Streamline plot and contours of velocity along vertical symmetry plane, bottom wall and several axial cross-sections for $h_o = 1.2$ mm case under laminar flow conditions: (a) $\Delta P = 20$ Pa and (b) $\Delta P = 200$ Pa

elastic wall and rigid bottom wall and is forced to follow the circular side walls of the idealised airway. Thus, the swirling strength of the inner recirculation core is increased with increasing flow rate as the outer streams follow the curvature of the walls.

Figure 4.16 shows streamline and velocity contour plot for a case where flow inside the idealised pharyngeal airway is modelled using a k-ω SST turbulence model. Similarly, a three-dimensional recirculation region is formed downstream of the tongue replica and a tendency for the flow stream to migrate towards the side walls with increasing expiratory effort is also evident, as indicated by both streamlines and peak contours. Recirculation regions are typically accompanied by low pressure vortex cores and therefore significant low pressure regions immediately downstream of the tongue replica are not unexpected. Indeed, as shown in Figure 4.17, the pressures downstream of the narrowest opening in the airway are negative, with local minimums in each cross-sections either located centrally or tended towards the pharyngeal side walls.

Although not included in the scope of the current investigation, the collapse of side walls in the oropharynx region also represent a typical mode of occlusion in OSAHS. The cross-flow pressure gradients, as shown in Figure 4.17, may encourage the collapsibility of the side walls in the pharyngeal airway. Plotting the pressure distribution along the circumference close to the side walls at each of the cross-sections, shows that all the pressure in the vicinity of the pharyngeal side walls are negative, although the severity of this negative pressures seems to be reduced further downstream. This reduced suction pressure near the wall with downstream flow is also shown in the axial pressure distribution of Figure 4.19. Nevertheless, the interaction of negative air flow pressure with the side walls would suggest tendency of side wall deflecting inwards, perhaps, most likely at regions closer to constricted section.

Examining this circumferential distribution of pressure along the pharyngeal side walls in Figure 4.17, it is not clear whether the side wall tends to collapse in the anterior-posterior or lateral (left-right) direction during expiration, although many investigators have observed that the cross-sections in occluded airways in OSAHS patients tend to

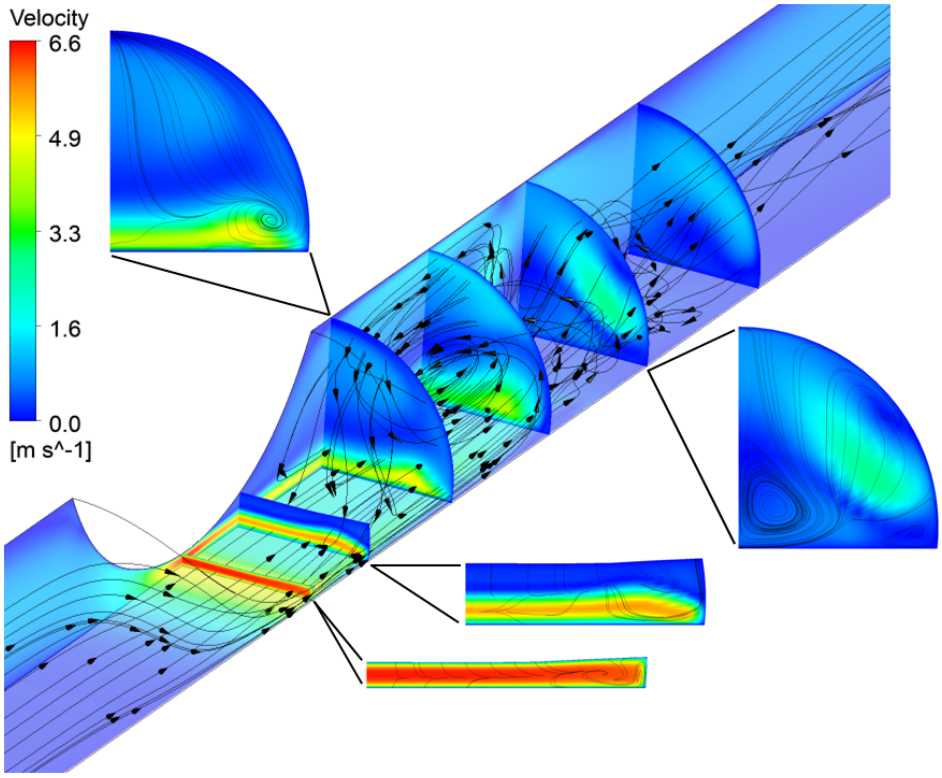

(a)

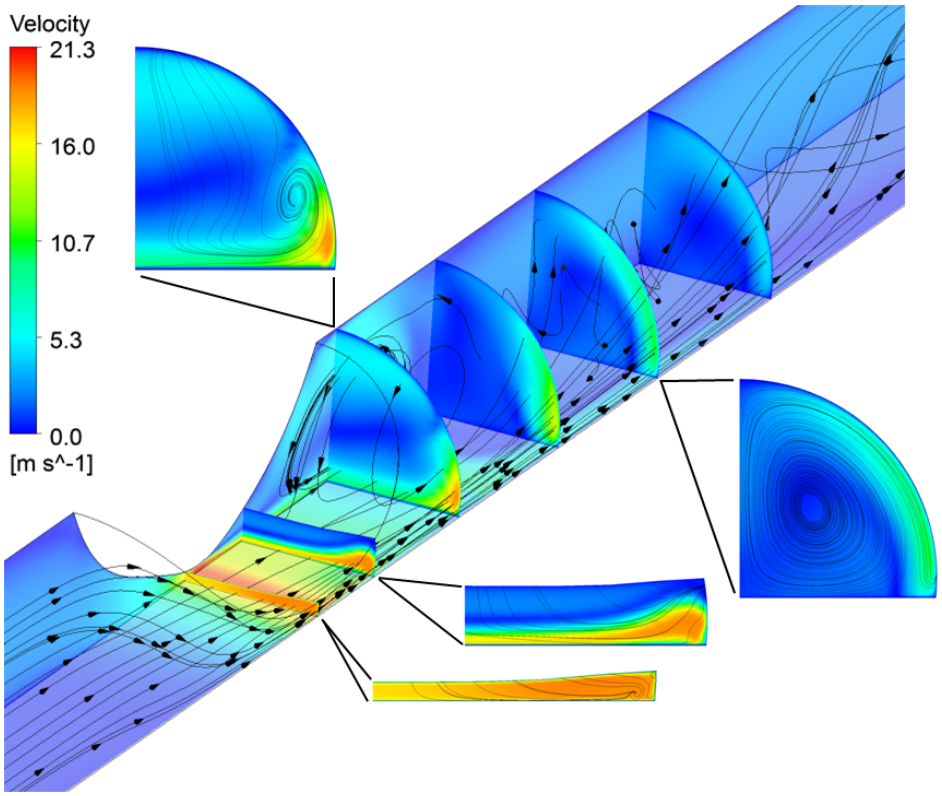

(b)

Figure 4.16: Streamline plot and contours of velocity along vertical symmetry plane, bottom wall and several axial cross-sections for $h_o = 1.2$ mm case with k-ω SST turbulence model: (a) $\Delta P = 20$ Pa and (b) $\Delta P = 200$ Pa

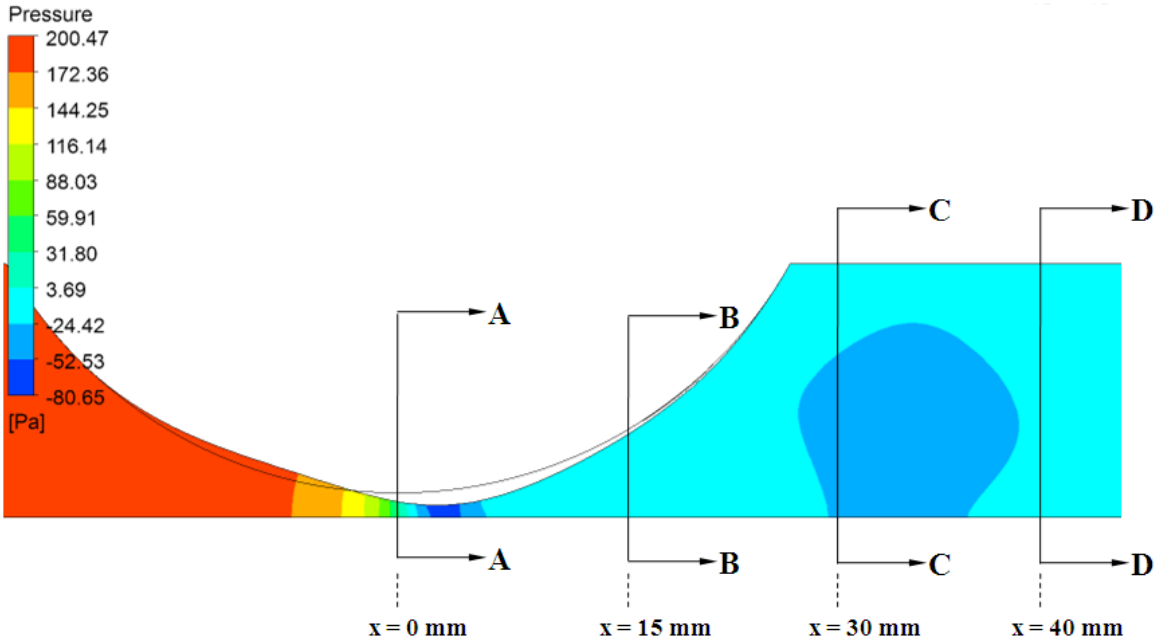
Pressure
200.47
172.36
144.25
116.14
88.03
59.91
31.80
3.69
-24.42
-52.53
-80.65
[Pa]
A
B
C
D
A
B
C
D
x = 0 mm
x = 15 mm
x = 30 mm
x = 40 mm

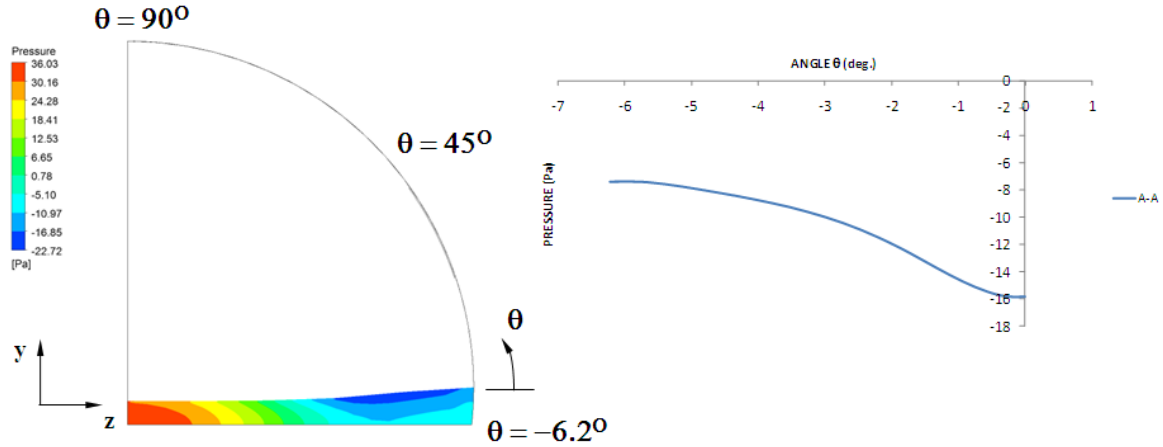
θ = 90°
Pressure
36.03
30.16
24.28
18.41
12.53
6.65
0.78
-5.10
-10.97
-16.85
-22.72
[Pa]
θ = 45°
y
z
θ
θ = −6.2°
ANGLE θ (deg.)
PRESSURE (Pa)
A-A

(a)

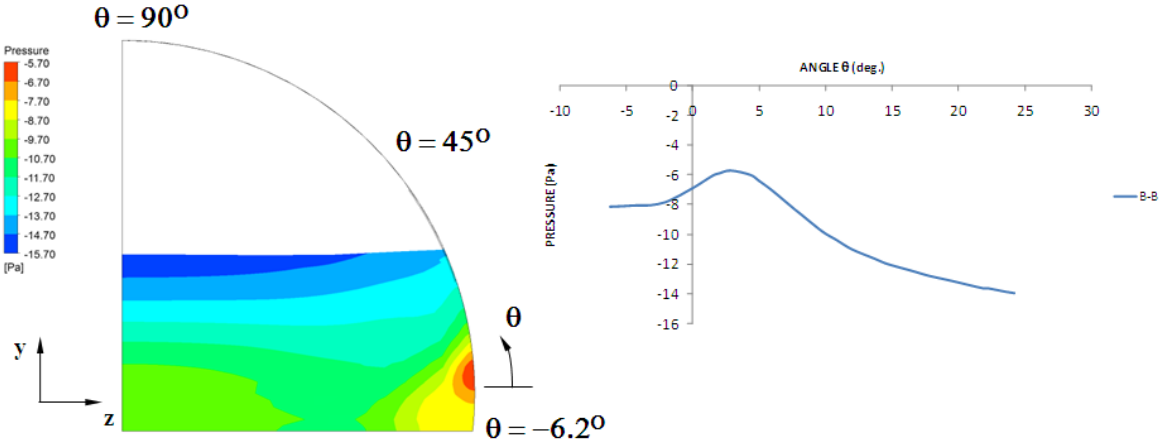
θ = 90°
Pressure
-5.70
-6.70
-7.70
-8.70
-9.70
-10.70
-11.70
-12.70
-13.70
-14.70
-15.70
[Pa]
θ = 45°
y
z
θ
θ = −6.2°
ANGLE θ (deg.)
PRESSURE (Pa)
B-B

(b)

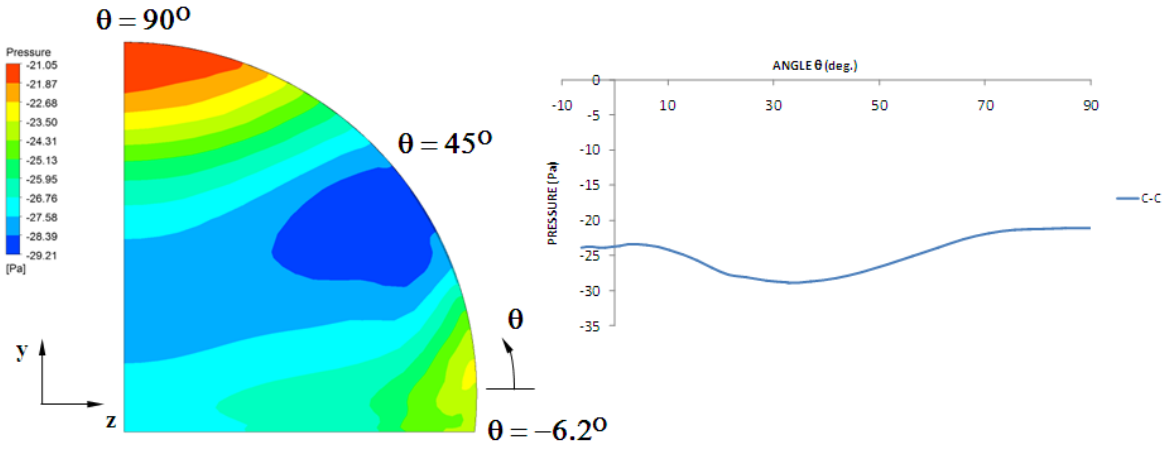

(c)

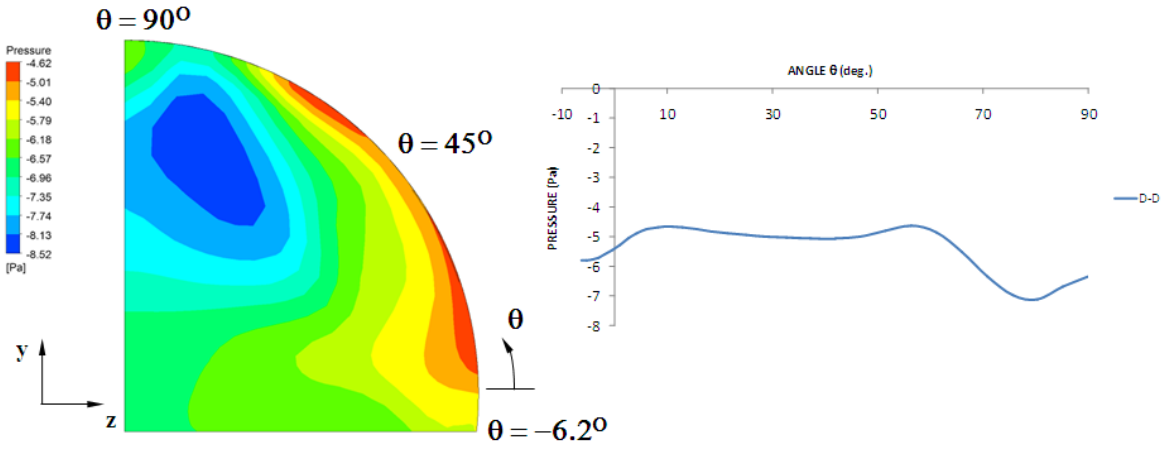

(d)

Figure 4.17: Plots of pressure contour and circumferential pressure distribution along side walls under expiratory flow conditions using k-ω SST turbulence model, for case $h_o = 1.2$ mm and $\Delta P = 200$ Pa, at several cross sections along the pharyngeal airway: (a) Section A-A (b) Section B-B (c) Section C-C and (d) Section D-D

be elliptical with the minor axis directed laterally (see for example Lucey *et al.* (2010); Balint (2001)). Section C-C shows higher suction (negative) pressure towards the side of the pharyngeal wall, but further downstream, section D-D shows that maximum suction pressure tends to be at the top of the pharyngeal wall. It would be expected that this pharyngeal wall collapse would be more pronounced during inspiratory breathing, as the pressures developed in the airway are entirely negative (suction), as opposed to localised suction pressures during expiration.

Indeed, examining an inspiratory case with $h_o = 1.2$ mm and setting the inlet boundary condition with atmospheric pressure, while a suction pressure is prescribed at the outlet of the 3D model, the magnitudes of the suction pressure near the pharyngeal walls are larger compared to magnitudes during expiration, as shown in Figure 4.18.

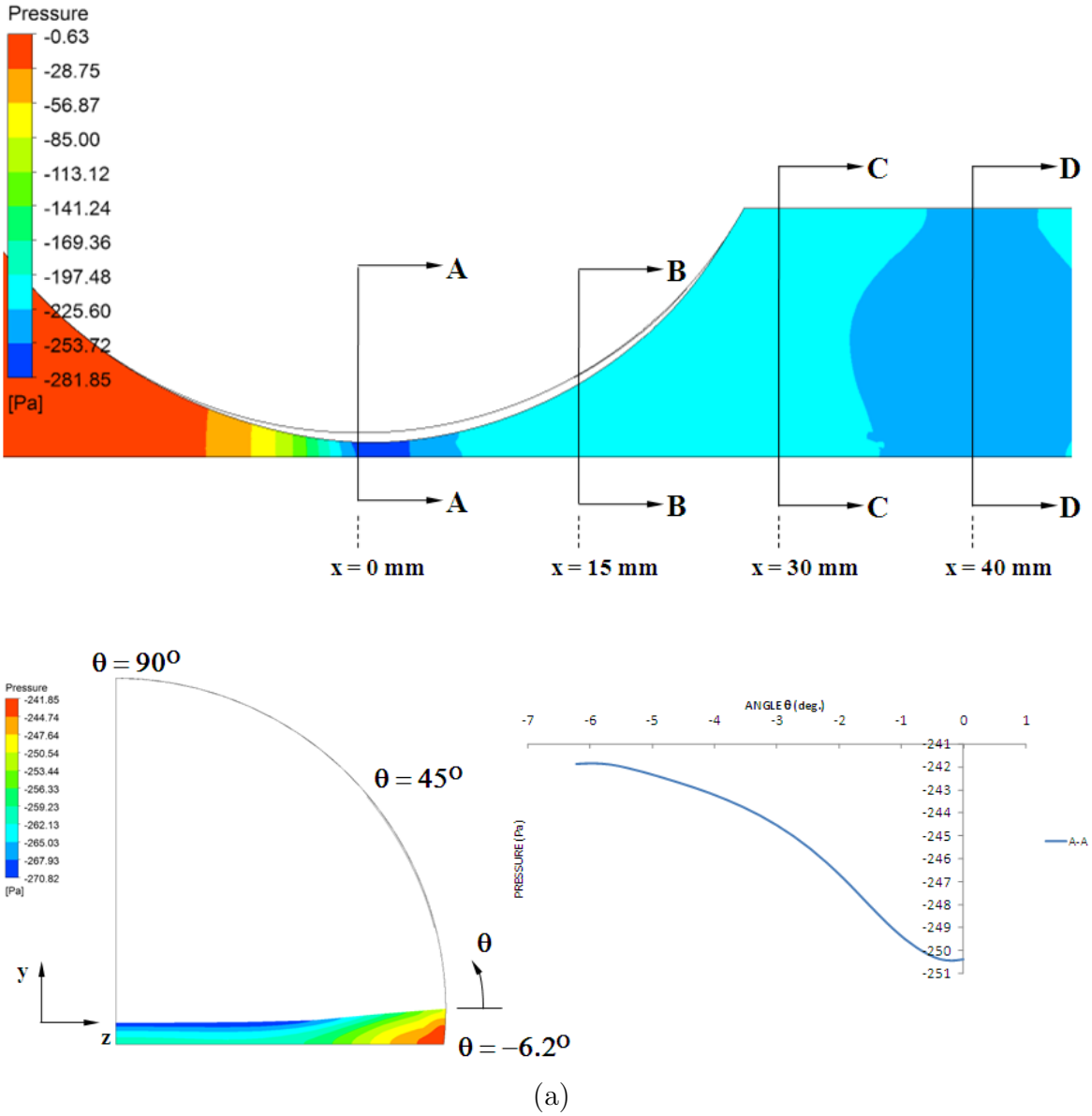

(a)

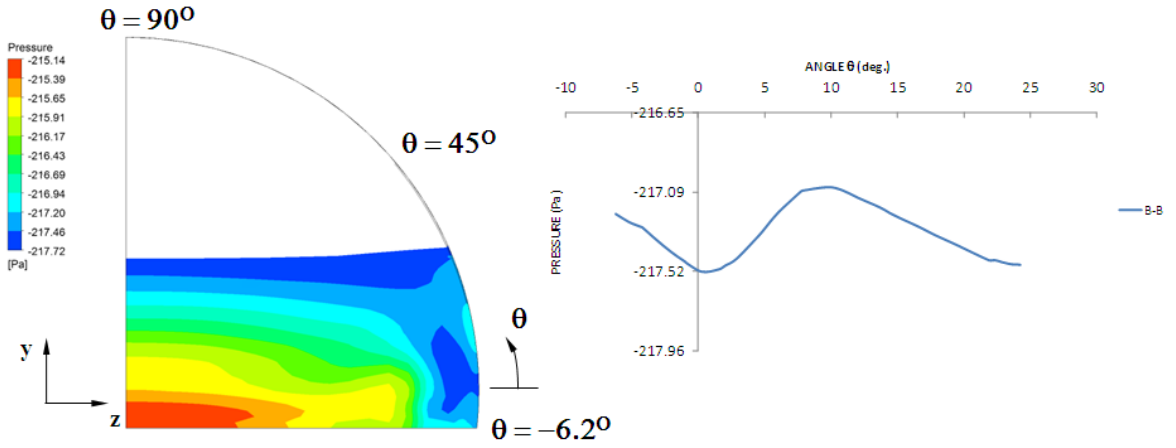

(b)

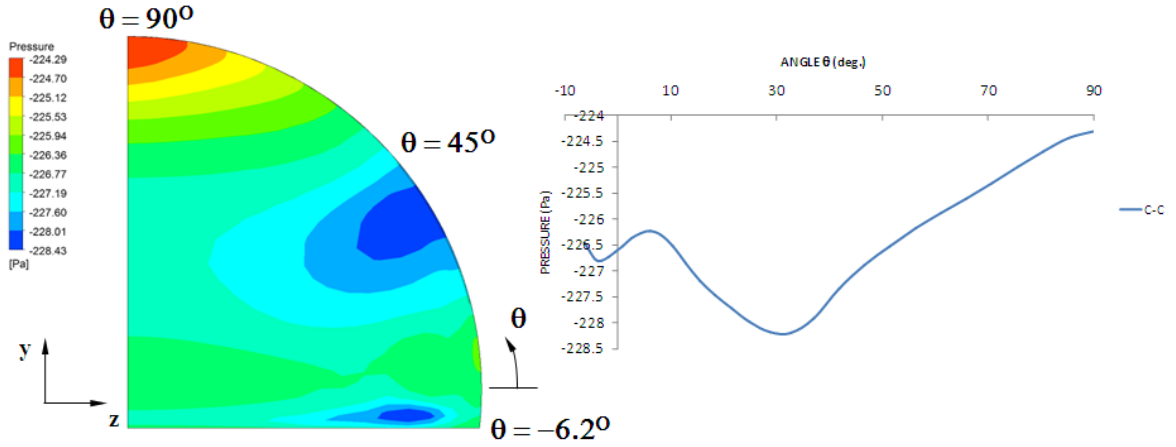

(c)

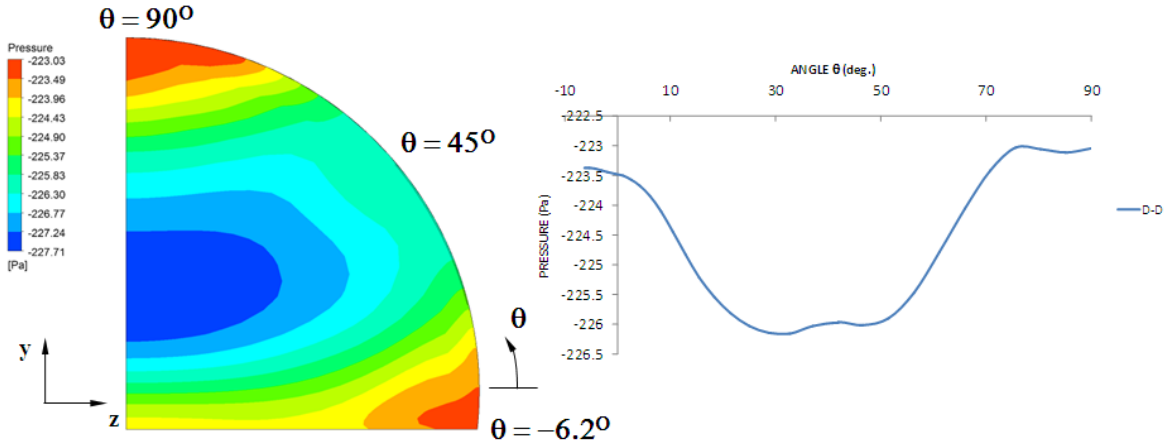

(d)

Figure 4.18: Plots of pressure contour and circumferential pressure distribution along side walls under inspiratory flow conditions with k-ω SST turbulence model, for case $h_o = 1.2$ mm and $\Delta P = 200$ Pa, at several cross sections along the pharyngeal airway: (a) Section A-A (b) Section B-B (c) Section C-C and (d) Section D-D

Examining the circumferential distribution of the near-wall pressures, as plotted on the right column of Figure 4.18, shows that local maximum suction pressure near the walls are located towards its side rather than near the top (or anterior), for all cross-sections selected. Thus, the cross-flow pressure gradients corresponding to cross-sectional morphology of the airway and asymmetry of the tongue deflection, in addition to 3-D recirculation generated downstream, may promote pharyngeal wall collapse which seems to be tending laterally, as clinically observed (Lucey *et al.*, 2010) and is more pronounced during inspiration than expiration.

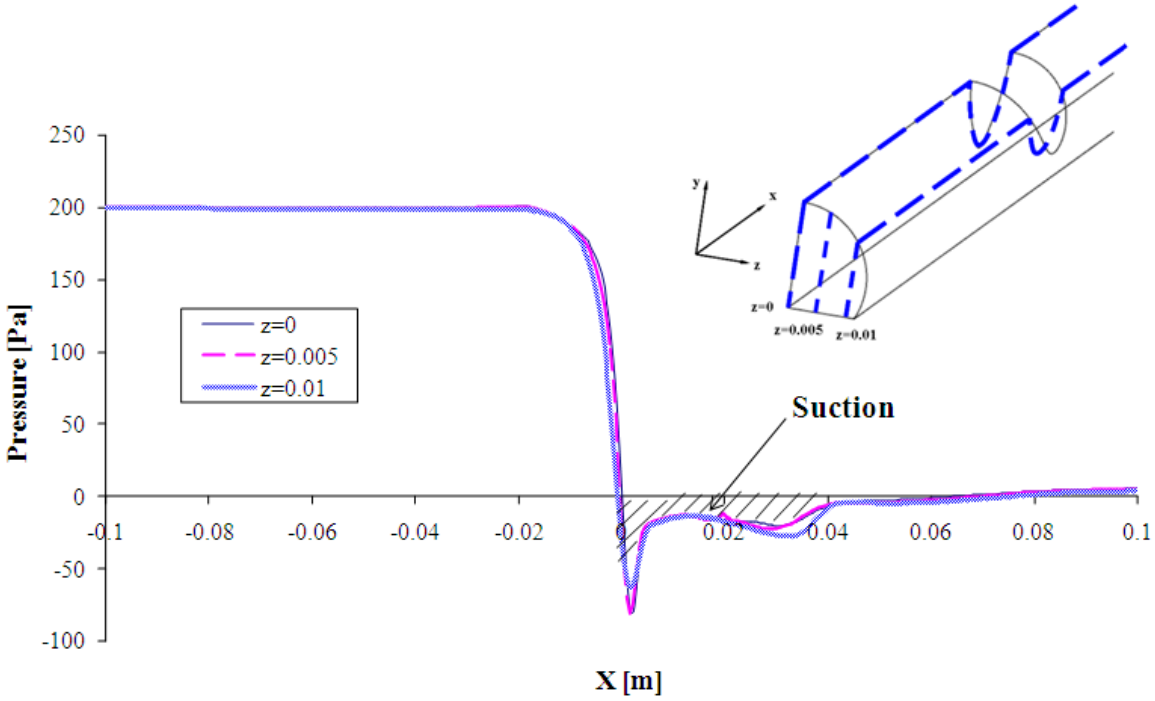

Figure 4.19: Pressure profile along several axial planes along top wall for case with k-ω SST turbulence model at $\Delta P = 200$ Pa for a $h_o = 1.2$ mm case (note that elastic wall is within -0.02136 m $< x < 0.02136$ m)

Focusing on the constriction region, the pressure profile is also influenced by the lateral distribution of the cross-sectional opening and velocity at the constriction. This is evident from pressure profile plots along the axial direction, located at several lateral x-y plane locations ($z = 0$ m, $z = 0.005$ m and $z = 0.01$ m) shown in Figure 4.19. The minimum suction pressure influencing collapse in the vicinity of the constriction is shown to be somewhat reduced closer to the side walls where a larger opening is

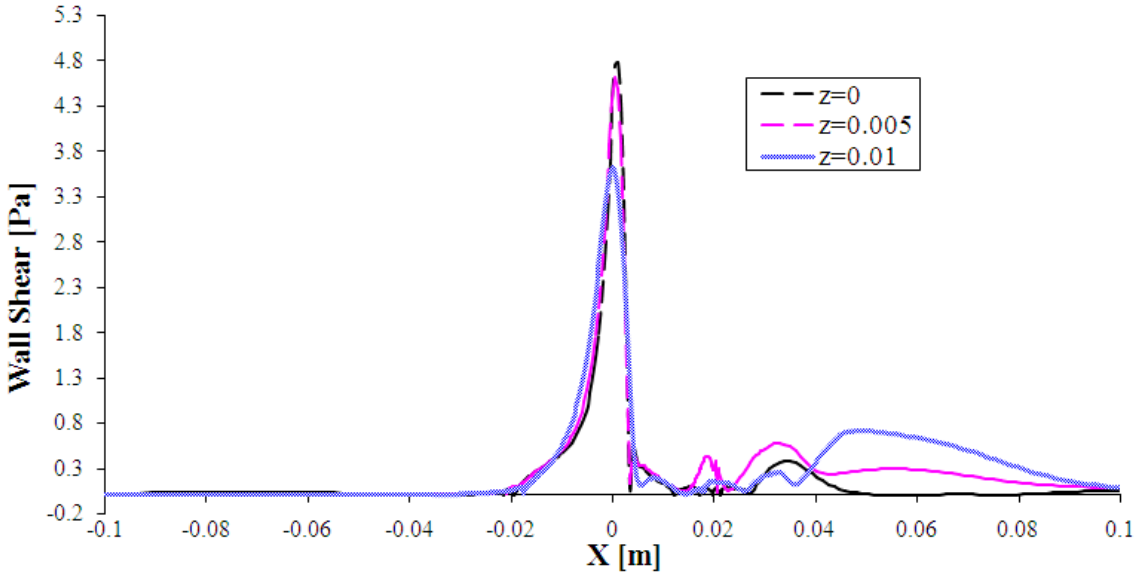

(a)

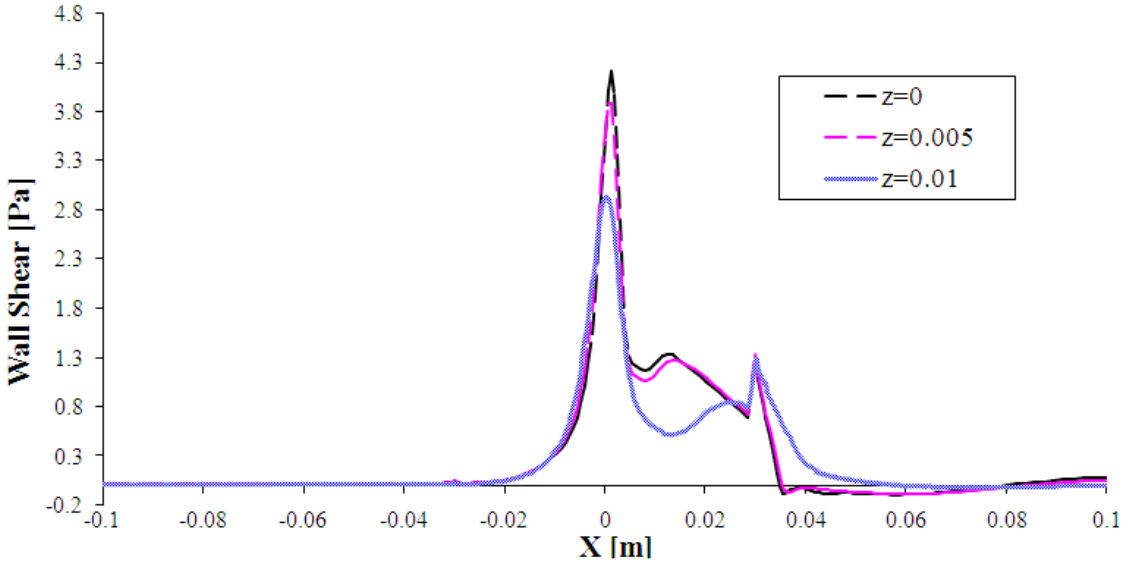

(b)

Figure 4.20: Wall shear profile along several axial planes for $h_o = 1.2$ mm case with k-ω SST turbulence model at: (a) Top wall and (b) Bottom wall (note that elastic wall is within -0.02136 m $< x < 0.02136$ m)

anticipated. Figure 4.19 also confirms the negative pressures downstream of the tongue replica around the recirculation region, which eventually tails off further downstream, as mentioned earlier.

The influence of the side wall on the lateral pressure and velocity profile is expected to influence the location of flow separation off both the tongue replica (elastic wall) and oropharynx base (rigid bottom wall). Figure 4.20 presents the axial shear profile along the top and bottom walls, at several lateral locations $z = 0$ m, $z = 0.005$ m and $z = 0.01$ m. Those profiles reveal a downstream shift in the position of minimum wall shear as the flow approaches the side walls, suggesting a delay in flow separation as the side wall is approached. As a result, flow recirculation occurring downstream of the tongue replica tends to be smaller towards the side walls. This suggests a sharper tongue deflection profile towards its symmetrical plane as more back flow impinge on the downstream portion of the tongue replica.

Based on the hydraulic diameter $D = 4A/P$, where A is taken as the cross-sectional area at the inlet and P is the inlet perimeter, the Reynolds numbers Re simulated in this investigation range from 274 - 9520 (i.e. from laminar to turbulent), as summarised in Table 4.2.

Table 4.2: Variation of Re with initial opening h_o cases used in parametric study

	Initial opening (mm)					
ΔP (Pa)	0.8	1.2	2.0	3.0	5.0	11.0
20	274	733	905	1190	1949	4320
200	719	1173	2497	3426	5877	9520

Employing either laminar or k-ω SST turbulence model for the flow, the accuracy of the laminar simulation is expected to diminish for conditions at higher Reynolds numbers, where transitional turbulent flow structures are present, and conversely, the simulation with k-ω SST turbulence model would deviate from laminar conditions that are expected at lower Reynolds numbers. Nevertheless, the results for either flow regime, similar to those observed in previous works, showed that a narrower opening along the airway predisposes patients to airway occlusion and hence more severe flow

rate limitation.

The complex three-dimensional shape of the airway anatomy could perhaps develop flow features that trigger earlier transition to turbulence in the pharyngeal airway. Hence, consideration of turbulence for comparison with laminar conditions is perhaps necessary. Despite employing a k-ω SST turbulence model, flow rates are reasonably unchanged from those predicted assuming the flow is laminar. However, within the constriction region a much sharper pressure drop is expected if the airway flow is turbulent and this leads to severe collapse of the base of the tongue. This would perhaps suggest the importance of considering turbulent flow in pre-operative treatments and the importance of delivering positive air pressure at the proper flow regime.

Compliance of the pharyngeal airway is a function of both its tissue constituents and degree of muscle activation. Therefore, neurological factors which influence the musculatory control of the pharyngeal tissues (and hence its compliance) are also important in these apnoeic syndrome. As suggested by the results, lack of pharyngeal stiffness encourages greater wall collapse, possibly exacerbating these apnoeic conditions.

4.5 Concluding Remarks

Numerical investigation of a three-dimensional model of the airway-tongue replica originally proposed by Chouly *et al.* (2008, 2009) and Van Hirtum *et al.* (2005), has been undertaken, considering either laminar or low-Re turbulent flow prevailing in the pharyngeal airway. The low-Re turbulent fluid-structure interaction simulation predicts a more severe pressure drop in the constriction compared to a laminar fluid-structure interaction, reflecting a similar trend as the turbulent rigid pharynx simulation by Shome *et al.* (1998). However, in comparison with the 40% increase in pressure drop predicted by assuming pharynx boundaries are rigid, a 100% increase in pressure drop is shown if the flexibility of the pharynx boundaries is taken into account (i.e. in the present case, a flexible tongue interfacing with air flow). Similar flow rate limitation is observed with laminar flow, although more pronounced narrowing of the area behind

the tongue is anticipated if the flow is transitional or turbulent.

A parametric study reflecting some anatomical and neuromuscular factors that affect OSAHS in the airway was undertaken, illustrating the tendency of narrower pharyngeal opening to apnoeic obstruction. The parametric investigation also suggests that increased compliance of the tongue is also equally important in the pathogenesis of apnoeic obstruction. In addition, some three-dimensional flow features relevant to the airway-tongue replica reveal the tendency of the airflow to migrate towards the side walls, as maximum collapse occurs towards the center of the base of the tongue. Furthermore, negative cross-flow pressures generated along the pharyngeal side walls suggest the likelihood of side wall collapse, which could be further explored by modelling flexible side walls instead of a rigid assumption used in the present study.

Brown *et al.* (1985) had successfully measured changes in the cross-sectional area along the pharyngeal airway during expiratory and inspiratory breathing pressures, on both apnoeic and non-apnoeic patients using an acoustic reflection technique, allowing pharyngeal compliance to be estimated as a function of the distance from the mouth. For future work, this varying stiffness along the pharyngeal airway could be incorporated in order to capture the interaction between multiple segments of differing compliance within the pharyngeal airway and how they influence collapse and reopening of the lumen. Ultimately, a real pharyngeal airway model could be used for the fluid-structure investigation.

Chapter 5

Instability of Soft Palate

This chapter presents investigation of the soft palate dynamics in relation to snoring and sleep apnoea. Two-dimensional channel flow over a flexible cantilever plate has been used to idealise the dynamics of the soft palate during oronasal inhalation. This is presented in the introductory section 5.1, following background works on the subject of snoring and its relation to apnoea. The soft palate dynamics are further explored by investigating two conditions - presented in two parts, i.e. (i) influence of palatal obstruction and (ii) influence of contact or impact with pharyngeal walls.

Firstly, the modelling of an obstructive channel and the results on palatal instability are discussed in section 5.2. Those results are assessed in relation to sleep apnoea and potential for non-invasive detection of palatal occlusion, followed by a brief conclusion of this section. This work was published in Rasani *et al.* (2011*a*).

Secondly, in section 5.3, the development of a palatal impact model is outlined, followed by results and discussion of its influence on palatal instability. Further evaluation of those results in relation to apnoeic snoring is also discussed, followed by a brief conclusion at the end of the section.

Finally, a concluding remark for this chapter is presented in section 5.4.

5.1 Introduction

Although snorer's do not necessarily suffer from obstructive sleep apnoea, the fact that most apnoeic patients do exhibit snoring suggests the close relation between the two phenomena. Snorers are at higher risk of obstructive sleep apnoea (Young *et al.*, 1993; Huang *et al.*, 1995), which affects about 4% of the general adult population and has been linked to hypertension and heart failure (Bertram, 2008). Instability of the soft palate and the pharyngeal walls has been implicated in the biomechanics of snoring and sleep apnoea. At sufficiently high velocities, the soft palate loses its stability through a flutter mechanism, which seems to be the most common type of snoring (Huang *et al.*, 1995).

A number of studies with flows around cantilevered plates have been performed with interest in understanding palatal snoring. Idealising palatal dynamics as a cantilever plate in axial flow, Huang (1995) analytically solved a linear beam model applied with pressure loads estimated from Theodorsen's classical solution for wing aerodynamics. This enabled Huang to show that the circulatory component of the fluid loading resulting from reaction to the trailing wake vortices is responsible for the irreversible flow to plate energy transfer that destabilises the system. Coupling a linear finite difference model of a cantilever beam to a Navier-Stokes finite element solver for viscous flow in a channel, Balint & Lucey (2005) showed both divergence and flutter mechanism influencing the stability of the soft palate depending on the inlet conditions .

As the biomechanics and affected soft tissues of OSAHS and snoring are very similar, snoring signals may carry relevant information on the conditions of the upper airway during sleep. With the current expensive and cumbersome polysomnographic diagnosis of OSAHS rendering it inappropriate for mass screening, many researchers have explored snoring signals as alternative means for detecting and diagnosing OSAHS (see for example, Mesquita *et al.* (2010); Cavusoglu *et al.* (2008); Abeyratne *et al.* (2005); Sol-Soler *et al.* (2007, 2002); Lee *et al.* (2001); Dalmasso & Prota (1996); Fiz

et al. (1996)). This chapter intends to explore palatal snoring in relation to possible OSAHS diagnosis through palatal snoring signals.

5.2 Influence of Obstruction on Palatal Instability

This investigation is interested in looking at the influence of local obstruction on the stability of the soft palate during oronasal inhalation. To that end, a channel flow around a flexible cantilevered plate is modeled and a generous blockage is introduced in one of the channels, as depicted in figure 5.1. This may perhaps represent a more realistic oropharyngeal airway, where the channel widths are non-uniform with the presence of localised obstruction such as the base of the tongue. Following the channel geometry employed in Balint & Lucey (2005), a channel half-width of 5 mm is modeled, with upstream distance between the root of the cantilever plate and inlet set to 50 mm and a downstream length to the outlet of 250 mm is prescribed, to ensure sufficient flow development both prior to reaching the cantilever plate and upon exiting the channel. The width of the obstruction is fixed but its depth, D is varied from 0-4 mm. A uniform velocity is applied at the inlet and the focus is to examine the difference in the inlet velocity required for onset of plate instability, with varying obstruction depths. The intention is to estimate a relationship between the critical velocity and the palatal obstruction depth.

5.2.1 Method

Fluid Model

The fluid dynamics for a two-dimensional, laminar, incompressible flow in the channel domain shown in figure 5.1, could be typically characterised by the unsteady Navier-Stokes and continuity equation. In order to account for fluid mesh deformation that follows the structural motion, these fluid governing equations are recast in an Arbitrary Eulerian-Lagrangian frame of reference, given by (3.16) and (3.17), described earlier in chapter 3. The fluid mesh velocity is solved using a Laplacian Diffusion model,

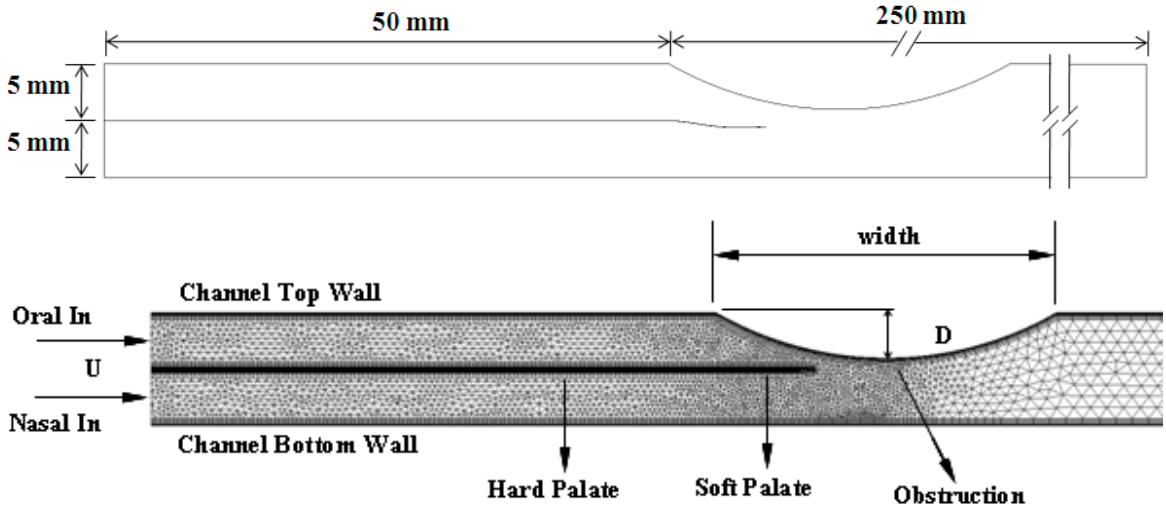

Figure 5.1: Idealised model of oral and nasal passage through upper airway showing the computational domain and grids, where D denotes the obstruction depth

which smoothes the mesh velocity from a magnitude matching the plate motion near the fluid-cantilever plate interface, to zero at the fluid domain boundaries.

The top wall, bottom wall and dividing 'hard palate' are defined as no-slip wall boundaries, while the outlet boundary is set to typical stress-free conditions. The channel length has been set to allow sufficient flow development towards the cantilever plate and also to allow fully developed flow towards the outlet boundary. In addition, finer boundary layer meshes are defined near the dividing 'hard palate', flexible cantilever plate and channel walls. Finer meshes are also located at regions around the vicinity of the obstruction and the tip of the cantilever plate, where steeper flow gradients are anticipated.

Cantilever Plate Model

The dynamics of the cantilever plate is described using equation of motion for a continuum i.e. equation (3.20) which, neglecting structural damping for this case, simplifies to

$$\rho_s \frac{\partial d}{\partial x_i} = \nabla \cdot \sigma_{ij} + \mathbf{f} \tag{5.1}$$

where the variables are as described in section 3.2 and $\mathbf{f}$ represents the fluid force exerted on the top and bottom surface of the plate (both fluid pressure and shear),

which varies with time. The first term on the RHS (right hand side) of (5.1) represents the internal force in the structure, which for a linear thin plate (of thickness h, Young's modulus E and Poisson ratio ν), is mainly influenced by its bending stiffness $B = Eh^3/12(1-\nu^2)$.

The leading edge of the flexible cantilevered plate is fixed to the 'hard palate', while its trailing edge is free.

Fluid-Structure Coupling

The coupling between the fluid and structural solver is achieved by enforcing force equilibrium and kinematic compatibility at the common fluid-structure interfaces. The steady-state solution for a given channel inlet velocity is used as the initial condition for the transient fluid-structure system. The fluid pressure and shear from the fluid solver is transferred to the structural solver and the plate displacement from the resulting structural dynamics is transferred back to the fluid mesh deformation - which for similar time step size, translates to matching structural and fluid velocities at the fluid-structure interface.

Considering A_1 and A_2 respectively as the top and bottom surface of the plate, the energy equation of the dynamic cantilever plate can be expressed as (Balint & Lucey, 2005; Zienkiewicz & Taylor, 2000)

$$\frac{d}{dt}\left\{\underbrace{\frac{1}{2}\int_V \rho\dot{\mathbf{d}}^2\,dV}_{\text{kinetic energy}} + \underbrace{\frac{1}{2}\int_V \sigma\cdot\epsilon\,dV}_{\text{strain energy}}\right\} = \left\{\underbrace{\int_{A_1}\sigma^f\dot{\mathbf{d}}\,dA + \int_{A_2}\sigma^f\dot{\mathbf{d}}\,dA}_{\text{rate of work by fluid}}\right\} - \underbrace{d\int_V \dot{\mathbf{d}}^2\,dV}_{\text{rate of dissipation}} \tag{5.2}$$

where $\mathbf{d}$ is the displacement vector of the plate, ρ represents the plate density, σ represents the stress vector in the plate, ϵ is the strain vector in the plate, σ^f represents the fluid tractions acting on the plate surface and d denotes plate dissipation or damping parameter (for a case where damping is considered). Thus, the total plate energy (kinetic and strain energy on the LHS) is driven by the rate of work exerted by the aerodynamic forces. If this rate of work exceeds the structural damping resulting in

a net positive value on the RHS, the total plate energy grows with time and plate instability ensues (Balint & Lucey, 2005).

It is worthwhile to remark that, consistent with the framework used in ANSYS, in the case of viscous Newtonian fluid, the destabilizing aerodynamic force consists of both pressure and viscous shear stresses (i.e. $\sigma^f = -p\mathbf{I}+2\nu\nabla^S\mathbf{u}$ as mentioned earlier in section 3.3). For inviscid fluids or cases where viscous stresses are negligible (as argued in Balint & Lucey (2005) and Tetlow & Lucey (2009)), the aerodynamic traction is simply the pressure acting normal to the plate surface and hence, the rate of work is simply driven by the pressure difference between the top and bottom surface of the plate.

The internal strain energy of the plate resists the aerodynamic forces and thus, promotes stability of the plate. This stabilizing internal force consists of both bending and in-plane components, which for large plate deflection includes the non-linear coupling to bending that impose additional stiffening to transverse deflection, as described earlier in equation (3.22). Accordingly, for thin plates with small deflection, the strain energy is largely the bending contribution of the form $\frac{1}{2}B\int(\partial^2 w/\partial x^2)^2 dV$, where w represents the transverse displacements.

The transient fluid-structure system is perturbed by releasing the cantilever plate from an initial deformation corresponding to its second mode shape (with maximum tip deflection = 0.1 mm), following the approach employed in Balint & Lucey (2005) and Tetlow & Lucey (2009). An increase in total plate energy with time, indicating plate instability, implies an increasing amplitude of plate oscillation. Thus, alternatively, in order to judge instability, the structural displacement is monitored over time to identify amplitude growth or decay at the applied inlet velocity.

Model parameters

The physical parameters used in this fluid-structure system is based on the work by Balint & Lucey (2005), that gives a cantilever plate second mode frequency of 100 Hz, which falls within the typical snoring frequency range of 30-100 Hz (Balint &

Lucey, 2005). As such, the cantilever plate length used is 8.5 mm, $E = 880$ MPa, $\nu = 0.3333$, $\rho_s = 2272.73$ kg/m^3, air density $\rho = 1.18$ kg/m^3 and its dynamic viscosity $\mu = 1.982 \times 10^{-5}$ Pa/s.

5.2.2 Results and Discussion

Three cases were simulated - a case without obstruction (i.e. D = 0) and two cases with obstruction depths D = 2 and 4 mm. Consistent with the second mode frequency of 100 Hz, a suitable time step t = 0.0005 s is used in all the simulations. A run for case D = 0 with a time step an order of magnitude smaller, t = 0.00005 s, shows minimal difference in plate response (albeit a slight phase shift), suggesting adequate temporal discretization for the purpose of this study. This is illustrated in Figure 5.2.

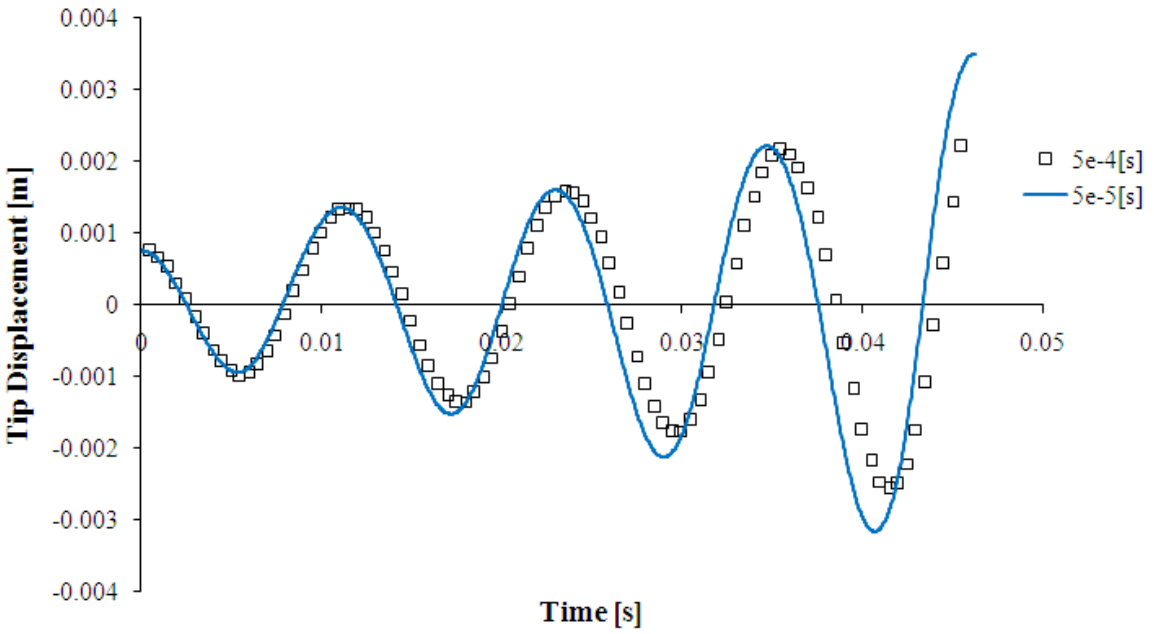

Figure 5.2: Comparison of plate oscillation for case with obstruction depth D = 0 mm, using time step sizes t = 0.0005 s and 0.00005 s

In addition, for verifying sufficient spatial discretization of the current model, a run with obstruction depth D = 4 mm was simulated with finer mesh where in general, the original grid size has been halved, resulting in a total 67322 elements in contrast to the original 20363 elements. The tip oscillation between the finer and original grids are practically indistinguishable, as shown in Figure 5.3(a), suggesting that the original

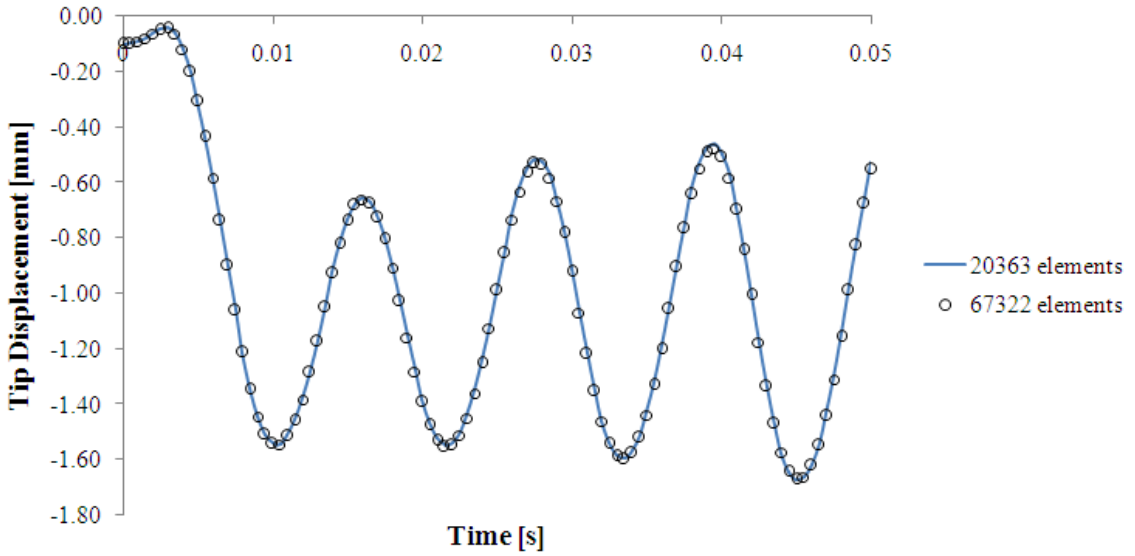

(a)

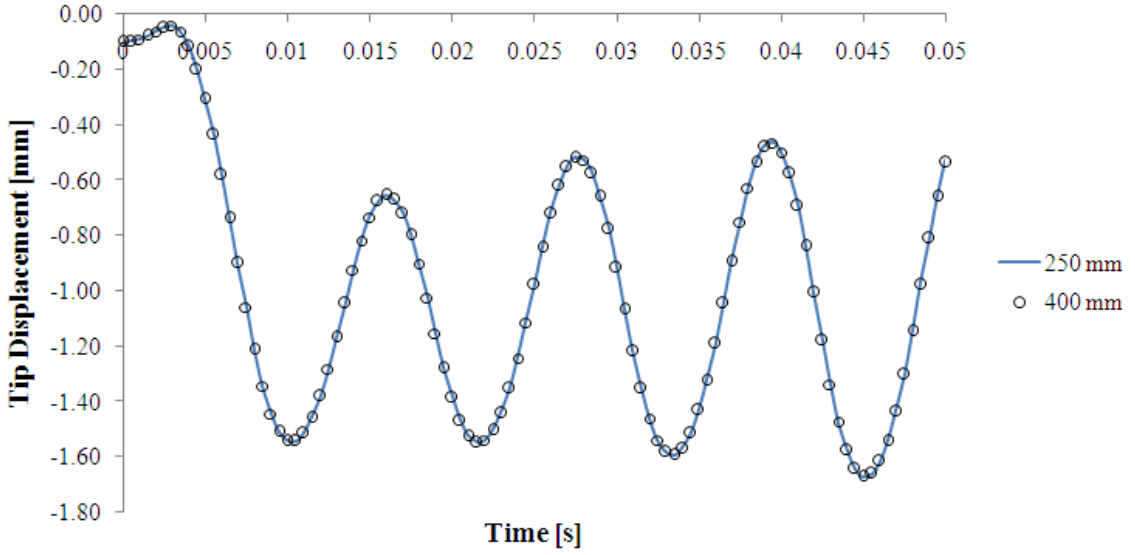

(b)

Figure 5.3: Numerical sensitivity studies: (a) Comparison of plate oscillation for case with obstruction depth D = 4 mm and fixed 250 mm downstream channel length, using current and finer grid sizes; and (b) Comparison of plate oscillation for case with obstruction depth D = 4 mm at current grid size, using current (250 mm) and longer (400 mm) downstream channel lengths

grid size used in the present investigation is sufficiently adequate for the purpose of this study.

Furthermore, the downstream length of the channel domain is known to influence the fluid resistance and inertance, which may affect the period of oscillation of the flexible plate (Balint & Lucey, 2005; Luo & Pedley, 1996). In order to assess the sensitivity of the cantilever plate response to downstream channel length, an additional run for case D = 4 mm is performed, but with 60% increase in downstream length to 400 mm (from the present 250 mm used in all the simulations). Comparisons depicted in Figure 5.3(b) show no significant difference in terms of amplitude and frequency response between both cases, suggesting that the current model, with downstream length of 250 mm, is sufficiently representative for configuration with longer channel lengths.

Critical Velocity

Several simulations were undertaken examining a case without obstruction (i.e. D = 0 mm), a case with obstruction depth D = 2 mm and a case with obstruction depth D = 4mm. In order to estimate critical velocity for onset of plate instability at each obstruction depth, various flow velocities were prescribed at the channel inlet and the plate oscillation over time is monitored. Flow-induced instability of the cantilever plate is considered to occur if its tip oscillation shows increasing amplitude over time. Figure 5.4 compares the velocity contours and cantilever plate positions at similar instants, for a channel with obstruction depth D = 4 mm, at prescribed inlet velocities U = 0.5 m/s and 0.8 m/s. In comparison to U = 0.5 m/s, the cantilever plate deflections at U = 0.8 m/s are more pronounced and exhibit growing amplitude over time, indicating flow-induced instability. In order to further quantify the critical velocity for this case with D = 4 mm, Figure 5.5(c) plots the tip oscillation at inlet velocities U = 0.6 m/s and 0.7 m/s. It can be seen that the plate motion grows at inlet velocity U = 0.7 m/s, implying plate instability, while at inlet velocity U = 0.6 m/s, its amplitude decays over time suggesting more stable condition.

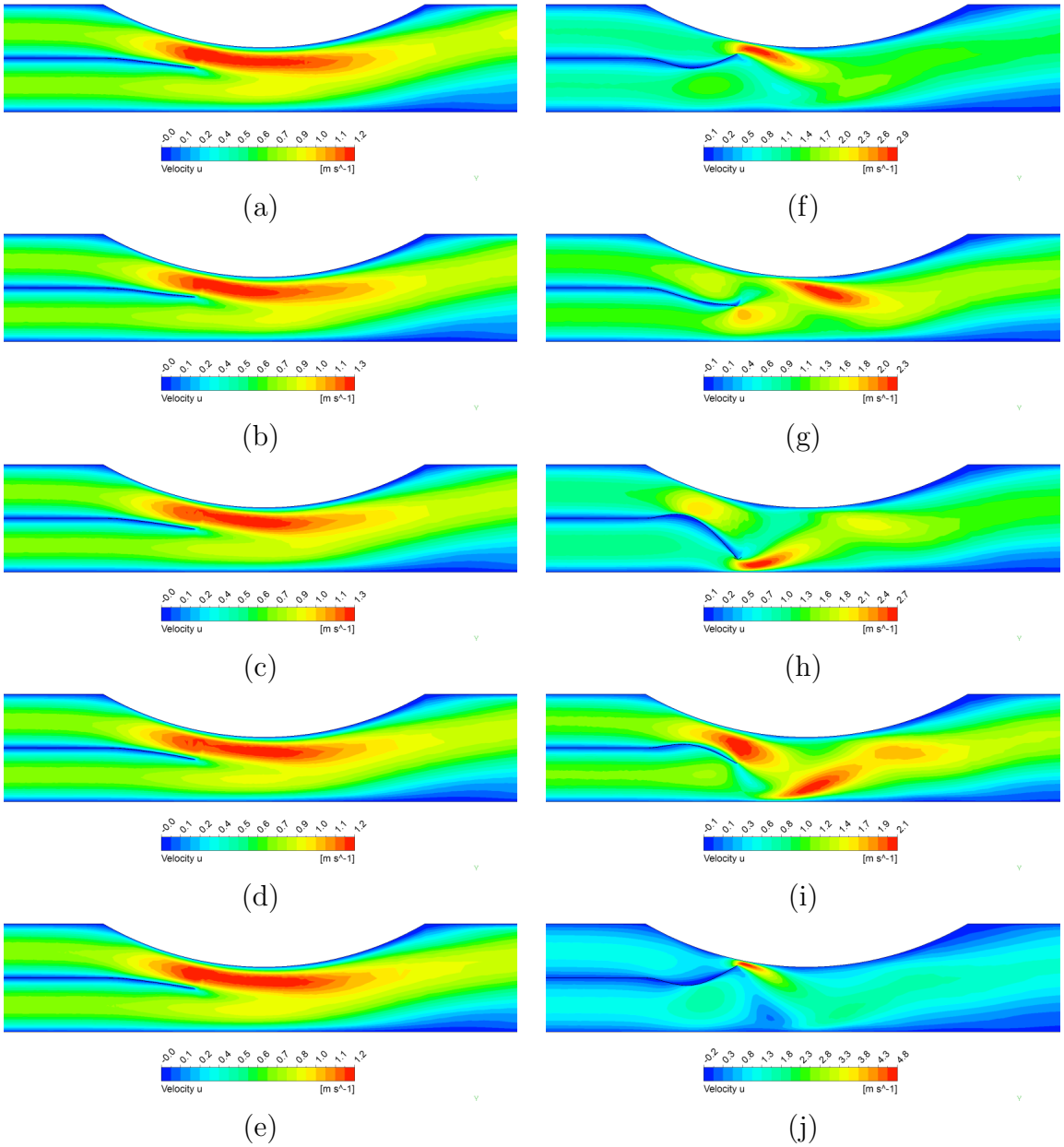

Figure 5.4: Comparison of instantaneous velocity contour and cantilever plate motion at similar instants, for channel with obstruction depth D = 4 mm: (a)-(e) inlet velocity U = 0.5 m/s, and (f)-(j) inlet velocity U = 0.8 m/s

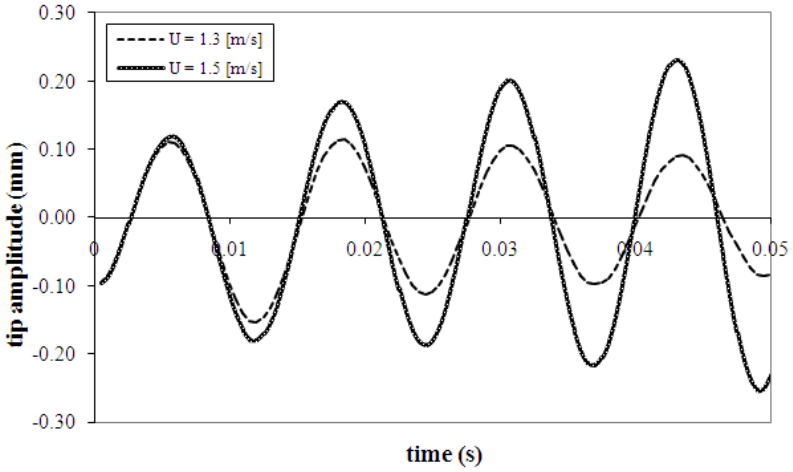

(a)

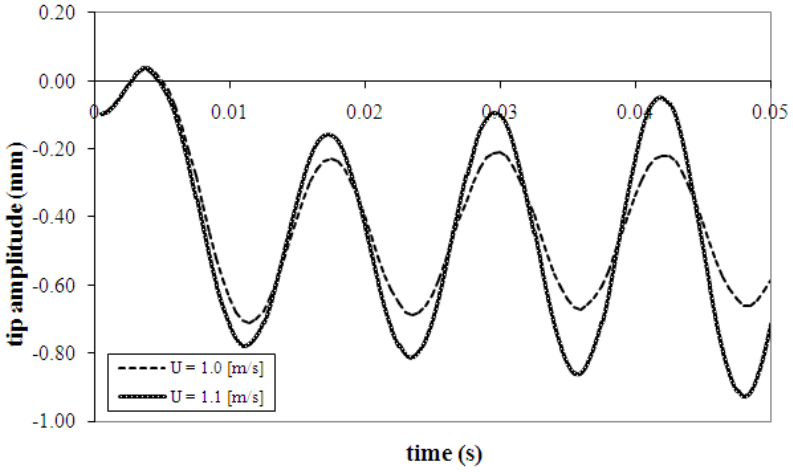

(b)

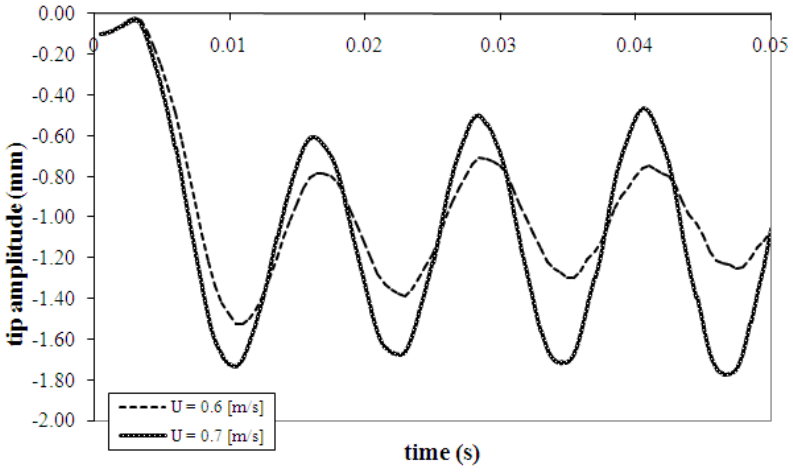

(c)

Figure 5.5: Plate oscillation at various inlet velocities for cases with obstruction depth: (a) D = 0 mm, (b) 2 mm, and (c) 4 mm

Figure 5.5 also shows tip oscillation history for a channel without obstruction (Figure 5.5(a)) and a channel with 2 mm obstruction (Figure 5.5(b)). It could be observed that for a channel without obstruction (D = 0), the tip oscillation decays over time for inlet velocity U = 1.3 m/s, but its amplitude increases with time at higher inlet velocity of U = 1.5 m/s. Similarly, for a channel with 2 mm obstruction (D = 2), the tip oscillation decays with time at inlet velocity U = 1.0 m/s, but it increases with time at a higher inlet velocity of U = 1.1 m/s. Table 5.1 presents a summary of the simulations performed for each of the obstruction depth examined. Results indicate that for channel with obstruction depth D = 4 mm, critical velocity for onset of plate instability lies between 0.6 m/s and 0.7 m/s i.e. U_{crit} = 0.65 m/s to within error of ± 0.05 m/s. Similarly, for D = 0 mm and D = 2 mm, instability of the cantilever plate is initiated at channel inlet velocities of approximately U_{crit} = 1.4 ± 0.1 m/s and 1.05 ± 0.05 m/s, respectively. Summarising these critical velocities against obstruction depths, Figure 5.6 shows that the critical velocity is lowered, almost linearly, with increasing obstruction depth or conversely, critical velocity is increased with reduction in obstruction.

Inlet velocity [m/s]	Obstruction Depth [mm]		
	D = 4	D = 2	D = 0
0.5	stable	×	stable
0.6	stable	×	×
0.7	unstable	×	×
0.8	unstable	×	×
1.0	×	stable	×
1.1	×	unstable	×
1.3	×	×	stable
1.5	×	×	unstable

Table 5.1: Summary of numerical simulations highlighting stability condition at various channel inlet velocities for obstruction depths D = 0, 2 and 4 mm. × indicates not run

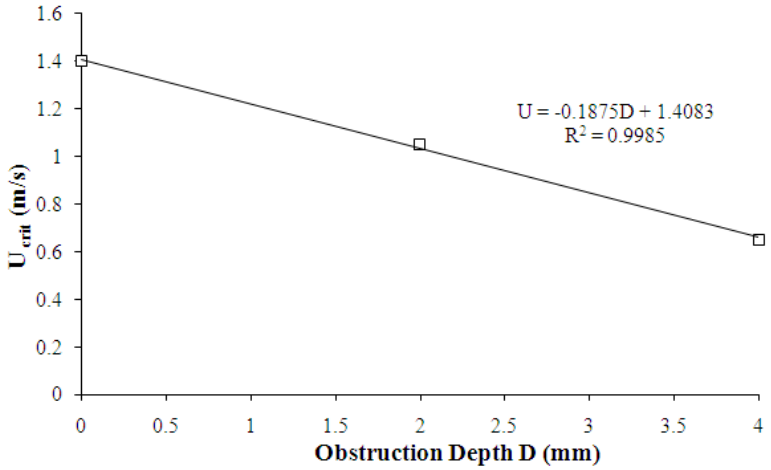

Figure 5.6: Variation of critical velocity with obstruction depth

Instability Mechanism

The plate displacements in figure 5.5 for cases with obstructions, shows a tendency for the plate to deform away from the obstruction i.e. towards the bottom wall, and oscillate about that position. This could perhaps be explained by the initially higher flow resistance on the upper channel - implying higher pressure gradient on the top channel compared to the bottom channel.

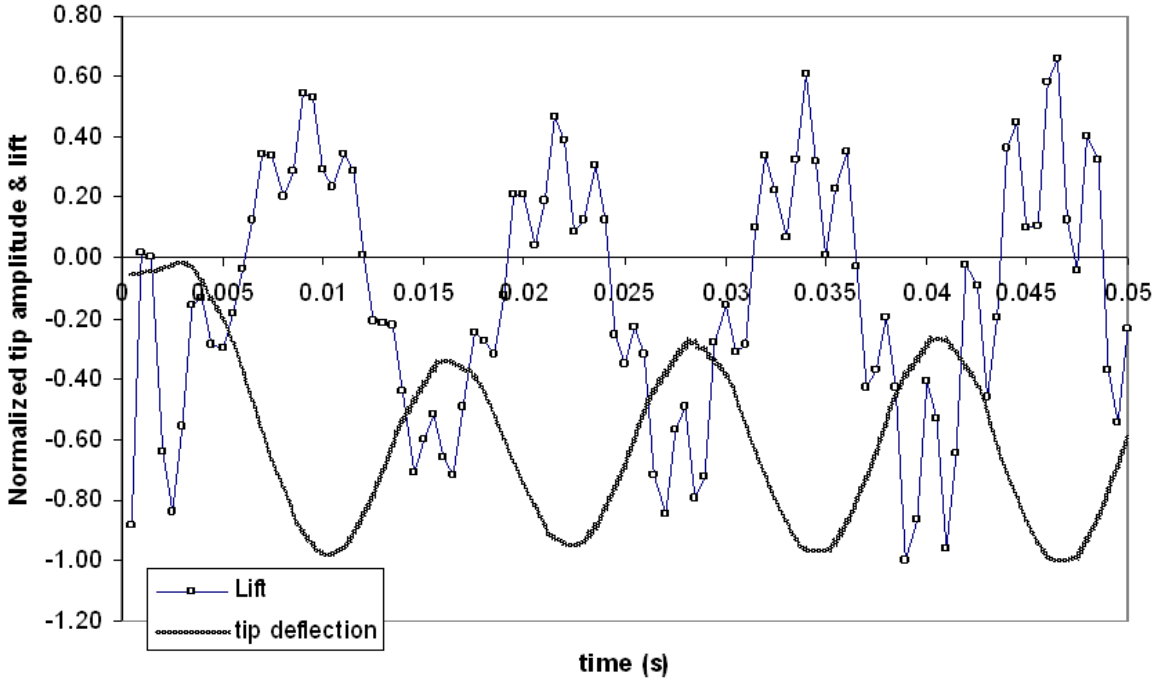

Figure 5.7: Normalised lift and tip displacement variation over time

The difference in this vertical lift force between the top and bottom surface of the plate is plotted in figure 5.7 over time. Initially, a downward (negative) lift acts on the cantilever plate before this aerodynamic force vary with the plate motion. This oscillation in lift and plate motion is also accompanied by vortices shed at the trailing edge of the cantilever plate, as illustrated in figure 5.8. These vortices shed alternately from the top and bottom surface, rolling-up downstream and dissipating towards the outlet.

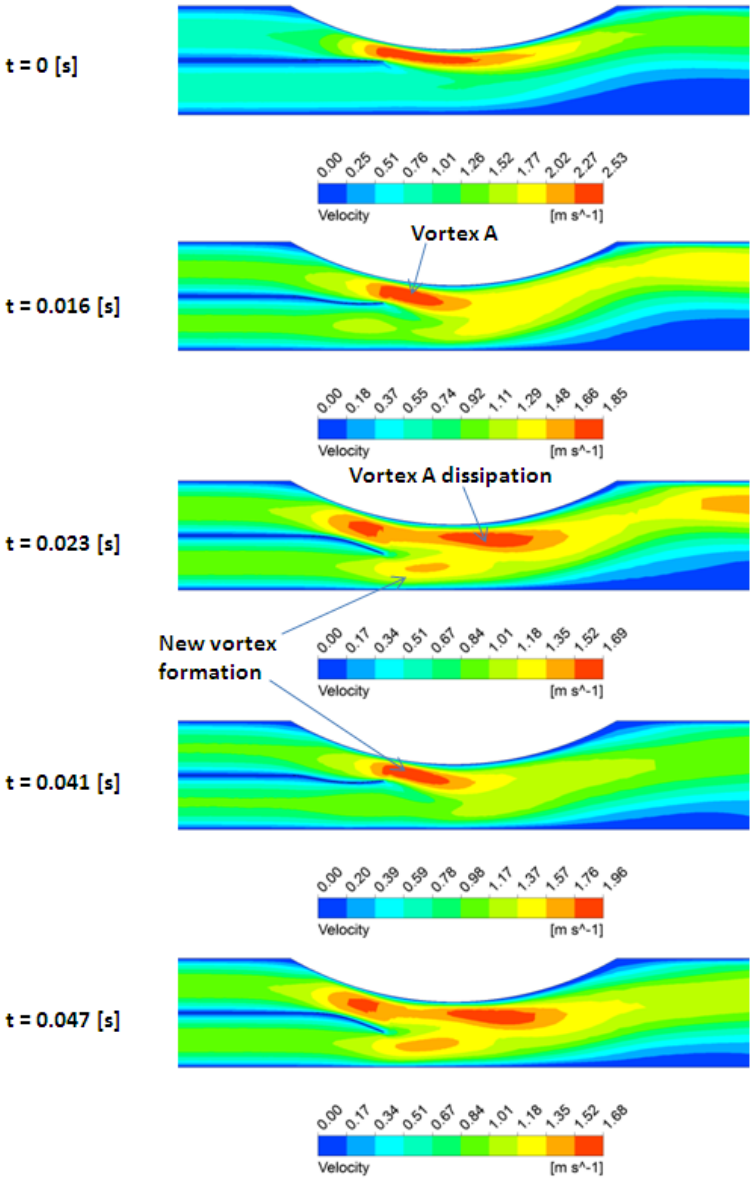

Figure 5.8: Velocity contour showing vortices shed from trailing edge of plate with time (from top to bottom) with corresponding plate oscillation

The apparent phase difference in oscillations between the lift force against the plate motion shown in figure 5.7, seems to be consistent with characteristics of a flutter-type instability. The maximum positive lift coinciding with the minimum deflection of the plate oscillation and vice-versa, feeds irreversible energy transfer, at the right instant, between the flow and structural motion. Unlike quasi-static divergence-type instability, which is driven by fluid traction exceeding the resisting internal traction of the plate, positive work rate on the RHS of (5.2) could also occur despite relatively lower magnitudes of fluid traction, if the fluid tractions (σ^f) is out-of-phase with the oscillating motion of the plate ($\dot{\mathbf{d}}$).

Application

A typical inhalation and expiration cycle data is depicted in Figure 5.9 (Fenn & Rahn, 1964). The respiratory volume flow rate against time closely resembles a sinusoidal wave. Since flow rate is directly proportional to velocity, a similar variation in the inhalation and expiration velocity over time is expected.

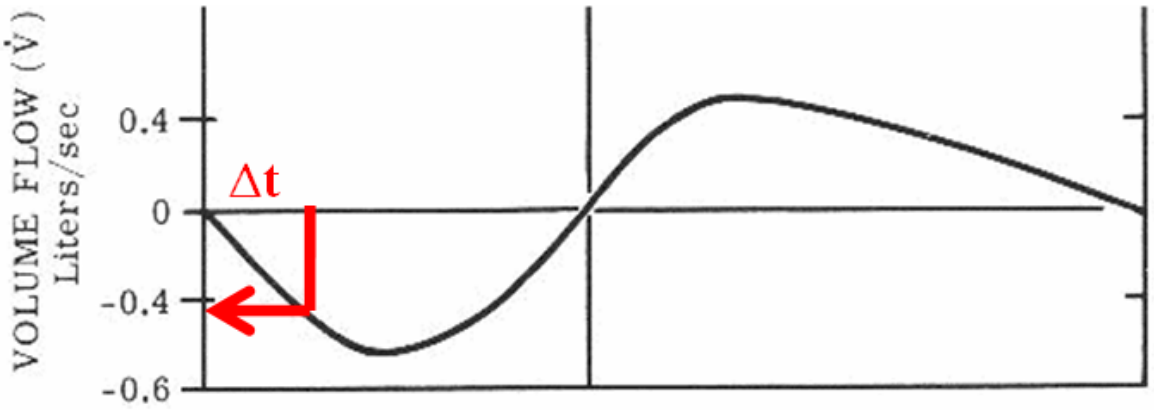

Figure 5.9: Typical inspiration and expiration data, showing flow rate variation with time (courtesy of (Fenn & Rahn, 1964))

Palatal snoring is characterised by the instability of the soft palate oscillation, growing in amplitude over time. This onset of palatal instability or snoring is a function of the inhalation inlet velocity. As discussed above, the presence of an obstruction in the vicinity of the soft palate reduces the critical velocity that initiates palatal instability and therefore snoring. Considering that inlet velocity gradually increases

over time during inhalation, earlier onset of snoring is anticipated for persons with palatal obstruction. Correlating inlet velocity with time from a breathing flow curve, the time difference from the start of inhalation to snoring, Δt, as denoted in Figure 5.9, may perhaps represent a key measurement for estimating the degree of obstruction in the vicinity of the soft palate.

Alternatively, snoring could occur between subsequent cycles of inhalation, and time lapse between snoring episodes, Δt_S, may represent another key measurement for estimating the degree of palatal obstruction. Assuming the inlet velocity during inhalation/expiration cycle is represented by a sinusoidal wave, as shown in Figure 5.10, if obstruction in the vicinity of soft palate intensifies (i.e. perhaps, tongue is collapsing further back) between breathing cycles, the onset of snoring from start of subsequent inhalation is expected to be earlier. As a result, a reduction in Δt_S is anticipated in this case and conversely, increase in Δt_S is expected if localised obstruction is alleviated.

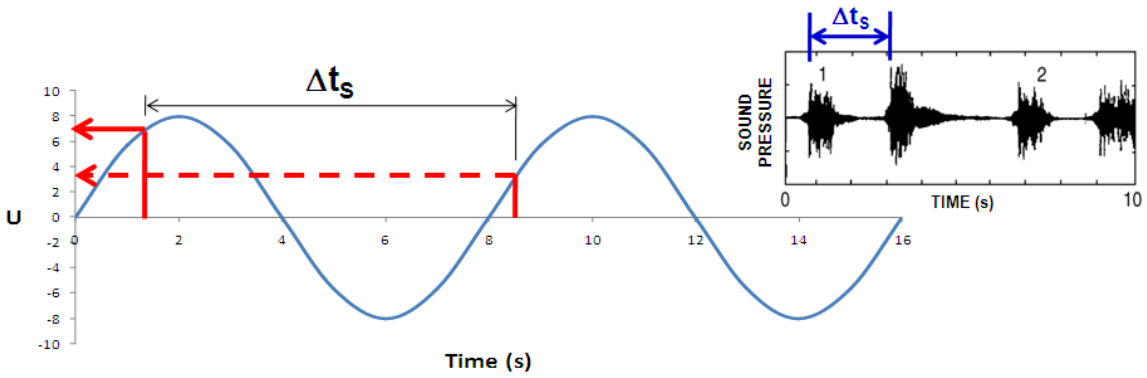

Figure 5.10: Schematic of inhalation/expiration velocity cycle with time, showing time lapse between onset of palatal snoring and subsequent inhalation cycle. Inset shows a typical snoring sound recording (courtesy of (Dalmasso & Prota, 1996)). Δt_S represents time lapse between snoring episodes

The availability of detecting snoring and breathing, for example through acoustic means, also suggests some potential to develop non-invasive techniques to detect and estimate degrees of palatal obstruction.

5.2.3 Pressure Inlet Model

The current 2-D channel model, based on prescribed velocity inlets and a zero pressure outlet, has been employed to investigate palatal instability with localised obstruction. However, question may arise on the actual boundary condition of both inlets, which in reality are at zero (atmospheric) pressure. This may influence the predicted fluid work transferred to the cantilever plate, as demonstrated in a recent work by Tetlow & Lucey (2009). For completeness, it is perhaps necessary to assess a condition where instead zero pressure is prescribed at the inlet. Furthermore, with the presence of a localised obstruction in the current configuration, flow resistance may be more pronounced, which may influence the predicted pressure gradients corresponding to specified inlet velocities.

In order to assess this, a simulation with obstruction depth D = 4 mm is performed, but with both inlets prescribed with zero pressure and the channel outlet applied with a mass flow rate that corresponds to mass flow rates if velocity inlets are prescribed. Two outlet mass flow rates are simulated, corresponding to earlier unstable case (see Figure 5.5(c)) where inlet velocity of 0.7 m/s is applied and another case if instead a velocity inlet of 1.0 m/s is applied.

Figure 5.11 compares tip oscillation for a case with 0.7 m/s velocity prescribed at the inlet and a corresponding case with similar mass flow rate but zero pressure applied at the inlet (in black circles). Clearly, the neutral position about which the tip oscillates is different for both cases, with the velocity inlet model predicting more pronounced deflection of the neutral position, in contrast to the model with zero pressure inlets. This may suggest that the pressure difference between the top and bottom of the cantilever plate may be larger in the velocity inlet model compared to the pressure inlet model. Comparison of the pressure distribution in the velocity inlet model, depicted in Figure 5.12, against pressure distribution in the zero pressure inlet model, depicted in Figure 5.13, shows that the pressure difference across the cantilever plate is indeed larger in the velocity inlet model. In contrast to uniform zero pressure at both top

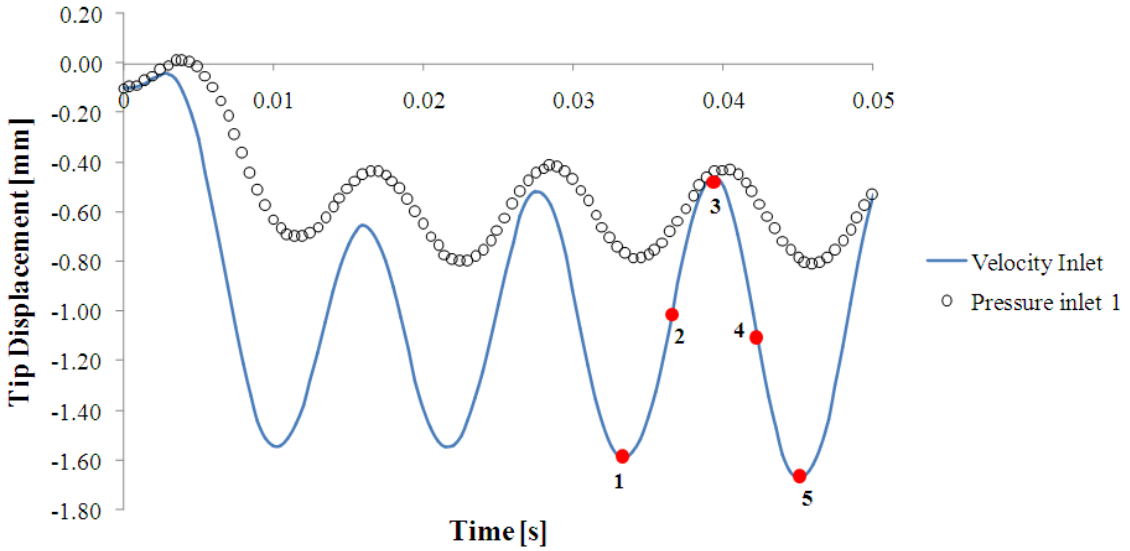

Figure 5.11: Comparison of tip oscillation for a case with prescribed inlet velocity of 0.7 m/s (corresponding to the bottom curve in Figure 5.5(c)) and a corresponding case with zero inlet pressure. Pressure inlet 1 denotes the case with mass flow rate equivalent to a 0.7 m/s inlet velocity. Points 1-5 denote instants reported in text and proceeding figures

and bottom inlets of the pressure inlet model, the pressure at the top inlet is higher than the bottom inlet in the velocity inlet model, owing to perhaps increased pressure necessary to maintain similar flow rates through each channel of significantly different flow resistance. Furthermore, the pressure gradients through each top and bottom channel in the velocity inlet model are higher than those in the pressure inlet model, as evidenced by the difference in maximum and minimum contour bands from both figures. This may suggest that the rate of fluid work on the cantilever plate, predicted in the velocity inlet model, is higher than those predicted in the zero pressure inlet model, which may translate to under-prediction of the critical velocity for onset of palatal flutter in the velocity inlet model compared to the pressure inlet model. This is demonstrated in Figure 5.11, where, although both models undergo similar flow rates, the velocity inlet model shows growing tip oscillation amplitude over time (albeit slowly) corresponding to plate instability, in contrast to the pressure inlet model which does not indicate signs of growth (although it may be close to onset of instability judging from visibly minimal reduction in amplitudes).

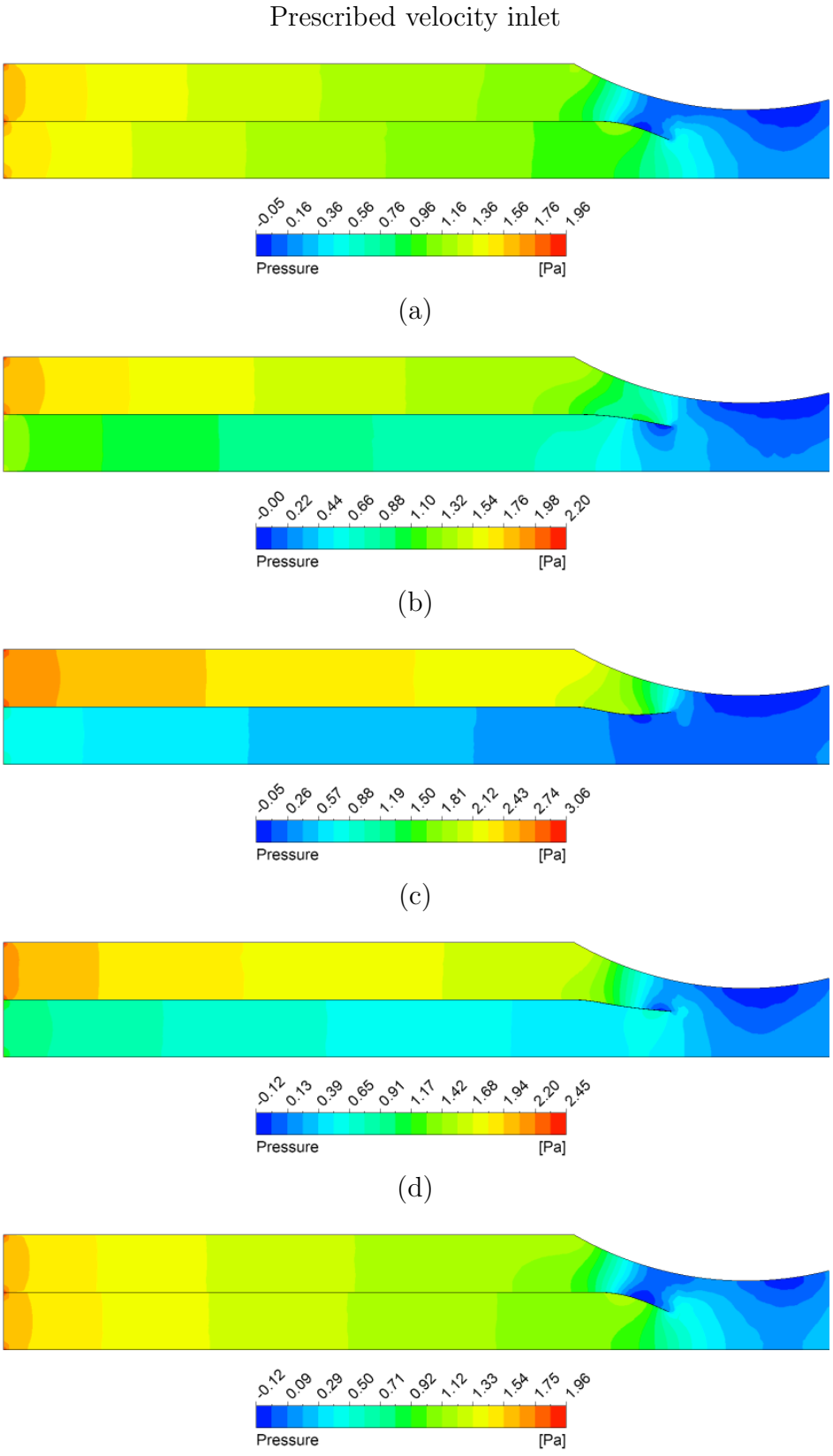

Figure 5.12: Instantaneous pressure contour for case with 0.7 m/s velocity applied at channel inlet corresponding to instants 1-5 labeled in Figure 5.11: (a) Point 1 (b) Point 2 (c) Point 3 (d) Point 4 (e) Point 5

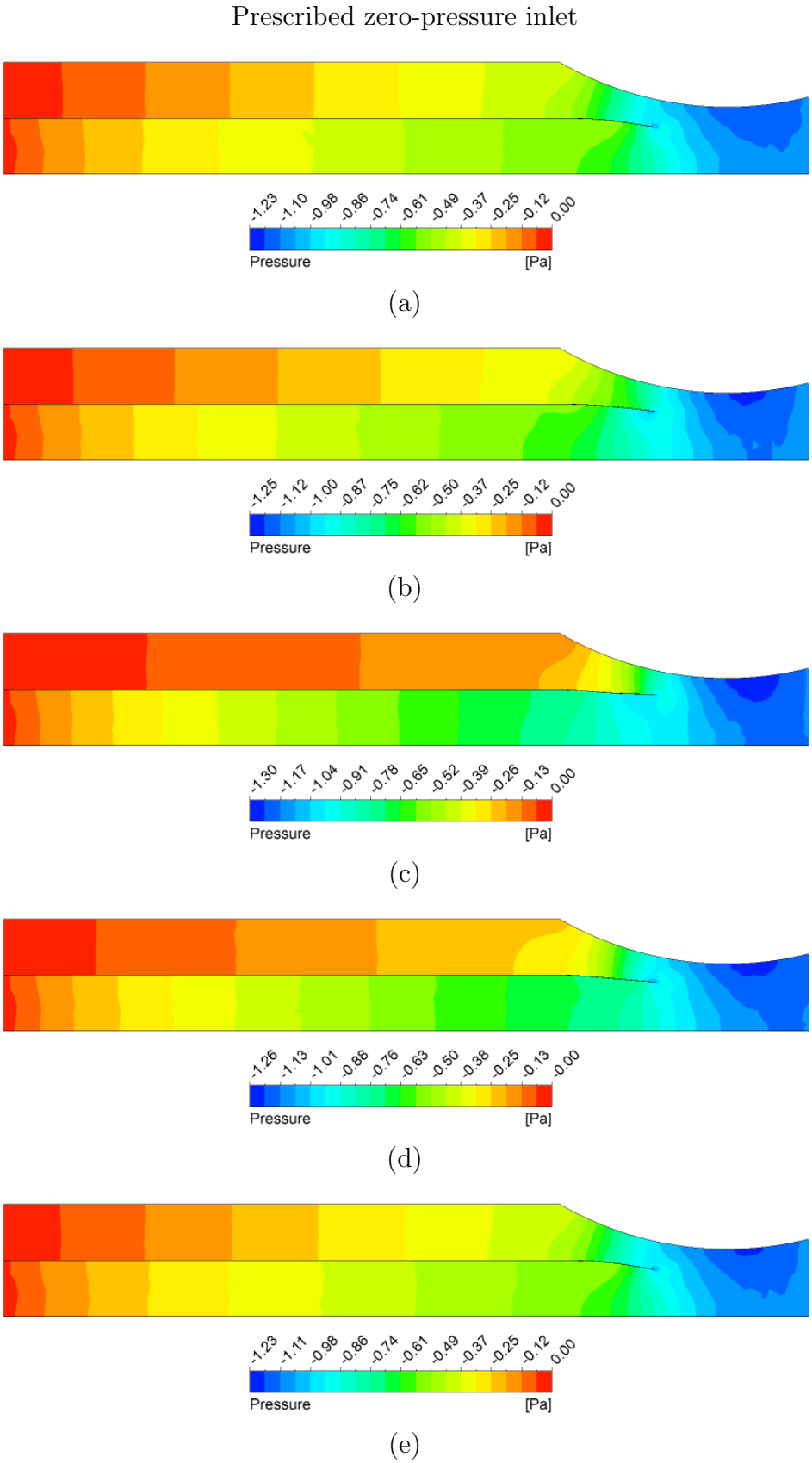

Figure 5.13: Instantaneous pressure contour for case with equivalent mass flow rate to that in Figure 5.12 but with zero pressure prescribed at channel inlet, corresponding to instants 1-5 labeled in Figure 5.11: (a) Point 1 (b) Point 2 (c) Point 3 (d) Point 4 (e) Point 5

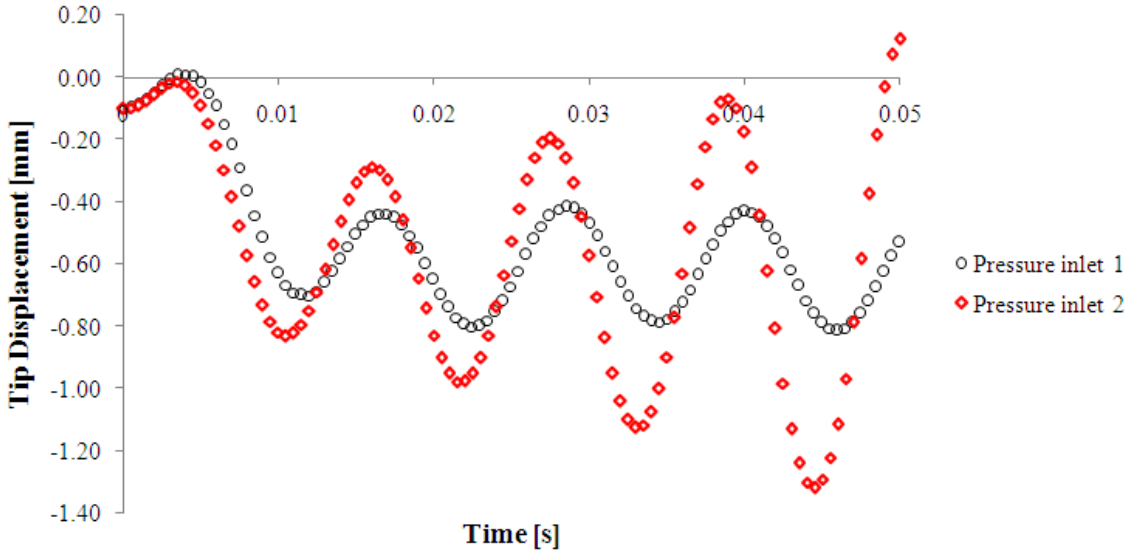

Figure 5.14: Comparison of tip oscillation for two cases with zero inlet pressure. Pressure inlet 1 denotes the case with mass flow rate corresponding to 0.7 m/s inlet velocity, and Pressure inlet 2 denotes the case with mass flow rate corresponding to 1.0 m/s inlet velocity.

An additional simulation with zero pressure inlet but increasing the outlet mass flow rate to a value equivalent to those for a 1.0 m/s inlet velocity case, is performed. The tip oscillation history (shown in red diamond markers) is compared with the earlier zero pressure inlet case in Figure 5.14, showing growth in oscillation amplitude over time corresponding to cantilever plate instability. Judging from the rapid growth in amplitude, the critical velocity for this pressure inlet model is perhaps closer to 0.7 m/s rather than 1.0 m/s. Thus, suggesting that for a zero pressure inlet model, the predicted critical velocity for onset of plate instability may be slightly higher than those predicted in the velocity inlet model. Hence, in agreement with the work by Tetlow & Lucey (2009), although a zero (atmospheric) pressure is applied, similar cantilever plate instability is present as in a velocity inlet model. It also important to remark that, unlike current velocity inlet model, which not surprisingly, shows positive pressure distribution in the channel, a zero pressure inlet model exhibits negative pressure through out the channel. This may be important for future development, when the channel wall collapse is intended to be taken into account for more realistic 2-D models.

5.2.4 Conclusion

Palatal snoring is modeled using a channel flow around a flexible cantilevered plate. The instability of the cantilever plate with a presence of localised obstruction was examined, showing a near-linear reduction in critical inlet velocity to initiate plate instability, with increasing obstruction depth. Conversely, with reduced obstruction depth, the critical inlet velocity is linearly elevated. The instability characteristics suggest a flutter mechanism is involved. Relating the relationship between the critical velocity and obstruction depth to the inhalation cycle, suggests possible measurement variables which could be exploited for non-invasive detection of airway obstruction, either through measurement of elapsed time from onset of inhalation to snoring, or perhaps separation time between snoring episodes.

Indeed, the current work is preliminary, with simplified airway geometry and modelling assumptions used. Numerical investigation needs to be further refined and is yet to be validated by clinical studies. However, recent clinical studies provide some supporting evidence. Mesquita *et al.* (2010) reported in their clinical studies that subjects with high Apnoea-Hypopnoea Index (AHI) tend to have more regular snores of time interval < 1 [s] compared to healthy subjects. This implies a shorter time difference between snoring episodes, suggesting a tendency for earlier onset of snoring corresponding to reduction in critical snoring velocity with localised occlusion.

Furthermore, in another clinical study, Cavusoglu *et al.* (2008) reported that apnoeic patients have larger variance of separation time between snoring episodes compared to benign snorers. Considering increased airway compliance reported in many apnoeic patients, perhaps due to control of pharyngeal muscle tone or build-up of softer fatty tissues (see for example, Brown *et al.* (1985)), greater variation in obstruction depth is postulated with the varying negative and positive pressures generated during breathing cycles. As a result, varying critical velocity for onset of snoring is anticipated in these cases.

Simulations using realistic geometry and verifying the validity of some assumptions,

for example, applying uniform velocity across the oronasal inlets, need to be further investigated, although some progress may perhaps have been presented with the discussion of zero pressure inlet cases. Further simulations for cases of nasal-only or oral-only breathing also need to be examined. Another area which may be explored is the response of the soft palate after impacting the bounding airway (or in this case, channel) walls and how this may influence the palatal snoring signal - this is investigated next.

5.3 Influence of Impact on Palatal Instability

It is anticipated that growing palatal oscillation at critical onset velocities may eventually lead to impact of the soft palate with pharyngeal walls, as evidenced in the idealised experiments by Huang *et al.* (1995). Previous analytical and numerical models have focused on investigating the instability of cantilever plates in channel flows (Auregan & Depollier, 1995; Guo & Paidoussis, 2000; Balint & Lucey, 2005; Tetlow & Lucey, 2009) but thus far, investigation of post-wall impact response of the unstable cantilever plate seems limited. Extending the 2-D channel flow surrounding cantilever plate model to include collision may facilitate understanding of more complex palatal snoring signals. The aim of the current investigation is to present development of an initial model with plate-wall collision, which may be further developed and refined for future work and to qualitatively explore the dynamic response of the cantilever plate.

Employing the previous mesh regularization or smoothing technique in an ALE framework may not be possible, since the fluid grids would collapse as the fluid-plate interface boundary approaches or impacts the bounding channel walls. While, a complete remeshing of the fluid grids at every timestep may be too computationally expensive. Instead, a fixed grid method is perhaps attractive and thus, an immersed boundary method (IBM) is applied.

5.3.1 Method

For the purpose of investigating post-impact response of the cantilever plate, a 2-D channel flow without localised obstruction (i.e. D = 0), corresponding to the original model in Balint & Lucey (2005); Tetlow & Lucey (2009), is used. In an immersed boundary method, the immersed boundary moves according to the local fluid velocities and its presence or influence on the surrounding fluid is represented as body forces. These interactions are numerically implemented using a smoothed Dirac-delta function, instead of a sharp, discontinuous Dirac-delta operator.

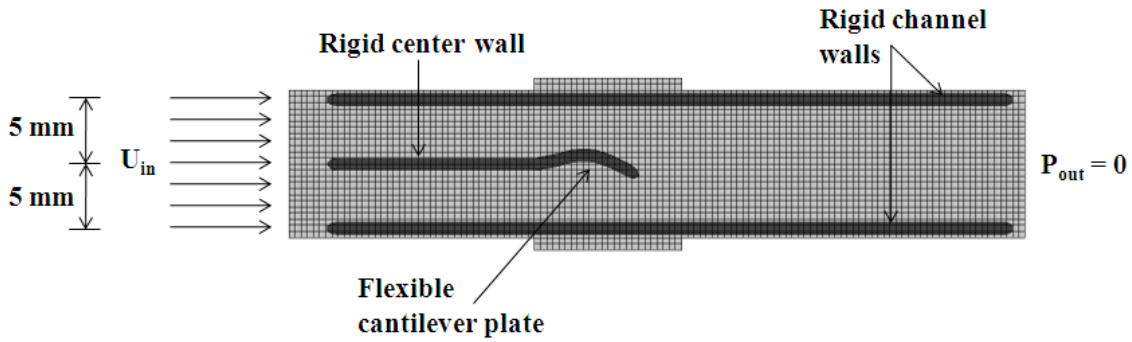

Figure 5.15: Schematic of 2-D channel flow surrounding flexible cantilever plate using immersed boundary method, showing fluid grids and immersed boundaries (in dark) representing top and bottom channel walls, separating rigid middle wall and flexible cantilever plate

Both rigid channel walls, rigid separating plate and flexible cantilever plate are represented as boundaries immersed in the fixed fluid grid, as depicted in Figure 5.15. Square uniform grids are employed for the fluid domain, appropriate for the applied smoothed Dirac function described in equation (3.59) that effectively spans two square mesh widths away from the center of the immersed boundaries, beyond which the smoothed Dirac-delta function diminishes. Similar to the previous configuration, the channel walls are placed 5 mm away from the center rigid and flexible plates. However, due to the approximation of the smoothed Dirac function that spreads the body force estimated from the immersed boundaries to two mesh widths away, the effective channel widths are slightly narrower, which may be improved with finer fluid grid sizes. A uniform velocity is prescribed at the inlet, with zero pressure defined at the outlet of

the fluid domain.

As described earlier in section 3.4, a 2-D Navier-Stokes equation in a fixed Eulerian frame of reference is solved with the appropriate body force densities, representing the immersed boundary resistance to fluid velocities, estimated using linear axial and bending beam equations. Air properties similar to those used in section 5.2 are employed where air density $\rho_o = 1.18$ kg/m^3 and its dynamic viscosity $\mu = 1.982 \times 10^{-5}$ Pa/s. In addition, for the flexible cantilever plate the following isotropic properties are used: Young's modulus $E = 0.1415$ MPa, Poisson ratio $\nu = 0.3333$, plate density $\rho = 125$ kg/m^3 and plate thickness $h = 0.2$ mm, allowing appropriate bending stiffness K_b, axial stiffness K_s and mass per unit length M to be estimated for equations (3.38), (3.39) and (3.46) respectively and more importantly, giving similar second fundamental frequency as in the system used for the partitioned ALE approach in section 5.2.

Unlike partitioned approach where smaller time steps may deteriorate the stability of the fluid-structure coupling (Causin *et al.*, 2005; Degroote *et al.*, 2010), immersed boundary methods require small time steps to ensure stability, especially with higher immersed boundary stiffnesses (Kim, 2003; Peskin, 2011). In the current investigation, a time step size of $1 \times 10^{-6}s$ is used. As demonstrated in Huang *et al.* (2007*b*), IBM have been used to include immersed boundary collision via a repelling force approach, although this approach may not be necessary (Peskin, 2011).

Similar to previous works, the fluid-structure system instability is investigated as an initial value problem, by releasing the cantilever plate from an initial deformation profile resembling its second fundamental mode shape. In order to quickly initiate plate-wall impact or collision, an initial displacement of 1 mm is applied instead of 0.1 mm used in earlier section 5.2, in conjunction with an appropriate critical inlet velocity.

5.3.2 Results and Discussion

In the current investigation, a velocity of 1.27 m/s is applied at the channel inlet, which has been shown to promote cantilever plate instability in unobstructed channel flow, corresponding to previous work in Balint & Lucey (2005). For comparison with current IBM approach, a similar simulation using a partitioned approach under an ALE framework is also performed, although this was not run to finish as the mesh quality deteriorates with growing plate oscillation. Velocity fields at several instances along initial complete cycle of plate oscillation, between both methods, are plotted in Figure 5.16. In addition to alternate formation of trailing edge wakes, the current IBM model also shows similar velocity distribution with the partitioned ALE approach, with peak velocities occurring at narrowed channel sections corresponding to locations where significant deflection of the tip and mid-section of the immersed flexible plate occur. Considering the coarser grids of the IBM model, comparison of the velocity magnitudes also suggest reasonable quantitative agreement between both methods, as evidenced by the contour values. This may suggest that, despite the numerical interpolation and spreading of the smoothed Dirac-delta function 'smearing' the boundary of the immersed flexible plate, reasonable flow resolution is obtained, although this is not as accurate as the partitioned ALE approach.

Extending the IBM simulation until plate-wall impact, Figure 5.17 plots the deflection history of the tip of the immersed flexible plate, showing increasing tip amplitude prior to collision with the channel walls, which is positioned at ± 5 mm. With each marker (solid blue diamonds) representing the tip deflection at every uniform time step, Figure 5.17 suggests that after plate-wall impact, immersed plate velocity is somewhat increased compared to before plate-wall impact. In addition, the period of tip oscillation is also reduced after impact, in comparison to before impact, suggesting a post-impact increase in oscillation frequency. Unlike the 'water hammer' affect where complete closure of collapsible tube leads to rapid reopening of the tube at twice the pre-contact frequency, as demonstrated in Huang *et al.* (1995), current immersed flex-

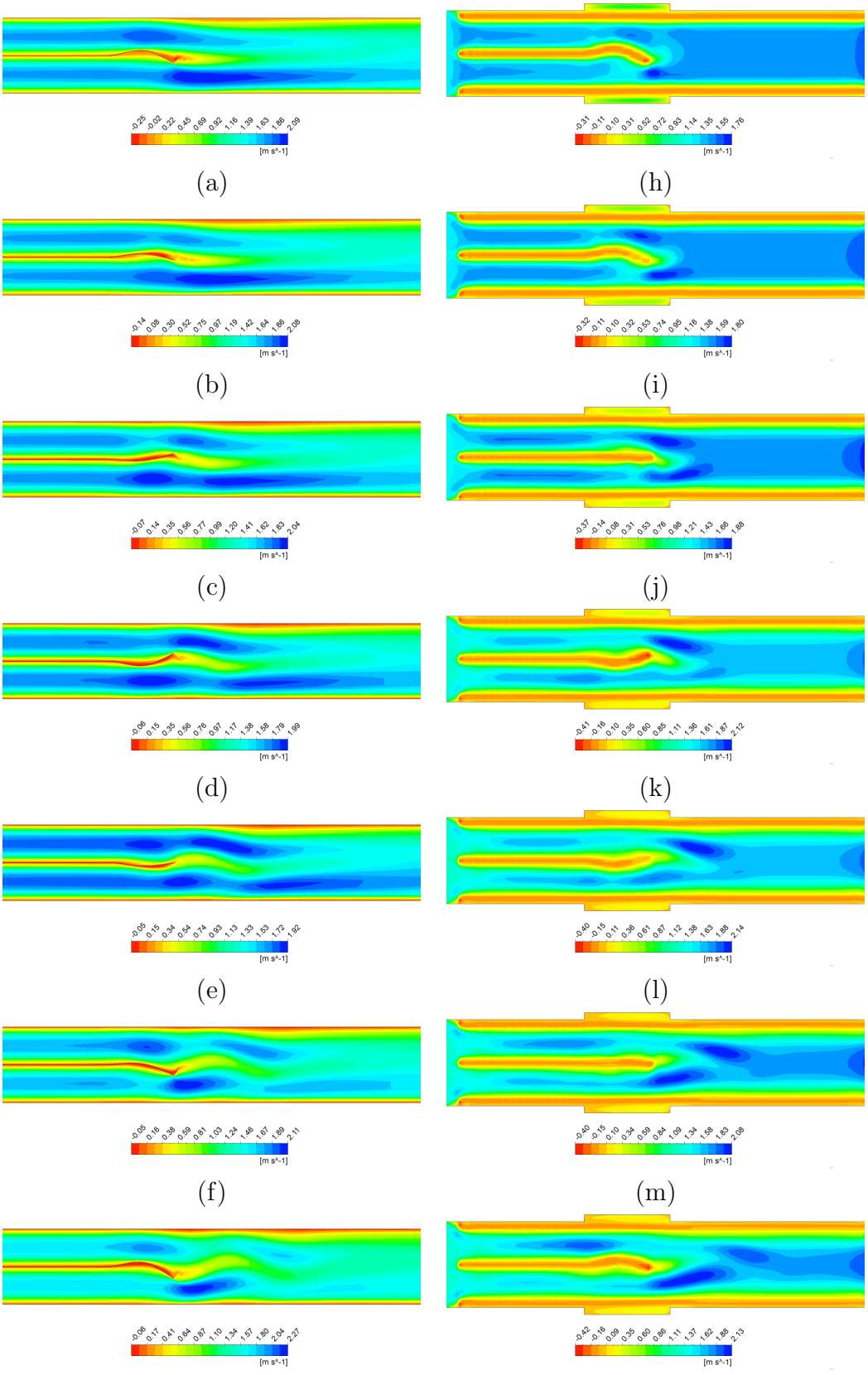

Figure 5.16: Comparison of instantaneous velocity contour at equivalent phase for one complete oscillation cycle of the cantilever plate between: (a)-(g) 2-D channel model using ALE framework; and (h)-(n) 2-D channel model using IBM

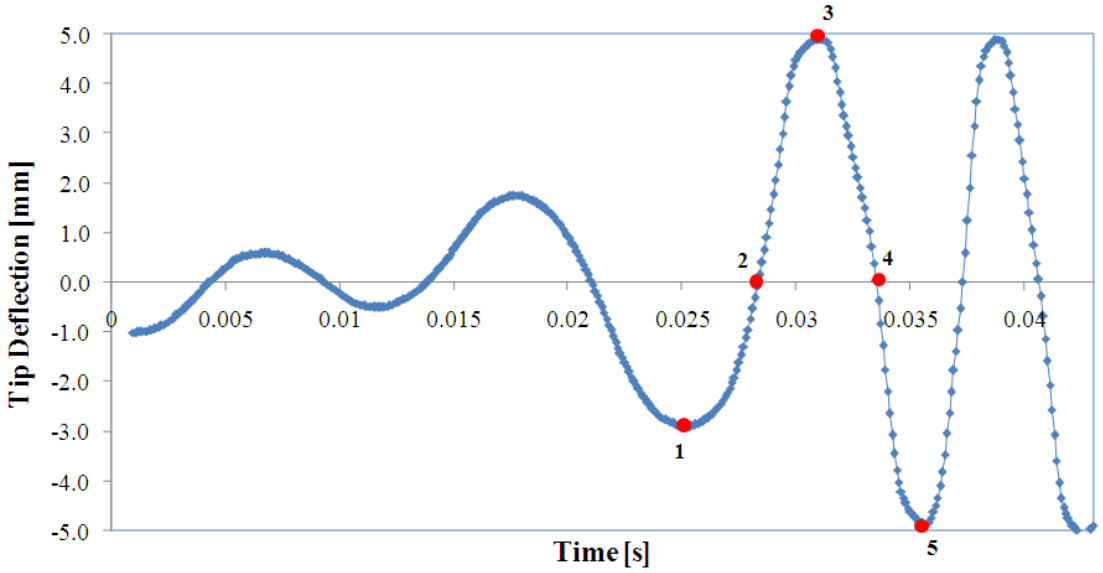

Figure 5.17: Plot showing oscillation history of tip of immersed cantilever plate. Points 1-5 denote instants referred in proceeding text or figures. Note that channel walls are located at ±5 mm

ible plate response after contact is not as rapid, although one of the channels is briefly closed. It is hypothesised that this is perhaps due to the presence of fluid resistance in the opposing channel. Nevertheless, increased frequency of immersed plate oscillation after impact, as opposed to lower pre-impact frequency, is anticipated to introduce additional complexity in the palatal snoring signal, which is perhaps consistent with the experimental findings in Beck *et al.* (1995). Further illustration of the immersed cantilever plate oscillation, corresponding to instants 1-5 labeled in Figure 5.17, is presented in Figure 5.18.

5.3.3 Conclusion

Palatal snoring was further investigated by idealizing collision into a 2-D channel-cantilever plate model. In order to avoid grid collapse and minimise computational resources, an immersed boundary method was employed. The current IBM model shows reasonable agreement in comparison with established partitioned FSI using an ALE framework. Post-impact results indicate increased frequency response of the cantilever plate, which may lead to more complex palatal snoring signals.

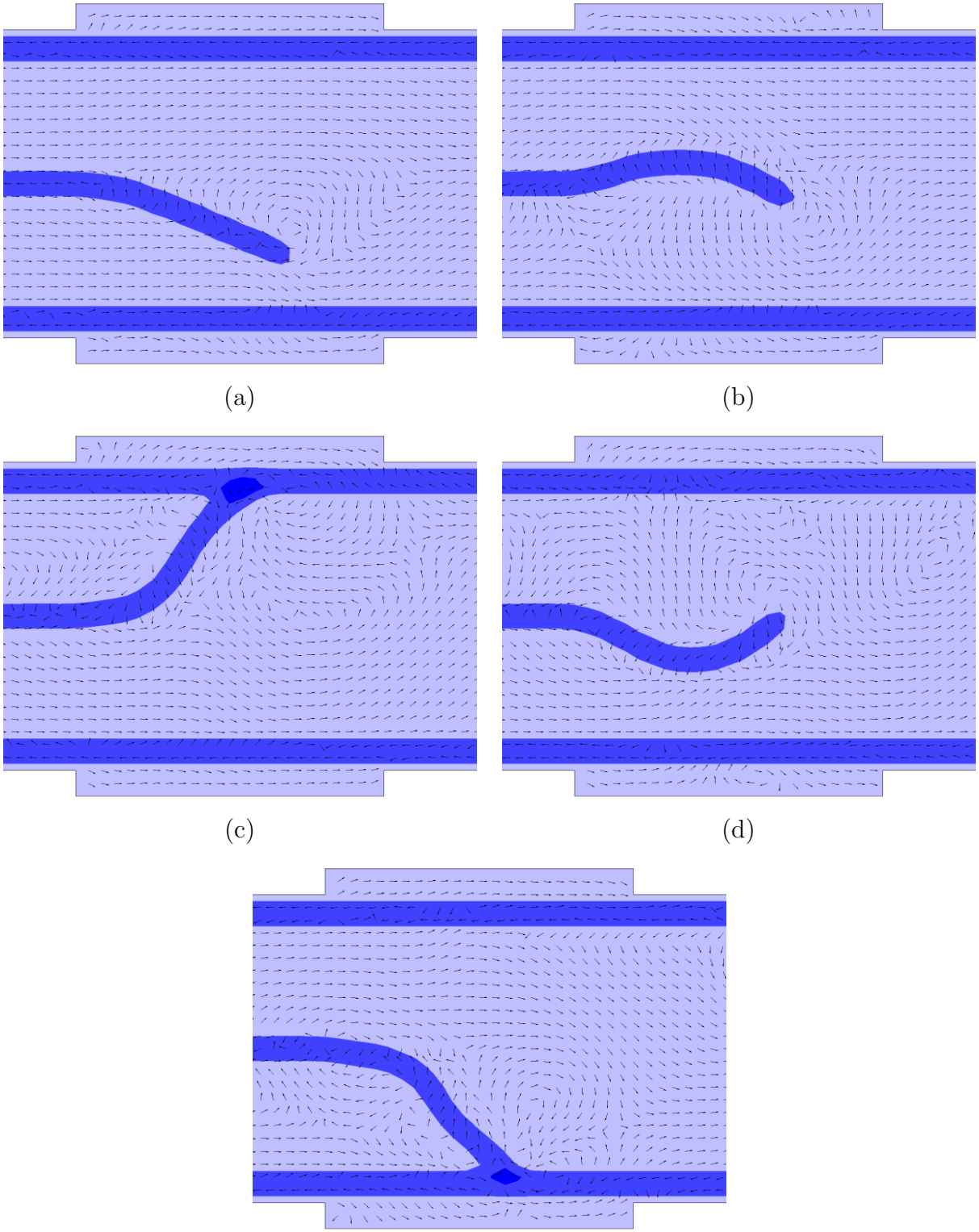

(a) (b) (c) (d) (e)

Figure 5.18: Plot of immersed flexible plate deflection and normalised velocity vectors, corresponding to instants 1-5 labeled in Figure 5.17: (a) Point 1 (b) Point 2 (c) Point 3 (d) Point 4 (e) Point 5

Although limited in duration, the current simulation does not indicate any reduction in oscillation amplitude nor any indication of stability after impact. This may perhaps change if a more realistic high and low inlet velocity cycle is applied instead of the current constant inlet velocity. Another factor which may influence this post-impact response and is recommended for future work, is the effect of channel wall flexibility, which at the moment has been assumed rigid. It may be possible that with more elastic or realistic channel wall properties, the post-impact response of the idealised soft palate may be further dampened.

Further developments and improvements to the current IBM model are clearly possible for improved accuracy and further analysis of palatal snoring signals. Much finer grids and more complex multi-grid algorithms, for instance, may be applied to improve accuracy and efficiency of the model. In addition to perhaps more complex 3-D models, more realistic material properties and non-uniform thickness representing the upper airway tissues also need to be considered.

5.4 Concluding Remarks

Idealisation of palatal snoring via 2-D channel flow surrounding a flexible cantilever plate from previous works has been extended to consider (1) presence of an obstructing with varying depth in the vicinity of the cantilever plate and (2) collision of cantilever plate with bounding channel walls, to investigate post-impact response of soft palate with pharyngeal walls.

A generous blockage is introduced in one of the channels and the influence of this obstruction on the stability of the soft palate is studied. An Arbitrary Eulerian-Lagrangian Navier-Stokes finite volume solver is coupled to the structural equation of motion from a finite element solver to model this fluid-structure system. Numerical results indicate that critical velocity for onset of plate instability is lowered with increasing obstruction depth. Relating this to the inhalation cycle and onset of snoring could help indicate the degree of palatal obstruction and warrants further investigation

for potential non-invasive detection of obstructive airway.

Instead of a partitioned FSI with mesh regularization approach, which limits the extent of cantilever plate deflection, an immersed boundary method is used to model the fluid-structure system and to idealise collision or contact between cantilever plate and channel walls. A body force density term, representing the reaction of a linear beam undergoing bending and elongation, is included into an Eulerian Navier-Stokes finite volume solver to effect the presence of an immersed cantilever plate and channel walls. Simulations suggest that cantilever plate oscillation is quicker after contact with channel walls, which may generate more complex palatal snoring signals. Current IBM model may represent an initial step in modelling more complex unstable palatal responses, which could be further developed in future work.

Indeed, the current idealised 2-D model for palatal snoring would not capture the actual complex flow present in a realistic 3-D upper airway. This issue is further investigated in the following chapter.

Chapter 6

Investigation on Realistic Upper Airway Model

In order to develop real-time computational means of using palatal snoring for diagnostic purposes, stability analysis using a 3-D realistic model for palatal snoring is undertaken and presented in this chapter. Development of the realistic pharyngeal airway model for flow-palatal interaction is first introduced in section 6.1. In section 6.2, numerical experiments for palatal instability are described and results are discussed. Finally, this chapter is concluded in section 6.3, summarising the findings and implications for future investigation.

6.1 Development of Upper Airway Model

Following previous work on 2-D models for investigation of palatal instability and proposed diagnostic purposes, developing a 2-D model is clearly ideal for real-time and efficient clinical diagnosis. However, it is necessary to compare these approximate snoring models to realistic 3-D upper airway models and assess how they deviate from a more realistic scenario. Therefore, this chapter intends to investigate the flow-induced instability of the soft palate under realistic flow conditions.

A detailed schematic of the upper airway and surrounding tissues is illustrated in Figure 6.1, showing the soft palate, uvula and surrounding musculature in the pharynx.

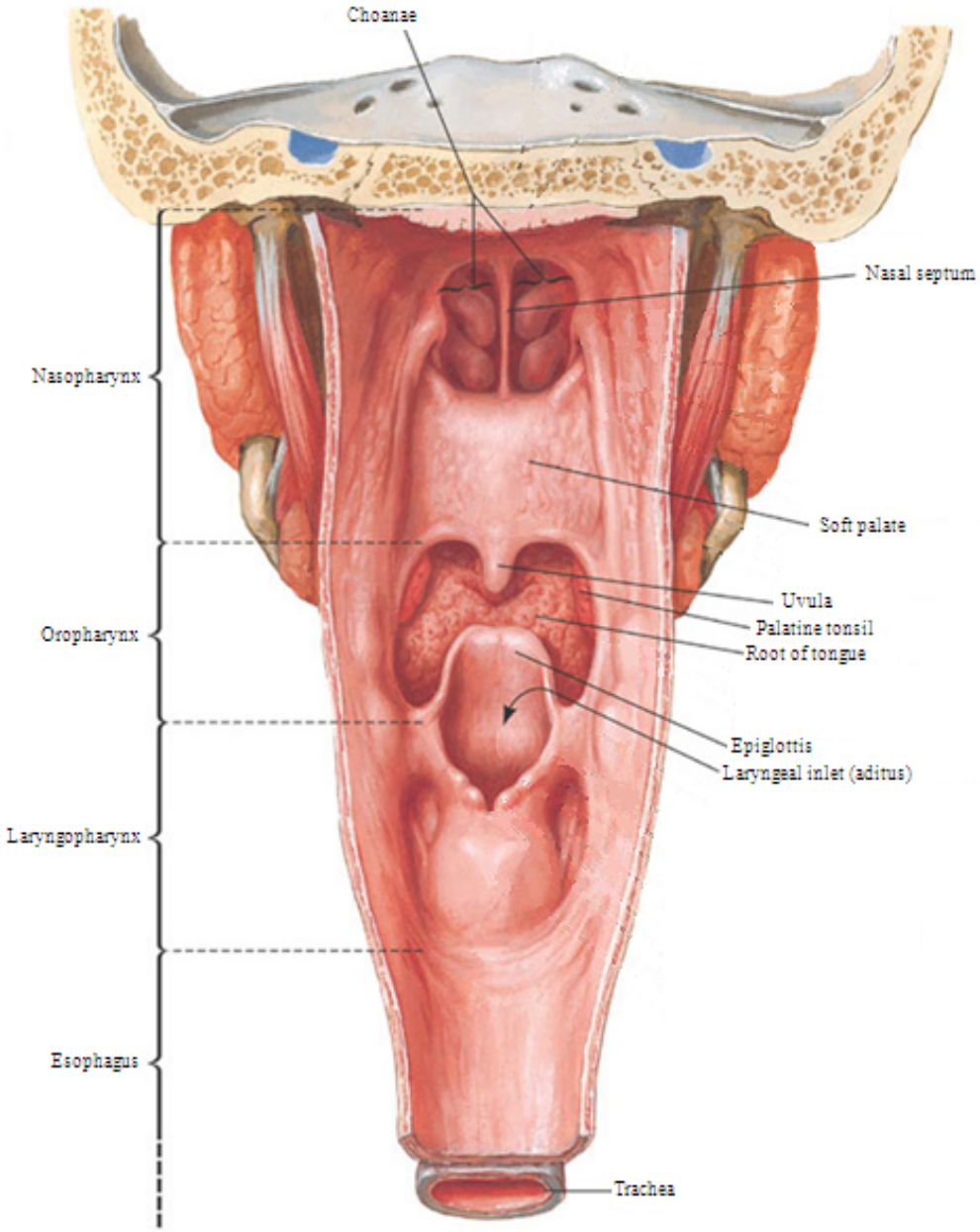

Figure 6.1: Posterior view of upper airway showing anatomy along the pharyngeal airway (courtesy of (Netter, 2011))

6.1.1 Upper Airway Model

A realistic upper airway geometry was constructed from raw computed tomography (CT) scans of an adult Asian male subject. Several coronal sections were captured at 1-5 mm elevation intervals using a CTI whole body scanner. These CT coronal slices along the upper airway were augmented and appropriate curve fitting technique employed to smoothly join subsequent sections, in order to define the complex surface boundary of the upper airway, before the final solid geometry was generated as shown in Figure 6.2. Further details of this 3-D reconstruction of a realistic upper airway geometry may be found in Inthavong *et al.* (2008, 2009).

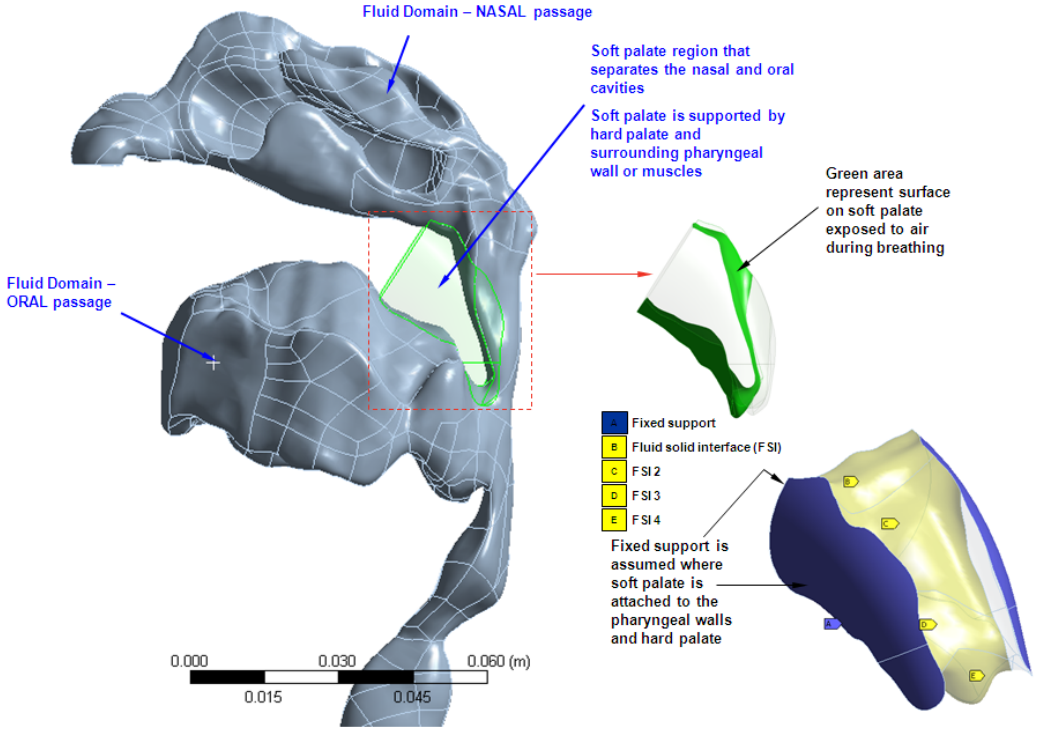

Figure 6.2: Solid geometry of upper airway model with soft palate reconstruction and modelling

The complex geometry through oral, nasal and pharynx passages are thus captured and the influence of flow curvatures could be more appropriately assessed compared to a 2-D model. Both nostrils and oral opening represent the inlet boundaries for the airway during inhalation, while the downstream end of the trachea represents the outlet boundary (which is set to a typical stress-free boundary condition with zero

pressure). The remaining outer surfaces of the upper airway geometry are modelled as rigid no-slip boundaries. Discretization of the upper airway geometry using 4-node tetrahedral elements with acceptable grid skewness resulted in $2,453,369$ elements, as shown in the mesh in Figure 6.3. In all the simulations, a density and dynamic viscosity of respectively, $\rho = 1.185$ kg/m^3 and $\nu = 1.831 \times 10^{-5}$ kg/ms have been used, representing typical air properties.

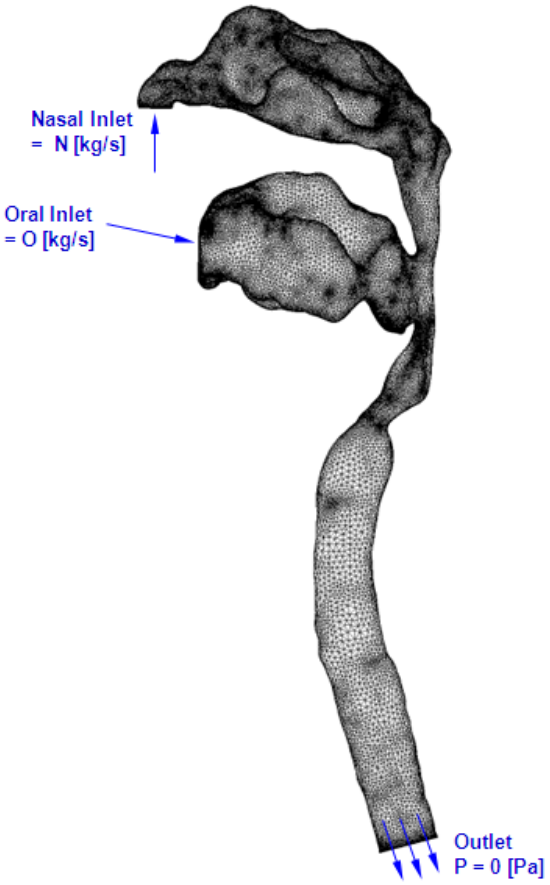

Figure 6.3: Sagittal view of upper airway mesh where variables N and O denote respectively the individual nasal and oral inlet flow rates in [kg/s], used in the numerical case studies. A stress-free boundary condition is defined at the outlet

An unsteady flow simulation representing oronasal inhalation in the upper airway with constant inlet flow rates $N = 0.0003$ kg/s for each nostril and $O = 0.0002$ kg/s at the mouth, was performed to verify and visualise this fluid model. A first-order backward Euler scheme for implicit time integration with time step of 0.001 s was employed, exhibiting sufficient stability and convergence during iterations. Both velocity

and pressure contours are illustrated in Figure 6.4, showing expected flow characteristics around nasal turbinates and narrow regions around the velo- and oro-pharynx.

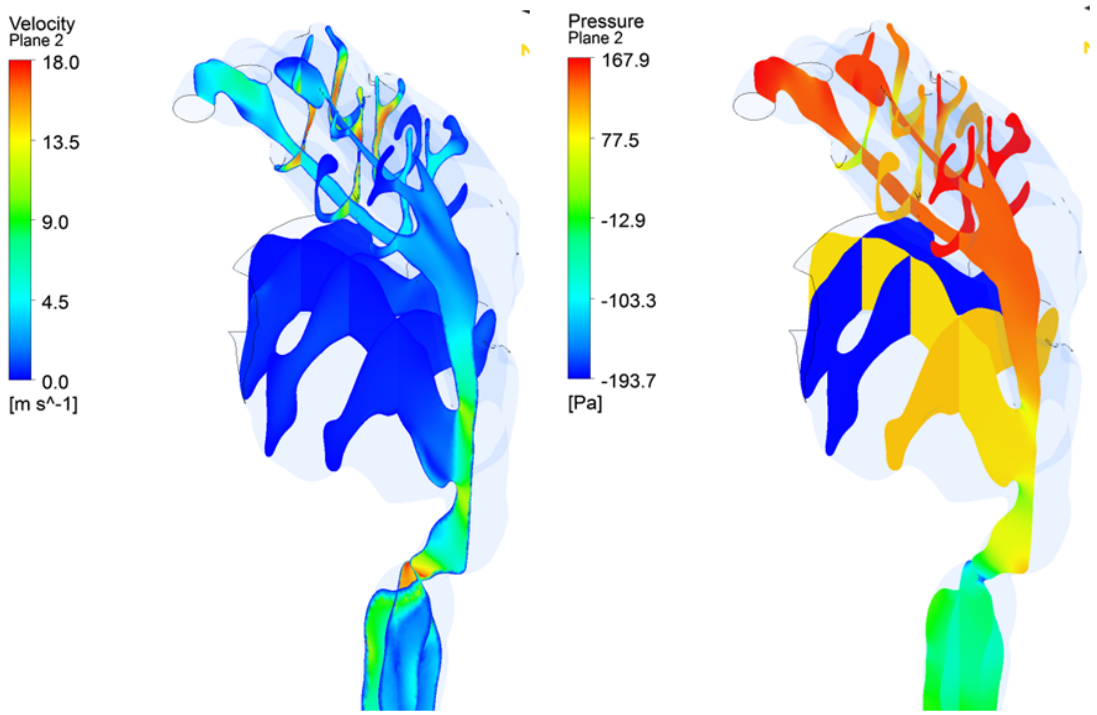

(a) (b)

Figure 6.4: Flow simulation for oronasal inhalation with $N = 0.0003$ kg/s and $O = 0.0002$ kg/s showing (a) Velocity contour and (b) Pressure contour on several frontal and mid-sagittal planes on the upper airway

6.1.2 Soft Palate Model

As shown in Figure 6.1, the oral and nasal passages are fully separated by the soft palate across the naso- and velo-pharynx widths. The soft palate is reconstructed from the cavity between the oral and nasal passage of the upper airway geometry by 'filling-in' material starting from the end of the nasal septum (i.e. where the two posterior nares passages meet) to the downstream tapered cavity representing the uvula. The resulting soft palate geometry is illustrated in Figure 6.2, giving an approximate length of 37 mm, which falls within range of reported soft palate lengths i.e. $28 - 40$ mm depending on age (Johnston & Richardson, 1999) or $29 - 46$ mm depending on snoring or non-snoring subjects (Fajdiga, 2005). It is perhaps worthwhile to note that soft

palate length tends to increase with age (Johnston & Richardson, 1999) and groups with OSAHS or snorers have been reported with characteristically longer soft palates than normal subjects (Fajdiga, 2005; Kurt *et al.*, 2011).

In terms of soft palate stiffness, large variations in soft palate modulus have been reported in the literature depending on the approach adopted (see for example, (Cheng *et al.*, 2011; Huang *et al.*, 2005*b*; Birch & Srodon, 2009)). However, a direct measurement of Young modulus of the soft palate was reported recently by Birch & Srodon (2009). Despite *ex-vivo* measurements of various mechanical properties on soft palates in adults, Birch & Srodon (2009) argued *in-vivo* validity of their measurements and reported a Young's modulus distribution on the soft palate which varies from a mean of 585 Pa at regions near the uvula to 1409 Pa near attachment regions. In order to avoid additional parameters that may complicate the analysis, in this thesis, a uniform and isotropic Young's modulus of 1000 Pa (which falls within the range reported above) is assumed for the soft palate. More realistic Young's modulus distribution over the soft palate is recommended for future work.

In addition, biological soft tissues are considered to be mainly composed of water (see for example, (Cheng *et al.*, 2011; Chouly *et al.*, 2006)). Therefore, a water-like density of $\rho = 1040$ kg/m^3 have been assumed, consistent with previous works on soft tissue modelling (see for example (Duck, 1990; Payan *et al.*, 1998)), which corresponds quite well with *ex-vivo* measurements of soft palate densities in Birch & Srodon (2009). Furthermore, Birch & Srodon (2009) also reported Poisson ratio between 0.30-0.45 for the soft palate, and therefore consistent with this, a uniform Poisson ratio of $\nu = 0.33$ is considered for the soft palate in the present model.

As shown in Figure 6.1, the soft palate is attached to the hard palate and pharyngeal side walls. Considering this, the soft palate model is assumed fixed at its sides and anterior end, as depicted in Figure 6.5. The remaining surfaces represent the surfaces that are exposed to air flow and are free to move. Similarly, 4-nodal tetrahedral elements are used to mesh the soft palate geometry, resulting in 755 elements. In

all the simulations, unlike thin plates undergoing small deflections, a non-linear large deformation strain-displacement relationship which accounts for coupling between in-plane (axial elongation or traction) and bending components, has been considered.

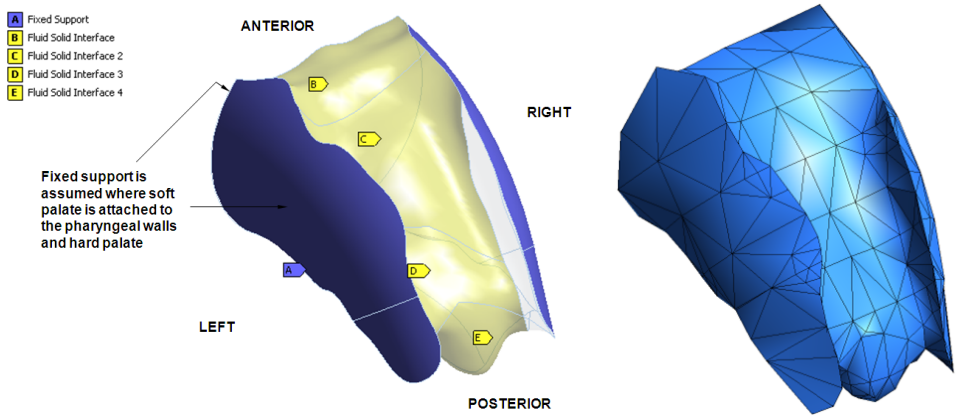

(a) (b)

Figure 6.5: 3-D solid reconstruction of soft palate geometry showing (a) Boundary conditions and (b) Mesh in isometric view

Palatal snoring is characterised by distinctively loud (high peaks) sounds at low frequencies compared to other forms of snoring (Osborne *et al.*, 1999; Brietzke & Mair, 2006; Quinn *et al.*, 1996; Agrawal *et al.*, 2002). In their digital sound trace analysis, Osborne *et al.* (1999) showed loud palatal rattling occurring at frequencies of approximately 20 Hz, while in another clinical study, Brietzke & Mair (2006) measured palatal snoring to fall within a frequency range of 20-320 Hz. Based on the current mechanical properties and soft palate model, an in-vacuo undamped transient dynamic simulation was performed by releasing the soft palate from an initial deformation shape with a maximum amplitude of 1 mm. The resulting tip deflection over time is plotted in Figure 6.6. Analysis of the oscillating period, gives an estimated frequency of close to 20 Hz, corresponding reasonably to clinically measured values.

In addition, although not exactly similar, free vibration of the soft palate released from this initial deformation shape, shows approximate resemblance in comparison to the second fundamental mode shape of the soft palate extracted from a separate modal analysis (Figure 6.7), which perhaps explain the approximate 20 Hz oscillation frequency of the released soft palate.

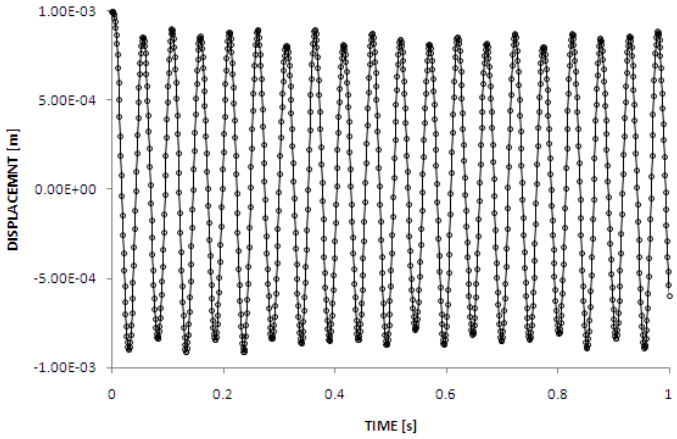

Figure 6.6: Free vibration of soft palate released from an initial deflection with maximum amplitude of 1 mm

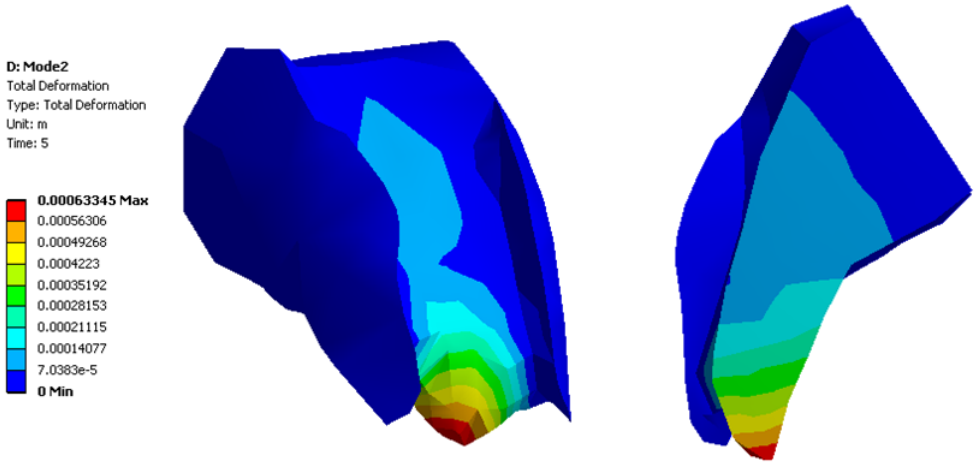

(a)

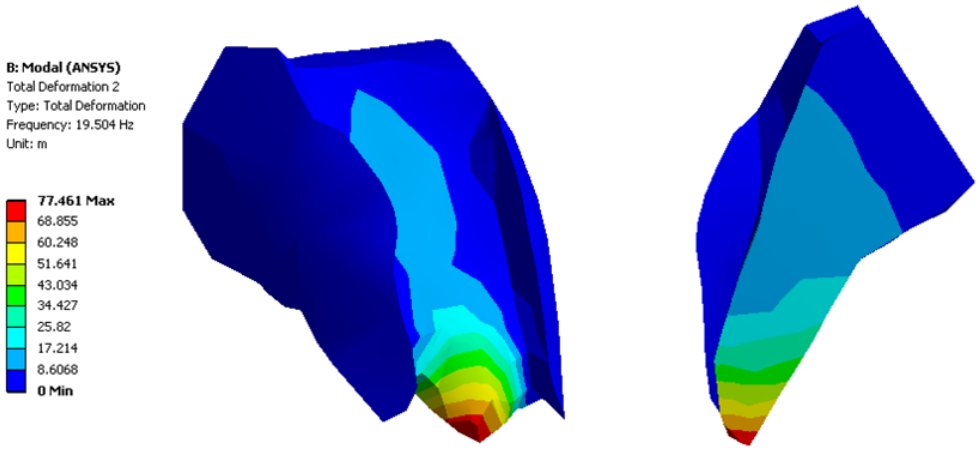

(b)

Figure 6.7: Deflection shape of (a) Free vibration of soft palate released from an initial shape with maximum deflection of 1 mm and (b) Second fundamental mode shape of soft palate corresponding to fundamental frequency of 19.5 Hz. Right column represents sagittal view from a cross-section sliced through the middle of the soft palate

6.1.3 Fluid-Structure Coupling

Both fluid (upper airway) and structural (soft palate) models above are coupled by imposing kinematic and dynamic continuity at the common interface between both domains, as described in section 3.3. This is implemented by successively, imposing fluid pressure and shear from the fluid solver to the interface in the structural domain, followed by matching the interface displacement in the fluid domain with the resulting structural displacement from the structural solver, at every time step. In order to facilitate boundary movement in the fluid domain, an ALE framework is used in the fluid solver and additional mesh motion for the fluid grids are solved using a Laplacian diffusion model as presented in section 3.1.3. This is perhaps clarified in Figure 6.8. For these exchange of variables between solvers, an under-relaxation factor of 0.5 was used to ensure stability in this explicit coupling scheme.

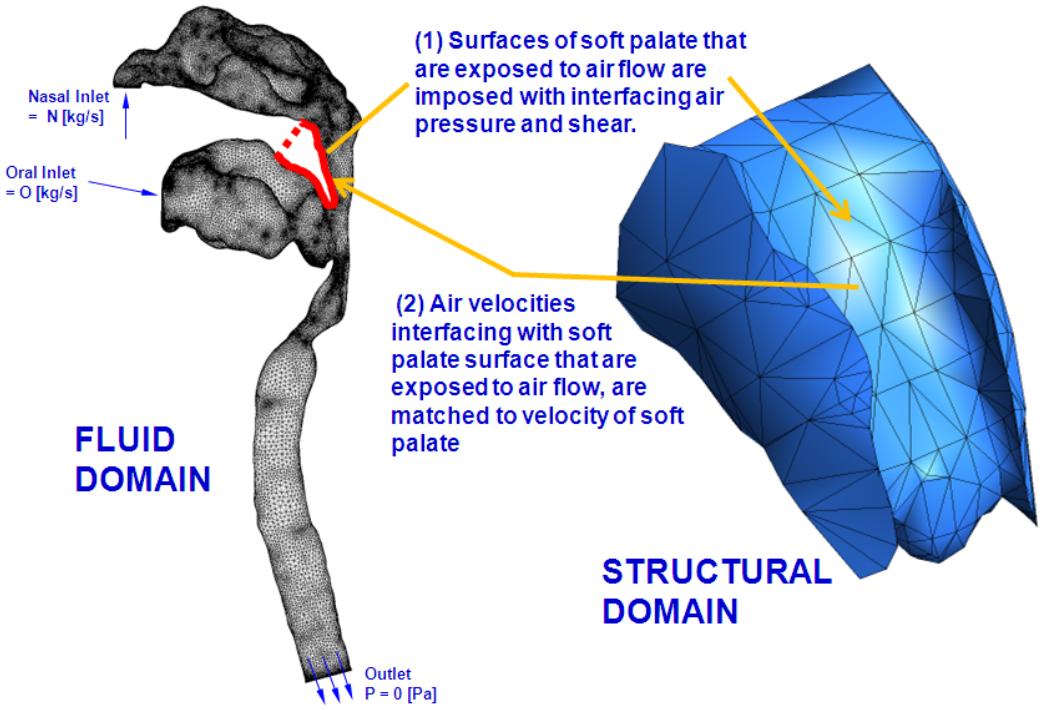

Figure 6.8: Schematic outlining procedure for fluid-structure coupling. Surfaces on fluid and structural domain representing common interfaces where appropriate solver variables interact are shown (highlighted by thick solid line for the fluid domain).

A system perturbation similar to the approach in Balint & Lucey (2005) and Tetlow

& Lucey (2009) is employed. In all the simulations, unsteady fluid-structure interaction is initiated from a configuration where the soft palate is initially deflected to a shape corresponding to that described in 6.1.2 above. In addition, the flow in the upper airway with this initial soft palate deflection is computed by time-marching to a quasi-steady flow condition, which represents the initial flow condition. From these initial conditions, the soft palate is released and the fluid-structural coupling commences. The following presents several cases for this fluid-structural coupling corresponding to palatal responses at different inhalation conditions.

6.2 Numerical Investigations

Inhalation flow rate during breathing has been reported at 0.0004 m^3/s to a maximum of typically 0.0010 m^3/s (Balint & Lucey, 2005), while another investigation reports that apnoeic episodes normally occur at flow rates less than 30 L/min i.e. equivalent to 0.0005 m^3/s (Van Hirtum *et al.*, 2005). Multiplying these values with air density, provides some basis for the constant mass flow rates (kg/s) to be used in the following numerical experiments. Several flow configurations were examined corresponding to oronasal inhalation, oral-only inhalation and nasal-only inhalation, which are identified by the following cases and mass flow rates in Table 6.1.

Inhalation Configuration	Case	Nasal Inlet Left	Nasal Inlet Right	Oral Inlet	Outlet
1. Oronasal	1a	0.00005 [kg/s]	0.00005 [kg/s]	0.00005 [kg/s]	0 [Pa]
	1b	0.0001 [kg/s]	0.0001 [kg/s]	0.0002 [kg/s]	0 [Pa]
	1c	0.0003 [kg/s]	0.0003 [kg/s]	0.0002 [kg/s]	0 [Pa]
2. Oral	2a	0 [kg/s]	0 [kg/s]	0.0006 [kg/s]	0 [Pa]
	2b	0 [kg/s]	0 [kg/s]	0.0010 [kg/s]	0 [Pa]
3. Nasal	3a	0.0001 [kg/s]	0.0001 [kg/s]	0 [kg/s]	0 [Pa]
	3b	0.0003 [kg/s]	0.0003 [kg/s]	0 [kg/s]	0 [Pa]
	3c	0 [kg/s]	0.0006 [kg/s]	0 [kg/s]	0 [Pa]

Table 6.1: Numerical case studies. Case 3c represents a nasal-only inhalation case where one of the nasal inlets is blocked

As discussed earlier in chapter 5, specifying inlet velocities instead of pressure conditions, still enable appropriate instability mechanisms to be captured, while optimizing computational stability and resources. Thus, all the numerical experiments are based on specifying mass flow rates at the inlet, while zero pressure is prescribed at the outlet.

Analogous to the energy system for cantilever plate in 2-D channel flow shown in (5.2), the energy for the soft palate dynamics is fundamentally a balance between the total energy of the plate (kinetic and strain) with the net work generated by the fluid flow, discounting any structural dissipation or damping i.e.

$$\frac{d}{dt}\left(\text{Plate kinetic energy} + \text{Plate strain energy}\right) = \text{Rate of fluid work} - \text{Rate of dissipation} \tag{6.1}$$

A positive value in the RHS of (6.1) signifies increasing plate energy with time, implying growing soft plate motion corresponding to a palatal instability. Positive RHS in (6.1) could occur either by fluid forces exceeding internal strain forces of the plate, which leads to unstable soft palate deformation in a quasi-static manner (divergence-type instability) or through out-of-phase fluid forces with respect to motion of the soft palate, resulting in dynamic instability of soft palate oscillations (flutter-type instability). Therefore, the influence of inhalation flow rates on the stability of the soft palate could be judged by monitoring either the total energy of the plate or ensuing plate oscillation amplitudes. In all the simulations, structural damping have been neglected.

In the following, points 'X2', 'tip' and 'X3' refer to points on the trailing edge of the soft palate shown in Figure 6.9. In addition, the positive x, y and z directions refer to the anterior to posterior direction, inferior to superior direction and lateral right to left direction, respectively.

6.2.1 Oronasal Inhalation

Cases 1a, 1b and 1c were simulated for the condition of inhalation through both oral and nasal openings, which is either habitual or perhaps triggered by increased nasal

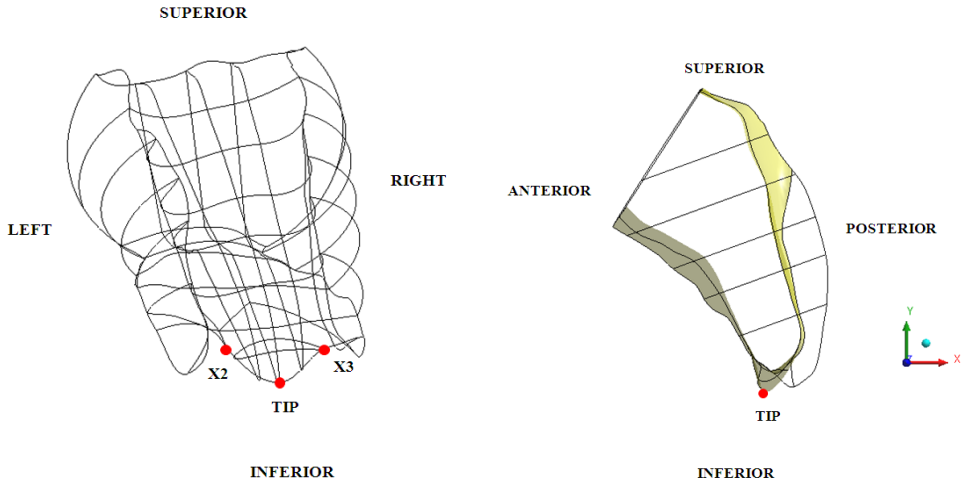

(a) (b)

Figure 6.9: Schematic of the soft palate highlighting (a) points X2, tip and X3, which represent, respectively, the left, center and right points on the trailing edge of the soft palate, referred to in the text, and (b) x, y and z directions referred to in text

resistance. Case 1a represents oronasal inhalation at relatively low flow rates where $N = 0.00005$ kg/s at each nasal inlet and $O = 0.00005$ kg/s at the oral inlet, assuming negligible soft palate damping. The deflection in the x-direction of the tip is plotted in Figure 6.10, showing no growth in tip amplitude oscillation over time. Indeed, the tip oscillation in case 1a is quite similar to oscillation for an in-vacuo case of undamped soft palate release. This would suggest there is no increase in soft palate energy, as it interacts with the low flow rate of inhaled air over time and therefore suggest no palatal instability occurring. In fact, monitoring the soft palate energy in Figure 6.11 shows a steady decrease in its total energy (kinetic and strain) over time, suggesting that (in the absence of damping) no additional work is transferred into the structural system from the oronasal flow. Closer examination of the tip oscillation (in blue) in Figure 6.10 also indicates lower oscillation amplitude at certain times in contrast to the in-vacuo case (shown by the dotted black markers), suggesting small amount of energy loss in the structural system.

The oronasal inhalation flow rates were further increased for case 1b, with $N = 0.0001$ kg/s in each nasal inlet and $O = 0.0002$ kg/s for the oral inlet. Similar to case 1a, the soft palate energy for case 1b also decreases with time, suggesting stable

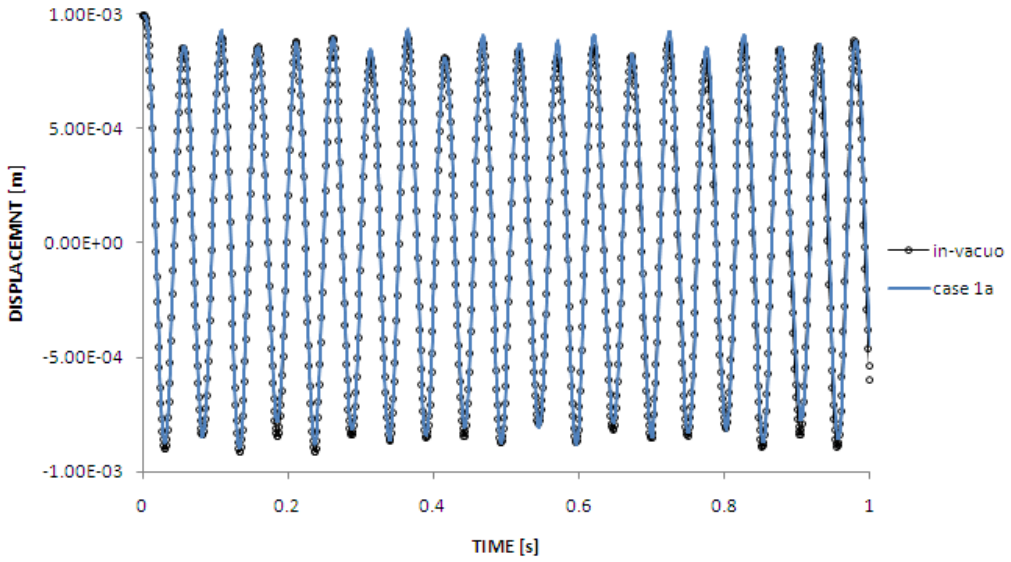

Figure 6.10: Plot of tip oscillation for oronasal flow interaction with soft palate of case 1a with in-vacuo free vibration of soft palate

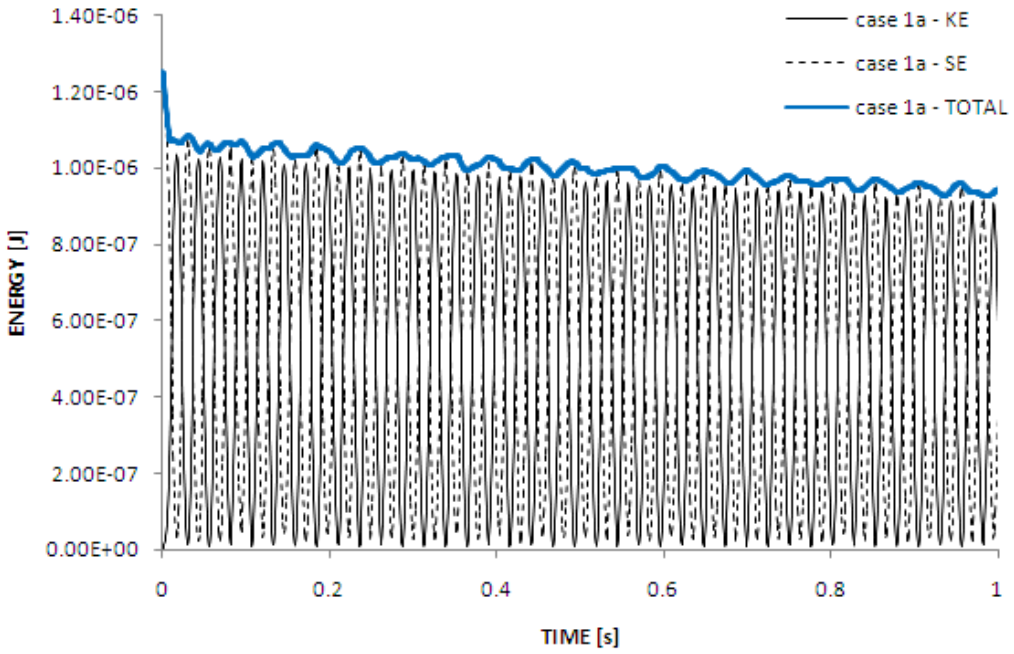

Figure 6.11: Plot of kinetic energy (KE), strain energy (SE) and total energy of the soft palate over time for case 1a

palatal oscillation occurring at these flow rates, although its energy oscillation and magnitude is more pronounced than those in case 1a, as indicated by Figure 6.12. This suggests increased oscillation amplitude at the higher oronasal flow rate of case 1b in comparison to case 1a, which is indeed evident from the comparative plots of tip deflection in Figure 6.13, showing peak oscillation of case 1b (dotted red) exceeding the peaks in case 1a (shown by the solid blue line).

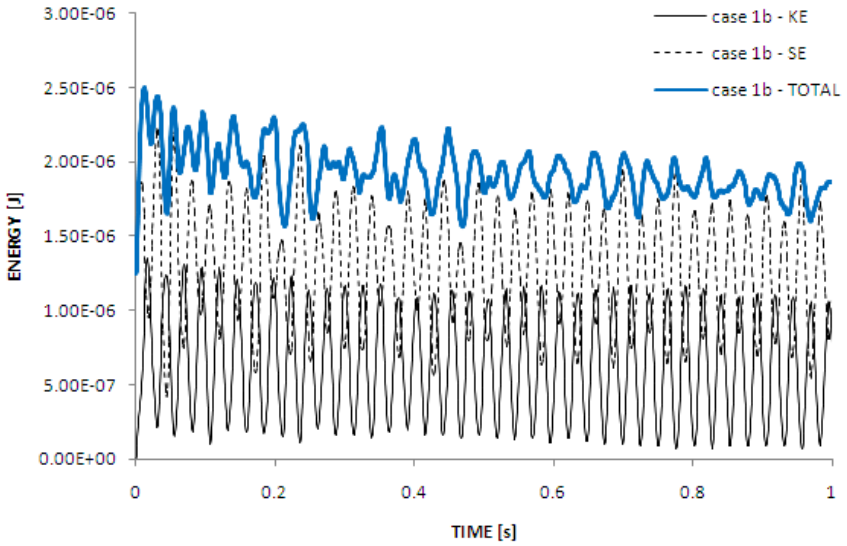

Figure 6.12: Plot of kinetic energy (KE), strain energy (SE) and total energy of the soft palate over time for case 1b

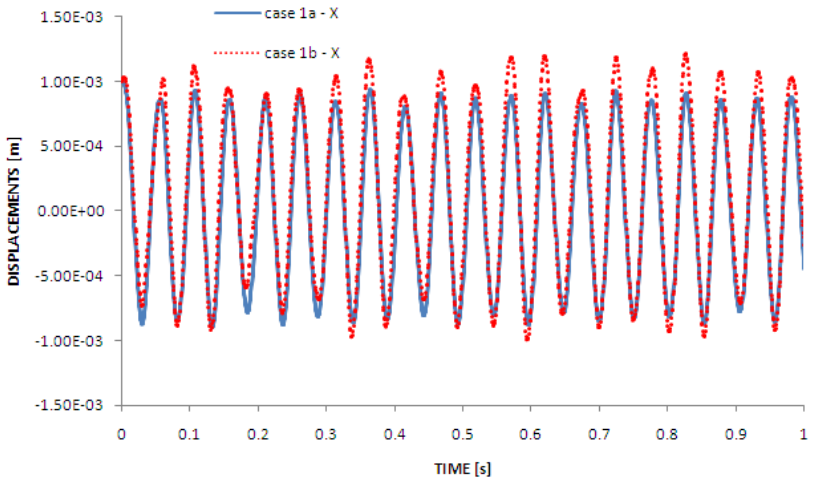

Figure 6.13: Plot of tip oscillation for oronasal flow interaction with soft palate of case 1b in comparison with case 1a

For case 1c, the oronasal inhalation flow rates were increased further to $N = 0.0003$

kg/s at each nasal inlet, corresponding to greater flow through the nose rather than through the mouth. The tip oscillation in x, y and z direction for this case is plotted in Figure 6.14, while the soft palate energy oscillation with time under these higher oronasal flow rates is plotted in Figure 6.15. Although not at steady rate, the tip amplitude in the x-direction clearly increases with time in this case, to magnitudes greater than the initial amplitude of 1 mm, corresponding to increase in total energy (kinetic and strain) of the soft palate. Thus, at these higher oronasal flow rates in case 1c, the interaction of the flow with soft palate leads to growth of the palatal oscillations over time and a palatal instability ensues. As the oral flow rate is kept constant to that of case 1b, this may suggest that a critical nasal inhalation flow rate exists between $N = 0.0003$ kg/s and $N = 0.0001$ kg/s, where onset of palatal instability occurs.

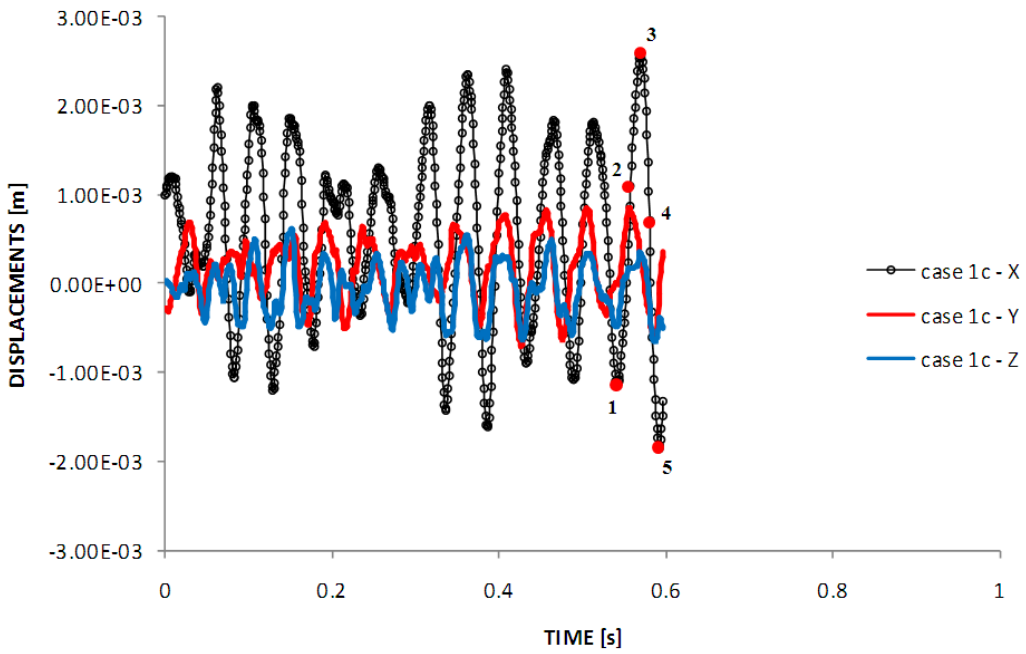

Figure 6.14: Plot of tip oscillation for oronasal flow interaction with soft palate in case 1c. Points 1, 2, 3, 4 and 5 refer to instants in the oscillation history used in text

Although not necessarily in phase, the tip deflections in the y and z directions also show evidence of increasing amplitude over time. The fact that all x, y and z deflections are not necessarily in phase, suggests the complex oscillation of the soft palate that may involve modes corresponding not only to bending, but also to elongation of the

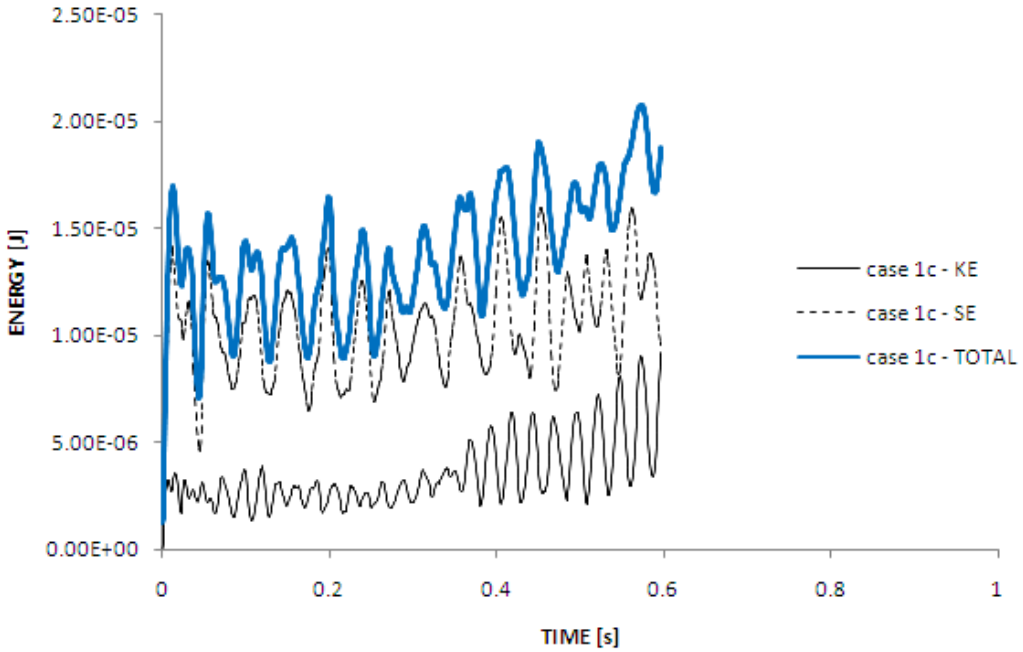

Figure 6.15: Plot of kinetic energy (KE), strain energy (SE) and total energy of the soft palate over time for case 1c

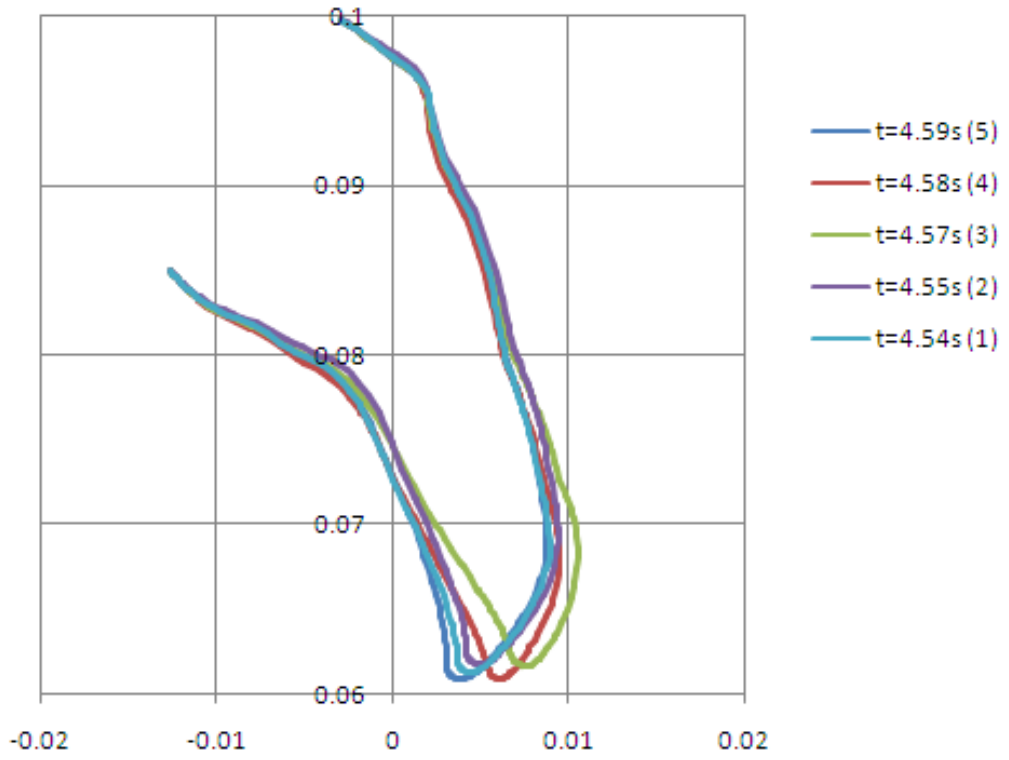

Figure 6.16: Soft palate profile for case 1c corresponding to instants 1-5 (in brackets) labeled in Figure 6.14. Horizontal and vertical axis represent x and y positions (in m)

soft palate. This may also be illustrated from examining the velum positions in the instantaneous plots of Figure 6.16 corresponding to instants 1, 2, 3, 4 and 5 of the tip deflection history indicated in Figure 6.14. This may highlight the limitation involved in using 1-D cantilever beam models, where aerodynamic forces imposed by flow pressures are assumed as acting transversely or normal to top and bottom surfaces which are parallel to each other, while neglecting the trailing surface, leading to pure bending modes. The asymmetry of the soft palate and flow curvatures may also play a role in influencing the direction of pressure forces or to a lesser extent, shear forces applied to the 3-D soft palate, which influence the deflection of the soft palate.

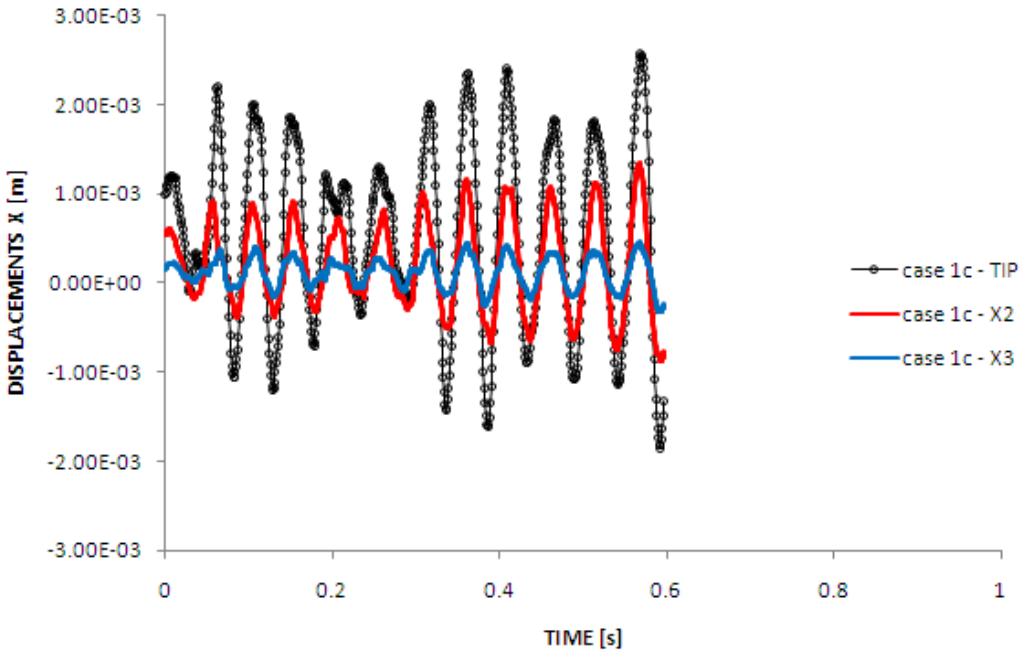

Figure 6.17: Plot of oscillation of points X2, tip and X3 labeled in Figure 6.9 at trailing edge of soft palate under case 1c conditions

Further three-dimensional characteristics of the soft palate oscillation could also be observed by plotting the time history of oscillation for points away from the tip. Comparison of the deflection history in the x-direction for points to the left and right of the tip, labeled X2 and X3 respectively, is shown in Figure 6.17. Although, the amplitudes differ, all three points on the trailing edge oscillate in phase with each other, at a frequency of approximately 20 Hz. Nevertheless, all three points show increasing

oscillation amplitude over time, indicating instability of the soft palate dynamics. This suggests the whole trailing edge to be moving together, with perhaps negligible twisting, at the current mode of instability, which may eventually lead to impact of the trailing edge of the soft palate with bounding pharyngeal walls. This may suggest the validity of cantilever-like behaviour of the soft palate, although the asymmetry and attachments to the side pharyngeal walls of the soft palate, lends to non-uniform distribution of the deformation in the lateral (left to right) direction.

Three-dimensional flow fields for this unstable case 1c are illustrated in Figures 6.18 and 6.19 for velocity and pressure respectively, corresponding to instants 1-5 labeled in 6.14. In addition to top and bottom surface of the soft palate, several horizontal cross-sections are taken across the airway passages above (or behind) and below (or forward) the soft palate surface, which respectively represent the pharynx and oral cavities. As the velocity contours in Figure 6.18 suggest, some cross-sectional distribution of flow velocities are evident in both pharynx and oral cavities, although the flow velocities in the oral cavity is relatively lower in contrast to those in the pharynx, which is not surprising considering the lower flow rate through the oral inlet and its relatively wider cross-sectional dimensions. In addition, flow velocities through the pharynx increases downstream towards the trailing edge of the soft palate, corresponding to narrowing of the pharynx cross-section. Interestingly, at regions close to the trailing edge of the soft palate, flow velocities are clearly peaking towards both left and right side walls of the pharynx, evidently more so when the tip deflection reaches its maximum at instant 3. This lateral cross-sectional variation in velocity may be due to complex curvature in the pharynx and the non-uniform deformation of the trailing edge of the soft palate, as indicated in Figure 6.17 earlier, which tends to narrow the pharynx more towards the center (or mid-sagittal plane) of the soft palate. Further downstream, the pharynx flow separates at the tip and meets the flow from the oral passage, forming a recirculation zone around the epiglottic cavity, as demonstrated later in the velocity vector plot.

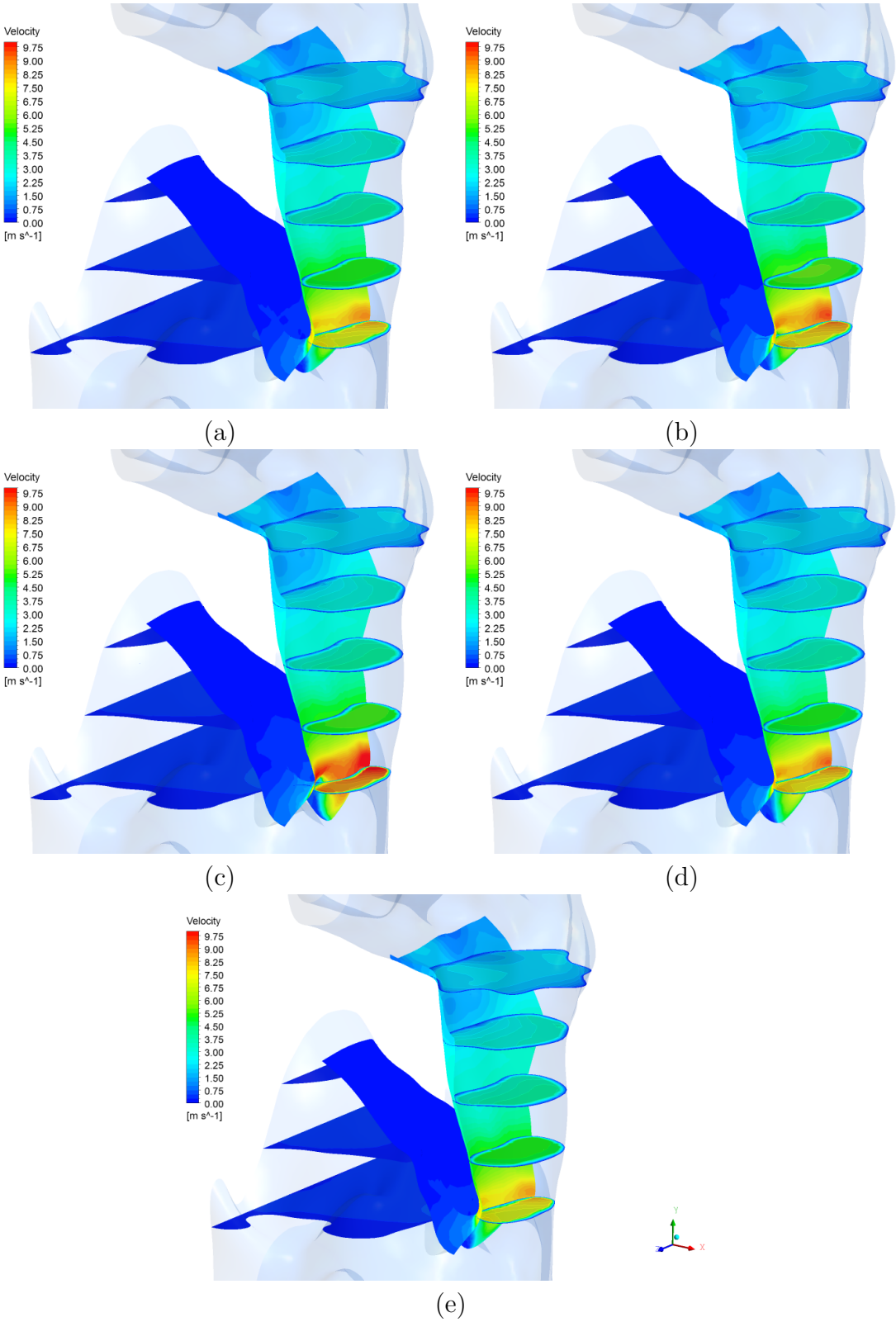

Figure 6.18: Instantaneous velocity flow fields near the surface of the soft palate and several cross-sections through upper airway, at instants 1-5 labeled in Figure 6.14 for case 1c: (a) t = 0.54 s (point 1) (b) t = 0.55 s (point 2) (c) t = 0.57 s (point 3) (d) t = 0.58 s (point 4) and (e) t = 0.59 s (point 5)

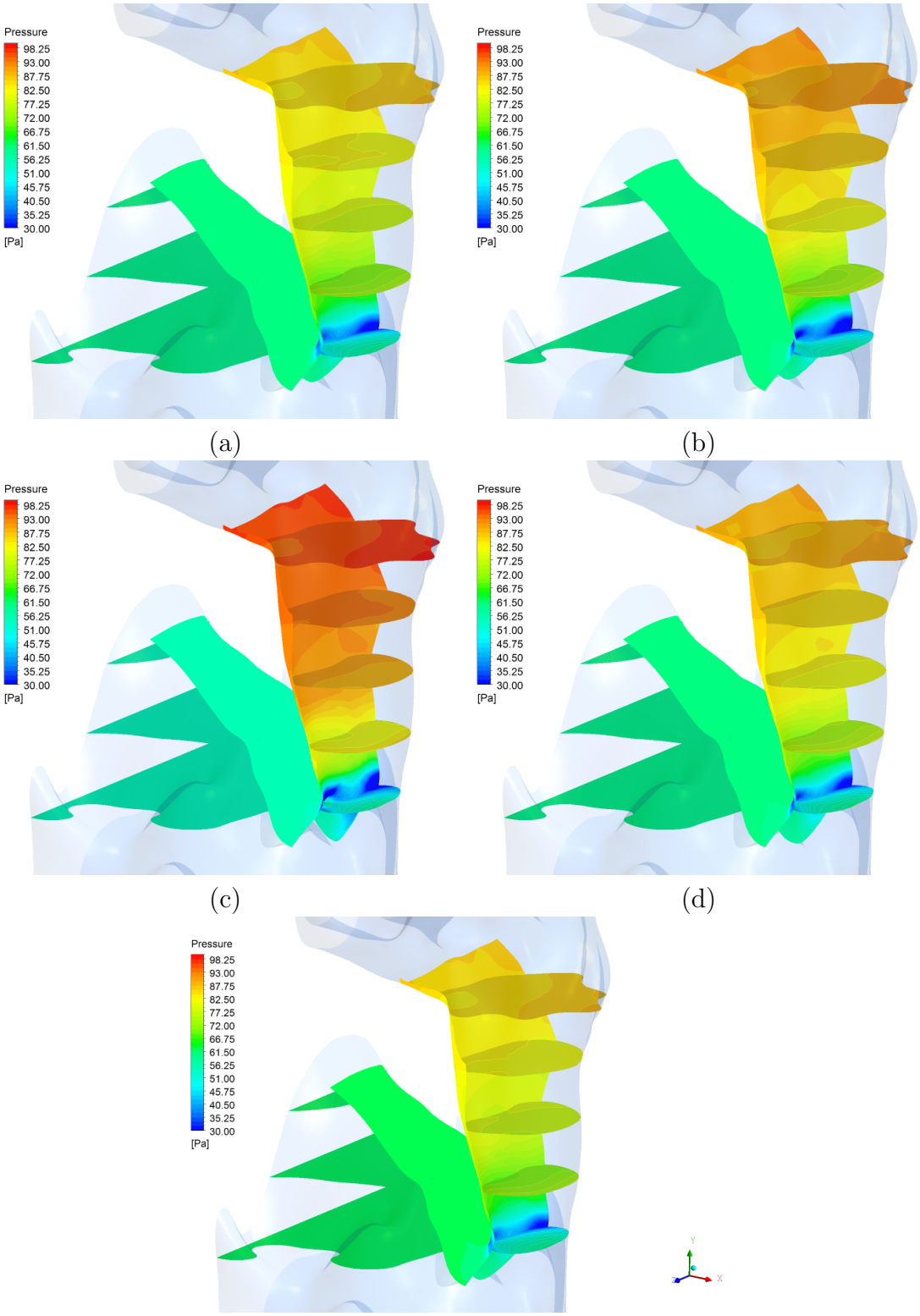

Figure 6.19: Instantaneous pressure fields near top and bottom surface of the soft palate and several cross-sections through upper airway, at instants 1-5 labeled in Figure 6.14 for case 1c: (a) t = 0.54 s (point 1) (b) t = 0.55 s (point 2) (c) t = 0.57 s (point 3) (d) t = 0.58 s (point 4) and (e) t = 0.59 s (point 5)

Figure 6.19 shows the pressure contours near the soft palate surface and several cross-sections through both pharynx and oral cavities. As indicated, the pressure distribution in the oral passage and bottom surface of the soft palate are relatively uniform compared to those in the pharynx region, where flow velocities are higher and hence more pronounced pressure gradients are expected. In the direction of the flow, pressure magnitudes through the pharynx decreases downstream towards the narrower regions of the trailing edge of the soft palate, corresponding to favourable pressure gradients associated with increasing flow velocities, as mentioned earlier. This pressure gradient in the direction of the flow is evidently more pronounced at peak tip deflection (instant 3), as indicated by the difference in pressure magnitudes between the first (top) and last (bottom) cross-sectional contours. Although towards the upper half of the soft palate top (or posterior) surface, the pressure distribution is relatively uniform across its width, which lends to validity of 2-D flow assumptions, this uniformity deviates further downstream with minimum pressures developing towards the side walls of the pharynx, as shown in Figure 6.19. This is consistent with variation in flow velocities that similarly peaks near the side walls of the pharynx prior to the trailing edge of the soft palate. Furthermore, the cross-sections in the pharynx feature cross-flow pressure gradients, which appear more pronounced towards the narrower, trailing edge of the soft palate, consistent with the findings in Lucey *et al.* (2010), although in the present simulations pressures are still positive owing to the current, more efficient approach of prescribing flow-rate inlets and zero pressure outlets. As shown in chapter 5, if pressure-driven inlets with flow-rate outlets are employed instead, similar cross-flow pressure gradients but with negative pressures are expected to develop in the airway, which may promote side wall collapse of the pharynx.

A velocity vector plot along the mid-sagittal plane in Figure 6.20(a) illustrates acceleration of flow in the pharynx as it approaches the narrower region towards the trailing edge of the soft palate. Subsequently, the flow in the pharynx separates from the soft palate as it merges with opposing flow from the oral cavity, developing a

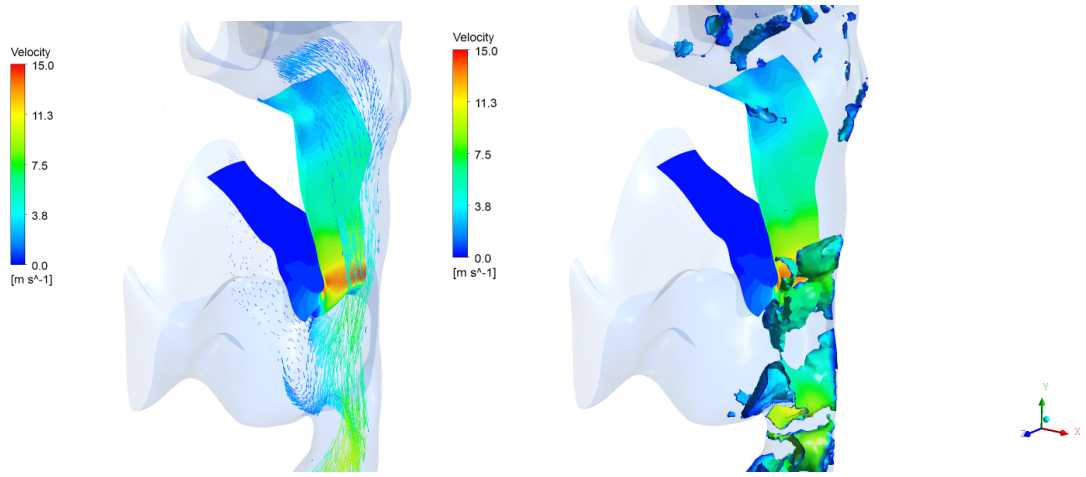

(a) (b)

Figure 6.20: Computed velocity distribution near top and bottom surface of soft palate for case 1c with (a) Velocity vector on the mid-sagittal plane of the upper airway (plane z = 0) and (b) Vortical structures developing through airway

recirculation region in the oral cavity. In addition, the vortical structures developing around the soft palate are shown in Figure 6.20(b) for a representative instant. A few methods to identify vortices are currently available, but similar to the approach in Huang & Sung (2010), a λ_2 criterion proposed by Jeong & Hussain (1995) is employed. Based on the eigenvalues of the squared symmetric and antisymmetric parts of the velocity gradient tensor, Jeong & Hussain define a vortex core as a zone having two of these eigenvalues less than zero. This is equivalent to requiring the median eigenvalue (λ_2) to be < 0 (Chakraborty *et al.*, 2005). Therefore, an isovalue of $\lambda_2 = -0.05$ is used here to identify the vortical boundaries. Figure 6.20(b) shows two vortical structures streaming from both left and right sides of the trailing edge of the soft palate, in addition to two distinct vortical tubes forming on the left and right side of the soft palate surface just upstream of its trailing edge. These seem to coincide with low pressure zones shown in Figure 6.19 and may correspond to flow velocities peaking close to the left and right side walls of the pharynx, as mentioned earlier, due to the non-uniform deflection across the width of the soft palate. Although not investigated further in this work, the vorticity of flow demonstrated by these vortical structures, may shed some light on the significance of time-dependent flow separation near trailing edge

of the soft palate, towards flow-palatal energy transmission, as mentioned in Balint & Lucey (2005).

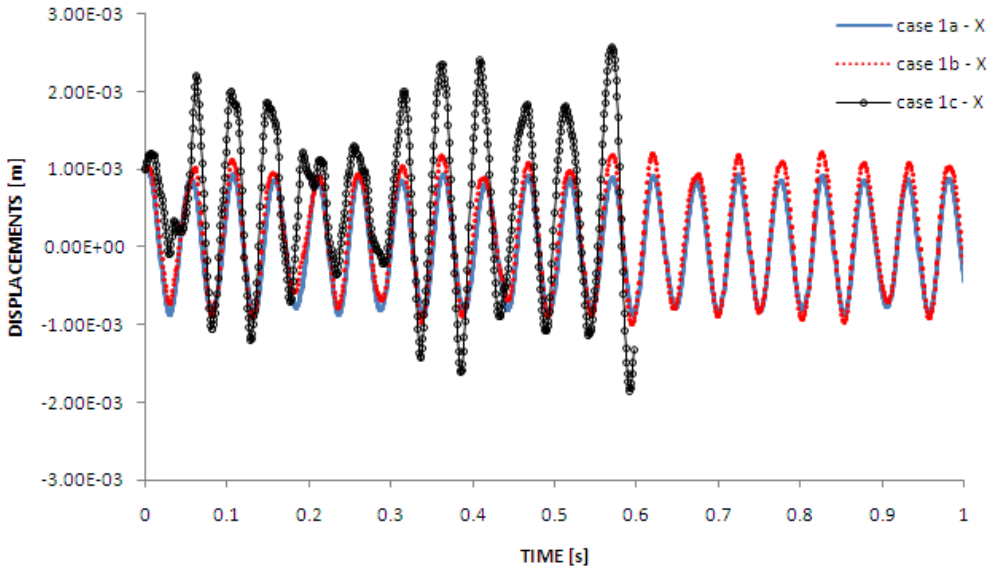

Figure 6.21: Comparison of tip deflection history between simulated oronasal inhalation cases

Finally, figures 6.21 and 6.22 show the comparison of respectively, tip deflection and total energy oscillation over time, for all three cases 1a, 1b and 1c. The oscillation ended prematurely in case 1c due to excessive mesh distortion following the growing soft palate deflection, associated with the mesh regularization technique employed. Nevertheless, the increasing amplitude of the soft palate is still evident, in contrast to the undamped constant amplitude of case 1a. Correspondingly, the total energy (kinetic and strain) oscillation of the soft palate in case 1c, shows much higher magnitudes and a general upward trend over time, in contrast to stable cases 1a and 1b, which show a decreasing trend over time. It is postulated that, unlike stable cases 1a and 1b, the interaction of the increased inhalation flow with the soft palate in case 1c leads to irreversible transfer of flow energy to the soft palate motion, thus promoting palatal instability similar to those shown in previous 2-D studies (Balint & Lucey, 2005; Huang, 1995). Unlike divergence-type instability mechanism that exhibits quasi-static growth in structural deflections, the palatal instability in this case shows indications

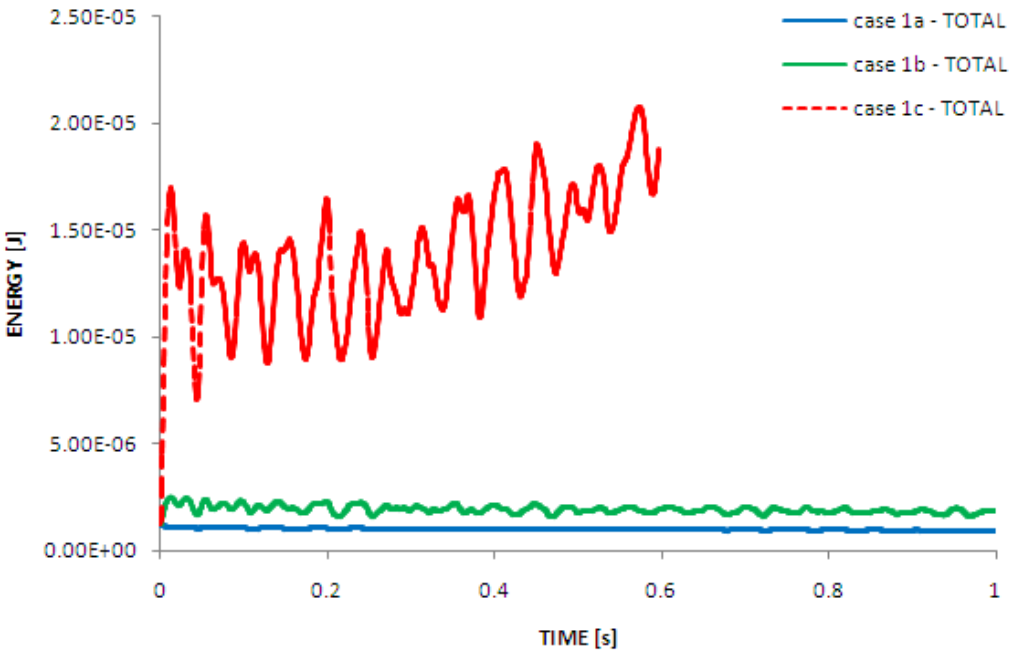

Figure 6.22: Comparison of oronasal inhalation cases showing total energy (kinetic and strain) history over time

of dynamic oscillations, suggesting flutter-type instability mechanism to be implicated in these oronasal conditions of palatal snoring. It is worthwhile to remark, that all three oronasal cases exhibit oscillation frequency of approximately 20 Hz, similar to the in-vacuo free vibration of the soft palate.

6.2.2 Oral Inhalation

Cases 2a and 2b were simulated to represent conditions where perhaps complete nasal blockage is experienced and inhalation is purely through the mouth. In case 2a, the flow rate through the oral opening is prescribed as $O = 0.0006$ kg/s. Both tip deflection and total energy history of the soft palate in respectively, Figures 6.23 and 6.24, shows no indication of growth over time, suggesting stability at the current oral flow rate.

The oral flow rate was further increased to $O = 0.0010$ kg/s in case 2b. Although the oscillation amplitude is greater than the initial 1 mm amplitude and greater than the oscillation amplitude demonstrated in case 2a, as shown in Figure 6.25, similarly, there was no indication of amplitude growth over time. This is further evidenced by

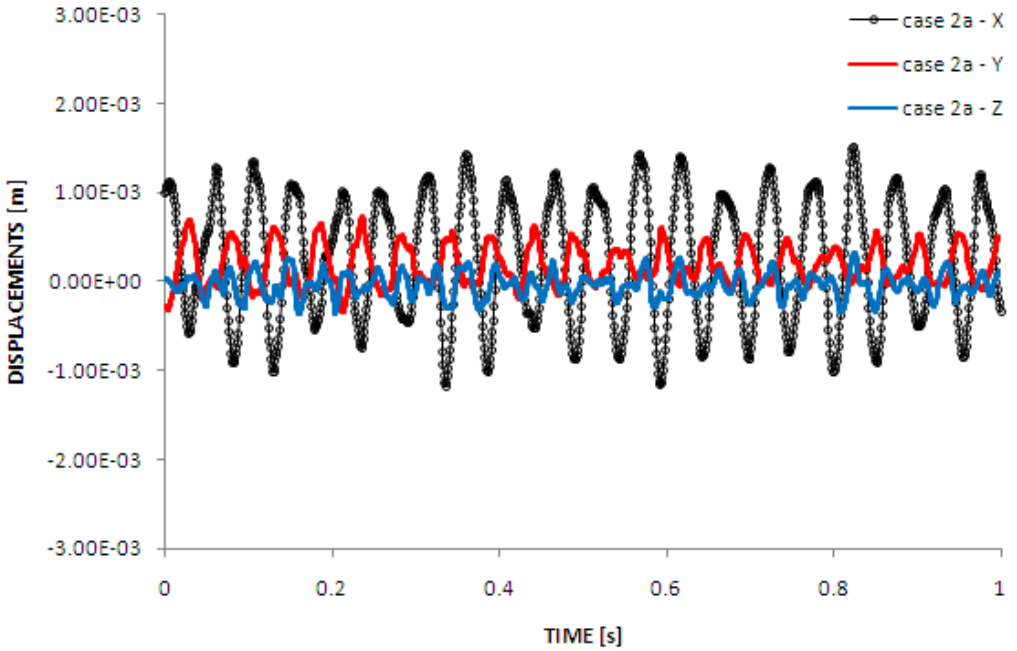

Figure 6.23: Plot of tip oscillation history in the x, y and z directions for oral flow interaction with soft palate of case 2a

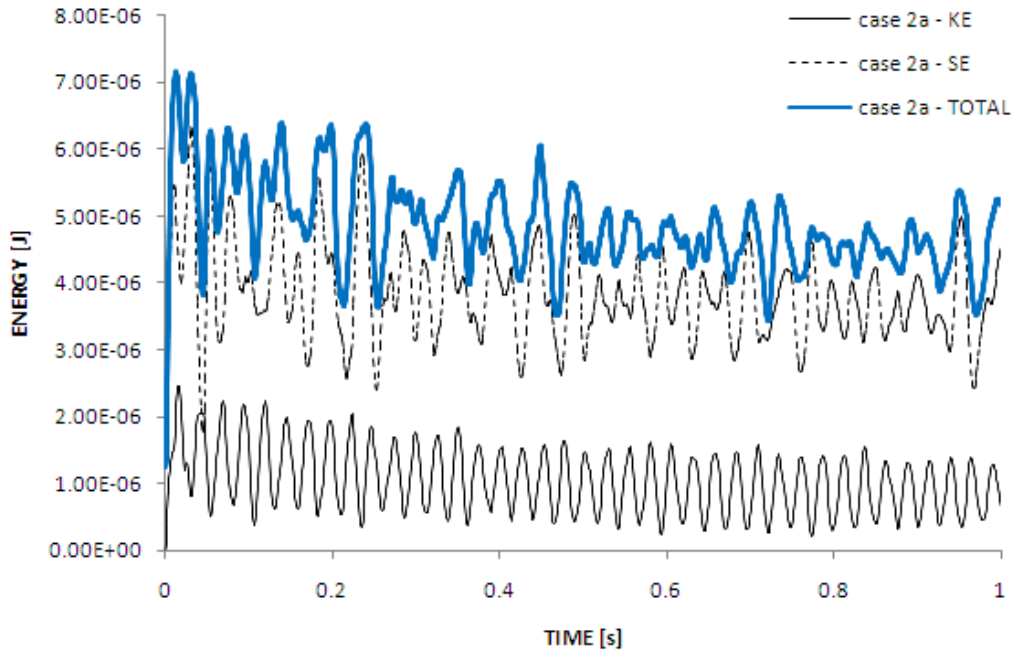

Figure 6.24: Plot of kinetic energy (KE), strain energy (SE) and total energy of the soft palate over time for case 2a

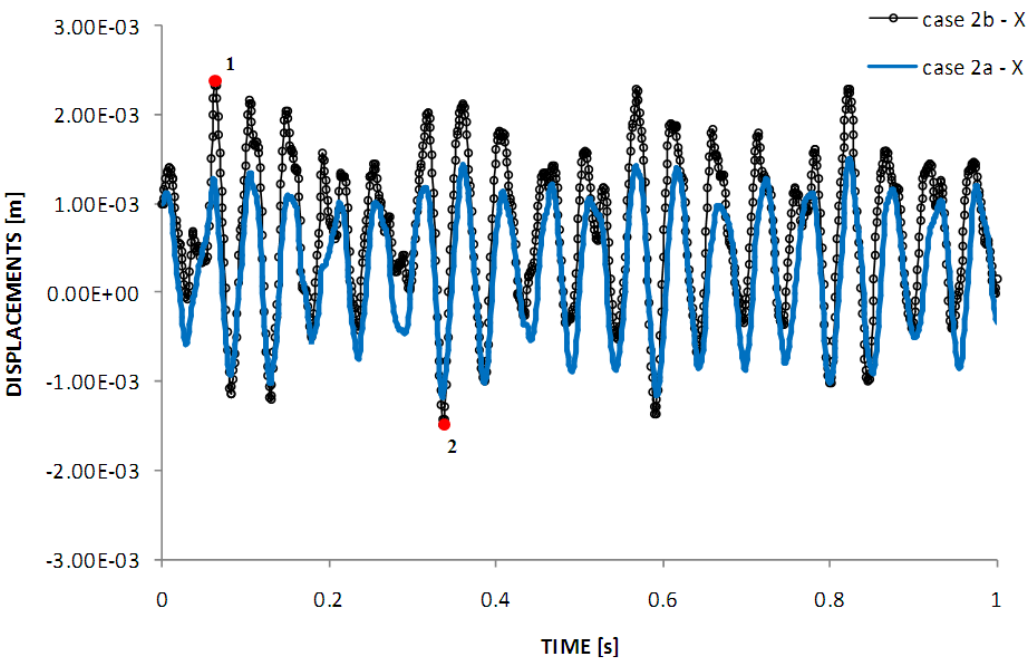

Figure 6.25: Plot of tip oscillation history in the x-direction for oral flow interaction with soft palate for case 2b in comparison with case 2a. Points 1 and 2 refer to instants in the oscillation history used in text

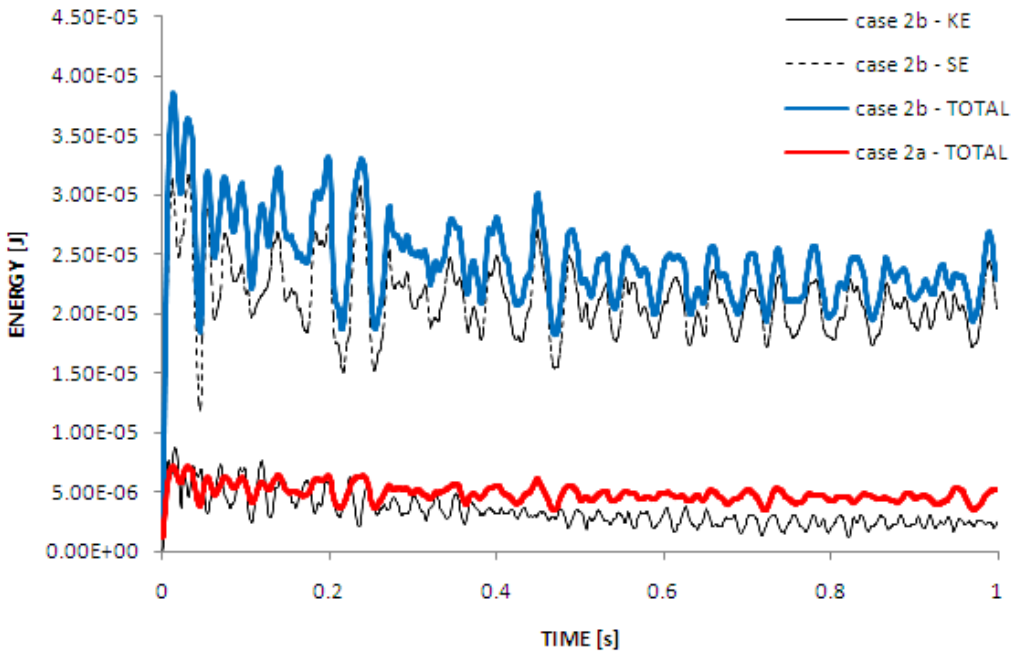

Figure 6.26: Plot of kinetic energy (KE), strain energy (SE) and total energy of the soft palate over time for case 2b and in comparison with total energy for case 2a

the total energy history of the soft palate in Figure 6.26, illustrating a downward trend over time, despite magnitudes much greater than the total energy of the soft palate in case 2a. The increased soft palate total energy in case 2b corresponds to increased flow pressure applied on the soft palate compared to case 2a, as indicated by the pressure plots in Figure 6.27. Nevertheless, the current oral flow interaction with the soft palate does not seem to yield palatal instability.

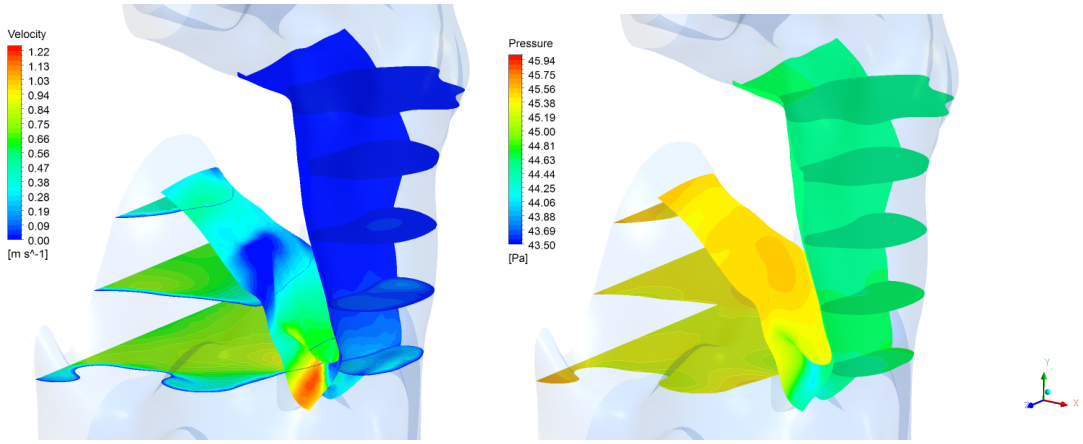

(a) 0.0006 kg/s flow rate

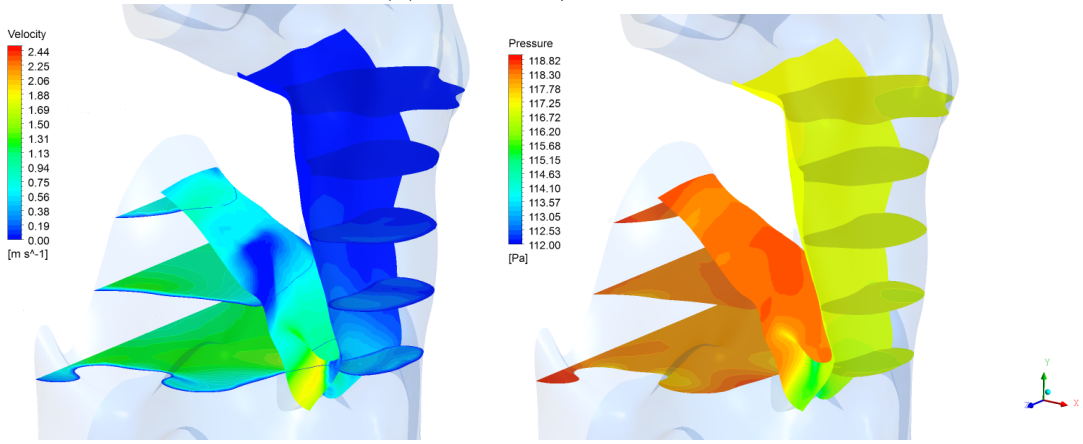

(b) 0.0010 kg/s flow rate

Figure 6.27: Instantaneous flow fields near top and bottom surface of the soft palate and several cross-sections through upper airway, corresponding to configuration at minimum tip deflection (instant 2 labeled in Figure 6.25) for: (a) case 2a (b) case 2b. Velocity and pressure contour on the left and right column respectively

This may suggest that for the current airway configuration, palatal instability may be more difficult to initiate through oral inhalation compared to oronasal inhalation. As shown in Figure 6.27, the flow velocity is greater in the oral passage (and bottom surface

of the soft palate) rather than on the pharynx side, which is expected considering inhalation is purely through the mouth. In particular, Figure 6.27 shows that the velocity magnitudes in both oral inhalation cases are far lower than those that develop in the oronasal inhalation cases, as indicated by the contour scales. This is perhaps not surprising, considering the much wider dimensions of the oral cavity in comparison to the pharynx. In particular, consistent with these relatively lower velocities in cases 2a and 2b, although streamwise pressure gradients are present in the oral passage, they are not as steep as those developed in the pharynx of the earlier oronasal inhalation cases, as indicated by the range of pressure scale in the pressure contour of Figure 6.27. Simultaneously, with the pressure equalizing as the oral passage meets the pharynx and marginal backflow in the pharynx under these pure oral inhalation cases, the pressure gradient in the pharynx is relatively negligible, which consequently lends to less significant pressure difference between the top and bottom surface of the soft palate, in contrast to the oronasal cases.

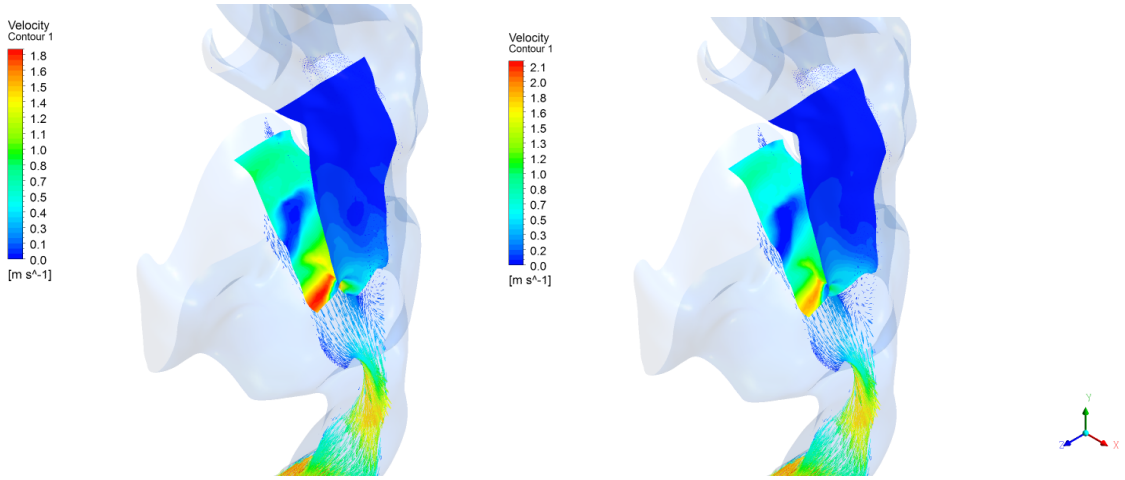

(a) (b)

Figure 6.28: Computed velocity distribution near top and bottom surface of soft palate and velocity vector on the mid-sagittal plane of the upper airway (plane z = 0) for case 2b corresponding to (a) Instant 1 and (b) Instant 2, labeled in Figure 6.25

In addition, unlike oronasal cases simulated previously, no recirculation zone is evident under current oral inhalation cases, as indicated by the vector plot in Figure 6.28 at either extreme of the tip deflection. This may highlight the lack of flow velocity

and pressure difference between opposing surfaces of the soft palate. Thus, in other conditions, when perhaps the tongue is further back and/or upwards, it is anticipated that palatal instability under oral inhalation may occur, during which the oral cavity may be more restricted, leading to more pronounced flow gradients.

This may also highlight the significance of flutter due to viscous effects in the boundary layers that develop in confined flows such as upper airways, as discussed by Balint & Lucey (2005), in contrast to trailing edge wake-induced reactions that prevails in flows without nearby walls, as discussed by Huang (1995). Plate instability in equal-width channel flow with one of the inlets closed was simulated in Balint & Lucey (2005). However, the influence of the width of the opened inlet on the instability has not been performed and further investigation in light of oral inhalation conditions, is needed.

6.2.3 Nasal Inhalation

Case 3 represents inhalation purely through the nose. Case 3a is simulated for an inhalation with relatively low flow rate of $N = 0.0001$ kg/s through both nasal cavities. The tip deflection in the x, y and z directions are plotted in Figure 6.29 showing no growth in amplitude over time, suggesting stable soft palate oscillation at the current inhalation flow rates. Corresponding plot of the total energy (kinetic and strain) history in Figure 6.30 shows downward trend of the total energy in the soft palate, confirming the stability of the soft palate interaction with the current flow.

In case 3b, inhalation through both nasal inlets were increased to $N = 0.0003$ kg/s. Figure 6.31 plots the tip deflection in the x, y and z directions for case 3b. Although not at constant rates, oscillation amplitudes are greater than the initial 1 mm amplitude and show increasing trend over time, in comparison to case 3a. Similar as in case 1c, with mesh regularization instead of complete remeshing, the oscillation ended prematurely due to excessive mesh distortion following the growing soft palate deflection. Note that in Figure 6.29 for case 3a, the tip deflection in the y-direction is

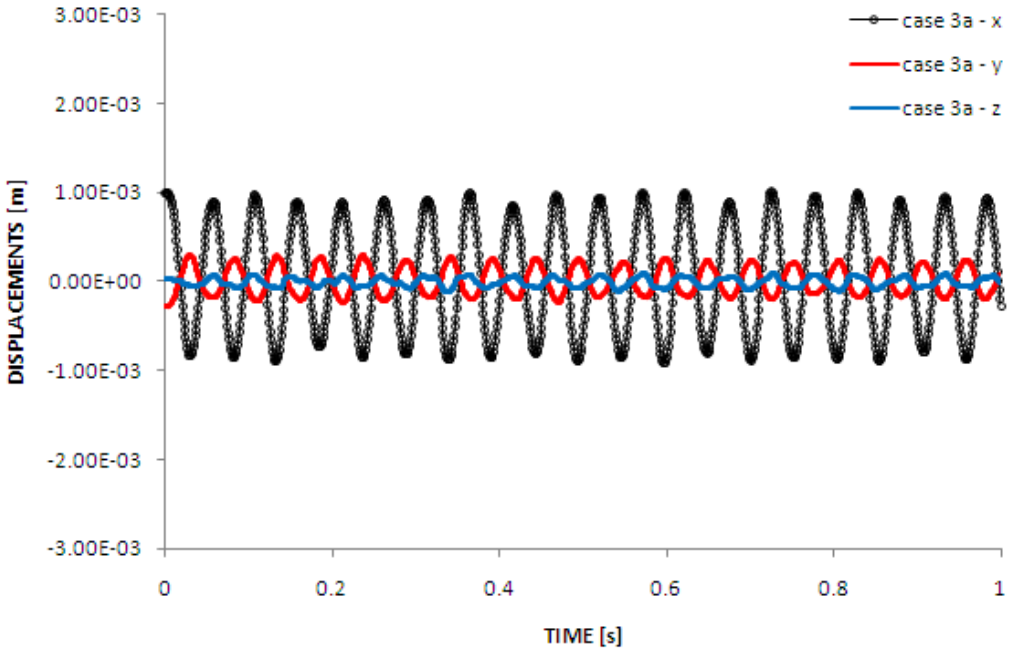

Figure 6.29: Plot of tip oscillation history in the x, y and z directions for nasal flow interaction with soft palate of case 3a

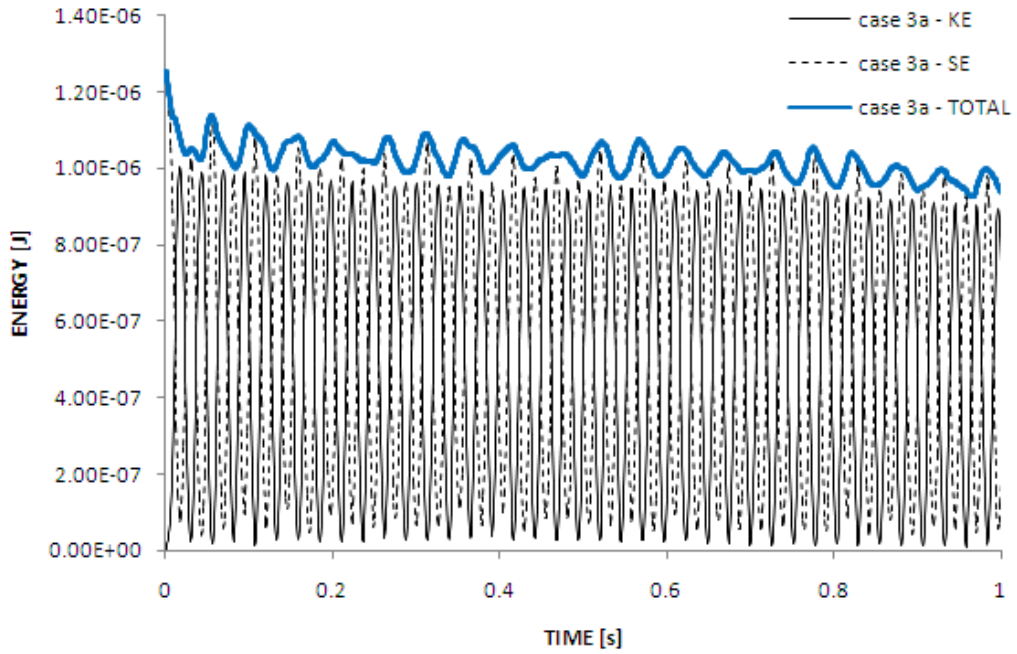

Figure 6.30: Plot of kinetic energy (KE), strain energy (SE) and total energy of the soft palate over time for case 3a

exactly out-of phase with the deflection in the x-direction, in contrast to the relatively small deflection in the z-direction that is in-phase with the deflection in the x-direction. However, for case 3b, Figure 6.31 indicates that the tip deflection in-y is tending to be in-phase with the growing tip deflection in-x. Thus, apart from increasing bending, this suggests increasing elongation and contraction of the soft palate, as it interacts with the inhaled flow and soft palate instability ensues.

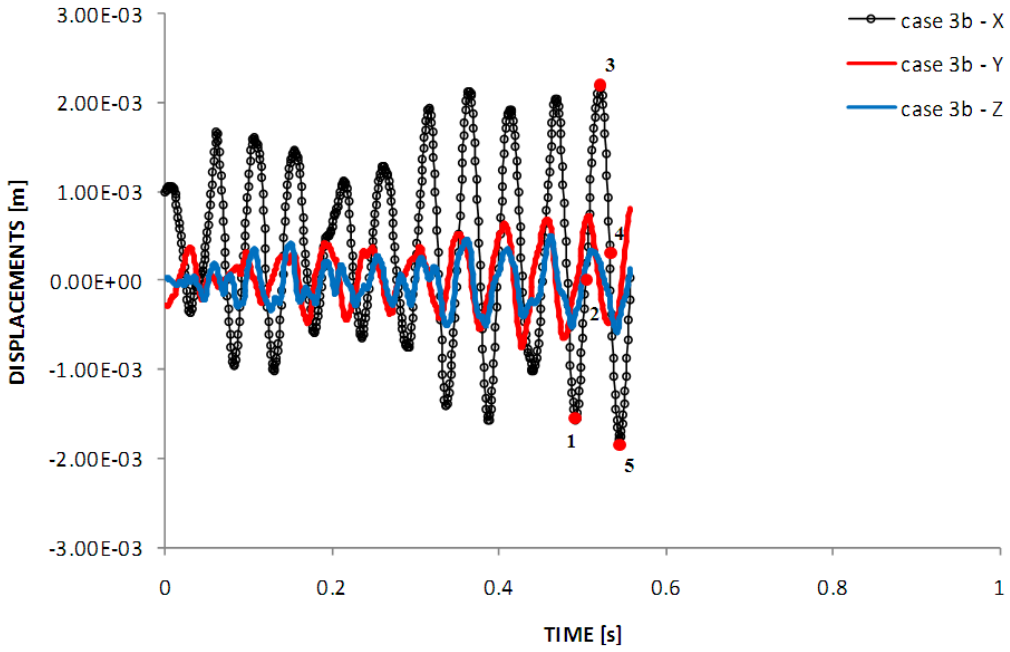

Figure 6.31: Plot of tip oscillation history in the x, y and z directions for nasal flow interaction with soft palate in case 3b. Points 1, 2, 3, 4 and 5 refer to instants in the oscillation history used in text

Figure 6.32 plots the total energy (kinetic and strain energy) history of the soft palate in case 3b. In comparison to case 3a, the total energy in case 3b is increasing over time, corresponding to the growing deflection of the soft palate as it interacts with the increased flow rate. Thus, suggesting irreversible transfer of energy from the increased flow to the soft plate occurring, via a flutter-type mechanism consistent with the oscillatory response of the soft palate. This would also suggest that a critical flow rate between the flow rates of cases 3a and 3b may be found, where palatal flutter initiates under this condition of pure nasal inhalation.

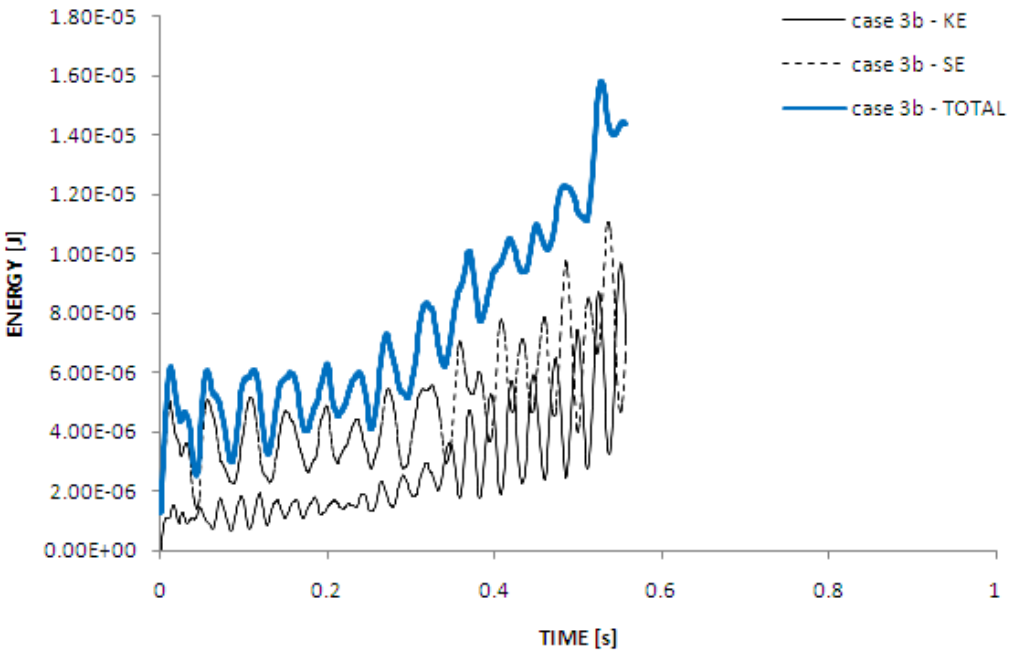

Figure 6.32: Plot of kinetic energy (KE), strain energy (SE) and total energy of the soft palate over time for case 3b

Examining the flow fields in these pure nasal inhalation cases, shows expected significant velocity and pressure on the pharynx rather than in the oral cavity, as demonstrated in Figures 6.33 and 6.34 respectively. Corresponding to increased flow velocity, streamwise pressure gradients are more pronounced than in pure oral inhalation cases, as indicated by the contour scales. In comparison to the oronasal inhalation cases, although the current velocity and pressure contours appear quite similar, in the absence of oral flow, pressures in the pharynx seems to develop lower and negative (suction) magnitudes, as indicated in Figure 6.34. This may correspond to flow acceleration and lower resistance with incoming flow from the opposing passage. This is also evidenced from the recirculation zone that develops in these pure nasal inhalation cases, which is located further upstream in the oral cavity, as illustrated in Figure 6.35, indicating a slightly later separation point near the top surface of the soft palate in the absence of opposing flow, in contrast to oronasal inhalation.

Similar to oronasal inhalation cases, pressure contours under pure nasal inhalation indicate that pressure magnitudes are reasonably constant across the width (i.e.

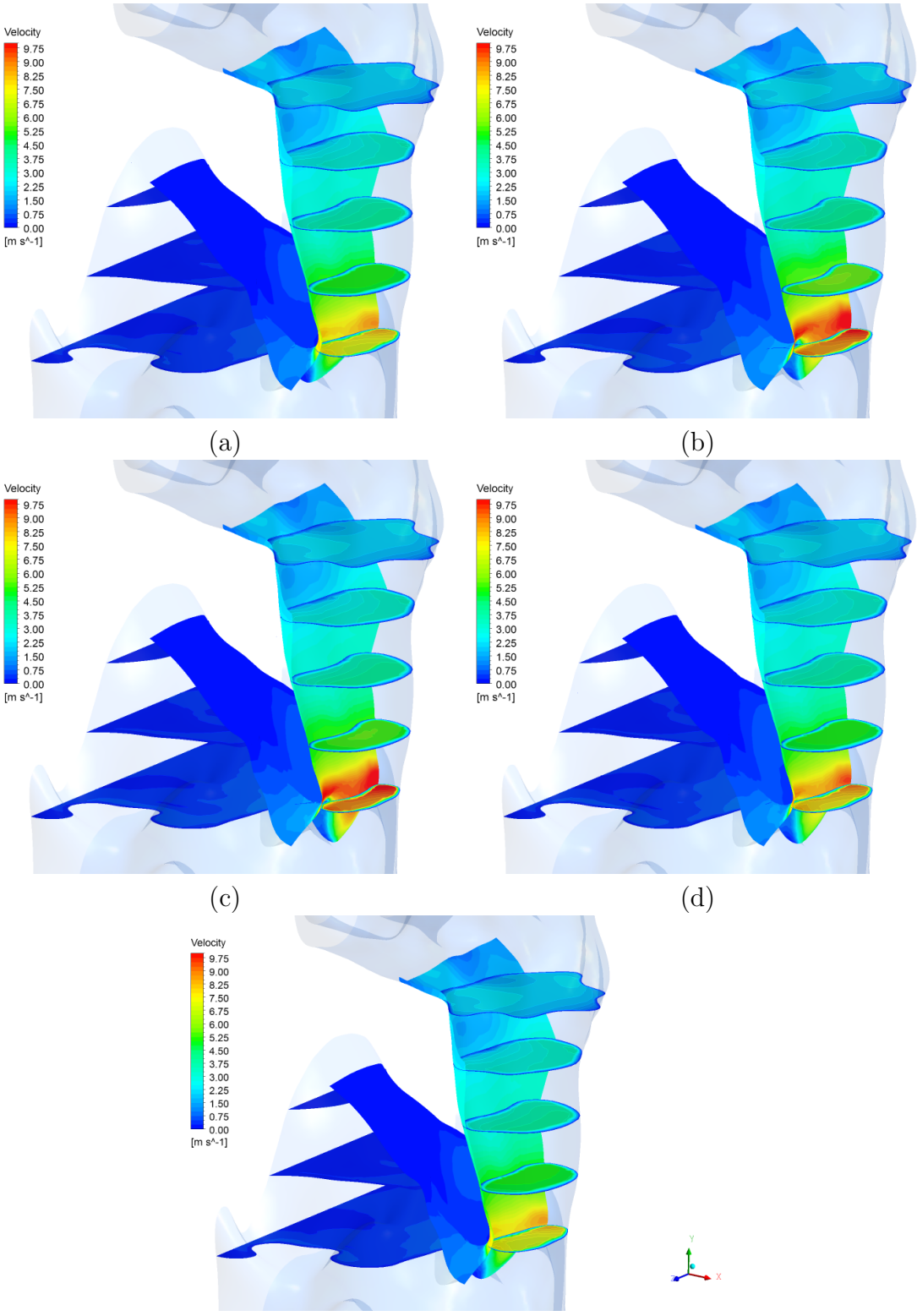

Figure 6.33: Instantaneous velocity fields near top and bottom surface of the soft palate and several cross-sections through upper airway, at instants 1-5 labeled in Figure 6.31 for case 3b: (a) t = 0.49 s (point 1) (b) t = 0.51 s (point 2) (c) t = 0.52 s (point 3) (d) t = 0.53 s (point 4) and (e) t = 0.54 s (point 5)

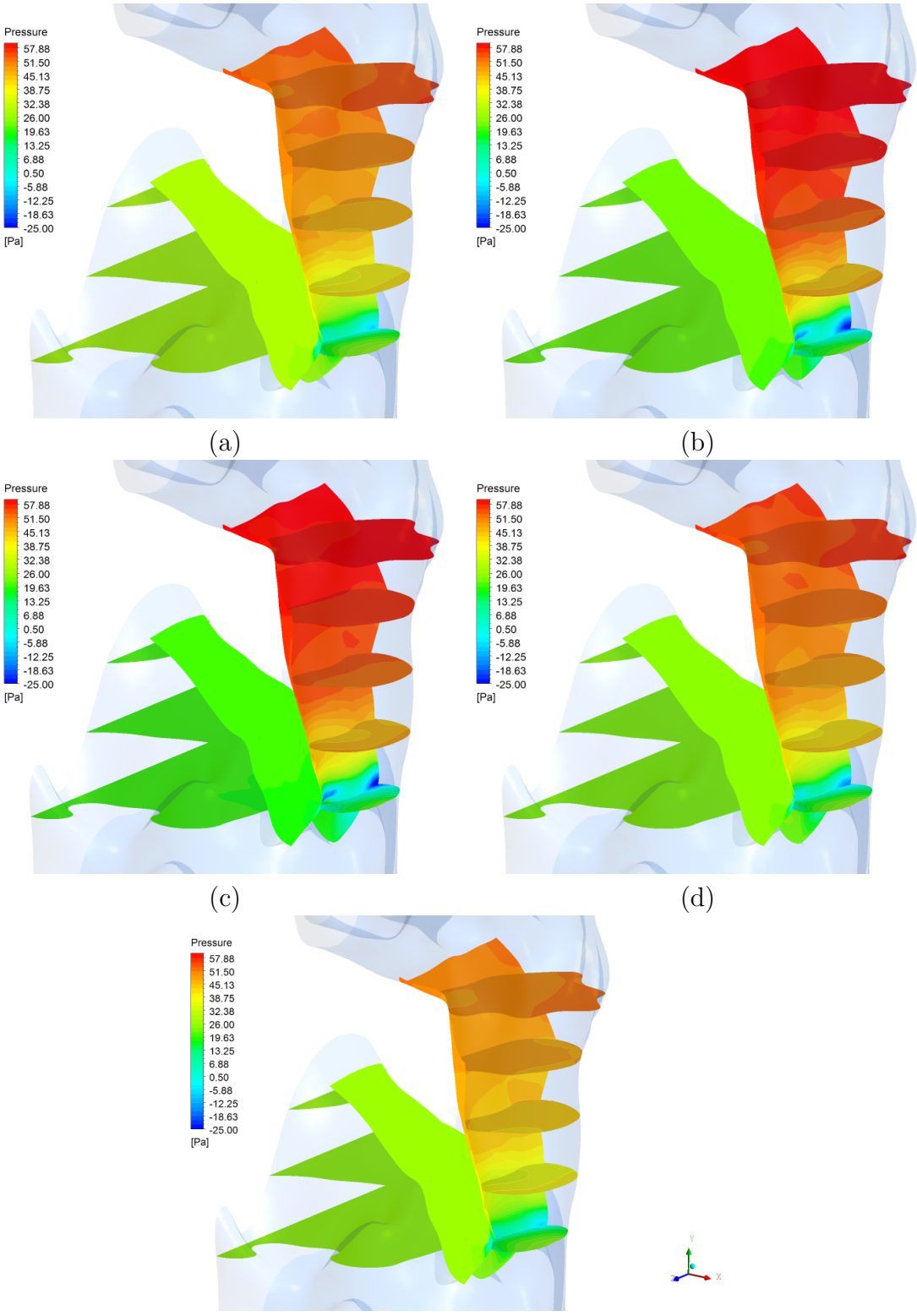

Figure 6.34: Instantaneous pressure fields near top and bottom surface of the soft palate and several cross-sections through upper airway, at instants 1-5 labeled in Figure 6.31 for case 3b: (a) t = 0.49 s (point 1) (b) t = 0.51 s (point 2) (c) t = 0.52 s (point 3) (d) t = 0.53 s (point 4) and (e) t = 0.54 s (point 5)

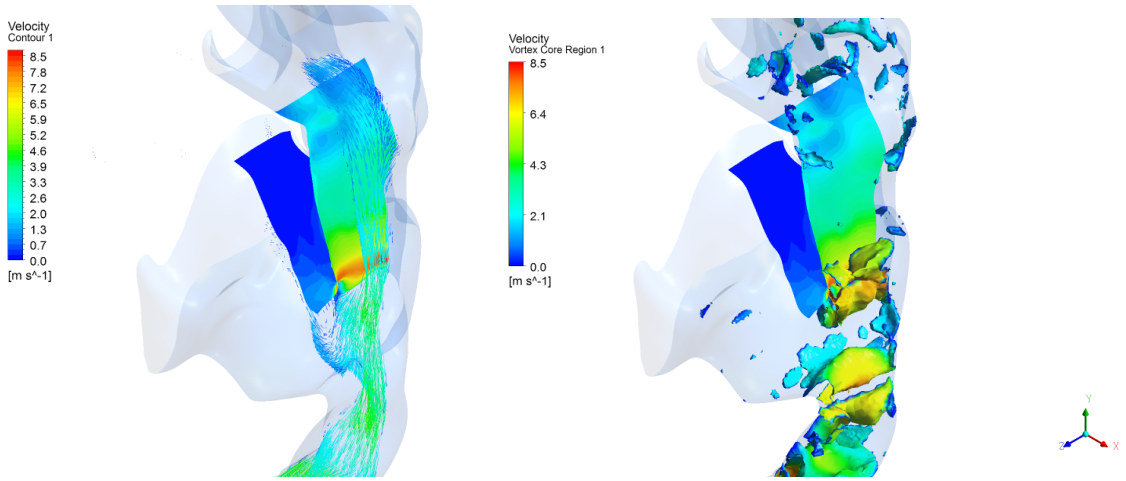

(a) (b)

Figure 6.35: Computed velocity distribution near top and bottom surface of soft palate for case 3b with (a) Velocity vector on the mid-sagittal plane of the upper airway (plane z = 0) and (b) Vortical structures developing through airway

spanwise) in the upstream half of the soft palate, but lose this uniformity further downstream as flow peaks towards the side walls of the pharynx, suggesting deviation from 2-D flow patterns assumed in channel flows. However, conditions where one of the nasal inlets is blocked or resistant to inhalation, may alter this relatively uniform spanwise pressure distribution along the upstream half of the soft palate surface, leading to more pronounced 3-D flow pattern instead. This condition is investigated next.

In case 3c, a similar total mass flow rate of 0.006 kg/s to case 3b is applied, but into the right nasal cavity. Similar to case 3b, palatal flutter is exhibited at this flow rate, as indicated by the growing tip deflection and total energy of the soft palate over time, in figures 6.36 and 6.37 respectively. In comparison, the history of tip deflection and total palatal energy over time in case 3c seems similar to that in case 3b, suggesting lack of sensitivity in palatal instability to upstream flow patterns. As indicated in figure 6.38, more pronounced 3-D flow patterns are exhibited in the upstream half of the soft palate in case 3c, which however, develops into a 3-D flow pattern further downstream that is similar to case 3b. Similarly, for case 3c, a λ_2 criterion with $\lambda_2 = -0.05$ is used to identify the vortical structures in Figure 6.39, showing more pronounced vortices in contrast to case 3b in the upstream half of the soft palate, which progresses to similar

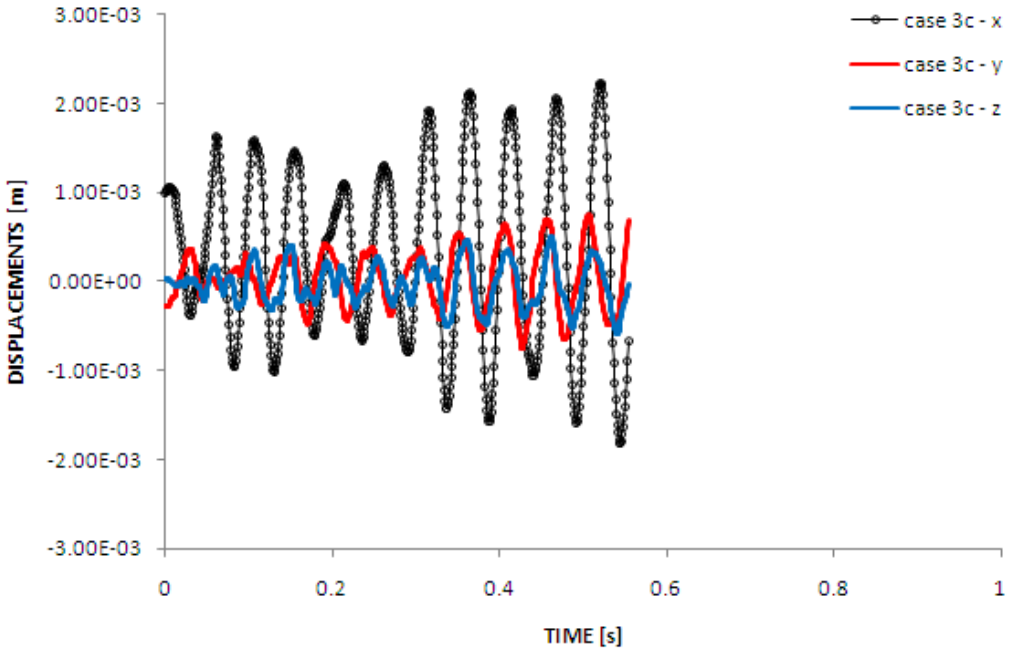

Figure 6.36: Plot of tip oscillation history in the x, y and z directions for nasal flow interaction with soft palate of case 3c

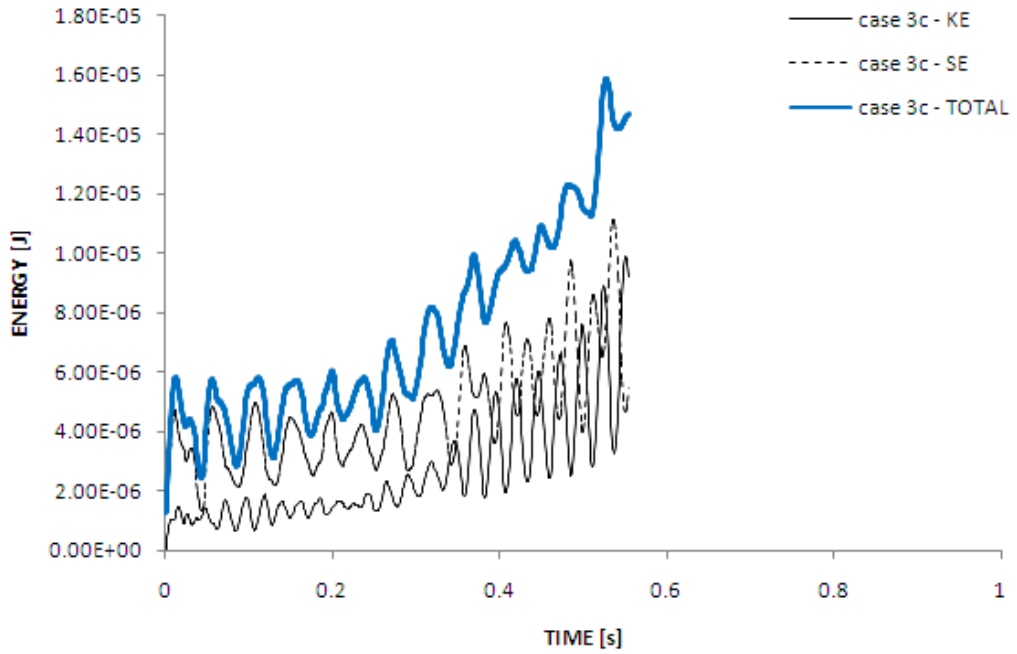

Figure 6.37: Plot of kinetic energy (KE), strain energy (SE) and total energy of the soft palate over time for case 3c

vortex patterns as in case 3b further downstream. This may suggest that, for a 3-D soft palate assumed fixed at its sides and upstream end, significant soft palate response and instability is perhaps attributed more to its flexible downstream half rather than its upstream half. Hence, supporting current treatments such as palatal stiffening, to be concentrated on the bottom half of the soft palate.

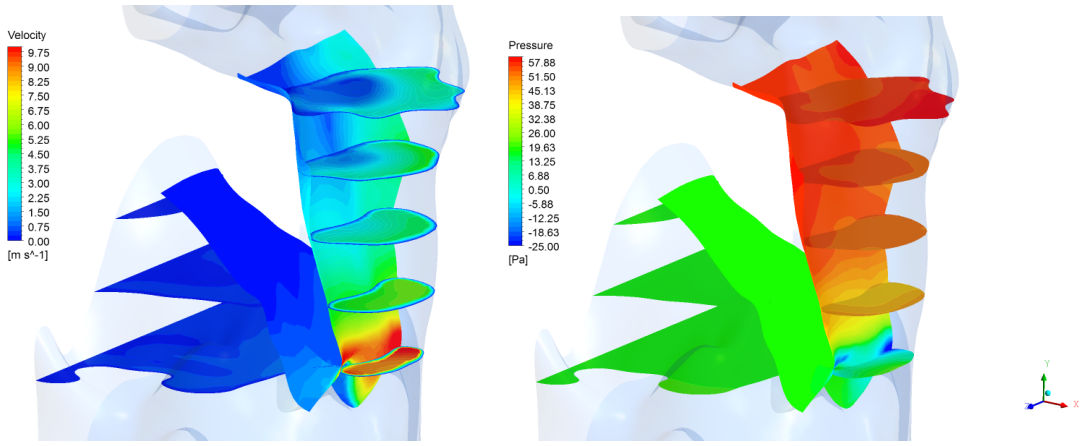

(a) (b)

Figure 6.38: Instantaneous flow fields near top and bottom surface of the soft palate and several cross-sections through upper airway, corresponding to configuration at maximum tip deflection for case 3c: (a) velocity contour and (b) pressure contour

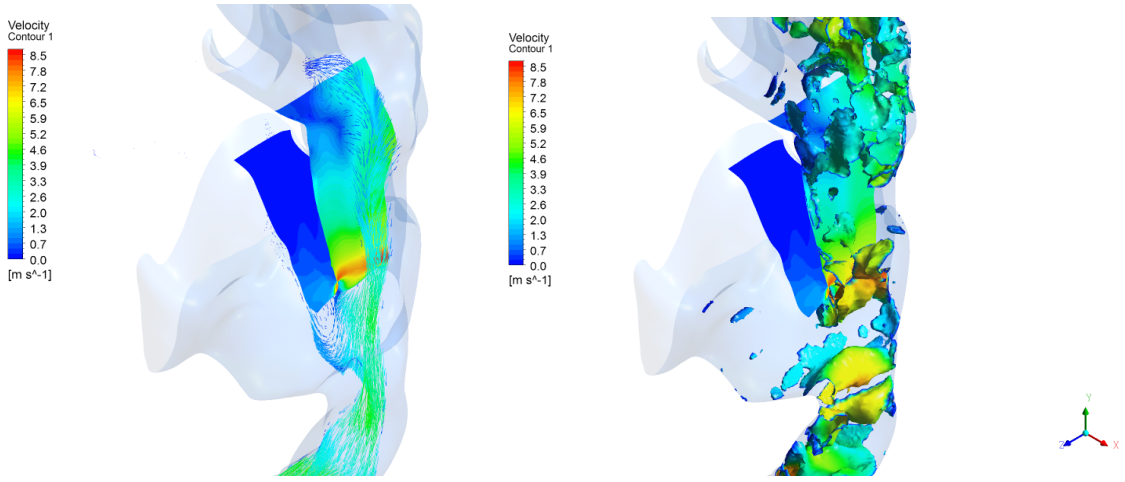

(a) (b)

Figure 6.39: Computed velocity distribution near top and bottom surface of soft palate for case 3c with (a) Velocity vector on the mid-sagittal plane of the upper airway (plane z = 0) and (b) Vortical structures developing through airway

6.3 Concluding Remarks

In the current chapter, a flow-induced instability of a soft palate was modeled using a realistic 3-D upper airway geometry. The soft palate was reconstructed by 'filling-in' material between the nasal and oral cavity, giving dimensions that are within clinically measured range, albeit tending towards the maximum range of values reported in the literature. A laminar, 3-D Navier-Stokes flow solver in an ALE framework was coupled to a 3-D non-linear large deformation finite element solver, via a partitioned approach. The flow-induced palatal instability was investigated as an initial value problem, similar to previous established approach. In addition to monitoring soft palate tip oscillation, corresponding total energy (strain and kinetic) history over time was also monitored to assess stability of the soft palate. Similar to 2-D channel models, both stable and unstable flow-induced responses of the soft palate were observed, depending on the imposed flow rate. Stable cases showed reduction in total palatal energy history, while unstable cases showed upward trend with time, suggesting irreversible transfer of flow energy to soft palate.

Flow gradients are more pronounced in the pharynx in contrast to the oral cavity, perhaps due to the much wider dimensions of the oral cavity in the current subject. This may explain the stability for oral-only inhalation cases, although extreme flow rates have been applied, unlike other simulated conditions of nasal-only inhalation and inhalation through both oral and nasal. Flow patterns show low pressure regions developing near the side walls of the pharynx near the trailing edge of the soft palate, corresponding to maximum velocity streams and localised vortical structures.

Unstable soft palate response suggests both bending and elongation components are present. In addition, soft palate deflection is more pronounced in its mid-section compared to its sides, consistent with the support condition of the soft palate.

Although visible, present simulation shows more complex palatal oscillation and total energy history in contrast to a 2-D channel model, highlighting a need to develop

a technique to formally quantify onset of palatal flutter. In addition, the current model has assumed rigid pharynx walls, which may be further modified to interact with the pharyngeal flow and thus capture possible side wall collapse. It is also proposed to modify the present laminar flow assumption to turbulent flow, using appropriate turbulence models, to investigate variations in critical onset of palatal flutter under turbulent flow.

Chapter 7

Concluding Remarks

The present thesis documents further examination of fluid-structure interaction in the upper airway, in regards to snoring and obstructive sleep apnoea/hypopnoea syndrome (OSAHS). In particular, the overall goal of the current project is to contribute further understanding and enhance development of computational modelling, for snoring and obstruction around the retropalatal/retroglossal region. The investigation was divided into three major parts, which were: (1) Idealised 3-D model for studying retroglossal obstruction, (2) Idealised 2-D channel flow to further examine palatal snoring and its potential to detect retroglossal obstruction and (3) Further realistic investigation of palatal snoring using a 3D realistic upper airway model.

Research questions have been posed in line with the goal of the current project. Responses to these research questions are summarised and recommendations for future work are proposed in section 7.1. Finally, section 7.2 presents potential tasks for future development of realistic computational modelling of upper airway for real-time diagnosis of snoring and OSAHS.

7.1 Response to Research Questions

In the current study, four research questions were formulated that addressed further areas and development of models, which may be explored, relevant to retroglossal/retropalatal snoring and obstruction. Summary of the findings to each research

questions are presented and scope for future work in each specific area are proposed.

In comparison to development of 2-D tongue replica occlusion model, how does a full 3-D model and different flow regime affect the fluid-structure interaction?

A laminar, asymptotic, reduced Navier-Stokes, 2-D model to capture real-time retroglossal occlusion was extended to a full Navier-Stokes, 3-D model in the current work. Simulation of progressive retroglossal obstruction with increasing breathing effort was performed, based on coupling quasi-steady flow, representative of quiet sleep breathing, with a hydrostatically pressurised linear thin shell to represent the tongue. Both non-linear flow rate limitation and linear reduction in opening underneath the tongue, with increasing intraluminal pressure difference, were exhibited similar to a 2-D model. Flow contraction to jet stream formation, which may lead to shear-induced turbulence, was demonstrated, similar to a 2-D model, although turbulence was not considered in the 2-D model. Modelling turbulence into the current 3-D model shows steeper pressure gradients developing underneath the tongue replica, that generates more severe collapse of the tongue base (and hence retroglossal narrowing), in contrast to laminar breathing. Further parametric investigations under both laminar and turbulent conditions, indicate similar trend of aggravating tongue collapse for cases with pronounced initial narrowing underneath the tongue and increased compliance of the tongue.

Obviously, unlike 3-D models, the presence of bounding side walls and lateral flow distribution or curvatures, are not captured in 2-D models. The current 3-D model shows more pronounced narrowing underneath the middle than at the side of the tongue replica, leading to flow stream migrating towards the side wall of the idealised pharynx. In combination with the curvature of the bounding side walls, a 3-D recirculation region forms downstream of the tongue replica and cross-flow pressure gradients develop. Furthermore, side wall pressures are found to be negative (suction) during expiratory flow, with higher suction pressures predicted towards the narrowed region. These side

wall suction pressures are also found to be more pronounced during inspiratory in comparison to expiratory breathing, suggesting possibility of side wall collapse.

The current model and investigation could be further improved to perhaps represent the oropharynx more closely. Some of the recommendations proposed for future works are:

- Current 3-D tongue replica model is based on isotropic and homogeneous assumptions. In reality, tongue properties are anisotropic, and with development of non-invasive measurement techniques, more accurate in-vivo properties of the tongue may be applied.

- Current steady simulations may also be extended to unsteady FSI simulations to allow complete, low and high, flow inhalation and expiration breathing cycle. This may represent more closely the actual flow and tongue deflection history during sleep, which may capture further variations in narrowing or reopening during breathing.

- In reality, the pharyngeal airway compliance may not be homogeneous and actually differs between inspiration and expiration, as demonstrated by Brown *et al.* (1985). Furthermore, collapse of pharynx side walls is also another mode of apnoeic obstruction and may also be flow-induced as suggested earlier. Therefore, it may be possible to model several segments of the pharyngeal airway with differing (and perhaps, breathing state dependent) compliance and include flow interaction with pharynx walls, which in this thesis have been assumed rigid.

What is the relationship between severity of localised obstruction and onset of palatal snoring, and could it be employed to detect palatal-tongue occlusion?

Palatal snoring is idealised by investigating flow-induced instability of a cantilever plate in a 2-D channel flow representing oral and nasal passages. A generous rigid blockage is introduced in the channel to model the presence of localised obstruction such

as the base of the tongue, which may represent a more realistic oropharyngeal airway where the channel widths are non-uniform. The width of the obstruction is fixed but its depth is varied, and the critical inlet velocity corresponding to each depth configuration is estimated. Several methods are available to determine critical velocity for onset of instability, but an initial value problem approach is perhaps more practical here, following previous works. The 'soft palate' is released from an initial deformation profile and instability of the 'soft palate' is judged from either increasing amplitude of plate deflection or increasing total plate energy, over time. Numerical simulations shows a linear reduction in critical inlet velocity with increasing obstruction depth or vice-versa. Although comparison with atmospheric inlet pressure model suggests that current velocity inlet model may underpredict the critical inlet velocity, similar 'soft palate' instability is observed. Correlating this relationship between critical velocity and obstruction depth to breathing flow curves of individuals, the time difference between start of inhalation to onset of palatal snoring, may represent a key parameter for non-invasive measurement of severity of retroglossal obstruction. Extending this to palatal snoring signals, time lapse between palatal snoring episodes, may perhaps represent a more practical measurement parameter for non-invasive detection or diagnosis of retroglossal obstruction.

Current investigation represents a preliminary step with many simplifying assumptions, which perhaps warrants further investigation for development of potential non-invasive diagnosis via palatal snoring signals. Some of the recommendations proposed for future works are:

- Present investigation have looked at a flow condition where inhalation occur through both oral and nasal inlets at equal flow rates. Further parametric study is necessary, in order to investigate any potential relationship between obstruction depth and onset of instability, for cases with non-uniform inlet flow rates, which include nasal-only or oral-only inhalation.

- At present, the onset of instability is visually judged based on graphical representation of the cantilever plate oscillation amplitudes over time. A more formal approach to quantify onset of instability needs to be further developed for consistency and accuracy.

- Current configuration have been based on equal widths through both oral and nasal channels, which is unlikely to represent actual conditions. Apart from local obstruction depth, channel width ratios need to be included in the variables which affect critical inlet velocity. Further, parametric investigation is necessary to find a more complete relationship for estimating critical inlet velocity.

- Correlating current simplified 2-D model results to actual conditions or clinical application represent a challenging task. Further in-vitro experiments and simulations using realistic upper airway models are first necessary.

How does palatal collision with surrounding pharyngeal walls influence soft palate oscillation and hence, palatal snoring signals?

Further investigation of palatal snoring, in terms of response of 'soft palate' after contact with bounding walls, is addressed in chapter 5. It may be necessary to include this in computational models aimed at further understanding and decomposing palatal snoring signals. In order to avoid repetitive complete remeshing and fluid grid collapse anticipated with mesh regularization approach, an immersed boundary method was employed to model the interaction between an immersed 'soft palate' and channel flow, in a fixed fluid grid domain. Flow-induced instability of the immersed 'soft palate' was similarly investigated as an initial value problem, by releasing it from an initial deformation profile at constant inlet velocity. Prior to impact, growing oscillation amplitude of 'soft palate' at a uniform frequency is demonstrated, corresponding to palatal instability. After impact with channel walls, 'soft palate' response showed increase in oscillation frequency and thus, transverse velocity. Although one of the channels was briefly closed, the palatal response was not as rapid as a reopening collapsible tube,

perhaps due to presence of flow resistance in the opposing channel. Not surprisingly, such frequency response change may complicate measured palatal snoring signals.

While many investigations have been undertaken to simulate flow-induced instability under axial flows, inclusion of wall contact seems limited. Present investigation represents a preliminary qualitative attempt towards more complete modelling of palatal snoring, which requires further experimental validation. In addition to this, further developments and improvements which may be recommended for future works are:

- Current IBM model is based on imposing body force densities that are estimated from linear theory of beam. This may be further extended to consider non-linear large deformation (and coupling of bending and in-plane components) to capture more realistic 'soft palate' response. This may be more easily implemented by using a forcing feedback scheme and solving separate fluid and structural dynamic equations as proposed in Huang *et al.* (2007*a*).

- Similarly, more realistic 'soft palate' properties may also be applied for better correlation with clinically measured snoring signals.

- It may also be possible to consider a flexible channel wall with realistic properties, instead of the current rigid assumption.

- Present investigation has looked at a constant flow velocity applied through the channel inlets. Instead, a realistic unsteady breathing flow profile, representing high and low tidal cycles, could be imposed that may simulate more closely an actual palatal response and hence, more complete snoring signals.

- It is also proposed to design and experiment with flexible plate in channel flow, perhaps using high-speed filming, to validate and further investigate palatal contact.

How does a realistic 3-D model compare with simplified 2-D channel model of the upper airway in regards to predicting palatal snoring?

Finally, realistic modelling of palatal snoring was presented in chapter 6 to address the current research question. A 3-D realistic upper airway model, representing both nasal and oral passages, through the pharynx and finally exiting the larynx, was employed. The soft palate was reconstructed by 'filling-in' material between the nasal and oral cavity, giving dimensions that are within clinically measured range, albeit tending towards the maximum. Similar to previous approach, the palatal instability is examined by monitoring either palatal deflection or total palatal energy history, resulting from flow-induced response of the soft palate that was released from an initial deformation, under constant inlet flow rates. Several cases of inhalation conditions were investigated, at various flow rates, representing three conditions: (1) inhalation through both nostrils and oral opening, (2) inhalation through oral inlet only and (3) inhalation through nostrils only. Although the current investigation was not intended to exactly quantify the critical flow rates for onset of palatal instability, at each condition, both stable and unstable flow-induced response of the soft palate was observed, except for the oral-only inhalation. This may be due to insufficient pressure gradients developing in the oral cavity, associated with the wide dimensions of the oral cavity in the current subject. Otherwise, similar to the 2-D channel models, unstable growth of palatal oscillation is evident and critical flow rate for onset of instability may be predicted, although it may not be as clear-cut as in 2-D models. Corresponding total energy (strain and kinetic) of the soft palate, may furnish better confirmation for onset of instability. Stable cases showed reduction in total palatal energy history, while unstable cases showed upward trend with time, suggesting irreversible transfer of flow energy to soft palate at such flow rates.

In comparison to 2-D channel models, a realistic model captures more accurate flow curvatures and airway dimensions specific to each patient. Although towards the upstream half of the soft palate, pressure distribution may perhaps be reasonably ap-

proximated by a 2-D uniform width flow pattern, this deteriorates further downstream towards the trailing edge of the soft palate. Higher velocity streams form closer to the side wall of the pharynx, with corresponding low pressure regions. Furthermore, although there are indications of in-phase unstable oscillation along the width of the trailing edge of the soft palate, the deflection along this trailing edge is larger in the mid-section than its sides, which obviously is not captured in 2-D models.

To the author's knowledge, modelling of palatal snoring has been largely based on 2-D channel flow and limited attempts have been made under a 3-D realistic setting. Appropriately, this current work simply represent one more step towards better understanding of palatal instability and may be further developed for future analysis of snoring sounds. Further scope for future works that may be recommended include:

- The current soft palate model, although based on some measured properties, have been averaged and assumed isotropic. Hence, further improvement by considering more realistic properties and distribution of soft palate stiffness, for example based on the findings in Birch & Srodon (2009), may better reflect actual response of soft palate.

- Present model have assumed laminar flow through the upper airway. Interaction of turbulent flow with the soft palate may be explored by employing appropriate turbulence models into the flow computations.

- In addition, current FSI model has assumed rigid pharynx walls. Appropriate pharynx wall stiffness or compliance could be modeled to better capture more complete physiological systems where flow-induced pharyngeal wall deformation is considered.

- Similar to the 2-D channel model, an improved method to formally quantify onset of palatal flutter may need to be developed for consistency and accuracy.

- Current model represents a case where tongue-base obstruction is minimal. For

further development of palatal snoring signals as a means for diagnosing retroglossal obstruction, current investigation may be extended to simulate posterior tongue movement and variation with onset of palatal instability examined.

7.2 Towards Non-Invasive Diagnosis of OSAHS

The final goal is to sufficiently develop and apply patient-specific computational models for real-time diagnosis and treatment plans of OSAHS via snoring signals. Although a preliminary attempt is presented, further areas for improvement are still necessary for a complete model. Common to modelling of all physiological systems, one of the main issues for accurate simulation of FSI in the upper airway, is applying realistic material properties for the relevant tissues (Heil & Hazel, 2011). With progress in development of non-intrusive techniques for in-vivo measurements of tissue properties, such as those proposed in Cheng *et al.* (2011), current upper airway tissue modelling may be further improved with more accurate constitutive models.

Neurological factors play an important role in controlling upper airway tissue tones and therefore, compliance, which influence severity of both snoring and OSAHS. Current model has not considered neuromuscular control or reaction into the constitutive properties of the upper airway tissue. Recent developments of correlating electromyogram (EMG) readings to model genioglossal muscle activation in Huang *et al.* (2005*a*), may be further incorporated into patient-specific upper airway models and a similar approach employed for other upper airway tissues.

FSI simulation for the current realistic model in this project, with approximately 2.5 million elements, took approximately 100 hours to complete using 40 parallel processors. Further scope for completing simulation, appropriate for clinical application, may be further explored. Apart from obvious massive parallelization, there may be scope for developing appropriate reduced-order models to predict variation of critical flow rate with degree of palatal obstruction, using present 3-D realistic upper airway. Identifying key variables and undertaking appropriate parametric investigation, may

allow approximate multi-variable relationship to be established.

Finally, more accurate interpretation of palatal snoring signals for non-invasive measurement or diagnostic purposes, may require soft palate contact with pharyngeal walls to be modeled into the present 3-D realistic upper airway. Thus, applying a 3-D immersed boundary method may also be explored.

In summary, there are still many areas that require further research in employing computational means for analyzing and diagnosing both snoring and OSAHS. The work presented within has contributed to further enhance computational modelling towards such goals.

References

Abeyratne, Udantha R, Wakwella, Ajith S. & Hukins, Craig 2005 Pitch jump probability measures for the analysis of snoring sounds in apnea. *Physiological Measurement* **26**, 779–798.

Agrawal, S., Stone, P., McGuinness, K., Morris, J. & Camilleri, A. E. 2002 Sound frequency analysis and the site of snoring in natural and induced sleep. *Clinical Otolaryngology* **27**, 162–166.

Ahmed, S. A. & Giddens, D. P. 1983 Velocity measurement in steady flow through axisymmetric stenoses at moderate Reynolds Number. *Journal of Biomechanics* **16**, 505–516.

ANSYS Inc. 2010 *ANSYS CFX Solver Theory Guide - Release 12*.

Auregan, Y. & Depollier, C. 1995 Snoring: Linear stability analysis and in-vitro experiments. *Journal of Sound and Vibration* **188** (1), 39–54.

Ayappa, Indu & Rapoport, David M. 2003 The upper airway in sleep: Physiology of the pharynx. *Sleep Medicine Reviews* **7** (1), 9–33.

Baaijens, Frank P. T. 2001 A fictitious domain/mortar element method for fluid-structure interaction. *International Journal for Numerical Methods in Fluids* **35**, 743–761.

Balint, T.S. & Lucey, A.D. 2005 Instability of a cantilevered flexible plate in viscous channel flow. *Journal of Fluids and Structures* **20**, 893–912.

Balint, Tibor S. 2001 Dynamics of the upper airway. PhD thesis, University of Warwick.

Bearpark, Helen, Elliott, Lynne, Grunstein, Ron, Cullen, Stewart, Schneider, Hartmut, Althaus, Wilma & Sullivan, Colin 1995 Snoring and sleep apnea. a population study in Australian men. *American Journal of Respiratory and Critical Care Medicine* **151** (5), 1459–1465.

Beck, R., Odeh, M., Oliven, A. & Gavriely, N. 1995 The acoustic properties of snores. *European Respiratory Journal* **8**, 2120–2128.

Bertram, C.D. & Tscherry, J. 2006 The onset of flow-rate limitation and flow-induced oscillations in collapsible tubes. *Journal of Fluids and Structures* **22**, 1029–1045.

Bertram, C. D. 2008 Flow-induced oscillation of collapsed tubes and airway structures. *Respiratory Physiology & Neurobiology* **163**, 256–265.

Bertram, C. D., Raymond, C. J. & Pedley, T. J. 1990 Mapping of instabilities for flow through collapsed tubes of different length. *Journal of Fluids and Structures* **4**, 125–154.

Bertram, C. D., Raymond, C. J. & Pedley, T. J. 1991 Application of nonlinear dynamics concepts to the analysis of self-excited oscillations of a collapsible tube conveying a fluid. *Journal of Fluids and Structures* **5**, 391–426.

Birch, M. J. & Srodon, P. D. 2009 Biomechanical properties of the human soft palate. *Cleft Palate-Craniofacial Journal* **46** (3), 268–274.

Bradley, TD, Brown, IG, Grossman, RF, Zamel, N, Martinez, D, Phillipson, EA & Hoffstein, V 1986 Pharyngeal size in snorers, nonsnorers and patients with obstructive sleep-apnea. *New England Journal of Medicine* **315** (21), 1327–1331.

Brietzke, S. E. & Mair, E. A. 2006 Acoustical analysis of snoring: Can the probability of success be predicted? *Otolaryngology-Head and Neck Surgery* **135** (3), 417–420.

Brown, I. G., Bradley, T. D., Phillipson, E. A., Zamel, N. & Hoffstein, V. 1985 Pharyngeal compliance in snoring subjects with and without obstructive sleep apnea. *American Review of Respiratory Disease* **132** (2), 211–215.

Burman, Erik & Fernndez, Miguel A. 2009 Stabilization of explicit coupling in fluidstructure interaction involving fluid incompressibility. *Computer Methods in Applied Mechanics and Engineering* **198**, 766–784.

Carroll, John L., McColley, Susanna A., Marcus, Carole L., Curtis, Shelly & Loughlin, Gerald M. 1995 Inability of clinical history to distinguish primary snoring from obstructive sleep apnea syndrome in children. *Chest* **108**, 610–618.

Causin, P., Gerbeau, J.F. & Nobile, F. 2005 Added-mass effect in the design of partitioned algorithms for fluids-structure problems. *Computer Methods in Applied Mechanics and Engineering* **194**, 4506–4527.

Cavusoglu, M., Ciloglu, T., Serinagaoglu, Y., Kamasak, M., Erogul, O. & Akcam, T. 2008 Investigation of sequential properties of snoring episodes for obstructive sleep apnoea identification. *Physiological Measurement* **29**, 879–898.

Chakraborty, Pinaki, Balachandar, S. & Adrian, Ronald J. 2005 On the relationships between local vortex identification schemes. *Journal of Fluid Mechanics* **535**, 189–214.

Cheng, S., Gandevia, S. C., Green, M., Sinkus, R. & Bilston, L. E. 2011 Viscoelastic properties of the tongue and soft palate using MR elastography. *Journal of Biomechanics* **44** (3), 450–454.

Chouly, Franz, Van Hirtum, Annemie, Lagree, Pierre-Yves, Paoli, Jean-Roch, Pelorson, Xavier & Payan, Yohan 2006 Simulation of the retroglossal fluid-structure interaction during obstructive sleep apnea. In *Lecture Notes in Computer Science* (ed. M. Harders & G. Szekely), , vol. 4072, pp. 48–57. Berlin: Springer-Verlag.

Chouly, Franz, Van Hirtum, Annemie, Lagree, Pierre-Yves, Pelorson, Xavier & Payan, Yohan 2008 Numerical and experimental study of expiratory flow in the case of major upper airway obstructions with fluid-structure interactions. *Journal of Fluids and Structures* **24**, 250–269.

Chouly, Franz, Van Hirtum, Annemie, Lagree, Pierre-Yves, Pelorson, Xavier & Payan, Yohan 2009 Modelling the human pharyngeal airway: Validation of numerical simulations using in vitro experiments. *Medical & Biological Engineering & Computing* **47**, 49–58.

Dalmasso, F. & Prota, R. 1996 Snoring: Analysis, measurement, clinical implications and applications. *European Respiratory Journal* **9**, 146–159.

Davies, R J, Ali, N J & Stradling, J R 1992 Neck circumference and other clinical features in the diagnosis of the obstructive sleep apnoea syndrome. *Thorax* **47** (2), 101–105.

Degroote, Joris, Annerel, Sebastiaan & Vierendeels, Jan 2010 The influence of the structural model on the stability of coupling iterations in partitioned fluid-structure interaction simulations. In *V European Conference on Computational Fluid Dynamics ECCOMAS CFD 2010* (ed. J. C. F. Pereira & A. Sequeira). Lisbon, Portugal.

Degroote, Joris, Bathe, Klaus-Jrgen & Vierendeels, Jan 2009*a* Performance of a new partitioned procedure versus a monolithic procedure in fluidstructure interaction. *Computers and Structures* **87**, 793801.

Degroote, Joris, Bruggeman, Peter, Haelterman, Robby & Vierendeels, Jan 2008 Stability of a coupling technique for partitioned solvers in FSI applications. *Computers and Structures* **86**, 2224–2234.

Degroote, Joris, Swillens, Abigail, Bruggeman, Peter, Haelterman, Robby, Segers, Patrick & Vierendeels, Jan 2009*b* Simulation of fluidstructure interaction with the interface artificial compressibility method. *Communications in Numerical Methods in Engineering* **DOI: 10.1002/cnm.1276**.

Denissen, Nicholas A., Yoder, Dennis A. & Georgiadis, Nicholas J. 2008 Implementation and validation of a laminar-to-turbulent transition model in the Wind-US code (Tech. Memo. NASA/TM2008-215451). *Tech. Rep.* NASA/TM2008-215451. National Aeronautics and Space Administration.

Donea, Jean, Huerta, Antonio, Ponthot, Jean-Philippe & Rodriguez-Ferran, Antonio 2004 Arbitrary lagrangian-eulerian methods. In *Encyclopedia of Computational Mechanics*. John Wiley & Sons.

Duck, F. A. 1990 *Physical Properties of Tissue: A Comprehensive Reference Book*. London: Academic Press.

Eckert, Danny J. & Malhotra, Atul 2008 Pathophysiology of adult obstructive sleep apnea. *Proc Am Thorac Soc* **5** (2), 144–153.

Engleman, H M, Martin, S E & Douglas, N J 1994*a* Compliance with CPAP therapy in patients with the sleep apnoea/hypopnoea syndrome. *Thorax* **49** (3), 263–266.

Engleman, H. M., Martin, S. E., Douglas, N. J. & Deary, I. J. 1994*b* Effect of continuous positive airway pressure treatment on daytime function in sleep apnoea/hypopnoea syndrome. *The Lancet* **343** (8897), 572–575.

Engleman, Heather M. & Wild, Matt R. 2003 Improving CPAP use by patients with the sleep apnoea/hypopnoea syndrome (sahs). *Sleep Medicine Reviews* **7** (1), 81–99.

Fajdiga, Igor 2005 Snoring imaging* : Could Bernoulli explain it all? *Chest* **128**, 896–901.

Farhat, C. & Lesoinne, M. 2000 Two efficient staggered algorithms for the serial and parallel solution of three-dimensional nonlinear transient aeroelastic problems. *Computer Methods in Applied Mechanics and Engineering* **182**, 499–515.

Fenn, W. O. & Rahn, H. 1964 *Handbook of Physiology: Respiration*. Washington: American Physiological Society.

Ferguson, K. A., Cartwright, R., Rogers, R. & Schmidt-Nowara, W. 2006 Oral appliances for snoring and obstructive sleep apnea: A review. *SLEEP* **29** (2), 244–262.

Fernandez, Miguel Angel & Moubachir, Marwan 2005 A Newton method using exact jacobians for solving fluidstructure coupling. *Computers and Structures* **83**, 127–142.

Fiz, J. A., Abad, J., Jan, R., Riera, M., Maanas, M.A., Caminal, P., Rodenstein, D. & Morera, J. 1996 Acoustic analysis of snoring sound in patients with simple snoring and obstructive sleep apnoea. *European Respiratory Journal* **9**, 2365–2370.

Forster, Christiane, Wall, Wolfgang A. & Ramm, Ekkehard 2007 Artificial added mass instabilities in sequential staggered coupling of nonlinear structures and incompressible viscous flows. *Computer Methods in Applied Mechanics and Engineering* **196**, 1278–1293.

Gerbeau, Jean-Frdric & Vidrascu, Marina 2003 A Quasi-Newton algorithm based on a reduced model for fluid-structure interaction problems in blood flows. *Tech. Rep.* 4691. INRIA Research Report No. 4691.

Gerstenberger, Axel & Wall, Wolfgang A. 2008 Enhancement of fixed-grid methods towards complex fluidstructure interaction applications. *International Journal for Numerical Methods in Fluids* **57**, 1227–1248.

Goldstein, D., Handler, R. & Sirovich, L. 1993 Modelling a no-slip flow boundary with an external force field. *Journal of Computational Physics* **105**, 354–366.

Gotsopoulos, Helen, Chen, Carol, Qian, Jin & Cistulli, Peter A. 2002 Oral appliance therapy improves symptoms in obstructive sleep apnea: A randomized, controlled trial. *Am. J. Respir. Crit. Care Med.* **166** (5), 743–748.

Griffith, Boyce E., Luo, Xiaoyu, McQueen, David M. & Peskin, Charles S. 2009 Simulating the fluid dynamics of natural and prosthetic heart valves using the immersed boundary method. *International Journal of Applied Mechanics* **1** (1), 137–177.

Guo, C. Q. & Paidoussis, M. P. 2000 Stability of rectangular plates with free side-edges in two-dimensional inviscid channel flow. *Journal of Applied Mechanics* **67**, 171–176.

Hahn, I. 1992 Modelling nasal airflow and olfactory mass transport. PhD thesis.

Hazel, Andrew L. & Heil, Matthias 2003 Steady finite-Reynolds-Number flows in three-dimensional collapsible tubes. *Journal of Fluid Mechanics* **486**, 79–103.

Heil, Matthias 2004 An efficient solver for the fully coupled solution of large-displacement fluidstructure interaction problems. *Computer Methods in Applied Mechanics and Engineering* **193**, 1–23.

Heil, Matthias & Hazel, Andrew L. 2011 Fluid-structure interaction in internal physiological flows. *Annual Review of Fluid Mechanics* **43**, 141–162.

Heil, Matthias & Waters, Sarah L. 2008 How rapidly oscillating collapsible tubes extract energy from a viscous mean flow. *Journal of Fluid Mechanics* **601**, 199–227.

Huang, L. 1995 Flutter of cantilevered plates in axial flow. *Journal of Fluids and Structures* **9**, 127–147.

Huang, Lixi, Quinn, S. James, Ellis, Peter D. M. & Williams, John E. Ffowcs 1995 Biomechanics of snoring. *Endeavour* **19**, 96–100.

Huang, Lixi & Williams, John E. Ffowcs 1999 Neuromechanical interaction in human snoring and upper airway obstruction. *Journal of Applied Physiology* **86** (6), 1759–1763.

Huang, Wei-Xi, Shin, Soo Jai & Sung, Hyung Jin 2007*a* Simulation of flexible filaments in a uniform flow by the immersed boundary method. *Journal of Computational Physics* **226**, 2206–2228.

Huang, Wei-Xi & Sung, Hyung Jin 2010 Three-dimensional simulation of a flapping flag in a uniform flow. *Journal of Fluid Mechanics* **653**, 301–336.

Huang, Yaqi, Malhotra, Atul & White, David P. 2005*a* Computational simulation of human upper airway collapse using a pressure-/state-dependent model of genioglossal muscle contraction under laminar flow conditions. *Journal of Applied Physiology* **99**, 1138–1148.

Huang, Yaqi, White, David P. & Malhotra, Atul 2005*b* The impact of anatomic manipulations on pharyngeal collapse: Results from a computational model of the normal human upper airway. *Chest* **128**, 1324–1330.

Huang, Yaqi, White, David P. & Malhotra, Atul 2007*b* Use of computational modeling to predict responses to upper airway surgery in obstructive sleep apnea. *Laryngoscope* **117**, 648–653.

Huynh, John, Kim, Ki Beom & McQuilling, Mark 2009 Pharyngeal airflow analysis in obstructive sleep apnea patients pre- and post-maxillomandibular advancement surgery. *Journal of Fluids Engineering* **131**, 091101.

Inthavong, Kiao, Wen, Jian, Tian, Zhaofeng & Tu, Jiyuan 2008 Numerical study of fibre deposition in a human nasal cavity. *Journal of Aerosol Science* **39**, 253–265.

Inthavong, Kiao, Wen, Jian, Tu, Jiyuan & Tian, Zhaofeng 2009 From CT scans to CFD modelling fluid and heat transfer in a realistic human nasal cavity. *Engineering Applications of Computational Fluid Mechanics* **3**, 321–335.

Isono, Shiroh, Feroah, Thom R, Hajduk, Eric A., Brant, Rollin, Whitelaw, William A. & Remmers, John E. 1997*a* Interaction of cross-sectional area, driving pressure, and airflow of passive velopharynx. *Journal of Applied Physiology* **83** (3), 851–859.

Isono, Shiroh, Remmers, John E., Tanaka, Atsuko, Sho, Yasuhide, Sato, Jiro & Nishino, Takashi 1997*b* Anatomy of pharynx in patients with obstructive sleep apnea and in normal subjects. *Journal of Applied Physiology* **82** (4), 1319–1326.

Isono, Shiroh, Shimada, Akiko, Utsugi, Makoto, Konno, Akiyoshi & Nishino, Takashi 1998 Comparison of static mechanical properties of the passive pharynx between normal children and children with sleep-disordered breathing. *American Journal of Respiratory and Critical Care Medicine* **157**, 1204–1212.

Jan, R., Fiz, J. A., Sol-Soler, J., Blanch, S., Artis, P. & Morera, J. 2003 Automatic snoring signal analysis in sleep studies. In *Proceedings of the 25th Annual International Conference of the IEEE EMBS*, pp. 366–369. Cancun, Mexico.

Jeong, Jinhee & Hussain, Fazle 1995 On the identification of a vortex. *Journal of Fluid Mechanics* **285**, 69–94.

Jeong, Soo-Jin, Kim, Woo-Seung & Sung, Sang-Jin 2007 Numerical investigation on the flow characteristics and aerodynamic force of the upper airway of patient with obstructive sleep apnea using computational fluid dynamics. *Medical Engineering & Physics* **29**, 637–651.

Johnston, Chris D. & Richardson, Andrew 1999 Cephalometric changes in adult pharyngeal morphology. *European Journal of Orthodontics* **21**, 357–362.

Jones, T. M., Swift, A. C., Calverley, P. M. A., Ho, M.S. & Earis, J. E. 2005 Acoustic analysis of snoring before and after palatal surgery. *European Respiratory Journal* **25**, 1044–1049.

Katz, A. I., Chen, Y. & Moreno, A. H. 1969 Flow through a collapsible tube. *Biophysical Journal* **9**, 1261–1279.

Kim, Yongsam 2003 The penalty immersed boundary method and its application to aerodynamics. PhD thesis, New York University.

Kim, Yongsam, Lim, Sookkyung, Raman, Subha V., Simonetti, Orlando P. & Friedman, Avner 2009 Blood flow in a compliant vessel by the immersed boundary method. *Annals of Biomedical Engineering* **37** (5), 927–942.

Kurt, Gokmen, Sisman, Cemal, Akin, Erol & Akcam, Timur 2011 Cephalometric comparison of pharyngeal airway in snoring and non-snoring patients. *European Journal of Dentistry* **5**, 84–88.

Langtry, R.B. & Menter, F.R. 2005 Transition modeling for general CFD applications in aeronautics. *AIAA* pp. Paper 2005–522.

Le, D.V., White, J., Peraire, J., Lim, K.M. & Khoo, B.C. 2009 An implicit immersed boundary method for three-dimensional fluidmembrane interactions. *Journal of Computational Physics* **228**, 8427–8445.

Lee, T. H., Abeyratne, U. R., Puvanendran, K. & Goh, K. L. 2001 Formant-structure and phase-coupling analysis of human snoring sounds for the detection of obstructive sleep apnea. In *Computer Methods in Biomechanics and Biomedical Engineering - 3* (ed. J. Middleton, M. L. Jones, N. G. Shrive & G. N. Pande), , vol. 3, pp. 243–248.

Lesoinne, M. & Farhat, C. 1996 Geometric conservation laws for flow problems with moving boundaries, and deformable meshes and their impact on aeroelastic computations. *Computer Methods in Applied Mechanics and Engineering* **134**, 71–90.

Lucey, Anthony D., King, A. J. C., Tetlow, G. A., Wang, J., Armstrong, J. J., Leigh, M. S., Paduch, A., Walsh, J. H., Sampson, D. D., Eastwood, P. R. & Hillman, D. R. 2010 Measurement, reconstruction, and flow-field computation of the human pharynx with application to sleep apnea. *IEEE Transactions on Biomedical Engineering* **57** (10), 2535–2548.

Luo, X. Y., Hinton, J. S., T., Liew T. & K., Tan K. 2004 LES modeling of flow in a simple airway model. *Medical Engineering & Physics* **26**, 403–413.

Luo, X. Y. & Pedley, T. J. 1995 A numerical simulation of steady flow in a 2-D collapsible channel. *Journal of Fluids and Structures* **9**, 149–174.

Luo, X. Y. & Pedley, T. J. 1996 A numerical simulation of unsteady flow in a two-dimensional collapsible channel. *Journal of Fluid Mechanics* **314**, 191–225.

Luo, X. Y. & Pedley, T. J. 1998 The effects of wall inertia on flow in a two-dimensional collapsible channel. *Journal of Fluid Mechanics* **363**, 253–280.

Malhotra, A., Huang, Y. Q., Fogel, R. B., Pillar, G., Edwards, J. K., Kikinis, R., Loring, S. H. & White, D. P. 2002 The male predisposition to pharyngeal collapse - importance of airway length. *American Journal of Respiratory and Critical Care Medicine* **166** (10), 1388–1395.

Malhotra, Atul & White, David P. 2002 Obstructive sleep apnoea. *The Lancet* **360** (9328), 237–245.

Maltais, F., Carrier, G., Cormier, Y. & Series, F. 1991 Cephalometric measurements in snorers, non-snorers and patients with sleep apnoea. *Thorax* **46**, 419–423.

Matthies, Hermann G. & Steindorf, Jan 2003 Partitioned strong coupling algorithms for fluidstructure interaction. *Computers and Structures* **81**, 805–812.

Mesquita, J., Fiz, J. A., Sol-Soler, J., Morera, J. & Jan, R. 2010 Regular and non regular snore features as markers of SAHS. In *32nd Annual International Conference of the IEEE EMBS*, pp. 6138–6141. Buenos Aires, Argentina.

Mihaescu, Mihai, Murugappan, Shanmugam, Kalra, Maninder, Khosla, Sid & Gutmark, Ephraim 2008 Large eddy simulation and Reynolds-Averaged Navier-Stokes modeling of flow in a realistic pharyngeal airway model: An investigation of obstructive sleep apnea. *Journal of Biomechanics* **41**, 2279–2288.

Min, Y., Titze, I. & Alipour, F. 1994 Stress-strain response of the human vocal ligament. *Tech. Rep.* NCVS Status and Progress, 7:131137.

Mittal, Rajat & Iaccarino, Gianluca 2005 Immersed boundary methods. *Annual Review of Fluid Mechanics* **37**, 239–261.

Mylavarapu, Goutham, Murugappan, Shanmugam, Mihaescu, Mihai, Kalra, Maninder, Khosla, Sid & Gutmark, Ephraim 2009 Validation of

computational fluid dynamics methodology used for human upper airway flow simulations. *Journal of Biomechanics* **42**, 1553–1559.

Netter, Frank H. 2011 Netter Medical Imaging, viewed July 2011. http://www.netterimages.com.

Onate, E., Cervera, M. & Zienkiewicz, O. C. 1994 A finite volume format for structural mechanics. *International Journal for Numerical Methods in Engineering* **37**, 181–201.

Osborne, J. E., Osman, E. Z., Hill, P. D., Lee, B. V. & Sparkes, C. 1999 A new acoustic method of differentiating palatal from non-palatal snoring. *Clinical Otolaryngology* **24**, 130–133.

Owens, Robert L, Eckert, Danny J, Yeh, Susie Yim & Malhotra, Atul 2008 Upper airway function in the pathogenesis of obstructive sleep apnea: A review of the current literature. *Current Opinion in Pulmonary Medicine* **14** (6), 519–524.

Payan, Yohan, Bettega, Georges & Raphael, Bernard 1998 A biomechanical model of the human tongue and its clinical implications. In *Lecture Notes in Computer Science* (ed. W. M. Wells, A. Colchester & S. Delp), , vol. 1496, pp. 688–695. Berlin: Springer-Verlag.

Pedley, T. J. 1992 Longitudinal tension variation in collapsible channels: A new mechanism for the breakdown of steady flow. *Journal of Biomechanical Engineering* **114**, 60–67.

Peppard, Paul E., Young, Terry, Palta, Mari & Skatrud, James 2000 Prospective study of the association between sleep-disordered breathing and hypertension. *New England Journal of Medicine* **342** (19), 1378–1384.

Perez-Padilla, J. Rogelio, Slawinski, E., Difrancesco, L. M., Feige, R. R., Remmers, J. E. & Whitelaw, W. A. 1993 Characteristics of the snor-

ing noise in patients with and without occlusive sleep apnea. *American Review of Respiratory Disease* **147** (3), 635–644.

Peskin, Charles S. 2002 The immersed boundary method. *Acta Numerica* pp. 479–517.

Peskin, Charles S. 2011 Personal communication.

Quinn, S. J., Huang, L., Ellis, P. D. M. & Williams, J. E. Ffowcs 1996 The differentiation of snoring mechanisms using sound analysis. *Clinical Otolaryngology* **21**, 119–123.

Rasani, M. R., Inthavong, Kiao & Tu, Ji Yuan 2011*a* Instability of a cantilever plate in obstructed channel flow. In *International Conference on Biomedical Engineering and Biotechnology (BEB)*. Shanghai.

Rasani, Mohammad Rasidi, Inthavong, Kiao & Tu, Ji Yuan 2011*b* Simulation of pharyngeal airway interaction with airflow using Low-Re turbulence model. *Modelling, Simulation and Engineering* p. ID 510472.

Rasani, M. R., Inthavong, Kiao & Tu, Ji Yuan 2011*c* Three-dimensional fluid-structure interaction modeling of expiratory flow in the pharyngeal airway. In *IFMBE Proceedings* (ed. Noor Azuan Abu Osman, Wan Abu Bakar Wan Abas, Ahmad Khairi Abdul Wahab & Hua-Nong Ting), *5th Kuala Lumpur International Conference on Biomedical Engineering*, vol. 35.

Richards, D., Bartlett, D. J., Wong, K., Malouff, J. & Grunstein, R. R. 2007 Increased adherence to CPAP with a group cognitive behavioral treatment intervention: A randomized trial. *SLEEP* **30** (5), 635–640.

Robinson, G. V., Stradling, J. R. & Davies, R. J. O. 2004 Obstructive sleep apnoea/hypopnoea syndrome and hypertension. *Thorax* **59**, 1089–1094.

Rodenstein, Daniel O., Dooms, Georges, Thomas, Yves, Liistro, Giuseppe, Stanescu, Dan C., Culee, C. & Aubert-Tulkens, Genevieve 1990 Pharyngeal shape and dimensions in healthy subjects, snorers and patients with obstructive sleep apnoea. *Thorax* **45**, 722–727.

Schmidt-Nowara, W., Lowe, A., Wiegand, L., Cartwright, R., Perezguerra, F. & Menn, S. 1995 Oral appliances for the treatment of snoring and obstructive sleep-apnea - a review. *SLEEP* **18** (6), 501–510.

Sforza, E., Bacon, W., Weiss, T., Thibault, A., Petiau, C. & Krieger, J. 2000 Upper airway collapsibility and cephalometric variables in patients with obstructive sleep apnea. *American Journal of Respiratory and Critical Care Medicine* **161**, 347–352.

Shapiro, A. H. 1977 Steady flow in collapsible tubes. *ASME Journal of Biomechanical Engineering* **99**, 126–147.

Sher, AE, Schechtman, KB & Piccirillo, JF 1996 The efficacy of surgical modifications of the upper airway in adults with obstructive sleep apnea syndrome. *SLEEP* **19** (2), 156–177.

Shome, B., Wang, L.-P., Santare, M. H., Prasad, A. K., Szeri, A. Z. & Roberts, D. 1998 Modelling of airflow in the pharynx with application to sleep apnea. *Journal of Biomechanical Engineering* **120**, 416–422.

Slone, A.K., Pericleous, K., Bailey, C. & Cross, M. 2002 Dynamic fluid-structure interaction using finite volume unstructured mesh procedures. *Computers and Structures* **80**, 371–390.

Sol-Soler, J., Jan, R., Fiz, J. A. & Morera, J. 2002 Pitch analysis in snoring signals from simple snorers and patients with obstructive sleep apnea. In *Proceedings of the Second Joint EMBS/BMES Conference*, pp. 1527–1528. Houston, TX, USA.

Sol-Soler, J., Jan, R., Fiz, J. A. & Morera, J. 2003 Spectral envelope analysis in snoring signals from simple snorers and patients with obstructive sleep apnea. In *Proceedings of the 25th Annual International Conference of the IEEE EMBS*, pp. 2527–2530. Cancun, Mexico.

Sol-Soler, J., Jan, R., Fiz, J. A. & Morera, J. 2005 Variability of snore parameters in time and frequency domains in snoring subjects with and without obstructive sleep apnea. In *Proceedings of the 2005 IEEE Engineering in Medicine and Biology 27th Annual Conference*, pp. 2583–2586. Shanghai, China.

Sol-Soler, Jordi, Jan, Raimon, Fiz, Jos Antonio & Morera, Jos 2007 Automatic classification of subjects with and without sleep apnea through snoring analysis. In *Proceedings of the 29th Annual International Conference of the IEEE EMBS*, pp. 6093–6096. Cit Internationale, Lyon, France.

Stouder, S., Jones, L., Brietzke, S. & Mair, E. A. 2007 Does an oral appliance reduce palatal flutter and tongue base snoring? *Otolaryngology-Head and Neck Surgery* **136** (5), 827–831.

Strobel, Richard J. & Rosen, Raymond C. 1996 Obesity and weight loss in obstructive sleep apnea: A critical review. *Sleep* **19** (2), 104–115.

Sun, Xiuzhen, Yu, Chi, Wang, Yuefang & Liu, Yingxi 2007 Numerical simulation of soft palate movement and airflow in human upper airway by fluid-structure interaction method. *Acta Mech Sin* **23**, 359–367.

Tang, Liaosha & Paidoussis, Michael P. 2007 On the instability and the post-critical behaviour of two-dimensional cantilevered flexible plates in axial flow. *Journal of Sound and Vibration* **305**, 97–115.

Tang, Liaosha & Paidoussis, Michael P. 2008 The influence of the wake on the stability of cantilevered flexible plates in axial flow. *Journal of Sound and Vibration* **310**, 512–526.

Tetlow, G. A. & Lucey, Anthony D. 2009 Motions of a cantilevered flexible plate in viscous channel flow driven by a constant pressure drop. *Communications in Numerical Methods in Engineering* **25**, 463–482.

Thomas, P.D. & Lombard, C.K. 1979 Geometric conservation law and its application to flow computations on moving grids. *AIAA Journal* **17**, 1030–1037.

Troell, Robert J., Li, Kasey K., Powell, Nelson B. & Riley, Robert W. 2000 Radiofrequency of the soft palate in snoring and sleep-disordered breathing. *Operative Techniques in Otolaryngology - Head and Neck Surgery* **11** (1), 21–23.

Tu, J. Y., Yeoh, Guan Heng & Liu, Chaoqun 2007 *Computational Fluid Dynamics - A Practical Approach*. Butterworth-Heinemann.

Van Hirtum, A, Chouly, F., Lagree, P. Y., Paoli, J. R., Payan, Y. & Pelorson, X. 2007 When a fluid-structure interaction keeps you awake: A physical approach to obstructive sleep apnea.

Van Hirtum, Annemie, Pelorson, Xavier & Lagree, Pierre-Yves 2005 In vitro validation of some flow assumptions for the prediction of the pressure distribution during obstructive sleep apnoea. *Medical & Biological Engineering & Computing* **43**, 162–171.

Veldi, Marlit, Vasar, Veiko, Vain, Arved & Kull, Mart 2004 Obstructive sleep apnea and ageing: Myotonometry demonstrates changes in the soft palate and tongue while awake. *Pathophysiology* **11**, 159–165.

Vierendeels, J., Dumont, K. & Verdonck, P.R. 2008 A partitioned strongly coupled fluid-structure interaction method to model heart valve dynamics. *Journal of Computational and Applied Mathematics* **215**, 602–609.

Vierendeels, Jan, Lanoye, Lieve, Degroote, Joris & Verdonck, Pascal 2007 Implicit coupling of partitioned fluidstructure interaction problems with reduced order models. *Computers and Structures* **85**, 970–976.

Vos, W., De Backer, J., Devolder, A., Vanderveken, O., Verhulst, S., Salgado, R., Germonpre, P., Partoens, B., Wuyts, F., Parizel, P. & De Backer, W. 2007 Correlation between severity of sleep apnea and upper airway morphology based on advanced anatomical and functional imaging. *Journal of Biomechanics* **40**, 2207–2213.

Walker, Regina P, Levine, Howard L, Terris, David J, Hopp, Martin L & Butler, David M 2004 Soft palate implants: A new treatment for obstructive sleep apnea? [abstract]. *Otolaryngology - Head and Neck Surgery* **131**, 170.

Wall, Wolfgang A., Gerstenberger, Axel, Gamnitzer, Peter, Forster, Christiane & Ramm, Ekkehard 2006 Large deformation fluid-structure interaction advances in ALE methods and new fixed grid approaches. In *Fluid-Structure Interaction: Modelling, Simulation, Optimisation (Lecture Notes in Computational Science and Engineering)* (ed. Hans-Joachim Bungartz & Michael Schafer), , vol. 53, pp. 195–232. Springer Verlag.

Xia, Guohua & Lin, Ching-Long 2008 An unstructured finite volume approach for structural dynamics in response to fluid motions. *Computers and Structures* **86**, 684–701.

Xu, Chun, Brennick, Michael J., Dougherty, Lawrence & Wootton, David M. 2009 Modeling upper airway collapse by a finite element model with regional tissue properties. *Medical Engineering & Physics* **31**, 1343–1348.

Xu, Chun, Sin, SangHun, McDonough, Joseph M., Udupa, Jayaram K., Guez, Allon, Arens, Raanan & Wootton, David M. 2006 Computational

fluid dynamics modeling of the upper airway of children with obstructive sleep apnea syndrome in steady flow. *Journal of Biomechanics* **39**, 2043–2054.

Young, T., Evans, L., Finn, L. & Palta, M. 1997 Estimation of the clinically diagnosed proportion of sleep apnea syndrome in middle-aged men and women. *Sleep* **20**, 705–706.

Young, Terry, Palta, Mari, Dempsey, Jerome, Skatrud, James, Weber, Steven & Badr, Safwan 1993 The occurrence of sleep-disordered breathing among middle-aged adults. *New England Journal of Medicine* **328** (17), 1230–1235.

Yucel, Aylin, Unlu, Mehmet, Haktanir, Alpay, Acar, Murat & Fidan, Fatma 2005 Evaluation of the upper airway cross-sectional area changes in different degrees of severity of obstructive sleep apnea syndrome: Cephalometric and dynamic CT study. *AJNR American Journal of Neuroradiology* **26**, 26242629.

Zhao, Moyin, Barber, Tracie, Cistulli, Peter, Sutherland, Kate & Rosengarten, Gary 2010 Computational fluid dynamic study of upper airway flow to predict the success of oral appliances in treating sleep apnea. In *17th Australasian Fluid Mechanics Conference*. Auckland, New Zealand.

Zhu, Luoding & Peskin, Charles S. 2002 Simulation of a flapping flexible filament in a flowing soap film by the immersed boundary method. *Journal of Computational Physics* **179**, 452–468.

Zienkiewicz, O. C. & Taylor, R. L. 2000 *The Finite Element Method Vol 1: The Basis*, 5th edn. Oxford: Butterworth-Heinemann.